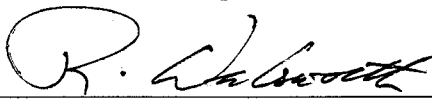HARVARD UNIVERSITY
Graduate School of Arts and Sciences

DISSERTATION ACCEPTANCE CERTIFICATE

The undersigned, appointed by the

Department of Chemistry & Chemical Biology

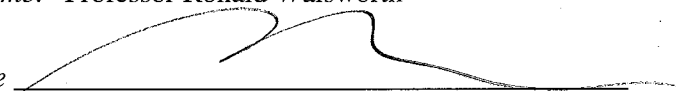have examined a dissertation entitled:

Nuclear Magnetic Resonance with Spin Singlet States and Nitrogen Vacancy Centers in Diamond

presented by : Stephen J. DeVience

candidate for the degree of Doctor of Philosophy and hereby certify that it is worthy of acceptance.

Signature _____

Typed name: Professor Ronald Walsworth

Signature _____

Typed name: Professor Matthew Rosen

Signature _____

Typed name: Professor Adam Cohen

Date: 05 May 2014

Nuclear Magnetic Resonance with Spin Singlet States and Nitrogen Vacancy Centers in Diamond

A dissertation presented

by

Stephen J. DeVience

to

The Department of Chemistry and Chemical Biology
in partial fulfillment of the requirements
for the degree of
Doctor of Philosophy
in the subject of

Chemistry

Harvard University
Cambridge, Massachusetts
May 2014

Thesis advisor   Author
Ronald L. Walsworth   **Stephen J. DeVience**

Nuclear Magnetic Resonance with Spin Singlet States and Nitrogen Vacancy Centers in Diamond

Abstract

Nuclear magnetic resonance (NMR) spectroscopy and magnetic resonance imaging (MRI) are techniques widely utilized by many scientific fields, but their applications are often limited by short spin relaxation times and low sensitivity. This thesis explores two novel forms of NMR addressing these issues: nuclear spin singlet states for extending spin polarization lifetime and nitrogen-vacancy centers for sensing small samples.

Part I presents studies of nuclear spin singlet states in organic molecules, beginning with a theoretical description of the singlet and related dressed quantum states before proceeding to the development of new techniques for singlet state spectroscopy. The long lifetimes and unique properties of singlet states makes them of interest for the storage of spin polarization, the study of slow dynamic processes, and the determination of molecular structure. Requirements for the creation of spin-locked singlet states are investigated and a model is derived for singlet state lifetime as a function of spin-locking power. A pulse sequence for targeting chemical species in complex mixtures, called "Suppression of Unwanted Chemicals using Contrast-Enhancing Singlet States" (SUCCESS), is then demonstrated for a number of biomolecules. Applications of singlet states in nearly-equivalent spins are explored, including the creation, manipulation, and readout of singlet states using a new technique called Spin-Lock

Induced Crossing (SLIC), and the transfer of polarization between singlet states. Finally, J-coupling spectroscopy using the SLIC pulse sequence is demonstrated at very low magnetic fields.

Part II presents the detection of NMR spectra from small numbers of nuclei in a nanoscale volume on a diamond surface using shallow nitrogen-vacancy (NV) centers as sensors. A theoretical description is developed for the NMR signal and the technique is demonstrated for proton, fluorine, and phosphorus NMR in a variety of samples. The method is then extended to micron-scale imaging of nuclear spin concentrations over a wide field of view, the determination of nitrogen-vacancy center depth, and the measurement of thin film thickness.

Contents

List of Figures

List of Tables

Publications

A large part of the work from chapter 3 has been published in:

DeVience, S. J., Walsworth, R. L. & Rosen, M. S. Dependence of nuclear spin singlet lifetimes on RF spin-locking power. *Journal of Magnetic Resonance* **218**, 5–10 (2012).

DeVience, S. J., Walsworth, R. L. & Rosen, M. S. Nuclear spin singlet states as a contrast mechanism for NMR spectroscopy. *NMR in Biomedicine* **26**, 1204–1212 (2013).

Walsworth, R. L., DeVience, S. J. & Rosen, M. S. Nuclear spin singlet states as a contrast mechanism for NMR spectroscopy (2013) US Patent Application PCT/US2013/028246.

The first half of chapter 4 has been published in:

DeVience, S. J., Walsworth, R. L. & Rosen, M. S. Preparation of Nuclear Spin Singlet States Using Spin-Lock Induced Crossing. *Physical Review Letters* **111**, 173002 (2013).

DeVience, S. J., Walsworth, R. L. & Rosen, M. S. Creation of nearly-equivalent nuclear spin singlet states using spin-lock induced crossing. US Patent Application PCT/US2014/019897.

Chapter 7 has been submitted for publication in:

DeVience, S. J., Pham, L. M., Bar-Gill, N., Belthangady C., Casola, F., Corbett, M., Lovchinsky, I., Sushkov, A. O., Zhang, H. Z., Lukin, M., Park, H., Yacoby & A., Walsworth, R. L. Nanoscale NMR Spectroscopy and Imaging of Multiple Nuclear Species. Submitted to *Nature Nanotechnology*.

Further publications are in preparation with material from chapters 4 and 5.

Acknowledgments

My experience at Harvard has been an enjoyable journey of scientific discovery, only made possible by the support and guidance of my wonderful advisors Ron Walsworth and Matt Rosen. I am particularly grateful to both for their enthusiasm toward exploring the unknown, as it was uncertain where my research might lead. Ron gave me encouragement to pursue ideas previously outside the group's focus, while consistently keeping the big picture of our research in view. Matt was always ready to try something new with his imager, and his technical expertise helped bring our ideas to fruition.

I am also indebted to my colleagues who consistently make great science possible. Linh Pham and I worked closely to demonstrate NV NMR, and I am thankful for her dedication and perseverence, as well as for the movie nights and the ample supply of candy she supplied to liven up the lab. Our project would also not be possible without the great fabrication skills of Huiliang Zhang and the help of Francesco Casola and Maddy Corbett. I am grateful to Nir Bar-Gill, Chinmay Belthangady, David Glenn, David Le Sage, and Alex Glenday for their constant technical and conceptual support. I want to especially thank David Phillips for his wise suggestions and fruitful conversations over many lunches. In addition, I thank my labmates for making the Walsworth lab a great place to work, including Alexei Trifonov, Chih-Hao Li, J. C. Jaskula, Keigo Arai, Erik Bauch, Nick Langellier, Paul Lee, and John Barry. From Matt Rosen's lab, I am especially grateful for the help from Brandon Armstrong and Mattheiu Sarracanie. Considerable assistance also came from Misha Lukin, Hongkun Park, Paola Cappellaro, Ashok Ajoy, Igor Lovchinsky, and Alex Sushkov. Thanks also to Adam Cohen for serving on my advising and thesis committees.

Of course my journey would not have been possible without the consistent support of my family, particularly my wife Eva, my uncle John Boehm, and my parents Mark and Andrea. Eva has stood by me during even the most trying times and has always added joy to my life outside the lab. My Uncle John helped get me started in science, and I am indebted to him for the nearly endless supply of books and free equipment over the years. Finally, I am forever grateful to my parents for their love and support, which have helped make my dreams possible.

Chapter 1

Introduction to Nuclear Spin

Singlet States

Nuclear spin relaxation was recognized as a critical behavior of nuclear spin systems from the very beginning of nuclear magnetic resonance (NMR) spectroscopy. In 1942, Prof. Cornelius Gorter of the University of Amsterdam conducted an experiment to measure an NMR signal in lithium chloride and potassium fluoride crystals at liquid helium temperatures [1]. After many days searching for a signal without success, he concluded that NMR on bulk samples was not possible. A few years later, after Purcell, Bloch, and colleagues succeeded in detecting bulk NMR signals [2, 3], Gorter figured out why his name was not among them: his samples were too pure! The spin-lattice relaxation times of his samples were on the order of minutes, which prevented his spin system from effectively exchanging energy with his apparatus.

The spin-lattice relaxation time, denoted T_1, describes the rate at which a spin system exchanges energy with its physical surroundings, or lattice. This parameter

sets limits on NMR experiments at both short and long timescales. A long T_1 can make experiment times unreasonable, as one must wait for the system to relax between successive measurements. Fortunately for most users of NMR spectroscopy, the spin-lattice relaxation time for liquids is on the order of seconds to minutes, and it can be controllably shortened with paramagnetic agents. On the other hand, a short T_1 can be a liability for experiments in which polarization must be preserved for long periods, such as in metabolic studies using hyperpolarized tracers and in measurements of slow processes, such as diffusion, chemical exchange, and coherence transfer mediated by weak couplings [4–7]. For decades, T_1 was seen as a fundamental maximum limit for experiment lengths that could only be increased using nuclei with lower gyromagnetic ratios, which are less sensitive to the environment but also more difficult to detect.

Early on, it was realized that interactions between spins could produce new spin states with different properties than the individual component spins. One such spin state with an extremely slow relaxation rate was discovered in molecular hydrogen [8]. The nuclear spins of a hydrogen molecule can pair into one of two spin-isomers, *para-* or *ortho*-hydrogen, with different physical properties. In *para*-hydrogen, the nuclear spins form an antisymmetric spin singlet state with total spin 0, whereas in *ortho*-hydrogen the spins populate three symmetric spin triplet states with total spin 1. Because the energy difference between the states is very small, at room temperature the population of each state is approximately equal, with 3/4 of hydrogen molecules in one of the three triplet states and 1/4 in the singlet state. However, at low temperature *para*-hydrogen is more stable and predominates. The two forms of hydrogen interconvert extremely slowly under normal conditions, as the strongest

relaxation mechanisms are unable to act between states of differing symmetry. This made it difficult to store liquid hydrogen for uses such as rocket fuel. At cryogenic temperatures, significant energy is released as *ortho*-hydrogen slowly relaxes to *para*-hydrogen, which left unchecked creates significant boiloff of the hydrogen. A solution was found in a catalyst that speeds up the interconversion during liquefaction [9].

Analogous singlet states were known to exist in other molecules with pairs of identical nuclear spins, but the singlet states cannot be addressed or detected directly with radiofrequency (RF) transitions and were generally ignored. The field of research was reawakened by Malcolm Levitt and coworkers, who showed that singlet spin states could be prepared in pairs of non-identical nuclei and preserved by moving the sample to a low magnetic field [10–12] or by spin-locking with a resonant RF field [13]. In both cases, resonance frequency differences between spins are suppressed to levels smaller than the spin-spin coupling, which causes the eigenstates to rearrange into singlet and triplet states. Just as *para*-hydrogen converts to *ortho*-hydrogen at a very slow rate, spin-locked singlet states were often found to relax at rates much slower than $1/T_1$; singlet states with lifetimes up to 37 T_1 have been measured in thermally-polarized samples [13–17]. These long-lived states were subsequently used to study slow processes such as diffusion, chemical exchange, and conformational dynamics *in vitro* [18–20].

Further advances allowed extended lifetimes to be achieved without awkwardly moving the sample to low field or applying microwave power for extensive time periods. Tayler *et al.* showed that for "nearly-equivalent spins," in which spin-spin coupling is significantly stronger than the resonance frequency difference, the small

admixture of triplet state allows magnetization to be transferred to the singlet state using an appropriate pulse sequence [21]. Feng *et al.* demonstrated a similar technique to create singlet states in identical nuclear spins on molecules with the appropriate symmetries [22]. Warren *et al.* showed that singlet states could also be formed by performing a chemical reaction to symmetrize the molecule and remove resonance frequency differences [23].

Despite the large repertoire of techniques for their manipulation, singlet states have not yet been extensively utilized for NMR spectroscopy, nor have they been exploited for clinical magnetic resonance imaging (MRI) applications. A major concern is that the RF power required for singlet state preparation and preservation in many demonstrations to date has been too high for human use. Moreover, while singlet state lifetimes of proton pairs can extend an order of magnitude longer than T_1, they are still generally shorter than T_1 for ^{13}C nuclei used in metabolic studies [4]. Part I of this thesis attempts to address such issues with new theoretical and experimental work on both spin-locked and nearly-equivalent singlet states.

The thesis begins by explaining the formation of nuclear spin singlet states, starting from basic NMR principles, in Chapter 2. The description differs slightly from previous works in its use of the dressed state formalism to describe the spin system during spin-locking. In Chapter 3, this formalism is used to predict the behavior of the spin-locked singlet state lifetime as a function of spin-locking power, which is explored experimentally to determine the RF power requirements for singlet experiments. Spin-locked singlet states are also utilized as part of a quantum filter to target molecules in a mixture when the target signals are hidden beneath a strong

spectral background. This scheme, titled SUCCESS for "Suppression of Unwanted Chemicals using Contrast-Enhancing Singlet States," makes use of the singlet state's symmetry properties rather than its extended lifetime, and is therefore applicable even to molecules whose singlet states are short-lived.

Chapter 4 describes novel techniques for the manipulation of nearly-equivalent singlet states. The dressed state formalism is used to derive a new pulse sequence for the transfer of magnetization between singlet and triplet states using Spin-Lock Induced Crossing (SLIC). SLIC is shown to provide a more efficient way to prepare the singlet state in nearly-equivalent spin pairs. It is then employed on multiple spin pairs to transfer polarization between two independent singlet states, which both allows for the measurement of small J-coupling differences whose detection is normally limited by spin-lattice relaxation and also opens the possibilities of creating a decoherence-free subspace for the storage of quantum information. Finally, SLIC is extended to more complex strongly-coupled spin states to perform J-coupling spectroscopy at low magnetic fields without the need for heteronuclei.

Chapter 2

The Quantum Origins of the Nuclear Spin Singlet State

This chapter presents the basic NMR theory needed to understand the properties of the nuclear spin singlet state and describes the conditions under which spin singlet states arise. The Hamiltonian and density matrix theory from this chapter will be used in subsequent discussions to derive pulse sequences for singlet state creation and to explore singlet relaxation properties. More extensive NMR theory can be found in references [24–27].

2.1   NMR Basics

Nuclear magnetic resonance is based on the manipulation and detection of nuclear spin states. Spin is a property of elementary and composite particles that describes the intrinsic angular momentum carried by the particle [28]. Particles with nonzero

spin include electrons, protons, neutrons, and photons. Unlike classical angular momentum, which results from a massive object rotating about an axis, spin angular momentum is an intrinsic property of the particle with no direct analogue in classical mechanics. Nevertheless, massive particles with non-zero spin possess a magnetic dipole moment just as a rotating charge does. Uncharged composite particles, such as the neutron, can also possess a magnetic moment because they are composed of charged particles (quarks) with nonzero spins and orbital angular momentum. Since the magnetic moment couples the particle to magnetic fields, the spin states can be controlled with external static and dynamic magnetic fields in a magnetic resonance experiment.

The total spin angular momentum of a particle or nucleus is described by the spin quantum number I, which is a fundamental property of the particle unaffected by electric or magnetic fields in its environment. (Note that I is typically used for nuclear spins and S for electron spins; however, in this chapter I refers to any type of spin.) I takes some value $n/2$, where n is an integer. For example, the electron, proton, and neutron all have spin quantum number $1/2$, while the ^{14}N nucleus has spin quantum number 1. When nuclei are constructed from protons and neutrons, the net spin is determined by the way the component spin vectors pair together. Sometimes spins pair up in the nuclear ground state to form spin-0 nuclei, as in the case of ^{12}C and ^{16}O. Nuclei with spin have values of I ranging from $1/2$ to 7, with even higher spin states possible for excited nuclear energy levels. This thesis will mainly concern itself with spin-1/2 nuclei, as they possess only a magnetic dipole moment. Higher-spin nuclei also possess higher moments, such as the electric quadrupole and magnetic

octupole, which couple them to electric field gradients and magnetic field gradients, respectively.

While the spin quantum number I describes the strength of the magnetic dipole moment, the secondary spin quantum number m_i is needed to describe its direction. It specifically describes the projection of angular momentum along an axis i of the spin system, and it takes a value from the range $-I, -I+1, ..., I-1, I$. Unlike I, the value of m_i can be manipulated in a magnetic resonance experiment with the proper application of magnetic fields.

The quantum numbers I and m_i are eigenvalues of the spin system determined by the action of angular momentum operators on the spin eigenstates. There are three angular momentum operators, $\hat{I}_i$, where $i = x, y, z$, which measure the angular momentum projected along each axis. The total angular momentum operator, $\hat{\boldsymbol{I}}$, is the sum of the angular momentum operators for the three axes, such that $\hat{\boldsymbol{I}} = \hat{I}_x \hat{\boldsymbol{x}} + \hat{I}_y \hat{\boldsymbol{y}} + \hat{I}_z \hat{\boldsymbol{z}}$. It is more convenient to work with the scalar operator $\hat{I}^2 = \hat{\boldsymbol{I}} \cdot \hat{\boldsymbol{I}}$, which allows us to define the angular momentum eigenvalue as

$$\hat{I}^2 |I, m_i\rangle = \hbar^2 I(I+1)|I, m_i\rangle, \tag{2.1}$$

where $\hbar$ is the reduced Plank constant. As a result of the uncertainty principle, the eigenvalues of $\hat{I}^2$ and $\hat{I}_i$ can only be known simultaneously for one axis, called the principle axis, which is generally chosen to be parallel to an applied static magnetic field and is labeled z. The angular momentum eigenvalue for axis z is given by

$$\hat{I}_z |I, m_z\rangle = \hbar m_z |I, m_z\rangle. \tag{2.2}$$

In this coordinate system, the operators $\hat{I}_x$ and $\hat{I}_y$ are not associated with their own eigenstates, but they instead produce interactions among the angular momentum

eigenstates $|I, m_z\rangle$. These operators are therefore best represented by the raising and lowering operators:

$$\hat{I}_x = \frac{\hat{I}^+ + \hat{I}^-}{2} \tag{2.3}$$

$$\hat{I}_y = \frac{\hat{I}^+ - \hat{I}^-}{2i}, \tag{2.4}$$

where

$$\hat{I}^+|I, m_z\rangle = \hbar\sqrt{(I - m_z)(I + m_z + 1)}|I, m_z + 1\rangle \tag{2.5}$$

and

$$\hat{I}^-|I, m_z\rangle = \hbar\sqrt{(I + m_z)(I - m_z + 1)}|I, m_z - 1\rangle. \tag{2.6}$$

The magnetic dipole moment that results from a particle's spin is given by the expectation value of the angular momentum vector:

$$\langle\boldsymbol{\mu}\rangle = \frac{gq}{2m}\langle\hat{\boldsymbol{I}}\rangle, \tag{2.7}$$

where $\boldsymbol{\mu}$ is the magnetic moment, g is the g-factor of the particle, q is the charge, and m is the mass of the particle. The g-factor takes the value $g = -2.002$ for the electron, $g = -3.826$ for the neutron, and $g = 5.586$ for the proton. For nuclei, the g-factors are calculated based on the number and pairings of protons and neutrons as well as contributions from orbital angular momentum and strong interactions within the nucleus.

All values of m_z are energetically degenerate unless there is a field present. A magnetic field breaks the symmetry of the spin system due to its interaction with the magnetic dipole moment. The energy of a magnetic dipole moment in a static magnetic field $\boldsymbol{B_0}$ is

$$E = -\boldsymbol{\mu} \cdot \boldsymbol{B_0}. \tag{2.8}$$

For convenience, we will define the principle axis (z-axis) to be parallel to $\boldsymbol{B_0}$, so that $B_x = B_y = 0$, and eigenstates are defined by the $\hat{I}_z$ operator. This allows us to correspond each angular momentum eigenstate $|I, m_z\rangle$ with an energy eigenstate $E(m_z)$. The energy is

$$E(m_z)|I, m_z\rangle = \hat{\mathcal{H}}_0|I, m_z\rangle = -\frac{gq}{2m}\hat{I}_z B_z|I, m_z\rangle = -\frac{gq}{2m}\hbar m_z B_z|I, m_z\rangle. \qquad (2.9)$$

For particles with $I > 1/2$, electric field gradients normally contribute significantly to the spin state energy as well due to the electric quadrupole moment.

Throughout this work, we will often find it most convenient to represent energy in terms of frequency with units of Hz, kHz, etc., implicitely dropping Planck's constant, h=energy/frequency. One must also be mindful that the gyromagnetic ratio is typically written in terms of rad/s:

$$\gamma_n = \frac{gq}{2m} \qquad (2.10)$$

We will more commonly use the resulting resonance frequency $\omega_0 = \gamma_n B_0$ in rad/s or $\nu_0 = \gamma_n B_0/2\pi$ in Hz. Then the energy eigenstates are given by

$$E(m_z)|I, m_z\rangle = -\nu_0\hat{I}_z|I, m_z\rangle. \qquad (2.11)$$

In organic molecules, the resonance frequencies of the nuclei differ from that of an isolated nucleus. The predominant cause is diamagnetic shielding from surrounding electrons. The resonance frequency ν_i for nucleus i can be calculated from its chemical shift δ_i by

$$\nu_i = (1 - \delta_i)\nu_0, \qquad (2.12)$$

where ν_0 is the resonance frequency of a reference spin in field B_0. The chemical shift δ is most commonly written in units of parts per million (ppm).

2.2 Rotating Frame Approximation

All quantum systems evolve in time according to the time-dependent Schrödinger equation

$$\frac{d}{dt}|\psi(t)\rangle = -i\hat{\mathcal{H}}|\psi(t)\rangle, \tag{2.13}$$

where $|\Psi(t)\rangle$ is a spin wavefunction. For a spin system, the wavefunction is written as a linear combination of the spin eigenstates of the system: $|\psi(t)\rangle = \sum_j c_j(t)|\phi_j\rangle$, where the constants are normalized such that $\sum_j |c_j(t)|^2 = 1$. Solutions for $c_j(t)$ can be found by solving

$$\frac{d}{dt}|\psi(t)\rangle = -i\omega_0 \hat{I}_z|\psi(t)\rangle. \tag{2.14}$$

The solution is

$$|\psi(t)\rangle = \exp(-i\omega_0 t\hat{I}_z)|\psi(0)\rangle, \tag{2.15}$$

where $|\psi(0)\rangle$ is the initial state of the spin system. In terms of the eigenstates, the time-dependent equation can be expressed as

$$|\psi(t)\rangle = \sum_j c_j \exp(-i\omega_0 t\hat{I}_z)|\phi_j\rangle, \tag{2.16}$$

where c_j is now independent of time.

The time dependence of the system can make calculations inconvenient. One can simplify the analysis by working in a rotating reference frame matched to the spin precession. This requires a transformation that makes the spin wavefunction time independent. The transformation is accomplished by writing a new wavefunction

$$|\psi(t)\rangle' = \exp(i\omega_{rot} t\hat{I}_z)|\psi(t)\rangle = \exp(-i(\omega_0 - \omega_{rot})t\hat{I}_z)\sum_j c_j|\phi_j\rangle. \tag{2.17}$$

It is evident that if $\omega_{rot} = \omega_0$, then the new wavefunction has no time dependence. The corresponding transformation for the Hamiltonian is

$$\hat{\mathcal{H}}' = \exp(i\omega_{rot}t\hat{I}_z)\hat{\mathcal{H}}\exp(-i\omega_{rot}t\hat{I}_z) - \omega_{rot}\hat{I}_z. \tag{2.18}$$

The first term is simply a rotating version of the original Hamiltonian. The second term represents the energy shift of the system resulting from the rotation. Because $\hat{I}_z$ commutes with itself, when $\hat{\mathcal{H}}_0\hat{I}_z = \omega_0\hat{I}_z$, transformation to the rotating frame simply shifts the energy such that $\hat{\mathcal{H}}_0'\hat{I}_z = (\omega_0 - \omega_{rot})\hat{I}_z$.

Now consider the spin system in the presence of an applied near-resonant RF field of amplitude B_1. If the field is applied at the rotating-frame frequency, ω_{rot}, then the Hamiltonian is

$$\hat{\mathcal{H}}_{RF} = \frac{\nu_n}{2}\left(\cos(\omega_{rot}t + \phi)\hat{I}_x + \sin(\omega_{rot}t + \phi)\hat{I}_y\right), \tag{2.19}$$

where ϕ is the phase of the RF field and $\nu_n = -\gamma_n B_1$ is called the nutation frequency or Rabi frequency. The expression can be rewritten in terms of exponentials. There is a theorem [27] stating that if three operators undergo cyclic commutation ($[\hat{A}, \hat{B}] = i\hat{C}$, $[\hat{B}, \hat{C}] = i\hat{A}$, and $[\hat{C}, \hat{A}] = i\hat{B}$) then

$$\exp(-i\alpha\hat{A})\hat{B}\exp(i\alpha\hat{A}) = \hat{B}\cos\alpha + \hat{C}\sin\alpha. \tag{2.20}$$

Since the angular momentum projection operators follow a cyclic commutation rule, one can write

$$\hat{\mathcal{H}}_{RF} = \frac{\nu_n}{2}\exp(-i(\omega_{rot}t + \phi)\hat{I}_z)\hat{I}_x\exp(i(\omega_{rot}t + \phi)\hat{I}_z). \tag{2.21}$$

Now when the full Hamiltonian $\hat{\mathcal{H}}_0 + \hat{\mathcal{H}}_{RF}$ is converted to the rotating frame by substitution into Eq. 2.18, it is easy to see that the result is a time-independent

operator

$$\hat{\mathcal{H}}' = \frac{\nu_n}{2} \exp(-i\phi\hat{I}_z)\hat{I}_x \exp(i\phi\hat{I}_z) + (\omega - \omega_{rot})\hat{I}_z, \qquad (2.22)$$

which is written more conveniently as

$$\hat{\mathcal{H}}' = \frac{\nu_n}{2} \left(\hat{I}_x \cos\phi + \hat{I}_y \sin\phi \right) + (\omega - \omega_{rot})\hat{I}_z. \qquad (2.23)$$

Thus a resonant RF field Hamiltonian can also be made independent of time, greatly simplifying the analysis of pulse sequences. Throughout this work we will generally be working in the rotating reference frame.

2.3   Density Operators: Pure and Mixed States

Consider the spin wavefunction for a single spin-1/2 nucleus, $|\psi\rangle = c_1|\phi_1\rangle + c_2|\phi_2\rangle$. If neither c_1 nor c_2 is zero, the spin is in a superposition state, as it can be found in either of the eigenstates. If an experiment could be conducted to detect the spin eigenstate, there would be a probability $p_1 = |c_1|^2$ of measuring the state $|\phi_1\rangle$ and probability $p_2 = |c_2|^2$ of measuring $|\phi_2\rangle$. Nevertheless, a measurement of the state $|\psi\rangle$ would always have an expectation value of 1, and so the spin system is considered to be in a pure state.

The same measurement results could be obtained if the system were in state $|\phi_1\rangle$ for part of the measurement time and $|\phi_2\rangle$ for part of the time, or if some fraction of identical spins were in state $|\phi_1\rangle$ while others were in $|\phi_2\rangle$. The system would then be said to reside in a mixed state. To represent this statistical information, it is convenient to employ the density matrix formalism. A density matrix ρ can be constructed from operators $\hat{A}_{ij}$ such that the expectation value $\langle \hat{A}_{ii}\rangle$ gives the

probability for the spin system to be in eigenstate $|\phi_i\rangle$. It is easily seen that such operators are defined by

$$\hat{A}_{ii} = p_{ii}|\phi_i\rangle\langle\phi_i|, \tag{2.24}$$

where p_{ii} is the probability of finding the system in eigenstate $|\phi_i\rangle$ and $|\phi_i\rangle\langle\phi_i|$ is the corresponding matrix operator for the state. Note that these operators lie along the density matrix diagonal. Coherent superposition states also contain off-diagonal matrix elements. For example, the probability that the system is in the superposition $|\psi\rangle = (|\phi_1\rangle + |\phi_2\rangle)/\sqrt{2}$ is

$$\hat{A}_{\psi} = p_{\psi}|\psi\rangle\langle\psi| = \frac{p_{\psi}}{2}\left(|\phi_1\rangle\langle\phi_1| + |\phi_1\rangle\langle\phi_2| + |\phi_2\rangle\langle\phi_1| + |\phi_2\rangle\langle\phi_2|\right). \tag{2.25}$$

The density matrix can represent both mixed states and pure states equally well. The purity of the density matrix is given by

$$\gamma = \text{tr}(\rho^2), \tag{2.26}$$

where a value of 1 represents a pure state, and 1/D is a fully mixed state for a D x D dimensioned density matrix.

All matrix operators can be mapped to combinations of the spin operators $\hat{I}_x$, $\hat{I}_y$, $\hat{I}_z$, and identity. For example,

$$|\phi_1\rangle\langle\phi_1| = \hat{I}_z + 1/2. \tag{2.27}$$

We will commonly write both spin states and Hamiltonians in terms of their corresponding matrix operators. For example, the Hamiltonian $\hbar\omega_0\hat{I}_z$ for a spin-1/2 system can be written as

$$\hat{\mathcal{H}} = \frac{1}{2}\hbar\omega_0\left(|\downarrow\rangle\langle\downarrow| - |\uparrow\rangle\langle\uparrow|\right), \tag{2.28}$$

where $|\uparrow\rangle$ represents the spin state aligned with B_0 and $|\downarrow\rangle$ represents the spin state anti-aligned with B_0. This can be conveniently represented as the matrix

$$\hat{\mathcal{H}} = -\hbar \begin{bmatrix} \frac{\omega_0}{2} & 0 \\ 0 & -\frac{\omega_0}{2} \end{bmatrix}, \tag{2.29}$$

which acts on the vector

$$|\psi\rangle = \begin{bmatrix} c_\uparrow |\uparrow\rangle \\ c_\downarrow |\downarrow\rangle \end{bmatrix}. \tag{2.30}$$

2.4 Multiple Spins and Spin-Spin Interactions

Thus far we have considered a single isolated spin. When multiple spins are present, new behavior can arise as a result of spin-spin interactions. Spins interact predominantly via magnetic dipole-dipole coupling, leading to both coherent and incoherent evolution of the spin system. Incoherent evolution causes relaxation and decoherence. Here we discuss how interactions produce coherent evolution that can change the physical properties of the spin system.

To keep track of the spin state of a multi-spin system, it is convenient to define product states that describe the different combinations of states obtainable. For example, a system with two spin-1/2 nuclei has product states $|\uparrow\uparrow\rangle, |\uparrow\downarrow\rangle, |\downarrow\uparrow\rangle$, and $|\downarrow\downarrow\rangle$. Spin-spin interaction terms contain products of single-spin operators and will therefore connect product states and drive evolution between them, just as single spin operators drive evolution of individual spin states. Product states have a magnetic quantum number that is a linear combination of the individual quantum numbers for their component spins, thus product states of two spin-1/2 nuclei can possess $m_z = 1$, $m_z = -1$, or $m_z = 0$, which are found from the application of the operator $\hat{I}_{1z} + \hat{I}_{2z}$

on the product state. Product states also have a total magnetic quantum number given by the operator $\hat{I}^2 = (\hat{\boldsymbol{I}_1} + \hat{\boldsymbol{I}_2})^2$. For two spin-1/2 nuclei this is expressed as

$$\hat{I}^2|I, m_z\rangle = \hbar^2 I(I+1)|I, m_z\rangle = \hbar^2 \left(\frac{3}{2} + 2\hat{\boldsymbol{I}_1} \cdot \hat{\boldsymbol{I}_1}\right)|I, m_z\rangle \tag{2.31}$$

$$= \hbar^2 \left(\frac{3}{2} + 2\hat{I}_{1z}\hat{I}_{2z} + \hat{I}_1^+\hat{I}_2^- + \hat{I}_1^-\hat{I}_2^+\right)|I, m_z\rangle. \tag{2.32}$$

All spin-spin interactions are mediated by magnetic dipole-dipole coupling between spin magnetic moments. The interaction has two parts: a tensor "dipolar" term describing the coupling between distant spins, and a scalar "contact" term describing the coupling between spins with overlapping wavefunctions. All spins interact via the dipolar component, but the contact term does not play a role in direct interactions between nuclei, since two nuclear wavefunctions do not overlap for the low-energy systems discussed in this thesis. However, the contact term does produce strong electron-nucleus interactions when the electron has s-orbital character, the only case in which the electron wavefunction overlaps a nucleus. Two nuclei can interact via the contact interaction in second-order via an electron whose wavefunction overlaps both nuclei. This is called J-coupling (or scalar coupling) and plays a significant role in molecular spin systems.

The dipolar component of the Hamiltonian between two spins, 1 and 2, is

$$\hat{\mathcal{H}}_{DD} = -\frac{\mu_0 \gamma_1 \gamma_2 \hbar^2}{4\pi}\left(\frac{3(\hat{\boldsymbol{I}_1} \cdot \boldsymbol{r_{12}})(\hat{\boldsymbol{I}_2} \cdot \boldsymbol{r_{12}})}{r_{12}^5} - \frac{\hat{\boldsymbol{I}_1} \cdot \hat{\boldsymbol{I}_2}}{r_{12}^3}\right), \tag{2.33}$$

where $\boldsymbol{r_{12}}$ is the vector connecting the locations of the two spins in space, r_{12} is the distance between the spins, γ_i is the gyromagnetic ratio of spin i, and μ_0 is the permeability of free space. The Hamiltonian is conveniently written in terms of the

single spin operators using the "dipolar alphabet":

$$\hat{\mathcal{H}}_{DD} = \frac{\mu_0 \gamma_1 \gamma_2 \hbar^2}{4\pi r_{12}^3}(\hat{A} + \hat{B} + \hat{C} + \hat{D} + \hat{E} + \hat{F}), \tag{2.34}$$

where

$$\begin{aligned}
\hat{A} &= (1 - 3\cos^2\theta)\hat{I}_{1z}\hat{I}_{2z} \\
\hat{B} &= -\frac{1}{4}(1 - 3\cos^2\theta)(\hat{I}_1^+\hat{I}_2^- + \hat{I}_1^-\hat{I}_2^+) \\
\hat{C} &= -\frac{3}{2}\sin\theta\cos\theta\exp(-i\phi)(\hat{I}_{1z}\hat{I}_2^+ + \hat{I}_1^+\hat{I}_{2z}) \\
\hat{D} &= -\frac{3}{2}\sin\theta\cos\theta\exp(i\phi)(\hat{I}_{1z}\hat{I}_2^- + \hat{I}_1^-\hat{I}_{2z}) \\
\hat{E} &= -\frac{3}{4}\sin^2\theta\exp(-2i\phi)(\hat{I}_1^+\hat{I}_2^+) \\
\hat{F} &= -\frac{3}{4}\sin^2\theta\exp(2i\phi)(\hat{I}_1^-\hat{I}_2^-). \tag{2.35}
\end{aligned}$$

The angles θ and ϕ describe the angles in spherical coordinates between the $\boldsymbol{z}$ axis and $\boldsymbol{r_{12}}$.

Each component of the dipolar term has a different type of effect on the spins. The term $\hat{A}$ simply perturbs the energy of the eigenstates, whereas the other terms connect product states, with $\hat{B}$ connecting product states of the same magnetic quantum number m_z, $\hat{C}$ and $\hat{D}$ connecting those one quantum number apart, and $\hat{E}$ and $\hat{F}$ connecting those two quantum numbers apart. The trigonometric terms cause components to dominate or disappear depending on orientation. For instance, at the magic angle $\theta = \arccos(\sqrt{1/3}) = 54.74°$, terms $\hat{A}$ and $\hat{B}$ become zero. For an ensemble of spins with random orientations, dipolar coupling produces energy shifts that broaden the resonance line significantly.

Fortunately, in liquid state NMR at moderate magnetic fields small molecules tumble at GHz rates, and the angles between spins average to zero within the spin

precession time. Dipolar coupling is therefore eliminated as a source of line broadening for liquids, although it still contributes to spin-lattice relaxation, spin-spin relaxation, and decoherence. In solids, the dipolar coupling can be decreased by spinning the sample at the magic angle to artificially produce reorientation.

The contact Hamiltonian between an electron and nucleus is

$$\hat{\mathcal{H}}_{contact} = -\frac{2}{3}\mu_0\gamma_e\gamma_n\hbar^2|\Psi(0)|^2\hat{\boldsymbol{I_1}} \cdot \hat{\boldsymbol{I_2}}, \tag{2.36}$$

where $|\Psi(0)|^2$ is the electronic wavefunction probability density at the nucleus and γ_e and γ_n are the electron and nuclear gyromagnetic ratios, respectively. The electron-mediated J-coupling interaction between two nuclei can be calculated from perturbation theory based on the contact interactions of each nucleus with the electronic wavefunction. In general, the interaction is described by a tensor connecting the two spin operators:

$$\hat{\mathcal{H}}_J = \hat{\boldsymbol{I_1}} \cdot \hat{J} \cdot \hat{\boldsymbol{I_2}}. \tag{2.37}$$

However, in the liquid state any anisotropy is averaged away by fast rotations, and one typically writes

$$\hat{\mathcal{H}}_J = J\hat{\boldsymbol{I_1}} \cdot \hat{\boldsymbol{I_2}} = J\left(\hat{I}_{1z}\hat{I}_{2z} + \frac{\hat{I}_1^+\hat{I}_2^- + \hat{I}_1^-\hat{I}_2^+}{2}\right). \tag{2.38}$$

The coupling strength J is a function of a number of structural parameters, including the bond order, bond angles, and the nuclear species involved. Note that the contact and scalar interactions can shift the energy of any product state but can only connect spin states with the same quantum number m_z.

When coupling connects product states, the bare-spin product states are no longer constants in time and are no longer the eigenstates of the system. The system is best

described by new "dressed" eigenstates that are linear combinations of the bare-spin product states. The new eigenstates can be found by diagonalizing the Hamiltonian matrix. For example, consider a system of two spin-1/2 nuclei with resonance frequencies ν_1 and ν_2 interacting via J-coupling. The spin wavefunction is

$$|\psi\rangle = \begin{bmatrix} c_{\uparrow\uparrow}| \uparrow\uparrow\rangle \\ c_{\uparrow\downarrow}| \uparrow\downarrow\rangle \\ c_{\downarrow\uparrow}| \downarrow\uparrow\rangle \\ c_{\downarrow\downarrow}| \downarrow\downarrow\rangle \end{bmatrix}, \tag{2.39}$$

and the Hamiltonian matrix for these states can be written as

$$\hat{\mathcal{H}} = h \begin{bmatrix} -\frac{\nu_1+\nu_2}{2} + \frac{J}{4} & 0 & 0 & 0 \\ 0 & \frac{\nu_2-\nu_1}{2} - \frac{J}{4} & \frac{J}{2} & 0 \\ 0 & \frac{J}{2} & \frac{\nu_1-\nu_2}{2} - \frac{J}{4} & 0 \\ 0 & 0 & 0 & \frac{\nu_1+\nu_2}{2} + \frac{J}{4} \end{bmatrix}. \tag{2.40}$$

Diagonalization of this matrix produces a new Hamiltonian containing only energy terms:

$$\hat{\mathcal{H}} = h \begin{bmatrix} -\frac{\nu_1+\nu_2}{2} + \frac{J}{4} & 0 & 0 & 0 \\ 0 & \frac{\sqrt{J^2+(\nu_2-\nu_1)^2}}{2} - \frac{J}{4} & 0 & 0 \\ 0 & 0 & -\frac{\sqrt{J^2+(\nu_2-\nu_1)^2}}{2} - \frac{J}{4} & 0 \\ 0 & 0 & 0 & \frac{\nu_1+\nu_2}{2} + \frac{J}{4} \end{bmatrix}. \tag{2.41}$$

The eigenstates of the new Hamiltonian are

$$|T_-\rangle = |\uparrow\uparrow\rangle$$

$$|\phi_0\rangle = \sin\frac{\theta_J}{2}|\uparrow\downarrow\rangle + \cos\frac{\theta_J}{2}|\downarrow\uparrow\rangle$$

$$|T_+\rangle = |\downarrow\downarrow\rangle$$

$$|\phi_S\rangle = \cos\frac{\theta_J}{2}|\uparrow\downarrow\rangle - \sin\frac{\theta_J}{2}|\downarrow\uparrow\rangle, \tag{2.42}$$

where θ_J is a mixing angle defined as

$$\theta_J = \arctan\left(\frac{J}{\Delta\nu}\right), \tag{2.43}$$

and $\Delta\nu = \nu_1 - \nu_2$. Note that because the J-coupling interaction only connects the two states with $m_z = 0$, only those two product states are mixed into new dressed eigenstates. When $J \gg |\Delta\nu|$, these two dressed states become

$$|\phi_0\rangle = |T_0\rangle = \frac{|\uparrow\downarrow\rangle + |\downarrow\uparrow\rangle}{\sqrt{2}},$$

$$|\phi_S\rangle = |S_0\rangle = \frac{|\uparrow\downarrow\rangle - |\downarrow\uparrow\rangle}{\sqrt{2}}. \tag{2.44}$$

The antisymmetric combination $|S_0\rangle$ is the singlet state, while the remaining three states are triplet states. Singlet and triplet describe the total angular momentum quantum number of the states, which is $I = 0$ for the singlet and $I = 1$ for the triplets.

Product states can also be dressed by single-spin operators acting on spins individually, for example through RF driving. If a spin-locking RF field is set to the average resonant transition frequency of the two spins (such as that given by eq. 2.21), the

rotating frame Hamiltonian for the bare-spin product states becomes

$$
\hat{\mathcal{H}} = h
\begin{bmatrix}
\frac{J}{4} & \frac{\nu_n}{2} & \frac{\nu_n}{2} & 0 \\[2mm]
\frac{\nu_n}{2} & \frac{\nu_2 - \nu_1}{2} - \frac{J}{4} & 0 & \frac{\nu_n}{2} \\[2mm]
\frac{\nu_n}{2} & 0 & \frac{\nu_1 - \nu_2}{2} - \frac{J}{4} & \frac{\nu_n}{2} \\[2mm]
0 & \frac{\nu_n}{2} & \frac{\nu_n}{2} & \frac{J}{4}
\end{bmatrix}.
\tag{2.45}
$$

Here ν_n is the effective spin nutation (Rabi) frequency resulting from the RF field, which drives single-quantum spin transitions. If we assume that J-coupling is small but non-zero, then diagonalizing this Hamiltonian yields four spin-locked eigenstates given by

$$
\begin{aligned}
|\phi_+\rangle &= \frac{1}{2}\left[(|\uparrow\downarrow\rangle + |\downarrow\uparrow\rangle) + \sin\theta_{SL}(|\uparrow\uparrow\rangle + |\downarrow\downarrow\rangle) + \cos\theta_{SL}(|\uparrow\downarrow\rangle - |\downarrow\uparrow\rangle)\right] \\
|\phi_0\rangle &= \frac{1}{\sqrt{2}}(|\uparrow\uparrow\rangle - |\downarrow\downarrow\rangle) \\
|\phi_S\rangle &= \frac{1}{\sqrt{2}}\left[\sin\theta_{SL}(|\uparrow\downarrow\rangle - |\downarrow\uparrow\rangle) - \cos\theta_{SL}(|\uparrow\uparrow\rangle + |\downarrow\downarrow\rangle)\right] \\
|\phi_-\rangle &= \frac{1}{2}\left[(|\uparrow\downarrow\rangle + |\downarrow\uparrow\rangle) - \sin\theta_{SL}(|\uparrow\uparrow\rangle + |\downarrow\downarrow\rangle) - \cos\theta_{SL}(|\uparrow\downarrow\rangle - |\downarrow\uparrow\rangle)\right].
\end{aligned}
\tag{2.46}
$$

The mixing angle θ_{SL} is controlled by the ratio of the spin-lock nutation frequency to the chemical shift splitting:

$$
\theta_{SL} = \arctan\left(\frac{2\nu_n}{\Delta\nu}\right).
\tag{2.47}
$$

At very large nutation rates ($\nu_n \gg \Delta\nu$), i.e., high RF spin-locking power, the spin-

locked eigenstates simplify to

$$|\phi_+\rangle = \frac{1}{2}(|\uparrow\downarrow\rangle + |\downarrow\uparrow\rangle + |\uparrow\uparrow\rangle + |\downarrow\downarrow\rangle)$$

$$= \frac{1}{\sqrt{2}}|T_0\rangle + \frac{1}{2}(|T_-\rangle + |T_+\rangle) \tag{2.48}$$

$$|\phi_0\rangle = \frac{1}{\sqrt{2}}(|\uparrow\uparrow\rangle - |\downarrow\downarrow\rangle) = \frac{1}{\sqrt{2}}(|T_-\rangle - |T_+\rangle) \tag{2.49}$$

$$|\phi_S\rangle = \frac{1}{\sqrt{2}}(|\uparrow\downarrow\rangle - |\downarrow\uparrow\rangle) = |S_0\rangle \tag{2.50}$$

$$|\phi_-\rangle = \frac{1}{2}(|\uparrow\downarrow\rangle + |\downarrow\uparrow\rangle - |\uparrow\uparrow\rangle - |\downarrow\downarrow\rangle)$$

$$= \frac{1}{\sqrt{2}}|T_0\rangle - \frac{1}{2}(|T_-\rangle + |T_+\rangle). \tag{2.51}$$

Note that the spin-locked singlet state $|\phi_S\rangle$ corresponds to $|S_0\rangle$ in this limit of large spin nutation frequency, whereas the three spin-locked triplet states are each mixtures of triplet states $|T_0\rangle$, $|T_+\rangle$, and $|T_-\rangle$.

Figure 2.1 shows the eigenstates and interactions for two spins under three sets of conditions: bare-spin product states, strong J-coupling, and strong resonant RF spin-locking. Note that in the presence of strong interactions, the new dressed-state energy levels are determined by the bare-spin interactions and the dressed states are coupled by the bare-spin energy differences. This swapping of energy and interaction terms is the basis for many phenomena studied in this thesis.

Although our examples have considered pairs of spin-1/2 nuclei, the definition of a singlet includes any correlated spin state with total angular momentum $I = 0$, which can encompass larger numbers of spins as well as higher-spin nuclei. For example, a four-spin state representing the product state of two singlets, $|S_0\rangle_1|S_0\rangle_2$, is also a singlet state, as is the state $(|T_+\rangle_1|T_-\rangle_2 - |T_0\rangle_1|T_0\rangle_2 + |T_-\rangle_1|T_+\rangle_2)/\sqrt{3}$. The possible singlet states for any set of spins can be found from a table of Clebsch-Gordan
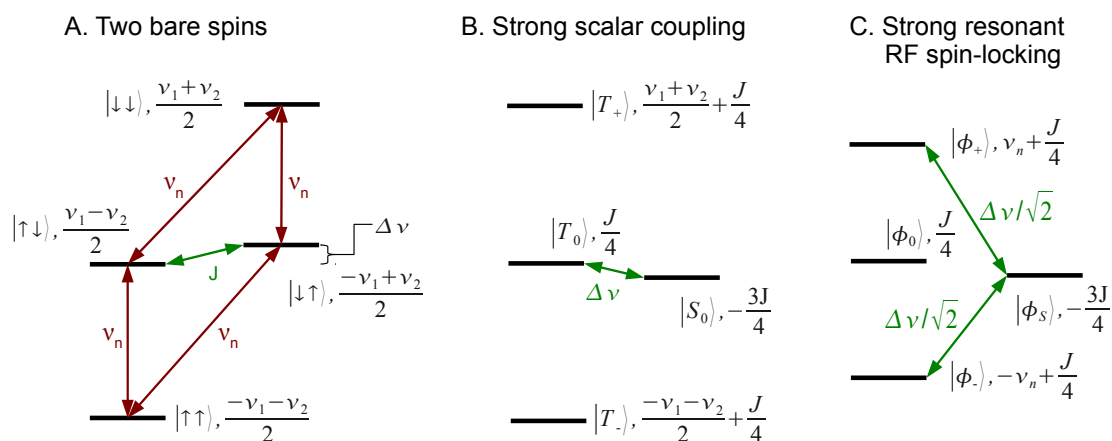
Figure 2.1: A system containing two spins with resonant transition frequencies ν_1 and ν_2 can be represented by four spin eigenstates. (A) In the bare-spin energy basis, there are four product states, and J-coupling or RF spin-locking interactions can drive transitions among the states (green and red arrows, respectively). (B) If the two spins are coupled strongly by scalar coupling ($J \gg \Delta\nu$, the chemical shift splitting), the product states are dressed into singlet and triplet states. Chemical shift differences can drive transitions between singlet and triplet. (C) Under strong RF spin-locking field ($\nu_n > 5\Delta\nu$), the product states are dressed into a singlet and three triplet states different from the scalar coupling case. Singlet-triplet transitions are again driven by chemical shift differences.

coefficients, although whether they actually define an eigenstate of the spin system will depend on the couplings among the spins.

We have shown that the nuclear spin singlet state can appear in two cases: large scalar coupling and strong RF spin-locking. While strong dipole-dipole coupling also produces dressed states, the dipole-dipole Hamiltonian's symmetry does not allow it to produce a singlet state. We will now turn our attention to experiments on singlet states created by strong spin-locking.

Chapter 3

Singlet States Produced by Spin-Locking

3.1 Effects of Spin-Locking Power on Singlet State Lifetime

The idea that singlet states could be produced from pairs of magnetically in-equivalent nuclei was first conceived and demonstrated by Malcolm Levitt and colleagues [10, 13]. Such inequivalent nuclear spins cannot form ideal, long-lived singlet states naturally, as the different local environments of the nuclear spins leads to rapid conversion to the triplet state and thus coupling to the environment, i.e., the singlet state is not an eigenstate of the system. Nonetheless, as Levitt *et al.* showed, a properly designed RF pulse sequence can prepare spins in a singlet state, which is then preserved from triplet interconversion by the application of a continuous resonant

RF field. This "spin-locking" field forces the average Hamiltonian of the two nuclear spins to be effectively equivalent, causing the singlet state to become an eigenstate of the system, as was shown in section 2.4. While the spin-locked singlet technique is applicable for a large variety of molecules [13–15, 20, 29], the large continuous RF power employed in spin-locking experiments to date implies an RF specific absorption rate (SAR) that is likely prohibitive for animal and human studies [30, 31].

Specifically, guidelines state that the SAR for a head image should not exceed 3.2 W/kg over a 6 minute period and should not exceed 6.4 W/kg over any 10 second period [31]. Although the actual SAR created by an MRI experiment must be calculated based on head and coil geometries, an estimate can be found by approximating the head as a sphere in a simple solenoidal coil. One can show [32] that the power dissipated by a linear AC magnetic field of amplitude B_{RF} with resonance frequency ν is

$$P_{diss} = \frac{\pi^3 D^5 \sigma \nu^2 B_{RF}^2}{120},$$ (3.1)

where σ is the conductivity of the brain, 0.4 S/m, and D is the head diameter. One must be careful to note that B_{RF} is twice the apparent B_1 field measured by the spin nutation frequency, because it also includes the counter-rotating polarization that does not contribute to the nuclear spin evolution.

Previous spin-locked singlet experiments used $B_1 = 82$ μT in a 9.4 T magnet [14]. Assuming a head diameter of 15 cm with a corresponding mass of 1.8 kg, the SAR would be 19 kW/kg! Even if one scales B_0 to a 1.5 T magnet typically found in the clinic and scales B_1 proportionally, SAR would be 12 W/kg, which would allow for only a 1/4 duty cycle.

With the goal of reducing the RF SAR to reasonable levels, we sought to find the minimum RF power required to preserve a spin-locked singlet state created from an arbitrary pair of spin-1/2 nuclei. We report measurements of singlet state lifetime for a variety of organic molecules and as a function of RF spin-locking field strength. We find that the measured RF power required to preserve a singlet state agrees well with the predictions of a simple theoretical model with inputs from the molecule's NMR spectrum. We also present measurements of a singlet-triplet coherence with an extended lifetime that does not require the use of RF spin-locking for preservation. Moreover, our findings demonstrate that for many molecules of interest, singlet lifetimes many times longer than T_1 can be achieved with much weaker RF spin-locking fields than have been used to date – more than an order of magnitude smaller than in previous studies – leading to both an RF power and an SAR more than 100 times lower. This result suggests that *in vivo* application of long-lived singlet NMR might be possible in biomolecules with the appropriate properties, despite limitations imposed by RF SAR.

3.1.1 Spin-Locking Pulse Sequence

The lifetime of a spin-locked singlet state can be measured with a simple experiment consisting of three stages: singlet state preparation, spin-locking, and singlet state readout. The long-lived singlet population is prepared most efficiently (up to 50% conversion) via a three-pulse sequence previously described by Levitt [33]. For the entirety of the sequence, the NMR transmitter frequency is set between the resonant frequencies of the two protons in the pair, so that the sum of resonance

frequencies in the rotating frame is zero. For thermally polarized spins, the system is initially in a state $I_{1z} + I_{2z}$. A $\pi/2$ pulse with phase x (i.e., positive rotation about the x-axis) is performed and followed by a delay τ_1, a π pulse, and a second delay τ_2, to produce the coherence $2I_{1y}I_{2z} - 2I_{1z}I_{2y}$. A $\pi/2$ pulse with phase -y then produces the state $-(2I_{1y}I_{2x} - 2I_{1x}I_{2y}) = i(I_1^+ I_2^- - I_1^- I_2^+)$, which is a zero-quantum coherence. A final delay τ_3 shifts the coherence phase to produce $I_1^+ I_2^- + I_1^- I_2^+$. This zero-quantum coherence represents the population $\rho_{ST} = |T_0\rangle\langle T_0| - |S_0\rangle\langle S_0|$ in the singlet-triplet basis. When $J \ll \Delta\nu$, the optimal delays are $\tau_1 = 1/(4J)$, $\tau_2 = 1/(4J) + 1/(2\Delta\nu)$, and $\tau_3 = 1/(4\Delta\nu)$. However, in cases where J-coupling is strong, the values must be computed from a model of the system's spin dynamics to take second-order effects into account. We used Levitt's *SpinDynamica* [34] package for *Mathematica* to simulate our systems and approximate optimal values. Figure 3.1a shows the spin dynamics during the preparation sequence before the application of spin-locking.

A long-lived coherence (LLC), as well as mixtures of the LLC and the singlet, can also be produced via a simpler two-pulse selective inversion sequence by removing the spin-echo component of Levitt's sequence. After the first $\pi/2$ pulse with phase x and the delay τ_1, the proton magnetizations become antialigned along the x-axis of the Bloch sphere. A $\pi/2$ pulse with phase -y then creates the population difference $I_{1z} - I_{2z}$. In the singlet-triplet basis, this represents the coherence $\rho_{LLC} = |T_0\rangle\langle S_0| + |S_0\rangle\langle T_0|$. However, J-coupling also leads to the formation of some $i(I_1^+ I_2^- - I_1^- I_2^+)$. The second delay, τ_2, can be used to choose the amount of $I_1^+ I_2^- + I_1^- I_2^+$, and thus long-lived singlet population, to mix with the long-lived coherence. Figure 3.1b shows the spin dynamics during the LLC preparation sequence before the application of spin-

locking. Note that either sequence can produce different mixtures of singlet and LLC depending on the time at which the RF spin-locking is first applied.
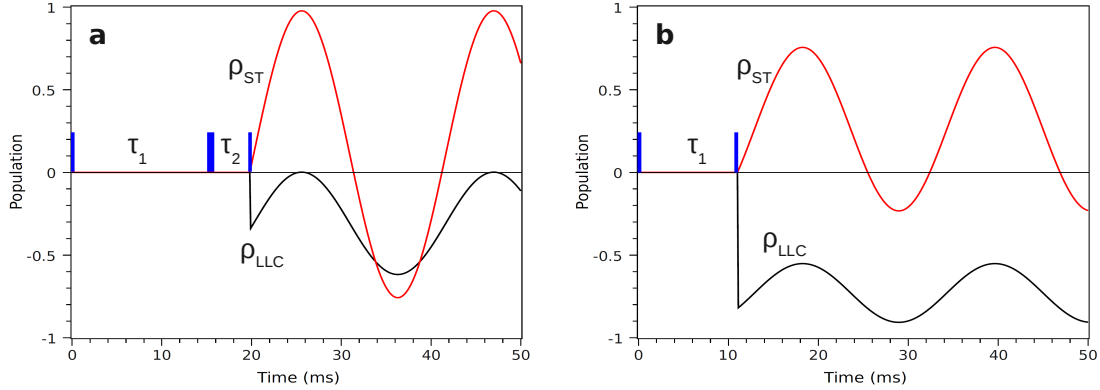
Figure 3.1: **(a)** Three-pulse sequence used to prepare the singlet-enhanced superposition ρ_{ST} by choosing the correct values for the delays. After the preparatory pulses, the amount of ρ_{ST} oscillates. **(b)** Two-pulse sequence used to create either a pure long-lived coherence, ρ_{LLC}, or a mixture of ρ_{LLC} and ρ_{ST}.

Following singlet state preparation, continuous RF spin-locking is applied for time τ_4. When the spin-locking is sufficiently strong, the singlet state becomes an eigenstate of the system and is therefore preserved from coherent evolution into other spin states. During this time, the singlet state relaxes with characteristic time T_S. Factors affecting singlet state relaxation will be discussed below.

To read out the singlet state, the RF spin-locking is removed and the system is allowed to evolve for a delay τ_5 before a $\pi/2$ pulse with phase x is applied and the free induction decay (FID) signal is acquired. Magnetization that was stored in the singlet state produces a unique antiphase signature (one peak positive, one peak negative). Figure 3.2 shows a complete sequence using this readout technique. Alternatively, the preparation sequence can be applied in reverse, omitting the final $\pi/2$ pulse. This transfers any polarization remaining in the singlet state back into
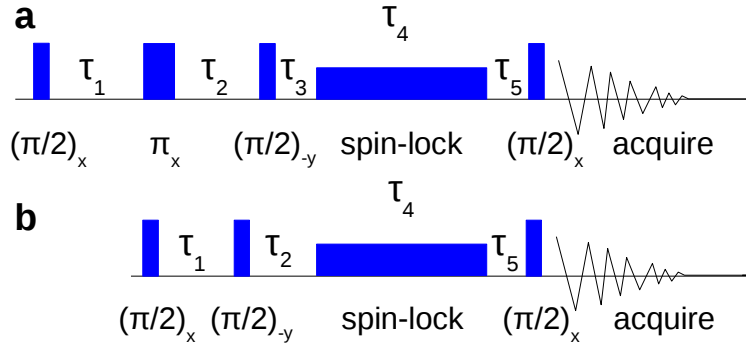
Figure 3.2: **(a)** The singlet-enhanced superposition state ρ_{ST} is initialized via a 3-pulse preparation sequence. **(b)** A long-lived coherence (LLC) between the singlet and triplet states ρ_{LLC}, as well as mixtures of the singlet and LLC states, are initialized via a 2-pulse preparation sequence. Both preparation sequences are followed by application of the RF spin-locking field and a signal acquisition pulse.

transverse magnetization, after which the FID is immediately acquired. The result is then a spectrum identical to a conventional $\pi/2$-FID acquisition, but with lower intensity. This technique will be discussed further in the next section. In either case, to remove any remaining triplet polarization, phase cycling is applied such that the experiment is repeated with both the first and last $\pi/2$ pulses applied with phase -x rather than x.

3.1.2 Singlet Relaxation as a Function of RF Power

In the singlet state, the total angular momentum quantum number is zero, and there is no net magnetic dipole moment. Hence interactions with the environment are weak and the rate of interconversion between singlet and triplet states is very slow, often much slower than the spin-lattice relaxation rate $1/T_1$. On the other hand, the triplet states have non-zero magnetic moments and couple strongly with the environment. Relaxation among the triplet states occurs on the timescale T_1.

Many relaxation mechanisms are forbidden by symmetry from converting the singlet state to triplet states. For example, magnetic dipole-dipole interactions between the singlet's two spins cannot couple the antisymmetric singlet state to the symmetric triplet states (Fig. 3.3). Since this intra-pair interaction is often the dominant driver of relaxation, the typical result is a singlet population with a lifetime T_S many times longer than the spin-lattice relaxation time T_1. Dipole-dipole interactions between the singlet spin pair and more distant spins can also lead to relaxation, but the singlet is protected from dipolar fluctuations common to both singlet spins: i.e., in the far-field the net dipole moment of the singlet is zero. Thus singlet state relaxation must instead occur through differential interactions on each spin of the singlet; these include chemical shift anisotropy (CSA), spin rotation (SR) due to collisions between molecules, and magnetic quadrupole interactions with a third spin [29, 35–38].

Since these three singlet relaxation mechanisms respond differently to the applied static magnetic field and temperature, the dominant effect can be determined experimentally. CSA has a strong magnetic-field dependence with a lifetime scaling as $T_{CSA} \propto 1/B_0^2$ [35]. Spin rotation collisions result in a lifetime scaling non-linearly with temperature as $T_{SR} \propto \exp(E/k_B T) \propto \frac{E}{k_B T}$ [35]. Magnetic quadrupole interactions, on the other hand, produce a singlet lifetime scaling linearly with temperature in the extreme-narrowing regime (when molecular rotation rates are much greater than the Larmor frequency). As demonstrated below, for the molecules used in the present study, the quadrupolar mechanism dominates singlet state relaxation, i.e., $T_S \approx T_Q$.

Magnetic quadrupole relaxation results from the two spins of the singlet interacting differently with a third spin. This relaxation mechanism was modeled at high

magnetic field by Tayler *et al.* [29], who derived an expression for the enhancement of the singlet lifetime[1]:

$$\frac{T_S}{T_1} = \frac{3b_{12}^2}{2\sum\limits_{j>2}(b_{1j}^2 + b_{2j}^2 - b_{1j}b_{2j}(3\cos^2\phi_{1j2} - 1))}.$$

(3.2)

Here spins 1 and 2 compose the singlet while j represents another nearby spin; $b_{jk} = \gamma_n^2/r_{jk}^3$ is a measure of the dipolar coupling strength between spins; and ϕ_{1j2} is the angle between the vectors connecting 1 with j and 2 with j. In principle, there is no limit to the singlet lifetime enhancement given the proper molecular geometry. However, in practice, other relaxation mechanisms gain importance if magnetic quadrupole relaxation is highly suppressed. In a previous study, equation 3.2 was found to agree well with measurements of singlet state lifetimes using high RF spin-locking power [29].

A detailed theoretical analysis of the singlet's lifetime during RF spin-locking has been given by Pileio and Levitt, who performed exact numerical calculations for the relationship between singlet lifetime and RF power [35, 36]. Here, we develop an approximate model that leads to a simple calculation of the measured singlet lifetime at a given spin-locking nutation frequency. Our model can easily be fit to measurements of singlet lifetime at a number of RF field strengths so that the maximum singlet lifetime can be extracted.

In the case that $\Delta\nu = |\nu_1 - \nu_2| \gg J$, there is little mixing of the bare spin-pair eigenstates. In this case unitary transformations, via the three-pulse sequence described in section 3.1.1, can transfer initial thermal spin polarization to the singlet

---

[1]Ref. [29] contains a typesetting error in which the summation has been taken over the whole expression rather than only the denominator.

a Two weakly-coupled spins   **b** Strong scalar coupling   **c** Strong resonant RF spin-locking
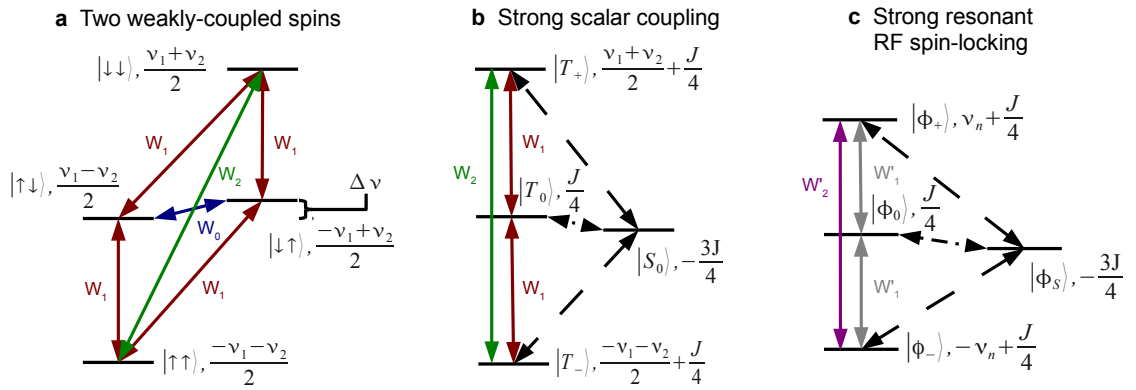
Figure 3.3: A system containing two spins with resonant transition frequencies ν_1 and ν_2 can be represented by four spin eigenstates. (A) For weak spin coupling, relaxation occurs via magnetic dipole-dipole interactions due to zero-, single-, and double-quantum transitions (with rates W_0, W_1, and W_2). (B) If the two spins are coupled strongly by scalar coupling ($J \gg \Delta\nu$, the chemical shift splitting), the bare-spin eigenstates are dressed into singlet and triplet states. The triplet states still interact via dipole-dipole interactions (solid lines), but singlet-triplet transitions are forbidden (dashed lines). (C) Dressing of the product states can also be induced by a strong RF spin-locking field ($\nu_n > 5\Delta\nu$), which produces a singlet state and three mixtures of triplet states. Singlet-triplet transitions are again forbidden. The new triplet states exhibit transition rates W_1' and W_2'.

state with at most 50% efficiency by creating the singlet-triplet population difference
[33]

$$\rho_{ST} = |T_0\rangle\langle T_0| - |S_0\rangle\langle S_0| \tag{3.3}$$

$$= |\uparrow\downarrow\rangle\langle\downarrow\uparrow| + |\downarrow\uparrow\rangle\langle\uparrow\downarrow|. \tag{3.4}$$

Similarly, the two-pulse sequence can transfer initial thermal spin polarization into a long-lived coherence between the singlet and triplet states with density matrix

$$\rho_{LLC} = |S_0\rangle\langle T_0| + |T_0\rangle\langle S_0| \tag{3.5}$$

$$= |\uparrow\downarrow\rangle\langle\uparrow\downarrow| - |\downarrow\uparrow\rangle\langle\downarrow\uparrow|. \tag{3.6}$$

A similar long-lived coherence has previously been studied as a way to extend T_2 [39, 40].

For both ρ_{ST} and ρ_{LLC}, population in the singlet state will be rapidly interconverted with the triplet states on a timescale $\sim 1/\Delta\nu$, providing strong coupling to the environment and thus rapid relaxation to the thermal state. However, as described in section 2.4, a strong on-resonance RF field can effectively maintain the singlet-enhanced superposition state ρ_{ST} [13, 33] by making $|S_0\rangle$ and $|T_0\rangle$ eigenstates of the system.

Consider again the dressed states formed by strong spin-locking:

$$|\phi_+\rangle = \frac{1}{2}(|\uparrow\downarrow\rangle + |\downarrow\uparrow\rangle + |\uparrow\uparrow\rangle + |\downarrow\downarrow\rangle)$$
$$= \frac{1}{\sqrt{2}}|T_0\rangle + \frac{1}{2}(|T_-\rangle + |T_+\rangle) \tag{3.7}$$

$$|\phi_0\rangle = \frac{1}{\sqrt{2}}(|\uparrow\uparrow\rangle - |\downarrow\downarrow\rangle) = \frac{1}{\sqrt{2}}(|T_-\rangle - |T_+\rangle) \tag{3.8}$$

$$|\phi_S\rangle = \frac{1}{\sqrt{2}}(|\uparrow\downarrow\rangle - |\downarrow\uparrow\rangle) = |S_0\rangle \tag{3.9}$$

$$|\phi_-\rangle = \frac{1}{2}(|\uparrow\downarrow\rangle + |\downarrow\uparrow\rangle - |\uparrow\uparrow\rangle - |\downarrow\downarrow\rangle)$$
$$= \frac{1}{\sqrt{2}}|T_0\rangle - \frac{1}{2}(|T_-\rangle + |T_+\rangle). \tag{3.10}$$

The spin-locked singlet state $|\phi_S\rangle$ corresponds to $|S_0\rangle$ in the limit of large spin nutation (i.e., large RF spin-locking field), whereas the three spin-locked triplet states are each mixtures of the states $|T_0\rangle$, $|T_+\rangle$, and $|T_-\rangle$. In this case, the initial density matrix ρ_{ST} is described well by equation 3.3. The singlet, $|S_0\rangle$, is well-protected by the RF spin-locking field, and after a short initial period during which the triplet states equilibrate, the remaining $|S_0\rangle$ component relaxes exponentially with the characteristic time predicted by equation 3.2.

In the high-RF-power regime, the long-lived coherence ρ_{LLC} is a sum of coherences containing $|\phi_+\rangle$, $|\phi_-\rangle$, and $|\phi_S\rangle$, which experience decoherence due to both dipole-dipole interactions and inhomogeneities in the RF spin-locking field.

If instead very small RF spin-locking power is applied ($\nu_n \ll \Delta\nu$), the singlet component of ρ_{ST} rapidly interconverts with the central triplet state, $|T_0\rangle$. When no RF power is applied, ρ_{ST} is a zero-quantum coherence that precesses in the transverse-plane, with a lifetime up to 3.25 T_1 if inter-pair dipole-dipole interactions are the sole relaxation mechanism [26]. The addition of a small amount of RF power quickly

decreases the lifetime of the ρ_{ST} coherence because the RF field efficiently drives single-quantum transitions but creates very little long-lived singlet component.

In the low-RF-power regime, the long-lived coherence ρ_{LLC} is well-described by equation 3.6 as a population difference between the two central bare-spin eigenstates. The conventional two-spin dipole-dipole relaxation model of Solomon [25, 41] predicts that in most cases $T_{LLC} = 3T_1$ (see appendix A.1).

For intermediate RF spin-locking power ($\nu_n \approx \Delta\nu$), a more complex analysis is required. For an arbitrary RF power, the initial state ρ_{ST} can be represented as

$$
\begin{aligned}
\rho_{ST} =& |\uparrow\downarrow\rangle\langle\downarrow\uparrow| + |\downarrow\uparrow\rangle\langle\uparrow\downarrow| \\
=& \frac{\cos^2\theta_{SL}}{2}(|\phi_+\rangle\langle\phi_-| - |\phi_+\rangle\langle\phi_+| + |\phi_-\rangle\langle\phi_+| - |\phi_-\rangle\langle\phi_-|) \\
&+ \frac{\cos\theta_{SL}\sin\theta_{SL}}{\sqrt{2}}(|\phi_-\rangle\langle\phi_S| - |\phi_+\rangle\langle\phi_S| + |\phi_S\rangle\langle\phi_-| - |\phi_S\rangle\langle\phi_+|) \\
&+ \frac{1}{2}(|\phi_+\rangle\langle\phi_+| + |\phi_+\rangle\langle\phi_-| + |\phi_-\rangle\langle\phi_+| + |\phi_-\rangle\langle\phi_-|) \\
&- \sin^2\theta_{SL}|\phi_S\rangle\langle\phi_S|, && (3.11)
\end{aligned}
$$

where the four spin-locked eigenstates are given by equation 2.46. Recall that

$$
\theta_{SL} = \arctan\frac{2\nu_n}{\Delta\nu}. \qquad (3.12)
$$

At moderate RF powers ($\nu_n > \Delta\nu$), ρ_{ST} is still mainly composed of the population $|\phi_S\rangle\langle\phi_S|$ and mixed triplet states. However, the eigenstate $|\phi_S\rangle$ no longer consists solely of the singlet $|S_0\rangle$. It also contains a triplet component $\cos\theta_{SL}(|T_-\rangle + |T_+\rangle)/\sqrt{2}$, which interacts with $|\phi_0\rangle$ via a double-quantum transition, with relaxation rate scaling as $\cos^2\theta_{SL}$. The triplet component also interacts with $|\phi_+\rangle$ and $|\phi_-\rangle$ via single-quantum transitions, with relaxation rate scaling as $\cos^2\theta_{SL}$; and via double quantum transitions, with relaxation rate scaling as $\cos^2\theta_{SL}\sin^2\theta_{SL}$.

The above scaling of the relaxation of ρ_{ST} suggests a model for the measured singlet lifetime as a function of RF spin-locking power:

$$\frac{1}{T_{S,measured}} = \frac{1}{T_L}\cos^2\theta_{SL} + \frac{1}{T_S} \tag{3.13}$$

$$= \frac{1}{T_L}\frac{1}{1 + (2\nu_n/\Delta\nu)^2} + \frac{1}{T_S}, \tag{3.14}$$

where T_L is the lifetime at low RF power and T_S is the maximum singlet lifetime, typically achieved at high RF power. Significantly, this model predicts that the measured singlet lifetime reaches 95% of its maximum value when the nutation rate ν_n is approximately 5 $\Delta\nu$.

Relaxation of the long-lived coherence ρ_{LLC} can be modeled using a similar analysis. In terms of the spin-locked eigenstates, we have:

$$\rho_{LLC} = |\uparrow\downarrow\rangle\langle\uparrow\downarrow| - |\downarrow\uparrow\rangle\langle\downarrow\uparrow|$$

$$= \cos\theta_{SL}(|\phi_+\rangle\langle\phi_+| - |\phi_-\rangle\langle\phi_-|)$$

$$+ \frac{\sin\theta_{SL}}{\sqrt{2}}(|\phi_S\rangle\langle\phi_+| + |\phi_+\rangle\langle\phi_S| + |\phi_S\rangle\langle\phi_-| + |\phi_-\rangle\langle\phi_S|). \tag{3.15}$$

At low RF spin-locking powers, the long-lived coherence is mainly composed of $|\phi_+\rangle\langle\phi_+| - |\phi_-\rangle\langle\phi_-|$, and these two eigenstates interact with one another via a zero-quantum transition. However, as the RF power is increased, these states begin to mix with $|T_+\rangle$ and $|T_-\rangle$, which opens up double-quantum transitions with relaxation rates scaling as $\sin^4\theta_{SL}$. A double-quantum transition with $|\phi_0\rangle$ also becomes available, with relaxation rate scaling as $\sin^2\theta_{SL}$. The latter relaxation rate increases more quickly with RF power and dominates at small θ_{SL}.

The above scaling suggests a simple model for the ρ_{LLC} relaxation rate:

$$\frac{1}{T_{LLC,measured}} = \frac{1}{T_{RF}} \sin^2 \theta_{SL} + \frac{1}{T_{LLC}} \tag{3.16}$$

$$= \frac{1}{T_{RF}} \frac{(2\nu_n/\Delta\nu)^2}{1 + (2\nu_n/\Delta\nu)^2} + \frac{1}{T_{LLC}}, \tag{3.17}$$

where $1/T_{LLC}$ is the relaxation rate at zero RF power and $1/T_{RF}$ is the additional relaxation rate due to the applied RF power.

We find that our model for the measured singlet lifetime agrees well with the detailed treatment of Pileio and Levitt (see eq. 43 in [35]), which contains terms up to eighth power in $\cos\theta_{SL}$. Our model includes only lowest-order terms, but satisfactorily describes the measured relationship between singlet lifetime and RF power, as described below. The two models deviate most at low RF powers ($\nu_n < \Delta\nu/2$), where higher-order terms in $\cos\theta_{SL}$ make larger contributions. Pileio and Levitt's numerical calculations for the relationship between singlet lifetime and RF power describe the singlet relaxation rate by

$$\frac{1}{T_S} \approx \frac{-b_{jk}^2 \tau_c}{160} \left[6(4\cos(\theta_\Delta) + \cos(2\theta_\Delta) - 17) \right.$$
$$\left. + \sqrt{6(281 + 360\cos(\theta_\Delta) + 196\cos(2\theta_\Delta) + 24\cos(3\theta_\Delta) + 3\cos(4\theta_\Delta))} \right], \tag{3.18}$$

where b_{jk} is the dipolar coupling strength, τ_c is the rotational correlation time of the molecule, and θ_Δ is the difference in tilt angles, which is defined as

$$\theta_\Delta = \arctan(\nu_j/\nu_n) - \arctan(\nu_k/\nu_n). \tag{3.19}$$

Here, ν_n is the nutation frequency induced by the RF field, while ν_j and ν_k are the resonance frequencies of the two spins. Note that this definition of θ_Δ differs from that given in eq. 24 of ref. [35], because eq. 43 requires a measurement of the tilt angle

away from the singlet-triplet basis rather than away from the Zeeman basis. Figure 3.4 compares the results of our simple model and the model of Pileio and Levitt for the dependence of the singlet state lifetime enhancement as a function of ν_n relative to the chemical shift difference $\Delta\nu = |\nu_1 - \nu_2|$ for a maximum singlet lifetime of $10\,T_1$. There is insignificant difference between the results of the two models once $\nu_n > \Delta\nu$.
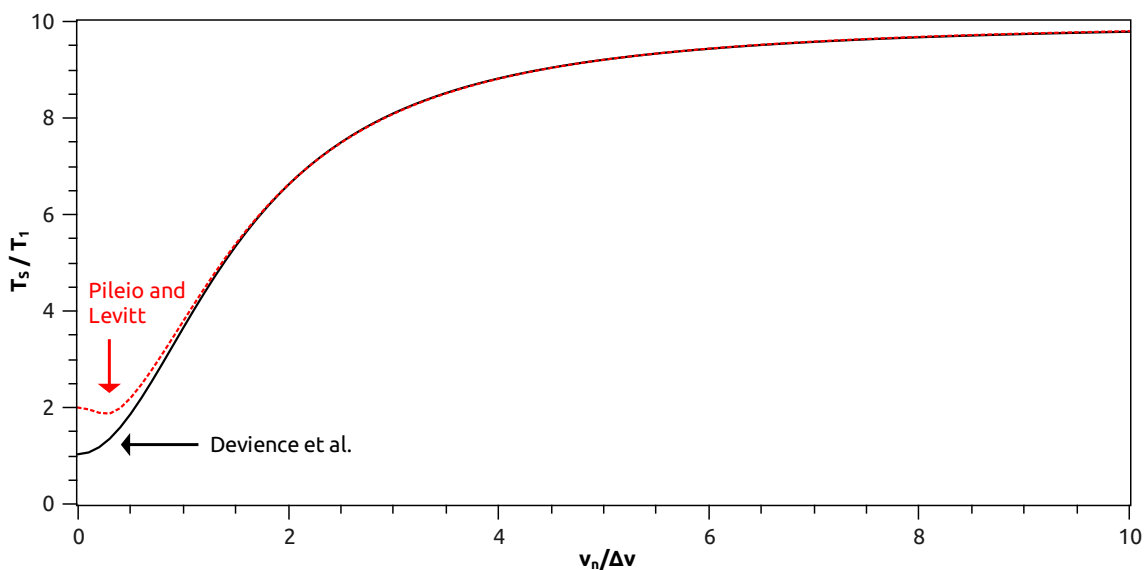
Figure 3.4: Comparison of the model given by eq. 3.16 and eq. 43 of ref. [35] for a singlet with lifetime $T_S = 10\,T_1$. The prefactor $b_{jk}^2\tau_c$ is set to $2/(3T_1)$, its value in the extreme-narrowing regime. A value of $T_L = 1.15\,T_1$ gives the best agreement between models. The models deviate most at very low RF powers, where higher-order terms become important.

3.1.3   Experimental Results

We performed NMR studies at 4.7 T of proton pair singlet states in a number of small organic molecules using a wide range of RF spin-locking powers. We chose citric acid and p-hydroxybenzoic acid, as Pileio *et al.* had previously studied these using

high RF power [14]. Additionally, we studied aspartic acid, *trans*-1,4-cyclohexanediol, and glycerol formal as examples of molecules with a range of structures.

Solutions of citric acid, aspartic acid, *p*-hydroxybenzoic acid (*p*-HBA), and 1,4-cyclohexanediol (1:1 *cis:trans* mixture, but creating singlet on *trans* isomer) were prepared in D_2O, with the addition of sodium hydroxide where necessary for dissolution. Glycerol formal was studied neat. Concentrations and conditions can be found in Table 3.1. All reagents were purchased from Sigma-Aldrich. All samples were prepared in 10 mm diameter NMR sample tubes and bubbled with nitrogen gas for three minutes. Spectra were acquired on a 200 MHz Bruker AMX spectrometer without sample spinning using a ^{1}H-BB dual-channel probe.

Table 3.1: Sample preparations for the study of long-lived states.

Molecule	Concentration	NaOH Concentration	Solvent
citric acid	0.26 M	0	D_2O
p-hydroxybenzoic acid	0.29 M	0.50 M	D_2O, H_2O
aspartic acid	0.020 M	1.0 M	D_2O
1,4-cyclohexanediol	0.41 M	0	D_2O
glycerol formal	neat	0	neat

Our experimental protocol (Fig. 3.2) initialized proton pairs into one of three different states: the singlet-triplet population difference ρ_{ST}, a long-lived coherence between singlet and triplet ρ_{LLC}, or a mixture of the two. Experiments shown in Fig. 3.2 were run on each compound using varying lengths for τ_4. Pulse sequence parameters can be found in Table 3.2. Between 8 and 32 averages were used to provide sufficient signal-to-noise. The intensity of each peak was then measured and plotted against τ_4. The resulting data were fit with a single exponential time decay. Multiple datasets were collected using different RF power levels for spin-locking. The RF power

Table 3.2: Delays, in ms, for pulse sequences used in the experiments: $\tau_1 - \tau_2 - \tau_3 - \tau_4 - \tau_5$

Molecule	Singlet	Coherence	Mixture
citric acid	12.5-3.7-6.0-τ_4-6.0	12.0-17.0-τ_4-15.5	12.0-12.0-τ_4-12.0
p-hydroxybenzoic acid	29.3-31.5-1.14-τ_4-1.14	2.0-3.75-τ_4-1.25	30.0-1.25-τ_4-1.25
aspartic acid	11.8-8.0-3.5-τ_4-4.0	-	7.4-7.0-τ_4-3.7
1,4-cyclohexanediol	-	-	4.2-3.0-τ_4-2.0
glycerol formal	-	-	31.0-15.0-τ_4-15.0

was characterized by measuring the nutation frequency induced by the RF B_1 field, which was calibrated by performing single-pulse experiments with increasing pulse lengths and measuring the frequency of the resulting sinusoidal curve. T_1 relaxation rates were measured with a conventional inversion-recovery experiment [27].

In all molecules studied, we measured the singlet (ρ_{ST}) lifetime to increase with the applied RF power, reaching a plateau at the maximum singlet lifetime, T_S, when $\nu_n > 5\Delta\nu$. In contrast, we found that the lifetime of the long-lived coherence decreases from its maximum value of T_{LLC} with the application of RF power. Both of these cases are well-modeled by equations 3.13 and 3.16 above. When we created a mixture of ρ_{ST} and ρ_{LLC}, the measured lifetime was that of the state with the longest lifetime at a given RF power, although the measured amplitude was lower as the contribution from the faster-relaxing state was quickly lost. We individually fit the two regimes of the mixed-state lifetime-vs.-RF-power measurements with the corresponding models for ρ_{ST} and ρ_{LLC}, which provided a good characterization of the system's behavior, as shown in Fig. 3.5a-c and Fig. 3.6a-b. Note that for each molecule studied, we found that the shortest mixed-state lifetime occurs near $\nu_n \approx \Delta\nu/2$. Results for maximum singlet and LLC lifetimes (T_S and T_{LLC}) are summarized in Table 3.3.

We also investigated possible mechanisms for proton-pair singlet relaxation. First,
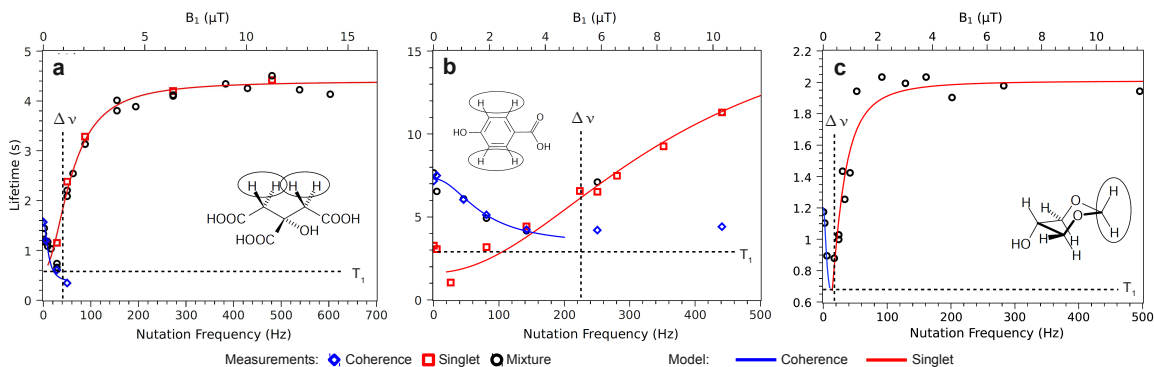
Figure 3.5: Measurements of the lifetimes of the singlet state, long-lived coherence (LLC), and a mixture of the two as a function of the effective RF spin-locking field B_1 for proton pairs in small organic molecules. Also shown are fits to models for the singlet and LLC lifetimes, as described in the main text. (A) Citric acid, $T_L = 500$ ms and $T_{RF} = 600$ ms; (B) p-hydroxybenzoic acid, $T_L = 2$ s and $T_{RF} = 7$ s; (C) glycerol formal, $T_L = 250$ ms and $T_{RF} = 1$ s; RF power is quantified by the induced nutation frequency about the B_1 field. Molecular structures are shown, protons of the singlet(s) are circled, and values for chemical shifts ($\Delta\nu$) and spin-lattice relaxation times (T_1) are indicated.

Table 3.3: Measured values of spin-lattice, singlet, and long-lived coherence (LLC) relaxation times.

Molecule	$T_1(s)$	$T_S(s)$	T_S/T_1	$T_{LLC}(s)$	T_{LLC}/T_1
citric acid	0.58 ± 0.03	4.5 ± 0.3	7.8 ± 0.7	1.5 ± 0.1	2.6 ± 0.2
p-HBA in D_2O	2.9 ± 0.1	16 ± 2	6.2 ± 0.8	7.3 ± 0.7	2.5 ± 0.3
p-HBA in H_2O	2.3 ± 0.1	5.8 ± 0.2	2.5 ± 0.1	3.9 ± 0.1	1.7 ± 0.1
aspartic acid	0.83 ± 0.03	7.48 ± 0.3	9.0 ± 0.5	2.3 ± 0.4	2.8 ± 0.5
1,4-cyclohexanediol	1.34 ± 0.02	3.9 ± 0.9	2.9 ± 0.7	2.90 ± 0.01	2.16 ± 0.03
glycerol formal	0.68 ± 0.01	1.91 ± 0.03	2.81 ± 0.06	1.37 ± 0.02	2.01 ± 0.04

we compared our measurements with those at other magnetic fields to probe the importance of chemical-shift anisotropy (CSA) relaxation (see Table 3.3). Our result of $T_S = 4.5$ s and 7.8-fold lifetime enhancement over T_1 for citric acid at 4.7 T is consistent with a previous measurement of 4.81 s and 7.6 T_1 at 9.4 T [14]. Due to hardware limitations, there was insufficient RF power to attain the maximum singlet lifetime for p-hydroxybenzoic acid. Nevertheless, a fit to data at finite RF power gave

42
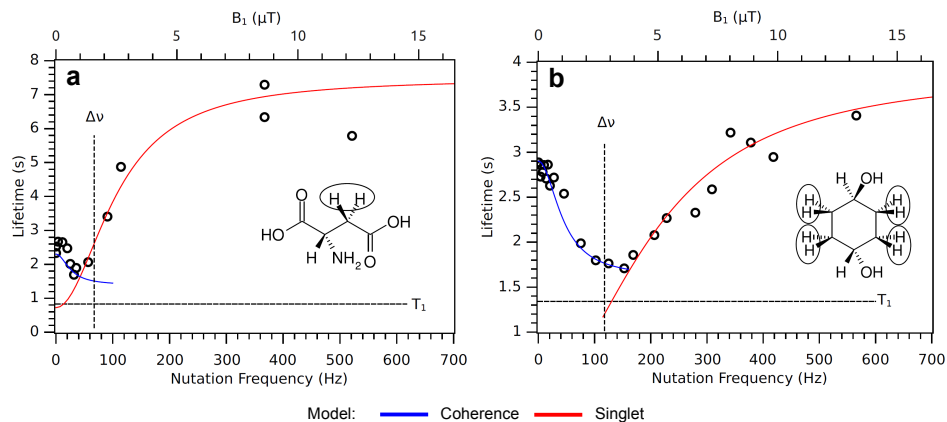
Figure 3.6: Measurements of a mixture singlet state and long-lived coherence as a function of the effective RF spin-locking field B_1 for proton pairs in small organic molecules. Also shown are fits to models for the singlet and LLC lifetimes, as described in the main text. (A) Aspartic acid, $T_L = 800$ ms and $T_{RF} = 3.5$ s; (B) *trans*-1,4-cyclohexanediol, $T_L = 350$ ms and $T_{RF} = 3.6$ s; RF power is quantified by the induced nutation frequency about the B_1 field. Molecular structures are shown, protons of the singlet(s) are circled, and values for chemical shifts ($\Delta\nu$) and spin-lattice relaxation times (T_1) are indicated.

$T_S = 16$ s and 5.5 T_1, which is consistent with previous measurements [14]. Since these singlet state lifetimes do not significantly depend on magnetic field strength, we conclude that CSA is not a primary mechanism of singlet relaxation.

To distinguish between the spin-rotation and magnetic quadrupole relaxation mechanisms, we performed singlet lifetime measurements at several sample temperatures. The temperature was controlled by supplying hot air to the probehead. Blown air was heated with a Hotwatt cartridge heater controlled by an Omron temperature control box, and the temperature of the sample was monitored with a resistance temperature detector (RTD) in the probehead. We found that the singlet lifetime increases linearly with temperature, which identifies the magnetic quadrupole relaxation mechanism as dominant in such proton-pair singlet state molecules (see ap-

pendix A.3).

Note that most previous proton-pair singlet measurements were conducted using deuterated solvents, which should result in weaker singlet-solvent interactions and larger enhancements of singlet state lifetime. To test whether such lifetime enhancement changed in a normally protonated solvent, we studied *p*-hydroxybenzoic acid in both D_2O and H_2O. We found that the enhancement of both the singlet and LLC lifetimes were significantly lower in H_2O (see Table 3.3). The enhancement is likely higher in D_2O due to the substitution of deuterium for the phenolic proton as well as reduced dipolar interactions with nearby solvent protons.

3.1.4 Discussion

The above experimental results and associated modeling establish an operational spin-locking condition $\nu_n^{opt} \approx 5\Delta\nu$ to realize maximum singlet lifetime with minimal RF power. In the context of this operational condition, we can reassess the past work by Levitt and colleagues using high-power RF spin-locking fields [13, 14, 33]. As shown in Table 3.4, most of the previous experiments employed $\nu_n \gg 5\Delta\nu$, i.e., they used much higher RF power than was needed to achieve a long singlet state lifetime, no doubt to achieve the longest lifetimes possible. For example, for citric acid Pileio *et al.* [14] used $\nu_n = 3.5$ kHz, whereas $\Delta\nu = 72$ Hz at 9.4 T, which is an order-of-magnitude higher spin-locking field than would be necessary for a typical long-lived singlet experiment.

Furthermore, we note that similarly low RF powers will be required for practical *in vivo* singlet-state creation in a wide variety of molecules using clinical MRI scanners,

where the static magnetic field is commonly between 1.2 and 7 T; see example values for ν_n^{opt} at 1.5 T given in Table 3.4. For example, at 4.7 T glycerol formal's protons have a frequency difference $\Delta\nu \approx 16$ Hz; hence $\nu_n^{opt} \approx 80$ Hz is sufficient to achieve significant singlet-state lifetime enhancement. For common biomolecules such as citric acid and aspartic acid, $\nu_n^{opt} < 100$ Hz at 1.5 T, which is well within the spin-locking regime commonly used in clinical MRI [42, 43]. Using equation 3.1, a 60 Hz spin-lock would produce a power dissipation of 140 mW/kg implying that it can be safely applied indefinitely *in vivo*. Alternatively, the long-lived coherence can be utilized without the need for any spin-locking if only moderate lifetime enhancements are required.

In summary, our measurements and theoretical description show that for many molecules long-lived nuclear spin singlet states and singlet-triplet coherences can be created using RF spin-locking powers that are more than two orders of magnitude lower than in previous studies and that the effectiveness of the spin-locking can be accurately predicted from spectral parameters. These insights will be useful in the development of new applications for singlet states *in vivo*, where the RF specific-absorption rate (SAR) must be minimized.

Table 3.4: Comparison of the chemical shift; optimal spin nutation frequency for RF spin-locking, $\nu_n^{opt} \approx 5\Delta\nu$; and values of ν_n used in previous experiments. Also listed are values for ν_n^{opt} for a clinical MRI scanner.

Molecule	$\Delta\nu$ (B_0 field)	ν_n^{opt}	ν_n, previous	ν_n^{opt} at 1.5 T
citric acid [14]	72 Hz (9.4 T)	360 Hz	3500 Hz	57 Hz
p-HBA [14]	445 Hz (11.75 T)	2224 Hz	3500 Hz	284 Hz
aspartic acid [17]	100 Hz (11.75 T)	500 Hz	2500 Hz	64 Hz

3.2 SUCCESS: Suppression of Undesired Chemicals with Contrast-Enhancing Singlet States

While the previous section explored the long-lived nature of the singlet state, this section will explore its spherically-symmetric nature, which can be employed as a way to isolate the singlet state signal. Because the singlet state has $I = 0$, it is invariant to rotation, i.e., $\hat{R}(x, y, z)|S_0\rangle = |S_0\rangle$. This is not the case for any other state with $I > 0$. By summing measurements after a set of carefully-chosen rotations, it is possible to remove the signal from states with $I > 0$ while retaining the singlet state signal. This is called polyhedral phase cycling and was first demonstrated for the singlet state by Pileio *et al.* [44]. It is also possible to replace or supplement phase cycling with gradient pulses to remove $I > 0$ states, as demonstrated in ref. [45]. Both techniques are considered examples of quantum filters, which have been used extensively in NMR to isolate signals from selected quantum coherences.

NMR spectroscopy provides a quantitative, non-destructive measure of chemical concentrations in complex mixtures both *in vitro* and *in vivo*. In many samples, the spectral lines are narrow while the range of resonance frequencies is broad, and there is little overlap of spectral lines. However, mixtures of biomolecules, such as blood, urine, and brain tissue, often contain a large number of compounds with many spectral lines overlapped by a few dominant metabolites [46–50]. Furthermore, some abundant metabolites, such as glutamine and glutamate, have such similar structures that their spectra are nearly identical and are difficult to resolve from one another. In these cases, no amount of signal averaging can improve the resolution.

While improved resolution can be achieved using higher-field instruments, this is often a costly solution, especially for MRI. An alternative solution employs quantum filters to remove undesired spectral components and to select those of interest. Quantum filtration works by creating a quantum coherence in a target spin system and then applying phase cycling or gradient filters to selectively suppress the coherences in either the target or the background spins [26]. Common applications include water and fat suppression as well as metabolite-specific enhancement in magnetic resonance spectroscopy, amino-acid-specific enhancement in protein spectroscopy, and metabolic analysis of blood and urine [51–61]. Nevertheless, quantum filters have had limited success differentiating the signals of similarly-structured molecules where the chemical shifts and coupling parameters are nearly identical [62, 63]. The spectral similarity makes it difficult to selectively produce the desired quantum coherence on only one type of molecule.

In this section, we demonstrate a technique called SUCCESS, or "Suppression of Undesired Chemicals using Contrast-Enhancing Singlet States," in which spin-locking and a singlet quantum filter are used to isolate the signal from a target molecule. We create and select nuclear spin singlet states on the target formed in pairs of coupled protons or pairs of coupled methylene groups. The multi-pulse sequence required to create, preserve, and measure the singlet state produces strong contrast even when the spectra of two molecules nearly overlap, as is the case in mixtures of glutamine and glutamate, and aspartate and N-acetylaspartate. SUCCESS also produces excellent suppression of signals from spin systems in which no singlet state can be created.

Current quantum filters utilize coherences comprised of superposition states pre-

cessing in the transverse plane and characterized by m_x and m_y [26]. For example, a double-quantum filter selects (or rejects) all double quantum coherences, which consist of two or more spin-1/2 nuclei in an $m_x + m_y = 1$ state, for example $I_{1x}I_{2x}$. However, states can also be selected or rejected based on their total spin quantum number, I. For instance, a singlet state with $I = 0$ can be selectively passed through a filter while a triplet state with $I = 1$ is removed.

Spin-locked singlet states have the additional benefit that continuous RF irradiation used to preserve the singlet simultaneously drives triplet states and other uncoupled spins to saturation more quickly than T_1. We can utilize this feature as a contrast mechanism by implementing the basic SUCCESS pulse sequence shown in Fig. 3.7a, which consists of three steps: (1) Prepare target spins in a singlet state, while minimizing singlet character in any other groups of spin. These singlets might be prepared on a specific molecule in a mixture, or a specific group within a larger molecule. (2) Apply a resonant RF field to preserve the spin singlet state and drive all other spin states to saturation. (3) Convert the singlet polarization back into transverse magnetization for readout. The spectrum should then consist only of peaks from any target spins prepared as a singlet state.

In real systems, the applied RF field contains a limited power across a limited bandwidth, so that saturation of the background spin systems is often incomplete. Background suppression can be improved using the polyhedral, spherically-symmetric phase cycle developed by Pileio *et al.*, which removes all non-singlet signals [44]. The addition of phase cycling leads to the SUCCESS sequence shown in Fig. 3.7b. The highest-order coherences removed by the phase cycle depends on the number of steps

chosen, as the closer one approximates a sphere the better one isolates the singlet. We chose a 24-step cycle that removes states up to $I = 3$, which is sufficient for molecules with up to 6 protons. Alternatively, a gradient filter can be implemented by applying x, y, and z gradients in succession to "spoil" non-singlet magnetization.

One further complication is that background molecules may contain singlet-producing groups with spectral components overlapping the target. Fortunately, the efficient preparation of a spin-locked singlet state requires a pulse sequence with three properly-chosen delays that depend on the scalar coupling and chemical shifts of each molecule. We find that through careful selection of these delays, a singlet can be created in the target molecule only. For example, the simulation results shown in Fig. 3.7c and 3.7d show that by properly selecting τ_2 and τ_3, a large amount of singlet can be produced in aspartate while at the same time little singlet is produced in N-acetylaspartate.

3.2.1   Proton Experiments

The SUCCESS technique was tested *in vitro* on three target molecules that are important brain metabolites: aspartate, threonine, and glutamine. The spectra of these molecules are overlapped by peaks from N-acetylaspartate, *myo*-inositol, and glutamate, respectively. The test mixtures are listed in Table 3.5. Each consisted of a target molecule and the interfering background substance dissolved in a pH 7.0 phosphate buffer. Concentrations were chosen to reflect typical ratios found *in vivo* but at higher absolute concentration. A control solution was also created for each target and background molecule alone in pH 7.0 phosphate buffer. Reagents were purchased from Sigma-Aldrich.
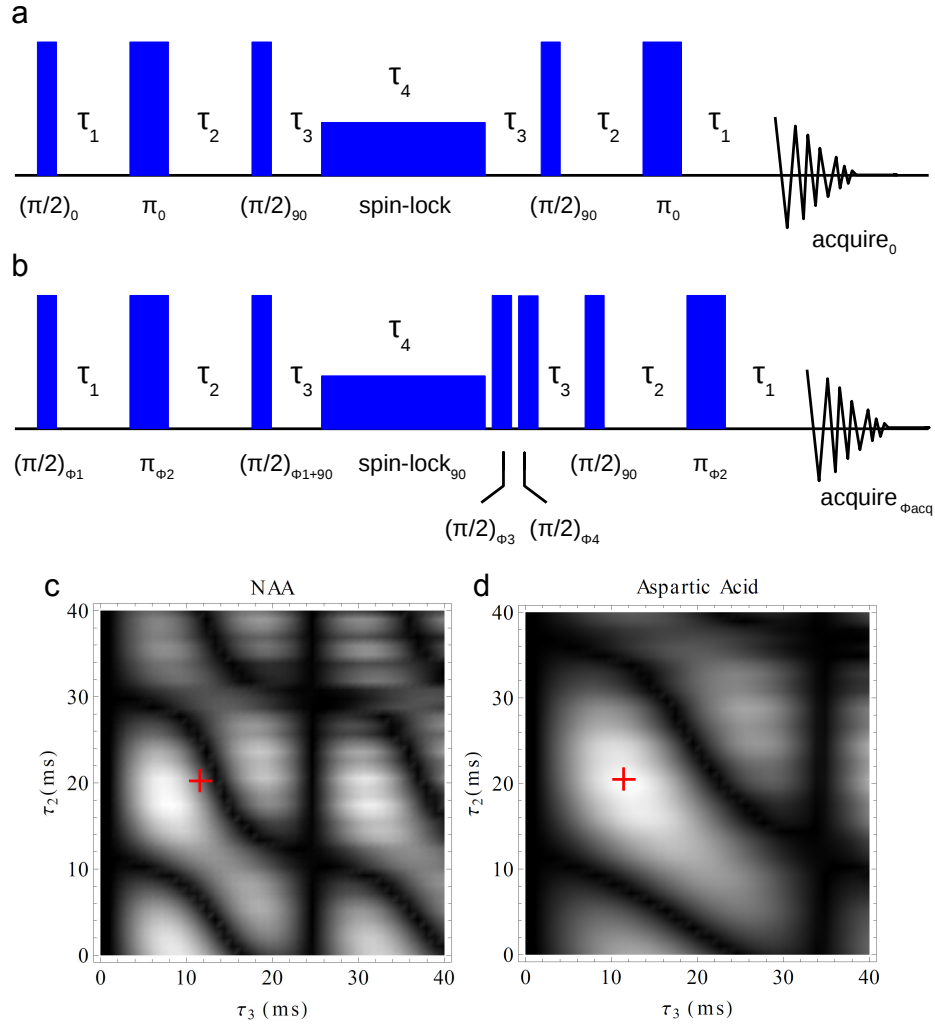
Figure 3.7: (a) Basic SUCCESS pulse sequence: The NMR transmitter frequency, ν_0, is placed at the average resonance frequency of the two target protons, at a chemical shift δ_{av}. The first three pulses then create a mixture of singlet and triplet states in the target spins. Continuous RF power, also applied at the average resonance frequency of the protons for time τ_4, preserves the singlet state while driving other states toward saturation. Finally, two of the first three pulses are repeated in reverse order to return the remaining singlet population into transverse magnetization for readout. (b) To improve suppression of non-singlet states, two filtering pulses can be added as part of a spherically-symmetric phase cycle. (c) and (d) Simulated intensity maps for aspartic acid and N-acetylaspartic acid show that pulse sequence delays can be chosen to create singlet mainly in one molecule and not in the other. The red cross marks the parameters used in the demonstration, which were chosen as a compromise between signal intensity and strong contrast. Higher contrast can be achieved with slightly longer values of τ_2 and τ_3, but with lower target signal intensity.

50

^{1}H NMR spectra were obtained using a Bruker 4.7 T vertical bore spectrometer with a 10 mm diameter probe. A transmitter power of 100 W required a $\pi/2$ pulse length of 26 μs and a π pulse length of 46 μs. Exponential apodization was applied to all spectra with either 0.5 Hz or 1.0 Hz line-broadening constants. Spectra of the mixtures and controls were first obtained with a "one-pulse" sequence by applying a $\pi/2$ pulse and acquiring an FID. Spin-lattice relaxation times of the molecules were measured in control solutions using an inversion recovery sequence. Measured J-couplings and peak positions of each molecule were then used to calculate optimal delays τ_1, τ_2, and τ_3 for singlet creation on the target. Singlet lifetimes were measured in the controls using the SUCCESS sequence in Fig. 3.7b by varying the relaxation delay τ_4. The 24-step phase cycle was used with parameters given in Table 3.6. SUCCESS spectra were acquired of each mixture, and the delays were experimentally optimized to produce the best contrast enhancement for the target molecule. Identical SUCCESS spectra were acquired for control solutions.

The effectiveness of the quantum filter was quantified in terms of the contrast enhancement, or the ratio

$$CE = \frac{C_R}{C_S} \tag{3.20}$$

where C_R is the contrast in a regular scan and C_S is the contrast in a SUCCESS scan. The contrast is defined as the intensity of the target peak divided by the intensity

Table 3.5: Sample concentrations for proton SUCCESS demonstrations.

Target Molecule (mM)		Background Molecule (mM)	
aspartic acid	3.0	N-acetylaspartic acid	11.4
threonine	50.0	*myo*-inositol	50.0
threonine	5.0	*myo*-inositol	50.0
glutamine	40.0	monosodium glutamate	80.0

Table 3.6: 24-step phase cycle used for SUCCESS.

Step	$\phi 1$	$\phi 3$	$\phi 4$	Acquisition
1	0	0	180	0
2	90	0	180	180
3	180	0	180	0
4	270	0	180	180
5	90	90	180	180
6	180	90	180	0
7	270	90	180	180
8	0	90	180	0
9	180	180	270	0
10	270	180	270	180
11	0	180	270	0
12	90	180	270	180
13	270	270	0	180
14	0	270	0	0
15	90	270	0	180
16	180	270	0	0
17	0	0	90	0
18	90	0	90	180
19	180	0	90	0
20	270	0	90	180
21	180	180	180	0
22	270	180	180	180
23	0	180	180	0
24	90	180	180	180

of the interfering background peak. For molecules with multiple peaks, the contrast was calculated for each set of target and background peaks that overlap.

We first tested SUCCESS on aspartate (ASP), which has a typical concentration of 3 mM in the brain. It contains a pair of protons, attached to a common carbon atom, whose long-lived singlet state has previously been investigated [17]. Its acetylated form, N-acetylaspartate (NAA), also exists in the brain at a concentration 3-6 times higher [50, 64–66]. The geminal protons of interest in both molecules produce a second-order spectral structure in the 2-3 ppm chemical shift range, with further splitting caused by a third nearby proton, whose peak appears near 4 ppm (Fig. 3.8a-b). In the control solutions, the singlet state lifetimes, T_S, were 5.6±1 s and 4.5±0.3 s for ASP and NAA, respectively, while spin-lattice relaxation times, T_1, were 1.3±0.2 s and 0.99±0.06 s for the proton pairs in ASP and NAA, respectively. Note that the singlet state lifetimes are around half the value obtained in [17], likely because we used water rather than D_2O as the solvent and did not remove dissolved oxygen.

The one-pulse spectrum of the mixture is dominated by NAA, and only the ASP peaks near 2.8 ppm are visible (Fig. 3.8c). Using an appropriate set of pulse sequence parameters, we achieved a SUCCESS spectrum with residual NAA magnetization of only 4% its original intensity in the control solution. The same SUCCESS sequence applied to the ASP control produced a spectrum that appeared similar to its one-pulse spectrum, but with a signal strength 25% its the original intensity (Fig. 3.8d-e). The result was contrast enhancement of 6 or greater for all ASP peaks compared with NAA. The SUCCESS spectrum of the mixture (Fig. 3.8f) appeared nearly identical to that of the ASP control, except for the weak residual NAA signal near 2.5 ppm.

Moreover, the water signal was suppressed by a factor of 6.5.

We next targeted the amino acid threonine (THR), which occurs at concentrations of around 500 μM in the brain [67, 68]. Threonine does not possess a pair of geminal protons, so the singlet must instead be created on the vicinal protons attached to carbons two and three. The target proton peaks lie near 3.6 and 4.2 ppm (Fig. 3.9a), and the downfield proton is strongly coupled to a methyl group ($\delta = 1.25$ppm), which produces a multiplet splitting pattern. A singlet lifetime, T_S, of 2.0±0.3 s and spin-lattice relaxation times, T_1, of 2.0±0.2 s and 2.2±0.1 s were measured for the vicinal protons. The singlet lifetime is actually shorter than T_1 because the interactions with the methyl group are strongly asymmetric with respect to the singlet spins. Interactions with the methyl group also lead to a SUCCESS spectrum that looks significantly different from the one-pulse spectrum. For example, the 4.2 ppm peak is inverted (Fig. 3.9e).

The upfield target proton is overlapped by peaks from the common metabolite *myo*-inositol (spectrum shown in Fig. 3.9b), which occurs in the brain at concentrations of 4-12 mM [50, 64]. At a 10:1 *myo*-inositol:threonine concentration ratio, the *myo*-inositol peaks completely cover the upfield threonine peak and make it unresolvable in our spectrometer. Even at a 1:1 concentration ratio the threonine peak is difficult to resolve (Fig. 3.9c-d). The optimized SUCCESS sequence suppressed the *myo*-inositol peaks to less than 0.7 % of their original intensity, while it preserved 12% of the threonine signal (Fig. 3.9e-f). The result was an average contrast enhancement of 17 times. When applied to the sample with equal concentrations of threonine and *myo*-inositol, the SUCCESS sequence reduced the intensity of myo-inositol so greatly
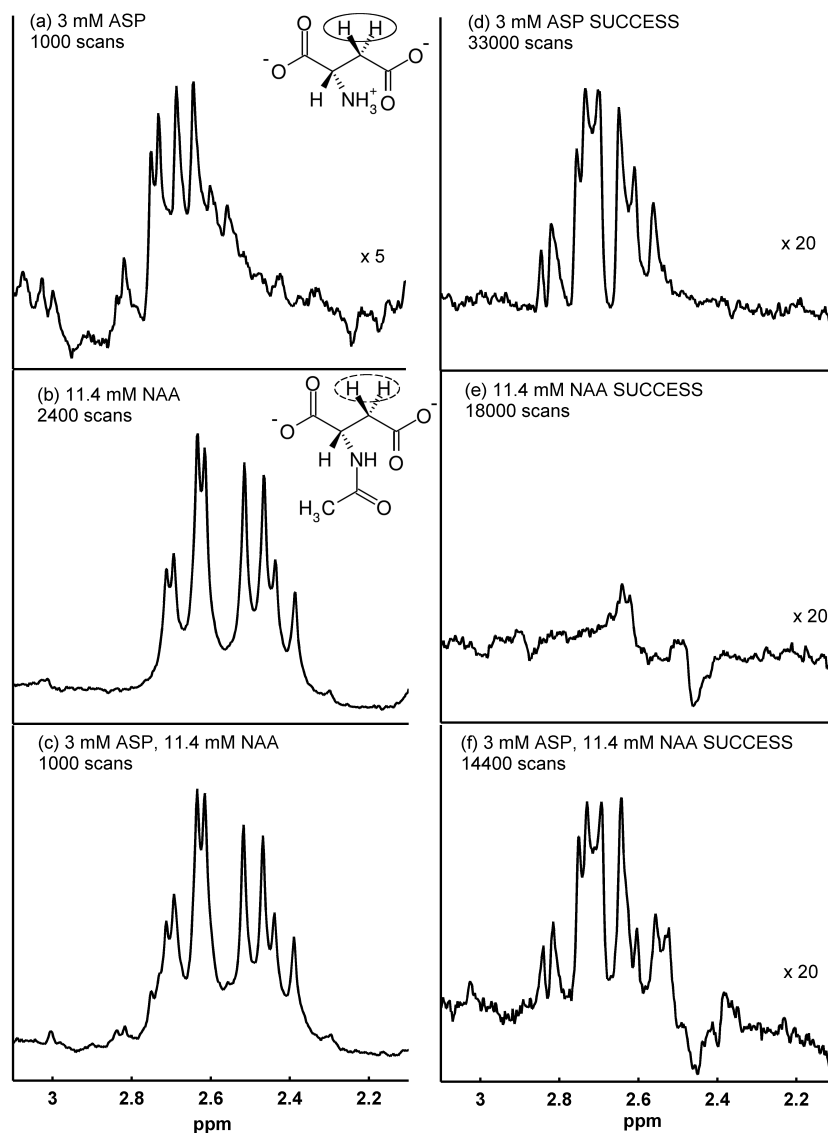
Figure 3.8: Spectra are shown for conventional (a-c) and SUCCESS (d-f) scans performed on solutions of N-acetylaspartate, aspartate, and their mixture. The SUCCESS scan of the mixture is nearly identical to that of aspartate alone. The target protons for singlet formation are indicated on each structure, with a solid line indicating the desired singlet, and a dashed line indicating the undesired singlet. SUCCESS parameters were $\delta_{av} = 2.71$ ppm, $\tau_1 = 9$ ms, $\tau_2 = 20.3$ ms, $\tau_3 = 11.5$ ms, $\tau_4 = 1$ s, and $\nu_n = 385$ Hz, line broadening 0.5 Hz.

that only the threonine peak was evident (Fig. 3.9g). When performed on the sample with a 10:1 concentration ratio, the resulting spectrum exhibited a threonine peak slightly more intense than *myo*-inositol, which allowed the previously hidden peaks to be identified (Fig. 3.9h). The water peak was suppressed by a factor of 32.

Finally, we applied SUCCESS to a mixture of glutamine (GLN) and glutamate (GLU). The typical glutamate concentration is twice that of glutamine in the brain (8 mM and 4 mM respectively) [50, 64, 67, 69]. These molecules have largely overlapping spectra that make individual measurements difficult [70], as well as similar chemical shifts and J-coupling strengths that make the application of quantum filters challenging. A number of spectral-editing techniques and quantum filters have been used to attack this problem [54, 62, 63, 71–74], but none has become a routine and reliable way to measure glutamine concentration.

Each molecule contains two methylene groups that can be viewed as pairs of strongly-coupled, unresolvable protons. A third lone proton couples to one of the methylene groups. The spectra therefore exhibit a complex splitting pattern (Fig. 3.2.1a-b), with methylene group peaks between 1.8 and 2.6 ppm, and the lone proton peak at 3.7 ppm. A mixture of the two metabolites produces a spectrum with many poorly-resolved peaks, and the upfield methylene groups cannot be resolved at all (Fig. 3.2.1c). Each methylene group is already strongly mixed into singlet and triplet states, but the resulting singlets cannot be easily manipulated for utilization in the quantum filter. Instead, a four-spin singlet state can be created by mixing the triplet states of the two methylene groups. This singlet is preserved by RF power just like a two-spin singlet, and it can be selectively created depending on the pulse sequence parameters,
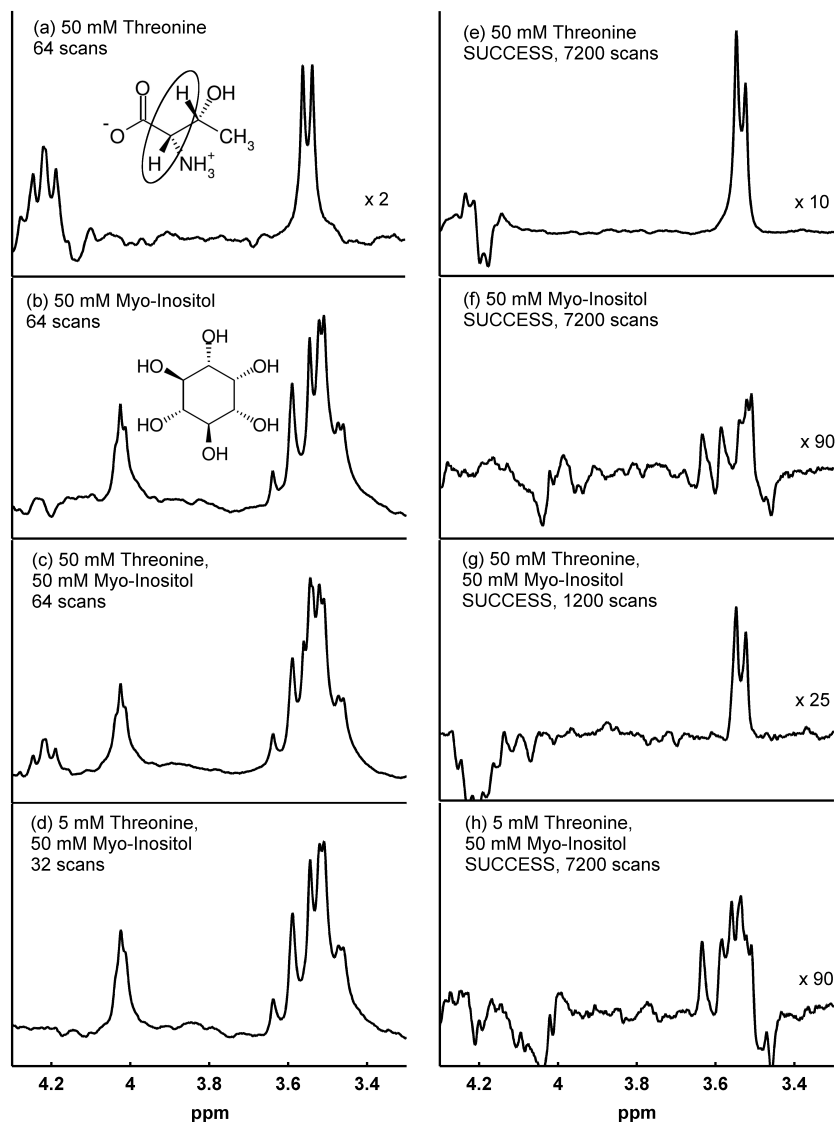
Figure 3.9: Spectra are shown for conventional (a-d) and SUCCESS (e-h) scans performed on solutions of *myo*-inositol, threonine, and two mixtures. The target protons for singlet formation on threonine are indicated. SUCCESS parameters were $\delta_{av} = 3.87$ ppm, $\tau_1 = 40$ ms, $\tau_2 = 52$ ms, $\tau_3 = 1.85$ ms, $\tau_4 = 200$ ms, and $\nu_n = 790$ Hz, except for frame (g), where $\tau_2 = 72$ ms and $\tau_3 = 4.8$ ms, line broadening 0.5 Hz.

but it does not possess an extended lifetime. Its symmetry does allow it to pass through the polyhedral singlet filter. Lifetimes of 0.70±0.09 s and 0.80±0.1 s were measured for this singlet in glutamate and glutamine, respectively. The measured T_1 times were 1.11±0.02 s and 0.92±0.02 s for glutamate, and 1.24±0.05 s and 1.01±0.04 s for glutamine. The singlet-state lifetimes were shorter than the spin-lattice lifetimes of their constituent methylene groups because dipole-dipole interactions within each methylene group are still allowed by symmetry and lead to relaxation. Nevertheless, the singlet lifetime is sufficiently long for SUCCESS to be effective.

SUCCESS parameters were experimentally optimized to obtain high contrast for glutamine. The glutamate signal was suppressed so that only 0.86% of its original intensity remained. In contrast, 5.7% glutamine signal was recovered, resulting in a contrast enhancement between 3 and 7 times. The SUCCESS spectrum of glutamine (Fig. 3.2.1d) appeared similar to the conventional spectrum, whereas that of glutamate consisted mainly of a single peak that was not fully removed (Fig. 3.2.1e). The SUCCESS spectrum of the mixture appeared similar to that of glutamine, except for the residual glutamate peak at 2.3 ppm (Fig. 3.2.1f). This residual peak did not interfere with any glutamine peaks, and so the positions of the upfield methylene peaks of glutamine were now measurable. The water signal was suppressed by a factor of 13.

We found that higher signal from glutamine could be obtained by moving the transmitter frequency ~ 40 Hz upfield from the average value, to $\delta_{av} = 2.05$ ppm, for the whole sequence and by applying a different set of delays. This created the same level of contrast while preserving 15% of the glutamine signal (Fig. 3.2.1a-c). Water

suppression was also higher, with a peak 38 times weaker than in a one-pulse scan.

3.2.2 Phosphorus Experiments

Phosphate-containing compounds play a critical role in biology as energy trans-porters. Since ^{31}P is a spin-1/2 nucleus like the proton, singlet states can be created from ^{31}P pairs allowing for the implementation of the SUCCESS sequence. As the structures in Fig. 3.12b show, both nicotinamide adenine dinucleotide (NAD$^+$) and adenosine disphosphate (ADP) contain a pair of coupled phosphorus nuclei, and it should be possible to create a spin-locked singlet on both. In contrast, adenosine triphosphate (ATP) contains three phosphorus nuclei and should not possess a sin-glet state. Here, we demonstrate the isolation of the ADP and NAD$^+$ spectra in the presence of ATP.

We performed ^{31}P SUCCESS measurements on a mixture containing 30 mM ATP, 3 mM ADP, and 3 mM NAD$^+$ in a pH 7.0 phosphate buffer. Continuous wave decoupling was applied to the proton channel throughout the pulse sequence to remove splittings from proton-phosphorus J-coupling. Figure 3.12a shows a spectrum of the mixture measured with a $\pi/2$-FID sequence. ATP and ADP exhibit a splitting pattern indicating that the ^{31}P resonance frequency differences are significantly greater than the ^{31}P-^{31}P J-coupling (additional ATP peaks at -20 ppm are not shown). For ADP, $J_{\mathrm{PP}} = 21.2$ Hz while $\Delta\nu = 128.9$ Hz. NAD$^+$ exhibits a second-order spectrum, indicating $\Delta\nu \sim J$, and one of its peaks lies directly beneath an ATP peak. For NAD$^+$, $J_{\mathrm{PP}} = 20.2$ Hz while $\Delta\nu = 24.2$ Hz.

Figures 3.12c and d show the results after applying the SUCCESS sequence to
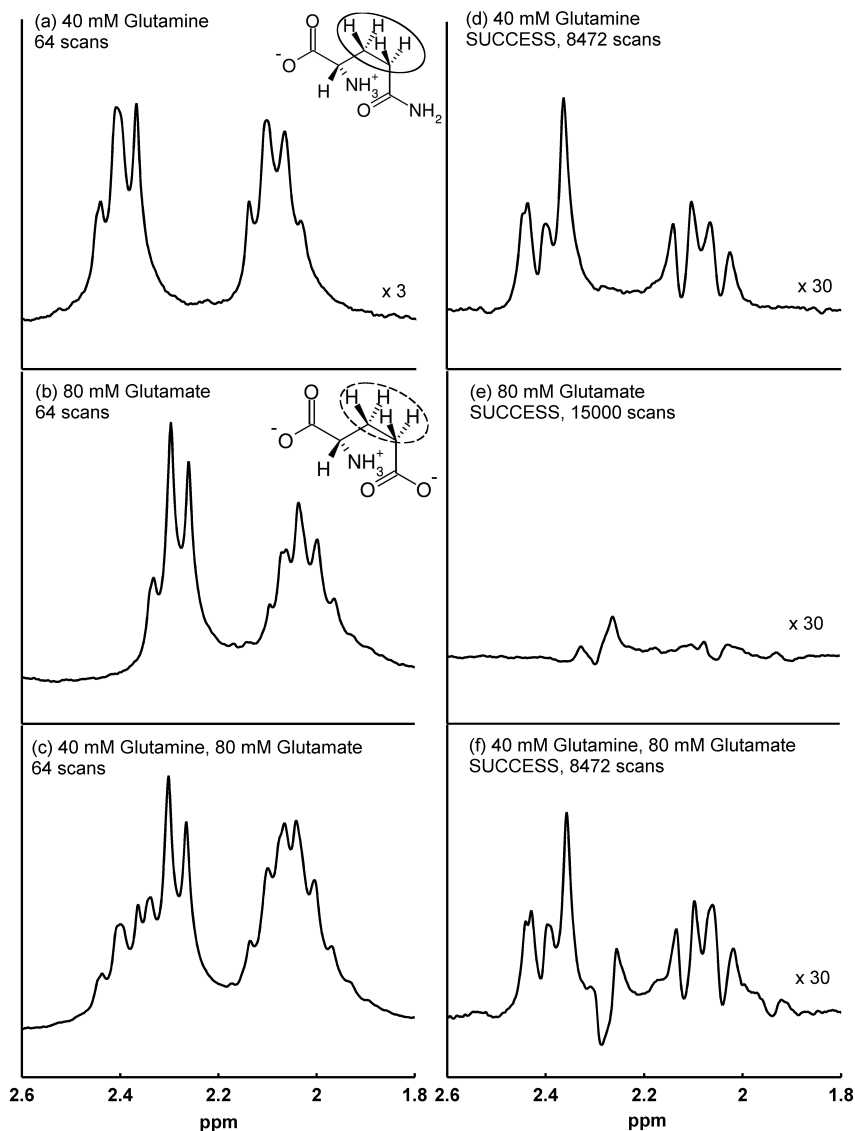
Figure 3.10: Spectra are shown for conventional (a-c) and SUCCESS (d-f) scans performed on solutions of glutamate, glutamine, and their mixture. The SUCCESS scan of the mixture is similar to that of glutamine alone, except for residual glutamate signal near 2.3 ppm. The target protons for singlet formation are indicated on each structure, with a solid line indicating the desired singlet, and a dashed line indicating the undesired singlet. SUCCESS parameters were $\delta_{av} = 2.23$ ppm, $\tau_1 = 22$ ms, $\tau_2 = 15$ ms, $\tau_3 = 11.1$ ms, $\tau_4 = 500$ ms, and $\nu_n = 385$ Hz, line broadening 1 Hz.
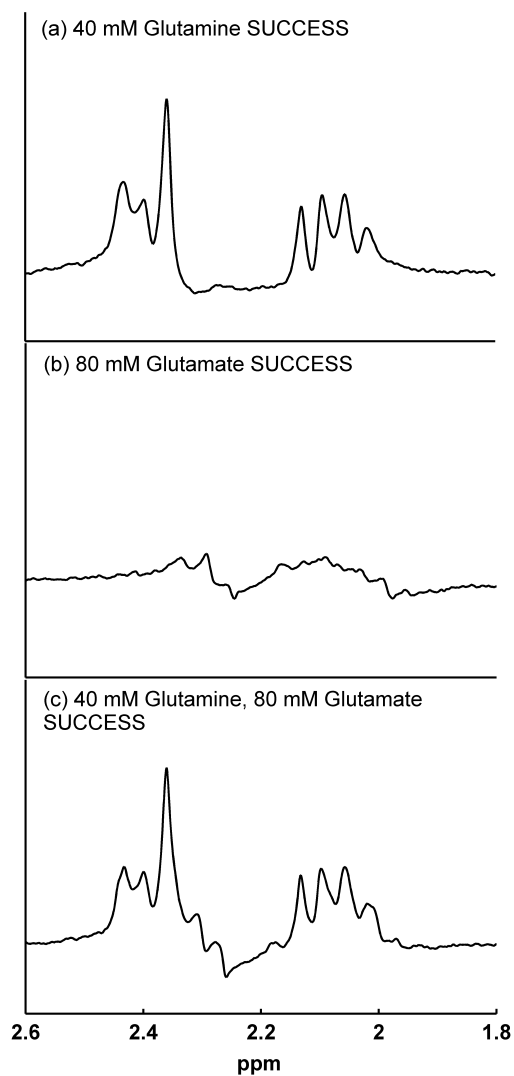
Figure 3.11: Spectra are shown for SUCCESS scans performed on solutions of glutamate, glutamine, and their mixture, in which the RF transmit frequency was shifted away from the average resonance frequency by 40 Hz, to $\delta = 2.05$ ppm. Glutamine signal dominates the spectrum of the mixture. Delays were $\tau_1 = 18$ ms, $\tau_2 = 9$ ms, $\tau_3 = 4.5$ ms, $\tau_4 = 100$ ms, and $\nu_n = 385$ Hz, line broadening 1 Hz.

target NAD^+. Approximately 50% of the NAD^+ signal is retained, compared with only 1.2% of the ATP signal, resulting in a factor of 42 enhancement for NAD^+ signal contrast. Figures 3.12e and f show the results after applying the SUCCESS sequence to target ADP. Approximately 39% of the ADP signal is retained, compared with only 2.6% of the ATP signal, resulting in a factor of 15 enhancement for ADP signal contrast.

While the phosphorus pairs provided excellent singlet states for SUCCESS, these singlets did not exhibit an extended lifetime. For lifetime measurements, we created 50 mM solutions of ADP and NAD^+ in pH 7.0 phosphate buffer. We found that for ADP, $T_S \approx 0.2T_1$, while for NAD^+, $T_S \approx 0.5T_1$. The short singlet lifetimes indicate strong relaxation from nearby spins interacting asymmetrically with the phosphorus nuclei, especially for ADP. At pH 7, the protons of both the ADP-β and the NAD^+ phosphate groups are dissociated, but one proton remains attached to the ADP-α phosphate group relatively strongly, likely driving relaxation. As a test, a basic 50 mM ADP solution was prepared in 0.5 M sodium hydroxide solution. This increased the dissociation of the α phosphate's remaining proton, thereby increasing T_1, T_S, and T_S/T_1 significantly. Table 3.7 summarizes the measured relaxation parameters.

Table 3.7: Measured values of spin-lattice and relaxation times for phosphorus spin pairs.

Molecule	$T_1(s)$	$T_S(s)$	T_S/T_1
ADP-α neutral	2.6 ± 0.2	0.49 ± 0.03	0.19 ± 0.02
ADP-β neutral	2.45 ± 0.08	0.532 ± 0.009	0.22 ± 0.01
ADP-α basic	3.9 ± 0.2	3.9 ± 0.7	1.0 ± 0.07
ADP-β basic	7.7 ± 0.3	4.2 ± 0.3	0.55 ± 0.04
NAD^+ neutral	2.87 ± 0.08	1.35 ± 0.01	0.47 ± 0.01
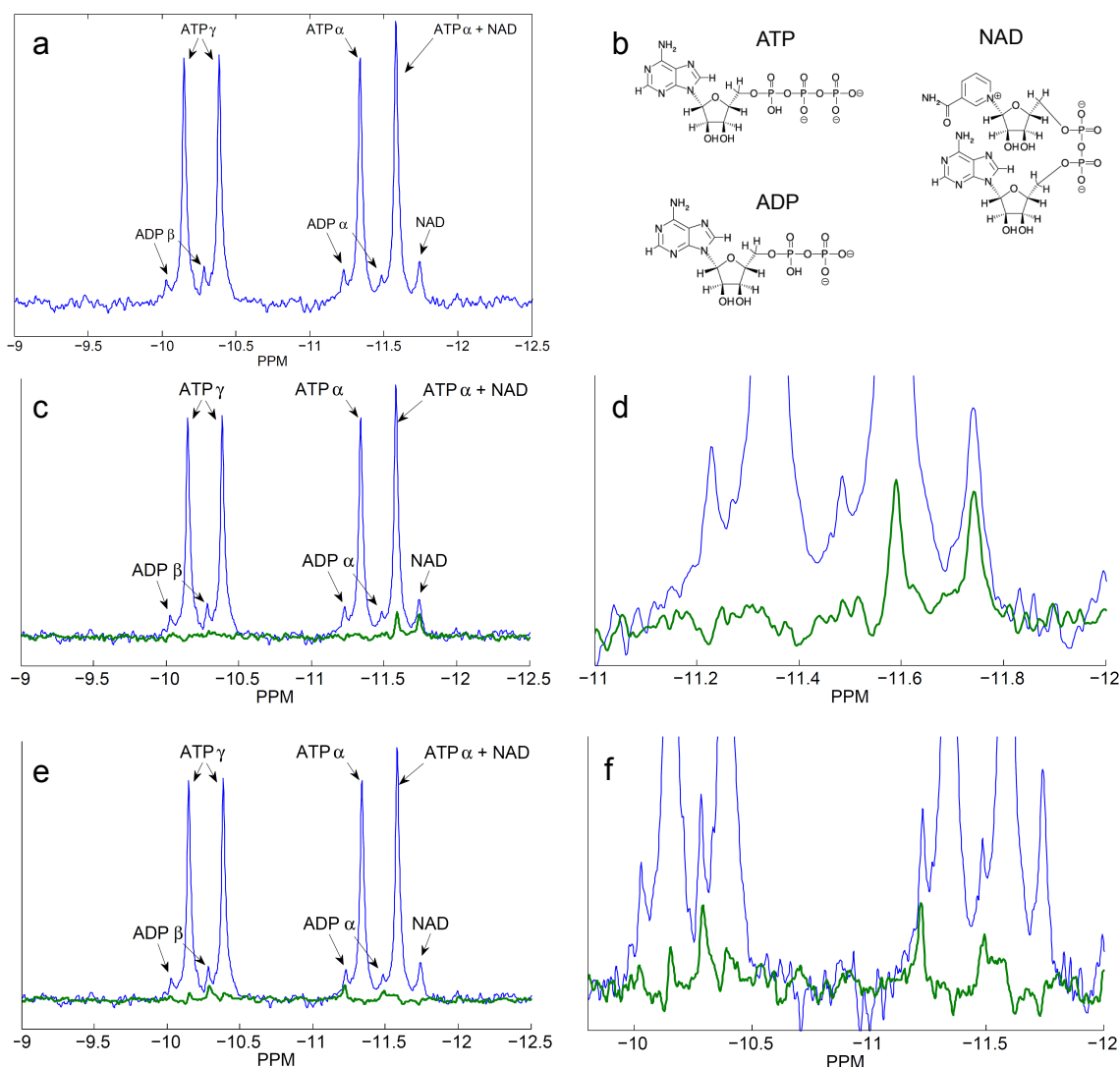
Figure 3.12: SUCCESS spectra for phosphorus NMR in ATP, ADP, and NAD$^+$. (a) Conventional spectra are shown for a solution of ATP, ADP, and NAD$^+$. Structures of the molecules are shown in (b). The SUCCESS scan of the mixture targeting NAD$^+$ (c, d green line) shows excellent suppression of the ATP signal while retaining 50% of the NAD$^+$ signal. SUCCESS parameters were $\delta_{av} = -11.675$ ppm, $\tau_1 = 15.5$ ms, $\tau_2 = 16$ ms, $\tau_3 = 12.5$ ms, $\tau_4 = 100$ ms, and $\nu_n = 615$ Hz. The SUCCESS scan of the mixture targeting ADP (e, f green line) similarly shows strong ATP suppression. SUCCESS parameters were $\delta_{av} = -10.74$ ppm, $\tau_1 = 12.02$ ms, $\tau_2 = 17.16$ ms, $\tau_3 = 2.57$ ms, $\tau_4 = 100$ ms, and $\nu_n = 615$ Hz. All spectra were acquired with CW ^{1}H decoupling at 150 Hz nutation frequency.

3.2.3   Improving Singlet Creation/Readout Efficiency

The three-pulse singlet creation/readout pulse sequence can produce an ideal density matrix $\rho = |S_0\rangle\langle S_0| - |T_0\rangle\langle T_0|$ when the two target nuclei of the spin pair are well-isolated from other spins. However, if a third spin couples to one or both spins of the pair, it perturbs the spin evolution of the target spins and reduces the creation of singlet state. One way to counter this effect is to split the π pulse of the echo into two $\pi/2$ pulses separated by a short delay. The short delay is chosen so that the interfering spin precesses 180° during its duration. This causes the perturbation from the interfering spin to have the opposite sign during τ_2 and τ_1, thereby minimizing its effect over the course of the sequence. Figures 3.13a and b show the modified SUCCESS sequence with and without polyhedral phase cycling, respectively.

We tested the modified sequence on threonine, since its singlet state is strongly affected by the adjacent methyl group. Using a 84 mM solution of threonine in pH 7.0 phosphate buffer, we found that with the full modified SUCCESS sequence, 38% of threonine magnetization could be transferred to singlet state, spin-locked, and returned to transverse magnetization for readout. Conversely, only 0.65% of *myo*-inositol magnetization was preserved using the same sequence. Performing SUCCESS on a mixture containing 8.4 mM threonine and 84 mM *myo*-inositol revealed strong contrast enhancement that made the threonine peaks clearly identifiable (Fig. 3.13d), much more so than in Fig. 3.9h. Moreover, the threonine peak at 3.55 ppm was properly phased rather than inverted.
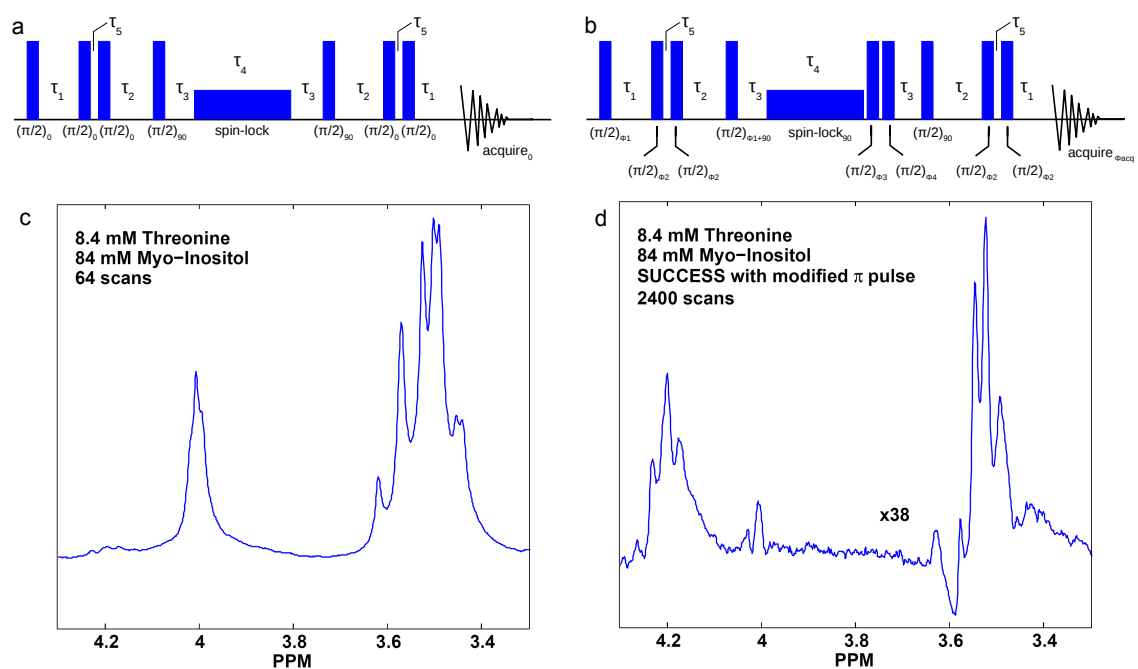
Figure 3.13: The modified SUCCESS pulse sequence is shown without (a) and with (b) polyhedral phase cycling. Note that the π pulses have been replaced with two $\pi/2$ pulses spaced by time τ_5. Spectra are shown for a conventional spectrum (c) performed on a solution of threonine and *myo*-inositol. The SUCCESS scan of the mixture targeting threonine (d) shows excellent suppression of the *myo*-inositol signal. SUCCESS parameters were $\delta_{av} = 3.87$ ppm, $\tau_1 = 44$ ms, $\tau_2 = 48$ ms, $\tau_3 = 1.87$ ms, $\tau_4 = 200$ ms, $\tau_5 = 0.95$ ms and $\nu_n = 790$ Hz, line broadening 0.5 Hz.

3.2.4 Discussion

While most singlet-state experiments have used specially-designed or selected molecules to produce singlet state lifetimes as long as possible, the singlet state can actually be prepared in nearly any coupled pair of protons. In many cases, surrounding spins will perturb the singlet and cause it to relax on the timescale $1/T_1$, but within this timeframe the singlet exists as a unique quantum state that can be preserved and filtered.

In many ways, the singlet state is no different from other quantum coherences; proton pairs can form double and zero-quantum coherences, which have both been used for a large number of quantum filter and spectral editing applications. However, the singlet has unique requirements for its creation and preservation that give SUCCESS greater selectivity. Three delays must be properly chosen rather than two for a typical zero-quantum coherence [26, 58]. Moreover, the preservation of the singlet requires RF power to be applied at a proper resonance frequency and at a sufficient intensity [33, 35, 75, 76]. Both singlet creation and preservation are most effective when the NMR transmitter frequency for the spin-locking field is set at the average chemical shift of the target spins. Singlets in other spin groups will be created and preserved less effectively. To properly preserve the singlet, the RF spin-locking frequency should also be at least 5 times higher than the resonance-frequency difference between target protons [75]. By using weaker spin-locking, singlets in molecules with widely-separated spectral peaks can be rejected in favor of those with more closely-spaced peaks. Additionally, since frequency differences due to chemical shift decrease as B_0 is lowered, lower-field spectrometers can use weaker spin-locking fields resulting

in lower RF specific absorption rates (SAR) [75].

The requirements for good singlet creation can also be a limitation. As the target proton pair is coupled to more surrounding protons in a molecule, the efficiency of singlet creation as well as the singlet purity decrease. In an ideal proton pair, at most 50% of the magnetization can be transferred to the singlet state, while the other half is transferred to the triplet state. In aspartate, the coupling strength to the third proton is around half the coupling strength between the target spins, so that nearly 50% transfer can still be achieved. However, in threonine, coupling with the neighboring methyl group is nearly the same strength as the coupling between the target protons. Simulations of the basic SUCCESS sequence show that the maximum amount of magnetization transferred to the singlet is reduced to only 25%. Although the modified SUCCESS sequence can improve the singlet preparation for some cases, it will become less effective as more perturbing spins are added.

Also consider that the highest contrast is not always achieved with the parameters that produce maximal target intensity. For example, *myo*-inositol contains an even number of protons that can form states with singlet character, and the best contrast for threonine is achieved when the delays minimize the amount of *myo*-inositol singlet created. With these parameters, only 20% of threonine magnetization is transferred into the singlet state. Moreover, RF power must remain on for a sufficiently long time to let the system evolve and to saturate triplet states. During this time, there is some singlet relaxation. These various polarization losses mean that the contrast improvements afforded by SUCCESS come with a tradeoff in experiment time or imaging resolution. Using delays optimized for the best singlet creation, the SUC-

CESS sequence requires either four times more scans, or voxels of twice the volume, to achieve the same signal-to-noise (S/N) ratio as one-pulse scans.

One method for improving the contrast enhancement might be to utilize gradient filters either alone or in conjunction with phase cycling. These have been demonstrated in measurements of singlet state lifetime to help remove residual triplet states [45]. One must take care that the specific gradient scheme chosen properly removes all other zero-quantum coherences and z-axis magnetization, as these require more than simple gradient crusher pulses for elimination.

The results presented here demonstrate that the SUCCESS quantum filtration technique utilizing nuclear singlet states can create strong and specific contrast enhancement in NMR spectroscopy, and it can improve the measurement of a number of brain metabolites, especially glutamine. Moreover, it highlights the ubiquity of singlet states and demonstrates one of their applications other than extended-lifetime studies. The SUCCESS technique promises to improve MR-based metabolic measurements and the diagnosis of disease without resorting to increasingly high-field spectrometers.

Chapter 4

Singlet States in Nearly-Equivalent Spins

In chapter 2, we showed that when J-coupling between two spins is much stronger than the resonance frequency difference, i.e., $J \gg \delta\nu$, then the singlet state is naturally one of the eigenstates. Such a spin pair is ideal for extending polarization lifetime because the singlet state does not require spin-locking for preservation. However, magnetization cannot be directly transferred to and from the singlet state using a conventional RF pulse, because the singlet-triplet transition is forbidden. In this chapter, we describe ways to access the singlet state via pulse sequences that employ pulse trains or weak spin-locking. We apply these sequences to measurements of J-coupling and singlet state relaxation in small organic molecules. We then extend the technique to larger spin groups and demonstrate that singlet order can be transferred between spin pairs, allowing us to perform NMR experiments in a singlet-singlet subspace.

4.1   SLIC: Spin-Lock Induced Crossing

Tayler and Levitt demonstrated that for a pair of nearly-equivalent spins, triplet/singlet polarization transfer can be achieved using a series of π pulse trains in which the pulse timing is synchronized to the J-coupling strength between nuclei [21]. This "M2S" sequence takes advantage of the small amount of mixing between singlet and triplet states that is present whenever $\Delta\nu > 0$. Feng and Warren also showed that the M2S sequence can create singlet states in certain heteronuclear systems even when $\Delta\nu = 0$ [22]. These results hold promise for creating hyperpolarized singlet states without the need for a symmetry-breaking chemical reaction or continuous spin-locking. However, in all results to date, the polarization transfer to the spin singlet state only occurs during the final third of the M2S sequence, and before this stage the spin polarization occupies states subject to conventional spin-lattice relaxation.

We show that better triplet/singlet polarization transfer efficiency can be achieved by replacing the M2S pulse trains with a continuous spin-lock whose nutation frequency is matched to the J-coupling between the target nuclear spins. At this spin-locking strength, the energy levels of the singlet state and one triplet state become equal in the rotating frame, which we call the "spin-lock induced crossing" (SLIC). Polarization transfer can occur for the duration of spin-locking, which minimizes polarization loss from triplet state relaxation and thus provides better efficiency for singlet state creation than the M2S technique. SLIC is analogous to the Hartmann-Hahn condition for polarization transfer between two magnetically inequivalent nuclear spins, except that for SLIC the nuclei are nearly identical and their spin symmetry subspaces are inequivalent [77].

We experimentally compare M2S and SLIC using liquid-state NMR of the tripeptide molecule phenylalanine-glycine-glycine (phe-gly-gly), which contains two nearly-equivalent proton spin pairs in which to prepare singlet states. We find that for these two proton spin pairs, singlet state creation with SLIC is 19% and 75% more efficient than with M2S. We also demonstrate the utility of SLIC for characterizing singlet state lifetimes as well as small J-couplings and chemical shift differences between nearly-equivalent nuclear spins.

4.1.1   M2S Sequence

A pair of spin-1/2 nuclei are considered "nearly-equivalent" when $J \gg \Delta\nu$. Under these conditions, the spin eigenstates are described by equations 2.42 and 2.43. Because $\Delta\nu > 0$, $|\phi_S\rangle$ and $|\phi_0\rangle$ do not perfectly describe singlet and triplet states, but have significant singlet and triplet character. This causes $|\phi_S\rangle$ to behave nearly like an ideal singlet state in terms of relaxation rate and symmetry properties, but its small triplet admixture ensures that there is still a Hamiltonian term connecting it to the triplet states. This Hamiltonian term produces evolution in the singlet-triplet basis that the M2S sequence harnesses to transfer magnetization between triplet and singlet states [21].

Figure 4.1a shows the M2S experimental protocol used to create a nuclear spin singlet state from triplet state polarization and then return the singlet state to transverse triplet state (i.e., measurable) polarization after an evolution time, τ_{evolve}. Figure 4.1b gives a simulation of spin state and coherence dynamics during singlet state preparation with M2S if relaxation is ignored [34]. The first $\pi/2$ pulse creates trans-

verse magnetization of the form $I_{1x} + I_{2x} = |T_+\rangle\langle T_0| + |T_0\rangle\langle T_+| + |T_-\rangle\langle T_0| + |T_0\rangle\langle T_-|$. The first pulse train, consisting of n_1 π pulses, is synchronized such that $|S_0\rangle$ and $|T_0\rangle$ are swapped, resulting in the singlet-triplet coherence $I_{1y} - I_{2y} = i(|T_+\rangle\langle S_0| + |S_0\rangle\langle T_+| + |T_-\rangle\langle S_0| + |S_0\rangle\langle T_-|)$. A second $\pi/2$ pulse converts it to the long-lived coherence $I_{1z} - I_{2z} = i(|T_0\rangle\langle S_0| + |S_0\rangle\langle T_0|)$. The second pulse train, consisting of n_2 π pulses, rotates the singlet-triplet coherence into a singlet-triplet population difference $|S_0\rangle\langle S_0| - |T_0\rangle\langle T_0|$ with relaxation time T_S [39, 75].

The number of pulses required for the M2S sequence increases as the resonance frequency difference ($\Delta\nu$) between the two nearly-identical nuclear spins decreases and hence the singlet state becomes closer to ideal. The ideal pulse sequence parameters are $\tau = 1/4J$, $n_1 = \pi/2\theta$, and $n_2 = \pi/4\theta$, where $\theta = \arctan(\Delta\nu/J)$ is the mixing angle away from the singlet-triplet basis. With these values, we find that the time required for maximum singlet state creation is

$$t_{\text{M2S,max}} \approx \frac{3\pi}{8\Delta\nu} = \frac{1.18}{\Delta\nu} \tag{4.1}$$

In many cases, the required M2S pulse sequence time approaches or exceeds T_1 of the nuclear spins. Note that the singlet-triplet coherences produced during the first 2/3 of the pulse sequence have a lifetime of at most $T_2/3 \approx T_1/3$ (for liquid-state NMR of small molecules), and significant spin polarization can be lost before it is transferred to the singlet state.

4.1.2 SLIC Sequence

Figure 4.1c shows the SLIC pulse sequence used to create a nuclear spin singlet state from triplet state polarization and return the singlet state to transverse triplet
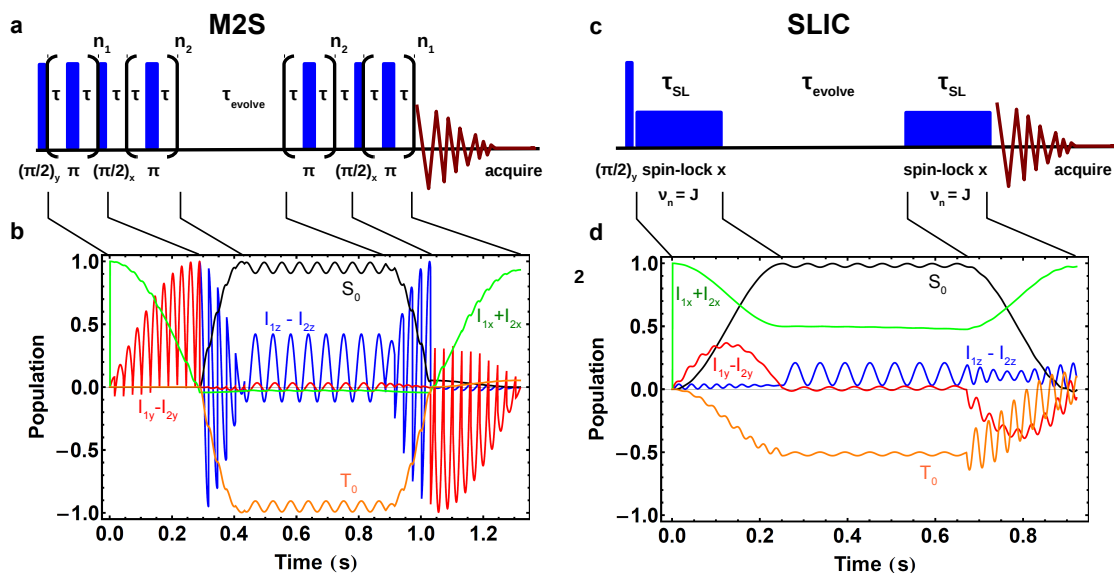
Figure 4.1: Simulated comparison of M2S and SLIC techniques applied to singlet state creation, evolution, and readout for a proton spin pair with chemical shift $\delta = 3.71$ ppm in the phe-gly-gly molecule. Guide lines connect points in the sequence with corresponding times in the simulation. (a) Schematic of M2S experiment: Following an initial $\pi/2$ pulse to create transverse triplet polarization, the M2S pulse sequence creates singlet state population by applying pulse trains with appropriate length and pulse spacing synchronized with the proton pair's J-coupling and resonance frequency difference. The system then evolves over τ_{evolve}, and the M2S sequence is applied in reverse order to convert singlet population back to transverse triplet polarization for inductive NMR detection. (b) Simulation of M2S experiment: Transfer, in a series of stages, of transverse (x-axis) triplet polarization to singlet-triplet coherences and finally to singlet and triplet state populations of equal magnitudes. Transfer to the singlet state population only occurs in the final 1/3 of the M2S preparation sequence. (c) Schematic of SLIC experiment: Transverse triplet polarization is created via an initial $\pi/2$ pulse and is then transferred to singlet state population by the application of spin-locking with $\nu_n = J$ for period τ_{SL}. For spin-locking, the transmitter frequency is set to the average resonance frequency of the nearly-equivalent spin pair. The system then evolves for τ_{evolve} and an identical spin-lock converts singlet population back to transverse triplet polarization for detection. (d) Simulation of SLIC experiment: Transfer of transverse triplet polarization to singlet state population begins immediately and occurs during a single spin-locking stage.

state polarization after an evolution time (τ_{evolve}) in analogy to the M2S experiment. However, instead of pulse trains, continuous spin-locking is applied on resonance with the nearly-equivalent spins at a nutation frequency equal to the J-coupling between spins, i.e., $\nu_n = J$. The simulation shown in Fig. 4.1d illustrates that such spin-locking transfers triplet state polarization directly from transverse polarization into singlet state population more quickly than in the M2S sequence.

An energy level analysis shows that selecting a nutation frequency $\nu_n = J$ matches the energies of the singlet state and one of the triplet states, creating a spin-lock induced crossing. At this energy, off-diagonal interaction terms $\Delta\nu/2\sqrt{2}$ become significant and induce oscillatory triplet/singlet polarization transfer. Consider two coupled spin-1/2 nuclei with identical resonance frequencies. As discussed in chapter 2, the system can be described by three triplet eigenstates, $|T_-\rangle$, $|T_0\rangle$, and $|T_+\rangle$, and one singlet eigenstate, $|S_0\rangle$. These are the symmetric and antisymmetric combinations of the product states given by equation 4.2:

$$|T_-\rangle = |\uparrow\uparrow\rangle$$
$$|T_0\rangle = \frac{|\uparrow\downarrow\rangle + |\downarrow\uparrow\rangle}{\sqrt{2}}$$
$$|T_+\rangle = |\downarrow\downarrow\rangle$$
$$|S_0\rangle = \frac{|\uparrow\downarrow\rangle - |\downarrow\uparrow\rangle}{\sqrt{2}} \tag{4.2}$$

The Hamiltonian for this system is described by

$$\mathcal{H}_0 = h \begin{bmatrix} -\frac{\nu_1+\nu_2}{2} + \frac{J}{4} & 0 & 0 & 0 \\ 0 & \frac{J}{4} & 0 & 0 \\ 0 & 0 & \frac{\nu_1+\nu_2}{2} + \frac{J}{4} & 0 \\ 0 & 0 & 0 & -\frac{3J}{4} \end{bmatrix}. \tag{4.3}$$

It is convenient to work in the rotating frame at the average resonance frequency of the spins, so that $(\nu_1 + \nu_2)/2 = 0$. Then

$$\mathcal{H}_{0,rot} = h \begin{bmatrix} \frac{J}{4} & 0 & 0 & 0 \\ 0 & \frac{J}{4} & 0 & 0 \\ 0 & 0 & \frac{J}{4} & 0 \\ 0 & 0 & 0 & -\frac{3J}{4} \end{bmatrix}. \tag{4.4}$$

If spin-locking is now applied on resonance with the triplet transitions with a nutation frequency ν_n, then the corresponding off-diagonal elements are added to the Hamiltonian:

$$\mathcal{H}_{SL} = h \begin{bmatrix} \frac{J}{4} & \frac{\nu_n}{\sqrt{2}} & 0 & 0 \\ \frac{\nu_n}{\sqrt{2}} & \frac{J}{4} & \frac{\nu_n}{\sqrt{2}} & 0 \\ 0 & \frac{\nu_n}{\sqrt{2}} & \frac{J}{4} & 0 \\ 0 & 0 & 0 & -\frac{3J}{4} \end{bmatrix}. \tag{4.5}$$

Since the spin-locking is applied for an extended period, we work with the new dressed

states that are formed. Diagonalization produces the dressed state Hamiltonian

$$
\mathcal{H}_{SL,dressed} = h
\begin{bmatrix}
\frac{J}{4} - \nu_n & 0 & 0 & 0 \\
0 & \frac{J}{4} & 0 & 0 \\
0 & 0 & \frac{J}{4} + \nu_n & 0 \\
0 & 0 & 0 & -\frac{3J}{4}
\end{bmatrix}.
\tag{4.6}
$$

The new dressed eigenstates are

$$
\begin{aligned}
|\phi_-\rangle &= \frac{1}{2}(|\uparrow\uparrow\rangle + |\downarrow\downarrow\rangle - |\uparrow\downarrow\rangle - |\downarrow\uparrow\rangle) \\
&= \frac{1}{2}(|T_-\rangle + |T_+\rangle) - \frac{1}{\sqrt{2}}|T_0\rangle \\
|\phi_0\rangle &= \frac{1}{\sqrt{2}}(|\downarrow\downarrow\rangle - |\uparrow\uparrow\rangle) = \frac{1}{\sqrt{2}}(|T_+\rangle - |T_-\rangle) \\
|\phi_+\rangle &= \frac{1}{2}(|\uparrow\downarrow\rangle + |\downarrow\uparrow\rangle + |\uparrow\uparrow\rangle + |\downarrow\downarrow\rangle) \\
&= \frac{1}{2}(|T_-\rangle + |T_+\rangle) + \frac{1}{\sqrt{2}}|T_0\rangle \\
|\phi_S\rangle &= \frac{1}{\sqrt{2}}(|\uparrow\downarrow\rangle - |\downarrow\uparrow\rangle) = |S_0\rangle.
\end{aligned}
\tag{4.7}
$$

The states $|\phi_0\rangle$ and $|\phi_S\rangle$ are split by energy J and are unaffected by the strength of spin-locking, whereas the energy of states $|\phi_-\rangle$ and $|\phi_+\rangle$ have a linear dependence on ν_n.

It is now evident that selecting a nutation frequency $\nu_n = J$ will match the energies of states $|\phi_-\rangle$ and $|\phi_S\rangle$, creating a spin-lock induced crossing. At this energy, any off-diagonal interaction terms between the two eigenstates become significant and drive magnetization transfer. A resonance frequency difference between the two spins is

one such off-diagonal term, which can be added to the Hamiltonian so that

$$
\mathcal{H}_{SL,dressed} = h
\begin{bmatrix}
\frac{J}{4} - \nu_n & 0 & 0 & \frac{\Delta\nu}{2\sqrt{2}} \\[2ex]
0 & \frac{J}{4} & 0 & 0 \\[2ex]
0 & 0 & \frac{J}{4} + \nu_n & -\frac{\Delta\nu}{2\sqrt{2}} \\[2ex]
\frac{\Delta\nu}{2\sqrt{2}} & 0 & -\frac{\Delta\nu}{2\sqrt{2}} & -\frac{3J}{4}
\end{bmatrix}.
\tag{4.8}
$$

When $\nu_n = J$, the off-diagonal terms cause magnetization to coherently oscillate between triplet and singlet states with a period $T = \sqrt{2}/\Delta\nu$, and maximum transfer occurs at half this time:

$$
t_{\mathrm{SL,max}} = \frac{1}{\Delta\nu\sqrt{2}} = \frac{0.707}{\Delta\nu}.
\tag{4.9}
$$

Comparison with equation 4.1 shows that SLIC produces singlet state polarization about 40% faster than M2S, which results in fewer relaxation losses. To compare the effectiveness of the two sequences, we performed simulations using Bloch equations to model relaxation and singlet-triplet polarization transfer. Figure 4.2 plots the calculated polarization transfer efficiency for M2S and SLIC as a function of the product $T_1\Delta\nu$. SLIC is found to be significantly more efficient than M2S for all ranges of parameters, and particularly for $T_1\Delta\nu < 1$.

4.1.3   Experiment

To assess the relative utility of the SLIC and M2S sequences for producing nuclear spin singlet states, we performed NMR measurements at 4.7 T on a 20 mM solution of the phenylalanine-glycine-glycine (phe-gly-gly) molecule dissolved in D_2O. Nitrogen gas was bubbled through the solution for 5 minutes to displace dissolved oxygen. A
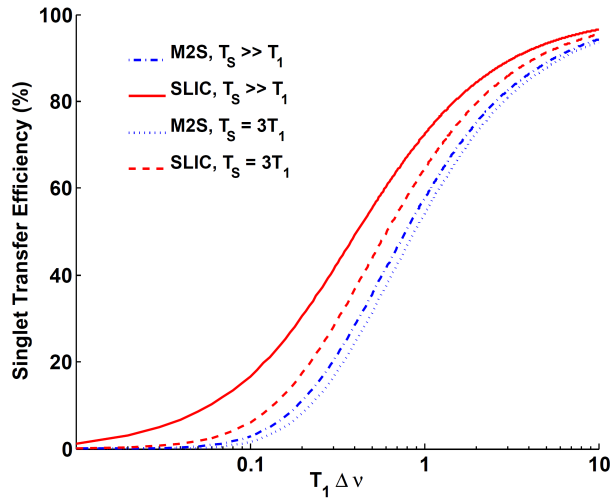
Figure 4.2: Simulations of ideal triplet/singlet polarization transfer efficiency for M2S (blue) and SLIC (red). Results are shown for $T_S \gg T_1$ and $T_S = 3T_1$. M2S was modeled in two steps: first, polarization transfer from $I_{1x} + I_{2x}$ with lifetime $T_2 = T_1$ to $I_{1y} - I_{2y}$ with lifetime $T_1/3$; second, polarization transfer from $I_{1z} - I_{2z}$ with lifetime $T_1/3$ to singlet state S_0 with lifetime T_S. Only one polarization transfer needed to be modeled for SLIC, between $I_{1x} + I_{2x}$ with lifetime $T_2 = T_1$ and S_0 with lifetime T_S. A maximum of 50% polarization transfer to the singlet state can be achieved by both sequences, which we define to be an efficiency of 100%. Note that both sequences are less efficient for smaller T_S/T_1 due to singlet relaxation.
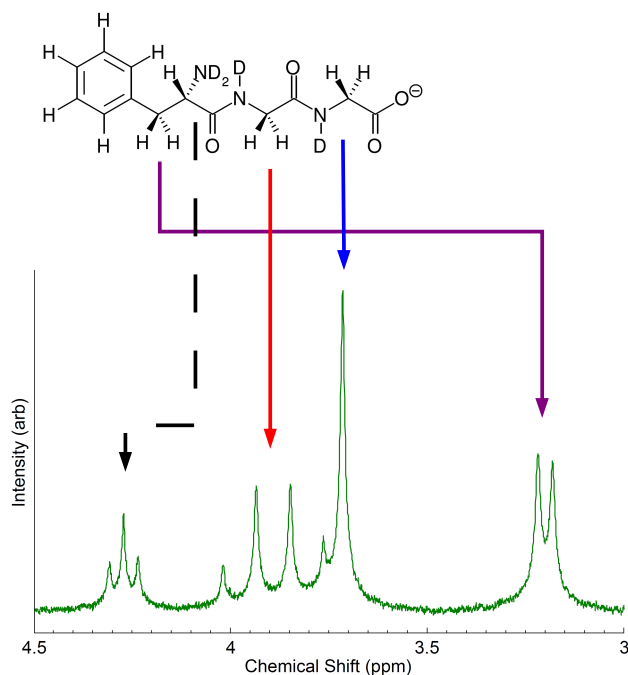
Figure 4.3: The phenylalanine-glycine-glycine structure is shown with its corresponding spectrum measured at 200 MHz. The aromatic proton resonances occurring near 7.3 ppm are not shown.

reference spectrum (Fig. 4.3) was acquired with one $\pi/2$ pulse followed by an FID acquisition, which shows that the molecule possesses two sets of nearly-equivalent proton pairs in which the protons are unresolved ($\delta = 3.20$ ppm and $\delta = 3.71$ ppm), and one proton pair exhibiting a second-order spectrum (centered at $\delta = 3.89$ ppm). Each proton of the pair at $\delta = 3.20$ ppm is split by a third neighboring spin ($\delta = 4.27$ ppm) with strength $J = 7.3$ Hz. The spin-lattice relaxation time, T_1, was measured for each nucleus using an inversion recovery sequence, and results are shown in Table 4.1.

Pulse sequences to implement SLIC are shown in Fig. 4.4. The transmitter frequency is set to the average resonance frequency of the proton pair of interest. A

79

Table 4.1: Spin-lattice relaxation times for protons of the phe-gly-gly molecule

Chemical Shift (δ)	T_1 (ms)
3.20	430±5
3.71	912±7
3.89	618±6
4.27	1760±20

a   SLIC sequence for detecting level crossing   **b**   SLIC sequence for singlet creation and readout
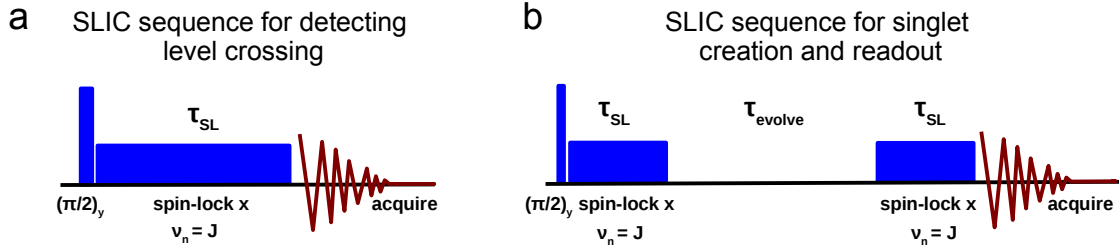
Figure 4.4: A typical experiment uses the SLIC sequence to create singlet state by applying on-resonance spin-locking with the nutation frequency matched to the J-coupling and with a duration appropriate for the resonance frequency difference. (a) The acquisition can be performed directly following singlet creation to detect the corresponding loss in x-axis magnetization, or (b) the system can be allowed to evolve, after which the singlet state can be converted back to transverse polarization for readout by applying spin-locking a second time.

$\pi/2$ pulse with phase y is applied to create a coherence between $(|T_-\rangle + |T_+\rangle)/\sqrt{2}$ and $|T_0\rangle$. Next, the phase is shifted 90° and spin-locking is applied with a nutation frequency $\nu_n = J$. In the resulting dressed state, the previous coherence becomes a population difference $|\phi_-\rangle\langle\phi_-| - |\phi_+\rangle\langle\phi_+|$. After a time $\tau_{\mathrm{SL}} = 0.707/\Delta\nu$, this is converted to a population difference $|\phi_S\rangle\langle\phi_S| - |\phi_+\rangle\langle\phi_+|$. Spin-locking is then removed. In Fig. 4.4a, an acquisition is performed immediately to measure the x-axis magnetization, $I_{1x} + I_{2x}$, whereas in Fig. 4.4b, the system is allowed to evolve for duration τ_{evolve} and both the singlet and triplet states are allowed to relax. The remaining singlet polarization is then read out by applying spin-locking again with phase x and nutation frequency $\nu_n = J$ for time τ_{SL} and then acquiring an FID with phase x.

Phase cycling is performed to remove residual triplet polarization by inverting the phase of both the $\pi/2$ pulse and the acquisition. The singlet state lifetime is found by measuring the remaining singlet population for a range of τ_{evolve} and fitting to a single exponential decay. We optimized the singlet state creation for SLIC using both sequences of Fig. 4.4 by scanning ν_n and τ_{SL} and measuring the NMR signal at the end of each sequence.

For comparison, we also performed the experiment using Tayler and Levitt's M2S sequence for preparation and readout of the singlet state, with the pulse sequence drawn in Fig. 4.1a, starting with the ideal values for τ, n_1, and n_2. However, the optimal number of pulses can vary significantly from the theoretical values when other spins couple to the target spin pair. We optimized parameters by scanning τ, n_1, and n_2 and measuring the NMR signal at the end of the sequence.

4.1.4 Results

We first addressed the nearly-equivalent proton spin pair with chemical shift δ = 3.71 ppm and T_1 = 912 $\pm$ 7 ms. For the M2S sequence (Fig. 4.1a) we found optimized parameters for singlet creation to be n_1 = 10, n_2 = 5, and τ = 14.4 ms, which indicates J = 17.4 $\pm$ 0.1 Hz and $\Delta\nu$ = 2.8 $\pm$ 0.3 Hz. We also found a singlet lifetime of T_S = 25.1 $\pm$ 0.8 s with no spin-locking applied during τ_{evolve}. We measured the NMR signal intensity (x-axis magnetization, proportional to the transverse triplet state polarization) at the end of the M2S sequence for τ_{evolve} = 5 s, which arises from the transfer of transverse triplet state polarization to singlet state population and then back to measurable transverse triplet state polarization after τ_{evolve}, and we

then used the singlet lifetime to extrapolate the singlet state population at $\tau_{\mathrm{evolve}} =$ 0. During τ_{evolve}, remaining triplet state polarization is lost to relaxation, and it does not contribute to the final signal. We compared this M2S NMR signal magnitude to a reference measurement arising from a single $\pi/2$ pulse applied to the sample, i.e., without singlet creation. From this analysis we estimate that 24% of the initial triplet state polarization was transferred to the singlet state and back to triplet for $\tau_{\mathrm{evolve}} = 0$, out of a theoretical maximum of 50%, yielding an efficiency of 69% for each application of the M2S sequence.

For the SLIC technique, we determined the optimal spin-lock nutation frequency by performing a truncated SLIC pulse sequence in which the NMR signal (x-axis magnetization) was acquired directly after the first spin-locking period. As a function of nutation frequency, the measured NMR signal exhibited a dip centered at $\nu_n =$ 17.5 $\pm$ 0.3 Hz with a relative depth of $\sim$ 25% (Fig. 4.5a), consistent with the SLIC condition of $\nu_n = J$ for optimal triplet/singlet polarization transfer. We then used this optimal spin-lock nutation frequency in the complete SLIC sequence with τ_{evolve} = 5 s (Fig. 4.1C) and optimized the spin-lock duration (τ_{SL}) to produce the strongest NMR signal and hence maximal singlet state creation. The measured dependence of the SLIC NMR signal on the spin-lock duration (Fig. 4.5B) exhibits a flat maximum for $\tau_{\mathrm{SL}} \approx 280$ to 360 ms. Using $\tau_{\mathrm{SL}} = 300$ ms provided about 34% polarization transfer from the triplet to the singlet state and back when extrapolated to τ_{evolve} = 0, indicating an 82% polarization transfer efficiency for each application of SLIC spin-locking. Although the matching condition is narrow, the B$_1$ homogeneity of our spectroscopy coil was sufficient to achieve good polarization transfer. Applications in
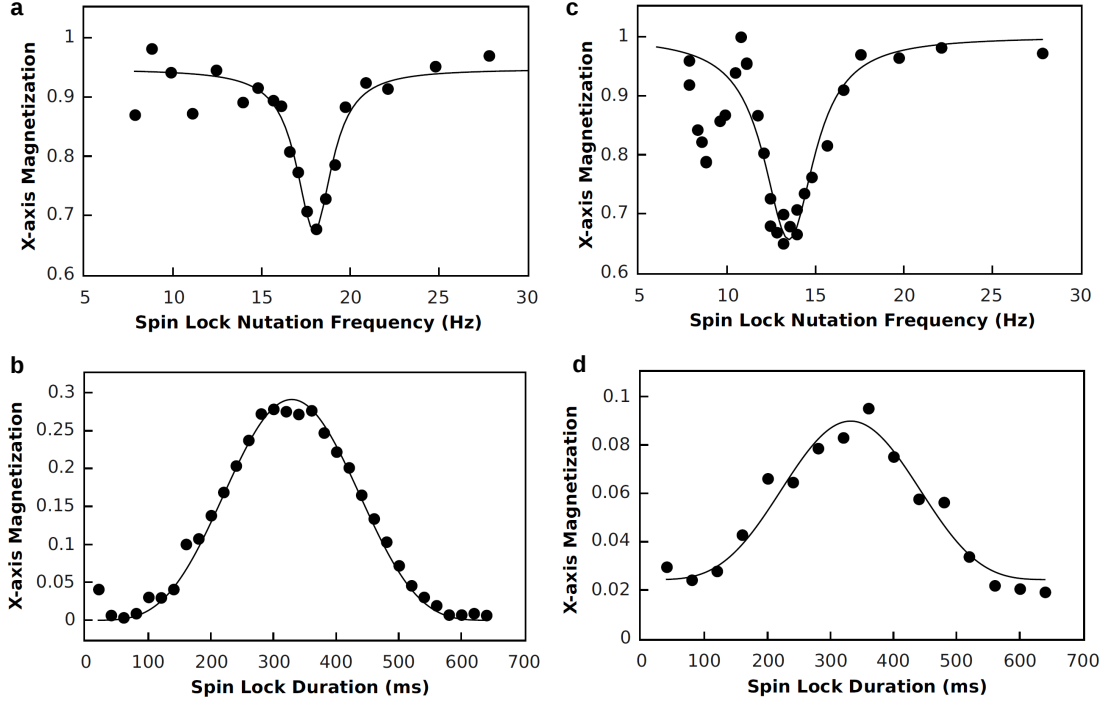
Figure 4.5: Experimental application of the SLIC technique to nuclear spin singlet state creation in the phe-gly-gly molecule. Results for $\delta = 3.71$ ppm proton pair: (a) The NMR signal (normalized x-axis magnetization, proportional to transverse triplet polarization) following the first SLIC spin-lock as a function of nutation frequency for $\tau_{SL} = 300$ ms exhibits a pronounced dip when the spin-lock nutation frequency equals the J-coupling. A Lorentzian is fit to the measurement to determine $\nu_n = J = 17.5 \pm 0.3$ Hz. (b) NMR signal after the complete SLIC experiment with $\tau_{evolve} = 5$ s (proportional to final transverse triplet polarization surviving transfer to singlet and back) as a function of spin-lock duration. Maximal singlet state creation is found for $\tau_{SL} \approx 280$ to 360 ms. We fit for amplitude, A, and $\Delta\nu$ with the function $I = A \sin^4(\pi\tau_{SL}\Delta\nu/\sqrt{2})$, and we find $\Delta\nu = 2.15 \pm 0.02$ Hz. Results for $\delta = 3.20$ ppm proton pair: (c) NMR signal following the first SLIC spin-lock as a function of nutation frequency for $\tau_{SL} = 332$ ms, with a Lorentzian fit to the data yielding optimal $\nu_n = J = 13.5 \pm 0.2$ Hz. (d) NMR signal after the complete SLIC experiment with $\tau_{evolve} = 500$ ms as a function of spin-lock duration. Maximal singlet state creation is found for $\tau_{SL} \approx 300$ to 400 ms. From a fit with the function $I = A \sin^4(\pi\tau_{SL}\Delta\nu/\sqrt{2}) + c$, we find $\Delta\nu = 2.13 \pm 0.06$ Hz.

magnetic resonance imaging may require a pulse sequence with a broader nutation frequency bandwidth.

We next applied the SLIC technique to singlet state creation in a second proton spin pair in the phe-gly-gly molecule, with chemical shift $\delta = 3.20$ ppm and T_1 $= 430 \pm 5$ ms. This proton spin pair is coupled to a third proton that decreases both the singlet lifetime ($T_S = 2.15 \pm 0.05$ s with no spin-locking applied) and the triplet/singlet polarization transfer efficiency. We followed the procedure outlined above to determine the optimal spin-lock nutation frequency $\nu_n = J = 13.5 \pm 0.2$ Hz, and the optimal spin-lock duration $\tau_{SL,max} = 332 \pm 9$ ms (Fig. 4.5c,d). We then applied the complete SLIC sequence with $\tau_{\text{evolve}} = 500$ ms and found about 12% polarization transfer to the singlet state and back when extrapolated to $\tau_{\text{evolve}} = 0$, which represents a transfer efficiency of 49% for each application of SLIC spin-locking. For comparison, we experimentally investigated singlet state creation with the M2S sequence. We determined optimized M2S parameters to be $n_1 = 4$, $n_2 = 5$, and τ $= 17.9$ ms, and measured that only 4% of the polarization was transferred from the triplet to the singlet state and back when extrapolated to $\tau_{\text{evolve}} = 0$, which represents a 28% efficiency for each application of the M2S sequence.

We also compared the effectiveness of M2S and SLIC using off-resonant transmitter frequencies. We performed singlet state creation and readout sequences using both M2S and SLIC at a number of transmitter frequency offsets with a constant $\tau_{\text{evolve}} = 500$ ms and measured the transfer efficiency. The resulting curves were fit with a Gaussian to determine a full width at half maximum (FWHM) effective bandwidth (Fig. 4.6). The effective bandwidth was similar for both sequences, with
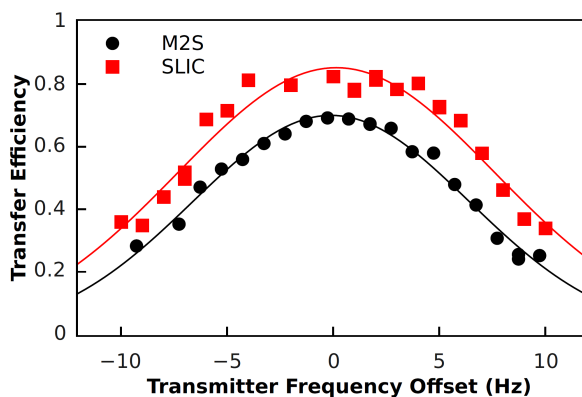
Figure 4.6: Triplet/singlet polarization transfer efficiencies for the $\delta = 3.71$ ppm spin pair using SLIC and M2S, measured as a function of transmitter frequency offset and fit with Gaussian functions. SLIC exhibits a higher efficiency and a 15% broader effective bandwidth.

FWHM bandwidths of 17.6 ± 0.6 Hz for SLIC and 15.3 ± 0.3 Hz for M2S.

4.1.5   Discussion

In summary, we introduced an improved and broadly applicable method, known as SLIC for "spin-lock induced crossing," for the creation of long-lived singlet states of nuclear spins in molecules and other many-atom systems. As an example, we applied our SLIC technique to two different nearly-equivalent proton spin pairs in the phenylalanine-glycine-glycine molecule and demonstrated that the SLIC experiment gives 40% and 300% more signal than the previous M2S technique for the transfer of triplet state polarization to singlet state population and then back to measurable transverse triplet state polarization[1]. SLIC is more effective than M2S primarily

---

[1]It was pointed out by G. Pileio that using composite π pulses, such as $(\pi/2)_x$-$(\pi)_y$-$(\pi/2)_x$, decreases the sensitivity to pulse errors and leads to higher M2S efficiency. The improvement from SLIC might not be as large if such pulses were implemented.

because the transfer to the long-lived singlet state begins immediately with SLIC, without the need for an initial transfer to a singlet-triplet coherence as with M2S. Though a singlet-triplet coherence can have an extended lifetime relative to a single-spin coherence time (T_2), it generally relaxes significantly faster than the singlet population lifetime (T_S), leading to greater polarization loss and less efficient singlet state creation for M2S than for SLIC. Additionally, the shorter length and lower peak power of SLIC ultimately results in significantly less power dissipation in the sample. The relative advantage of SLIC grows for molecules with small resonance frequency difference $\Delta\nu$ between the nuclear spins, which in many cases can be much smaller than $1/T_1$.

The SLIC pulse sequence has been further developed by Theis *et al.*, who demonstrated an adiabatic version (adSLIC) with a broader nutation frequency (B_1) bandwidth [78]. This makes it possible to accomplish more efficient singlet transfer when there is less accurate knowledge of the molecular J-couplings. Using adSLIC, Claytor *et al.* prepared singlet states in pairs of ^{13}C nuclei at natural isotopic abundance [45], allowing singlet states to be characterized without synthesizing costly isotopically-enriched samples.

4.2   Singlet State Transfer

When molecules possess four or more nuclear spins, it is possible to define singlet and triplet states in various combinations of paired nuclear spins. Such states were studied by the Warren group, who used M2S and adSLIC sequences to produce singlet states in symmetric molecules [22, 78]. In that technique, one singlet-triplet subspace

is defined on a pair of protons and another singlet-triplet subspace is defined on a pair of ^{13}C nuclei. The protons are coupled more strongly to the ^{13}C nuclei than to one another. The pulse sequence then performs the operation $|T_{0,H}T_{0,C}\rangle \rightarrow |S_{0,H}S_{0,C}\rangle$ to produce a long-lived singlet state. However, because the spins within each pair are identical, singlet states cannot be produced selectively in one spin pair or the other.

In this section, we study a different geometry consisting of two spin pairs whose intra-pair spin-spin couplings are strong but whose inter-pair couplings are much weaker. We selectively create the singlet state in one spin pair and use the weak coupling to transfer singlet order to the second spin pair. This technique makes it possible to measure weak J-coupling differences and to perform NMR experiments in a singlet-singlet subspace.

Using the glutamate molecule, we demonstrate how typical NMR experiments can be performed in the Bloch sphere defined by the two singlet states. We implement the equivalent of a Rabi experiment, in which polarization is coherently transferred back and forth between the singlet states of the two proton pairs. This allows us to measure the singlet-singlet interaction strength. We then perform a Ramsey experiment by creating a coherent superposition of singlet states and allowing the superposition to precess in the singlet-singlet basis. This provides a measurement of the energy difference between singlet states and demonstrates that a quantum mechanical phase is present despite the absence of a net dipole moment. These measurements represent a first step toward creating a decoherence-free subspace in which both phase and magnitude information can be stored for times longer than T_1 or T_2.

We also implement singlet state transfer to study weak coupling differences in the

phenylalanine-glycine-glycine (phe-gly-gly) molecule. The spin-spin relaxation time, T_2, normally sets a limit on the length of both FID measurements and coherence transfer experiments that allow the detection of scalar couplings [79]. Thus the coupling strength must generally be of at least the order $1/T_2$ to be detectable. However, because the nuclear spin singlet state can have a lifetime $T_S \gg T_1$, coherent interactions between singlet states are detectable on the order $1/T_S$. We subsequently measure a scalar coupling difference of ~ 10 mHz between spins in phe-gly-gly.

4.2.1 Theory

We consider two pairs (labeled by $i = 1$ and 2) of spin-1/2 nuclei, each with spins labeled $j = a$ and b. If the coupling between spins within each pair is strong compared with their resonance frequency difference ($J_{iaib} \gg |\nu_{ia} - \nu_{ib}|$), or if strong spin-locking is applied ($\nu_n \gg |\nu_{ia} - \nu_{ib}|$), then each spin pair is described by singlet and triplet eigenstates. As shown in chapter 2, these are

$$|\phi_+\rangle = \frac{1}{2}(|\uparrow\downarrow\rangle + |\downarrow\uparrow\rangle + |\uparrow\uparrow\rangle + |\downarrow\downarrow\rangle) = \frac{1}{\sqrt{2}}|T_0\rangle + \frac{1}{2}(|T_-\rangle + |T_+\rangle)$$

$$|\phi_0\rangle = \frac{1}{\sqrt{2}}(|\uparrow\uparrow\rangle - |\downarrow\downarrow\rangle) = \frac{1}{\sqrt{2}}(|T_-\rangle - |T_+\rangle)$$

$$|\phi_S\rangle = \frac{1}{\sqrt{2}}(|\uparrow\downarrow\rangle - |\downarrow\uparrow\rangle) = |S_0\rangle$$

$$|\phi_-\rangle = \frac{1}{2}(|\uparrow\downarrow\rangle + |\downarrow\uparrow\rangle - |\uparrow\uparrow\rangle - |\downarrow\downarrow\rangle) = \frac{1}{\sqrt{2}}|T_0\rangle - \frac{1}{2}(|T_-\rangle + |T_+\rangle). \qquad (4.10)$$

If interactions between spins of different pairs is weak compared with the interactions of spins within each pair, then the system can be described by 16 new product states formed from the singlet and triplet states of each spin pair. In the experiments we perform, we selectively create singlet state in either one spin pair or the other, so

we only need to consider product states containing the triplet states of one spin pair and the singlet state of the other, represented by $|TS_0\rangle$ and $|S_0T\rangle$. Here, the triplet component is some combination of the triplet states described by

$$|T\rangle_i = \alpha_i|\phi_+\rangle_i + \beta_i|\phi_0\rangle_i + \gamma_i|\phi_-\rangle_i. \tag{4.11}$$

To preserve normalization, we require

$$\alpha_i^2 + \beta_i^2 + \gamma_i^2 = 1. \tag{4.12}$$

The spins of pair 1 are also weakly coupled to the spins of pair 2, i.e., there are couplings J_{1a2a}, J_{1a2b}, J_{1b2b}, J_{1b2a}. These couplings produce an interaction between $|TS_0\rangle$ and $|S_0T\rangle$ with strength

$$C = \frac{J_{1a2a} + J_{1b2b} - J_{1a2b} - J_{1b2a}}{4}\left(\alpha_1\alpha_2 + \beta_1\beta_2 + \gamma_1\gamma_2\right). \tag{4.13}$$

Note that the interaction between a spin of one pair and the two spins of the other pair is antisymmetric, which is necessary to couple the two antisymmetric eigenstates. The interaction is mediated by the difference in *cis* and *trans* J-couplings within the molecule, where *cis* refers to two nuclei on the same side of the molecular backbone and *trans* refers to two nuclei on the opposite side of the molecular backbone. Although intramolecular configurations change rapidly in the molecules studied, there is a different average coupling $J_{iai'a}$ versus $J_{iai'b}$ no matter which particular spins are labeled a and b [80, 81].

The energy of each state is a function of the spin-locking nutation frequency, ν_n, and the intra-pair J-couplings:

$$E_1 = \frac{J_{1a1b}}{4} - \frac{3J_{2a2b}}{4} + (\alpha_1^2 - \gamma_1^2)\nu_{n,1}$$

$$E_2 = \frac{J_{2a2b}}{4} - \frac{3J_{1a1b}}{4} + (\alpha_2^2 - \gamma_2^2)\nu_{n,2}. \tag{4.14}$$

A Hamiltonian for $|TS_0\rangle$ and $|S_0T\rangle$ can then be written as

$$\mathcal{H} = h \begin{bmatrix} E_1 & C \\ C & E_2 \end{bmatrix}. \tag{4.15}$$

The interaction terms have no effect unless $|\Delta E| = |E_1 - E_2| < |C|$, i.e., transitions cannot take place as long as the coupling terms are smaller than the energy difference between the eigenstates. At zero spin-locking nutation frequency, this energy difference is simply $|\Delta E| = |J_{1a1b} - J_{2a2b}|$. However, a subset of states can be brought on resonance by spin-locking, which modifies the energy of those states containing α or γ terms. If the RF spin-locking transmitter frequency and power are chosen such that $|\Delta \nu_n| = |\nu_{n,1} - \nu_{n,2}| = |\Delta E|$, then two states are brought on resonance and coherent polarization transfer occurs. The singlet state population of each spin pair then exhibits an oscillation with period

$$\tau = \frac{2}{J_{1a2a} + J_{1b2b} - J_{1a2b} - J_{1b2a}}. \tag{4.16}$$

If spin-locking is applied to spin pair 1, then the difference in effective spin-locking nutation frequencies can be approximated by

$$\Delta \nu_n \approx \sqrt{\nu_{n,1}^2 + \Delta \nu_{12}^2} - \nu_{n,1}, \tag{4.17}$$

where $\Delta \nu_{12}$ is the average resonance frequency difference between spin pair 1 and spin pair 2.

By controlling the duration of spin-locking, unitary transformations can be performed, such as the equivalent of a π pulse:

$$|\phi_+ S_0\rangle \rightarrow |S_0 \phi_+\rangle, \tag{4.18}$$

and a $\pi/2$ pulse:

$$|\phi_+ S_0\rangle \to \frac{1}{\sqrt{2}} \left(|\phi_+ S_0\rangle + |S_0 \phi_+\rangle \right). \tag{4.19}$$

Note that although the product state describing singlet transfer contains a triplet state, we will perform experiments that only measure the singlet component of each spin pair. This might suggest that triplet state relaxation can be ignored. However, in actuality triplet-triplet interactions and relaxation affect the details of the transfer process. For instance, if the triplet states interconvert more slowly than $1/\tau$, then the interacting singlet states will be entangled with either $|\phi_+\rangle$ or $|\phi_-\rangle$, depending on the spin-locking phase (a $180°$ phase shift changes the sign of ν_n). One could subsequently perform the operations $|\phi_+ S_0\rangle \to |S_0 \phi_+\rangle$ followed by $|\phi_- S_0\rangle \to |S_0 \phi_-\rangle$ in two independent steps. On the other hand, if the triplet states interconvert more quickly than $1/\tau$, then the triplet states will always remain in equilibrium with one another and the singlet transfer will appear independent of the spin-locking phase. Then the triplet states play a purely ancillary role by bringing the singlet levels into resonance, and it is possible to view the system as a subspace defined by two singlet states. This is the case for our experiments because the two spin pairs are off-resonance by 52 Hz, and when one spin pair is spin-locked the other experiences the interaction term $\nu_1 \hat{I}_{1z} + \nu_2 \hat{I}_{2z}$, which connects states $|\phi_+\rangle$ and $|\phi_-\rangle$. Consequently, either spin-locking phase effectively drives the transition

$$|\phi_+ S_0\rangle + |\phi_- S_0\rangle \to |S_0 \phi_+\rangle + |S_0 \phi_-\rangle. \tag{4.20}$$

Whether a system is described by the first or second situation can be determined experimentally, as described below. Alternatively, the system can be analyzed by further dressing with the interaction $\nu_1 \hat{I}_{1z} + \nu_2 \hat{I}_{2z}$. Simulations show that this term

produces energy shifts making it possible to drive singlet transfer even when the effective spin-locking is equal for both spin pairs.

4.2.2   Experiment

Experiments were performed in a 200 MHz NMR spectrometer using an 80 mM solution of monosodium glutamate dissolved in pH 7.0 phosphate buffer and a 20 mM solution of phenylalanine-glycine-glycine (phe-gly-gly) dissolved in D_2O. For both samples, nitrogen gas was bubbled through the solution for 5 minutes to displace dissolved oxygen. The glutamate spectrum is identical to that in Fig. 3.2.1b and the phe-gly-gly spectrum is identical to that in Fig. 4.3.

Figure 4.7 shows the variety of pulse sequence combinations possible for singlet transfer experiments. Each experiment consists of three stages: singlet state preparation, a singlet transfer procedure, and singlet state readout. The particular pulse sequence used for preparation and readout depends on the targeted spin pair's J-coupling and chemical shift parameters. The SLIC sequence is used for nearly-equivalent spins while the three-pulse sequence is used for inequivalent spins. For either case, the singlet state is produced selectively in one of the two proton pairs, due to the differences in coupling strength and chemical shifts for each pair.

The singlet transfer procedure can consist of either a Rabi or a Ramsey experiment. In the Rabi experiment, CW spin-locking is applied to drive singlet transfer from one spin pair to another. Either the spin-locking duration τ_{SL} or spin-locking nutation frequency ν_n can be varied while the other is kept constant. In the Ramsey experiment, spin-locking with a fixed nutation frequency and duration is creates a
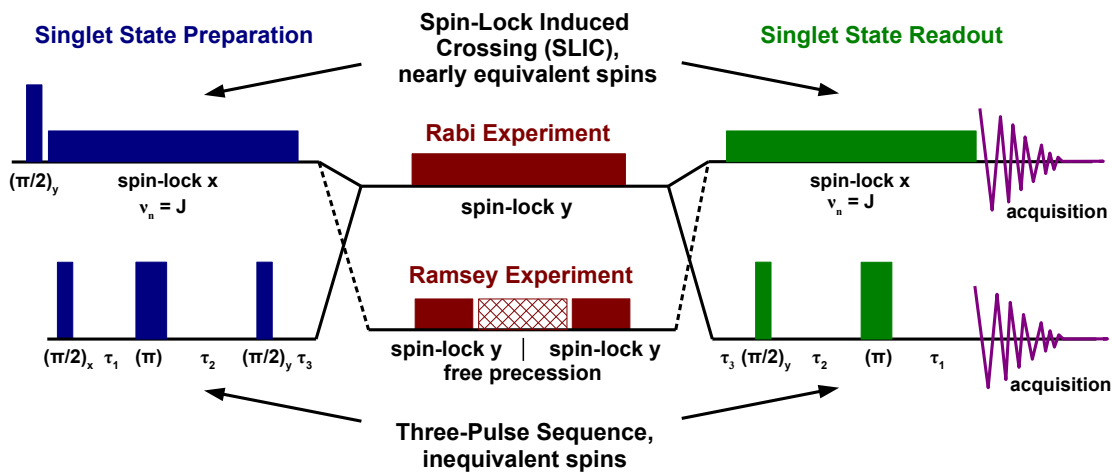
Figure 4.7: Pulse sequences for singlet state transfer measurements. Singlet state is selectively created on one spin pair with either a spin-lock induced crossing or a three-pulse sequence. A Rabi experiment can be performed to measure the singlet transfer rate to the second spin pair, or a Ramsey experiment can be performed to study a singlet-singlet coherence. Finally, singlet state is read from one spin pair or the other before a FID signal is acquired.

coherent superposition between the two singlet states. This is followed by free precession of the states for time τ_{Ramsey} and then a subsequent spin-locking application to read out the superposition. During the free precession period, spin-locking can be turned off, or it can be applied with a nutation frequency low enough to avoid inducing singlet transfer.

Finally, a readout sequence is selectively applied to one of the proton pairs to convert its singlet state to transverse magnetization, which is measured by acquiring the FID signal. Readout can be performed on either the same spin pair on which the singlet state was created, or on a different spin pair. Once again, the SLIC sequence is used for readout from nearly-equivalent spins while the three-pulse sequence is used for inequivalent spins.
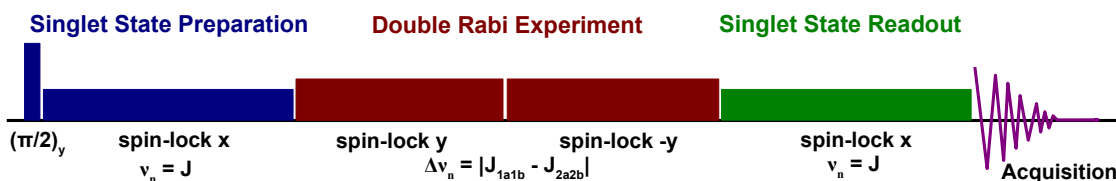
Figure 4.8: Double Rabi sequence for determining whether entanglement is lost between the singlet state of one spin pair and the individual triplet states of the other spin pair.

To determine whether the singlet state of one pair maintains entanglement with a triplet state of the other pair, or whether the triplet states mix and entanglement is lost, we perform the sequence shown in Fig. 4.8. During the Rabi sequence, spin-locking is first applied with phase y for duration τ_{SL}, and then applied a second time with phase $-y$ for duration τ_{SL}. If entanglement is maintained, then when $\tau_{\mathrm{SL}} = 1/(2|J_{\mathrm{cis}} - J_{\mathrm{trans}}|)$, maximal singlet state transfer occurs for each triplet case $|\phi_+\rangle$ and $|\phi_-\rangle$, and the singlet state transfer is maximized. On the other hand, if entanglement is lost, then a full period of singlet state transfer occurs for time $\tau_{\mathrm{SL}} = 1/(2|J_{\mathrm{cis}} - J_{\mathrm{trans}}|)$, and the amount of singlet transferred is zero.

4.2.3 Results

Glutamate

Figure 4.9a shows results for a singlet transfer Rabi experiment in glutamate. The singlet state was prepared on spin pair 1 (chemical shift $\delta = 2.04$ ppm) using the SLIC sequence with $\nu_n = 15.5$ Hz and a spin-lock duration of 157 ms. Black points show the normalized integrated signal of spin pair 2 ($\delta = 2.3$ ppm) when no spin-lock is applied ($\nu_n = 0$ Hz) during the transfer stage after reading out its singlet state

using the SLIC sequence with $\nu_n = 17$ Hz and a spin-lock duration of 145 ms. While some residual magnetization is present, it decays within ~ 200 ms, indicating that it arises from short-lived triplet states and that no singlet state has been created on spin pair 2. Moreover, we set an upper limit of 0.01 for the possible amount of singlet transferred. Red points show the same measurement when $\nu_n = 500$ Hz ($\Delta \nu_n = 2.7$ Hz) is applied during the transfer stage with the transmitter set to $\delta = 2.04$ ppm. The periodic oscillations indicate a coherent transfer of singlet state population between spin pairs 1 and 2. Blue points are results for the same experiment ($\nu_n = 500$ Hz, $\Delta \nu_n = 2.7$ Hz, transmitter at $\delta = 2.04$ ppm) when the singlet state is instead read out from spin pair 1. Notice that the oscillation has the same period but a $180°$ phase shift, which indicates that singlet state from spin pair 1 is lost in proportion to that gained by spin pair 2. Approximately 1/3 of the singlet state from spin pair 1 is not transferred, as it corresponds to the population of spin pair 2 in the $|\phi_0\rangle$ state. The period of the oscillation indicates a transfer frequency of 2.5 ± 0.1 Hz, which should equal the average difference between J_{cis} and J_{trans}. The total singlet state (purple points) exhibits a weak oscillation, which indicates that there is also a small amount of coherent transfer into a state other than the singlet state of spin pair 2. During the Rabi experiment, total singlet state population relaxes with a time constant $T_{\mathrm{Rabi}} = 1.8 \pm 0.1$ s, which is approximately twice T_1 (measured T_1 values are 0.92 ± 0.02 s and 1.11 ± 0.02 s for spin pairs 1 and 2, respectively). The Rabi experiment was repeated for a range of ν_n values during the singlet transfer stage and the amplitude of the oscillations was measured (Fig. 4.9b). A best-fit Lorentzian indicates a resonance condition $\Delta \nu_n = \Delta E = 2.25 \pm 0.08$ Hz.
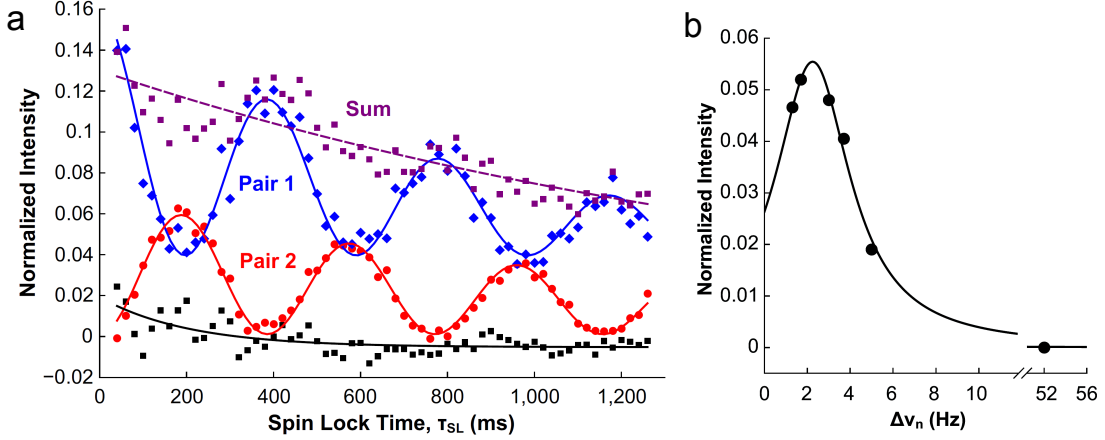
Figure 4.9: Measurement of coherent singlet state transfer in glutamate. (a) Singlet order is selectively prepared predominantly in spin pair 1 and is followed with spin-locking at a 500 Hz nutation rate during the evolution time. The singlet state is then read out from either spin pair 1 (blue points) or spin pair 2 (red points). Oscillations in the singlet state population of each spin pair indicate $f = |J_{\text{cis}} - J_{\text{trans}}| = 2.5 \pm 0.1$ Hz. If spin-locking is not applied, singlet transfer does not occur (black points). The small amount of residual magnetization decays with a time constant $T = 205 \pm 7$ ms, indicating that it arises from short-lived triplet states. The sum of singlet state measurements (magenta points) decays exponentially with time constant $T_{\text{Rabi}} = 1.8 \pm 0.1$ s. All intensities are integrated signals normalized to a conventional spectrum. Spin pair 1 results were fit with a function $A \cos^2(\pi f \tau_{\text{SL}}) \exp(-\tau_{\text{SL}}/T_{\text{Rabi}}) + c$ while spin pair 2 results were fit with a function $A \sin^2(\pi f \tau_{\text{SL}}) \exp(-\tau_{\text{SL}}/T_{\text{Rabi}}) + c$. (b) The amplitude of singlet transfer, extracted from the parameter A of the fit, is plotted for singlet transfer measurements performed with a range of spin-locking nutation frequencies. A Lorentzian fit gives a peak value of 2.25 ± 0.08 Hz for the resonance condition with a FWHM of 4.3 ± 0.4 Hz.

To perform a Ramsey experiment, we first prepared the singlet state in spin pair 1 and then performed a $\pi/2$ rotation in the singlet-singlet subspace by spin-locking with nutation frequency $\nu_n = 500$ Hz on-resonance with spin pair 1 ($\delta = 2.04$ ppm) for 100 ms. This created a coherent superposition state of the form $(|TS_0\rangle + |S_0T\rangle)/\sqrt{2}$. We next applied spin-locking for time τ_{Ramsey} with nutation frequency $\nu_n = 47$ Hz to mix triplet quantum states without inducing singlet transfer (we found that if spin-locking is not applied during the free precession period, we do not detect Ramsey oscillations). We then performed a second $\pi/2$ rotation using identical spin-locking as the first rotation. Finally, we read out the singlet state from either spin pair 1 or 2 using SLIC.

Figure 4.10a shows results of the Ramsey experiment when the transmitter is centered on the spin pair 1 resonance during the free precession time. When singlet state is read out from spin pair 2 (red points), the signal exhibits oscillations at $f = 2.33 \pm 0.03$ Hz, as calculated by fitting to the model function

$$A[\cos(2\pi f - \phi)\exp(-\tau_{\text{Ramsey}}/T_{2s}^*) + c]\exp(-\tau_{\text{Ramsey}}/T_{1s}). \qquad (4.21)$$

The oscillations represent the singlet-singlet coherent superposition precessing in the Bloch sphere defined by the singlet-triplet product states. We obtain a satisfactory fit ($\chi^2/\text{dof} < 1$) when a small phase correction of $\phi = 20°$ is applied to account for extra delays during the free precession time (such as the time needed to switch spin-locking power). The signals exhibit two forms of decoherence, dephasing with a characteristic time T_{2S}^* and depopulation with the singlet lifetime T_S. For readout from spin pair 2, we find values $T_S = 4.4 \pm 0.2$ s and $T_{2S}^* = 1.3 \pm 0.4$ s. When singlet state is read out from spin pair 1 (green points), the signal exhibits corresponding oscillations 180° out

of phase with those from spin pair 2, with values $f = 2.30 \pm 0.08$ Hz, $T_S = 2.91 \pm 0.05$ s, and $T_{2S}^* = 0.55 \pm 0.13$ s. The frequency of both measurements roughly matches the singlet transfer resonance condition and represents the energy difference between the two sets of singlet-triplet product states defining the Bloch sphere. The singlet state lifetimes are 2 to 4 times longer than T_1, and the singlet lifetime of spin pair 2 is longer than that of spin pair 1, because spin pair 2 is further from the downfield proton that drives singlet relaxation. For both cases, the measured dephasing time is $\sim 25\%$ of the singlet lifetime.

Figure 4.10b shows results when the transmitter is centered 90 Hz downfield from spin pair 1 during the free precession. When reading from spin pair 2 (red points), we find $f = 2.11 \pm 0.05$ Hz, $T_S = 2.2 \pm 0.2$ s, and $T_{2S}^* = 0.52 \pm 0.14$ s with ϕ set to zero phase shift. Reading from spin pair 1, we find $f = 2.17 \pm .06$ Hz, $T_S = 1.4 \pm 0.1$ s, and $T_{2S}^* > T_s$. We require a phase correction of $97°$ beyond the expected $180°$ shift. The off-resonant driving reduces the singlet lifetimes by half but improves the Ramsey contrast and significantly extends T_{2S}^* as measured from spin pair 1. Both sets of measurements also exhibit fast oscillations during the first 300 ms that are likely due to triplet state coherences. More studies are needed to understand why a phase shift occurs between the two measurements in this scenario. A significant phase shift might arise from the time delay required for changing the frequency. It is also possible that some singlet/triplet polarization transfer is occuring for spin pair 1 during the free precession time.

Finally, to confirm that the singlet state of spin pair 1 does not remain entangled with the triplet states of spin pair 2, we performed the double Rabi experiment
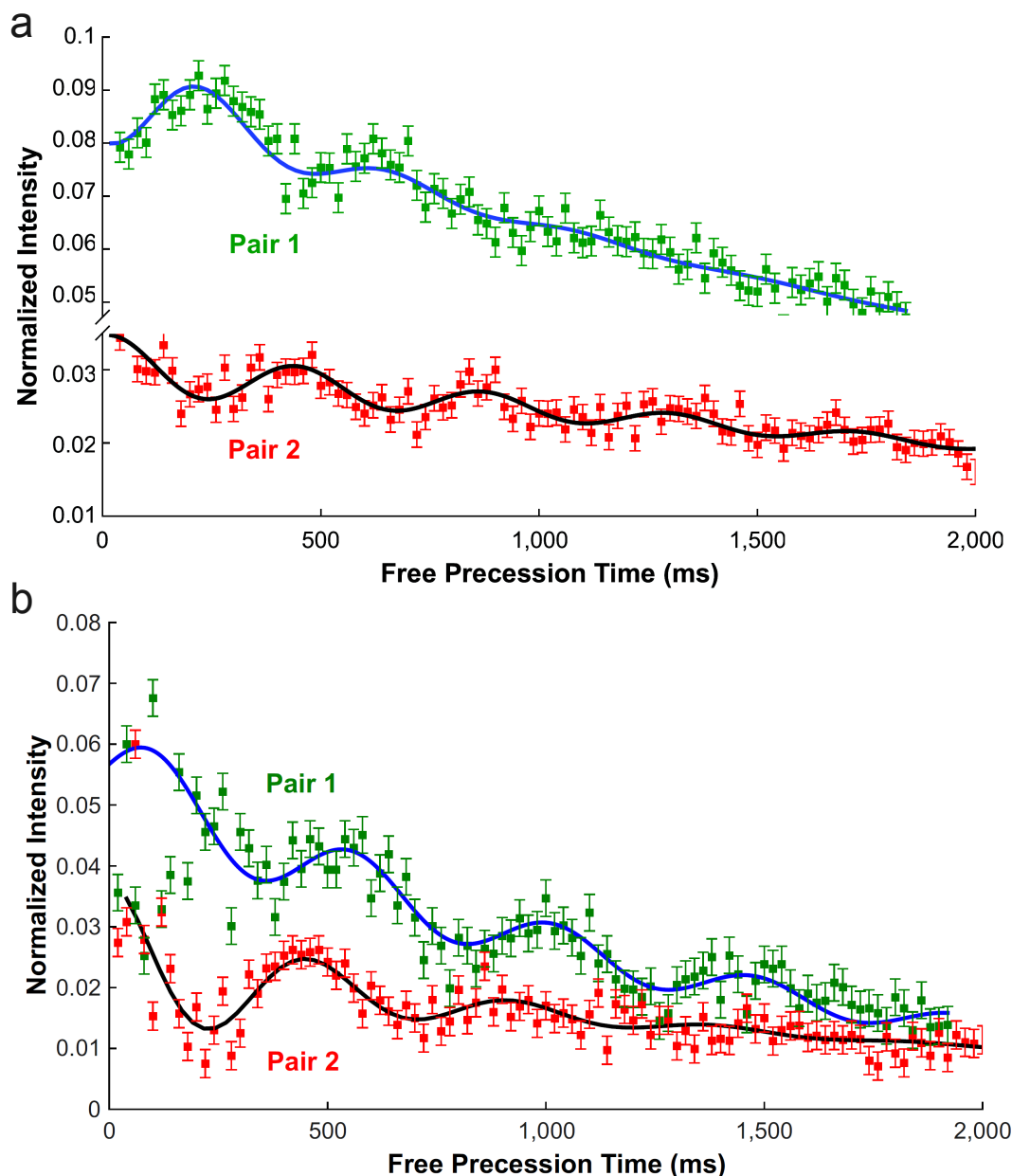
Figure 4.10: Measurement of Ramsey oscillations in the singlet-singlet subspace of glutamate. Spin-locking is applied at nutation frequency $\nu_n = 47$ Hz with the transmitter centered (a) on the pair 1 resonance frequency and (b) 90 Hz down-field from spin pair 1. Green and red points are measurements from pair 1 and 2, respectively. Black curves are sinusoidal fits with the function $A[\cos(2\pi f - \phi)\exp(-\tau_{\mathrm{Ramsey}}/T_{2s}^*) + c]\exp(-\tau_{\mathrm{Ramsey}}/T_{1s})$. Blue curves are sinusoidal fits with the function $A[-\cos(2\pi f - \phi)\exp(-\tau_{\mathrm{Ramsey}}/T_{2s}^*) + c]\exp(-\tau_{\mathrm{Ramsey}}/T_{1s})$. In both plots, intensity represents integrated signal normalized to a conventional spectrum.
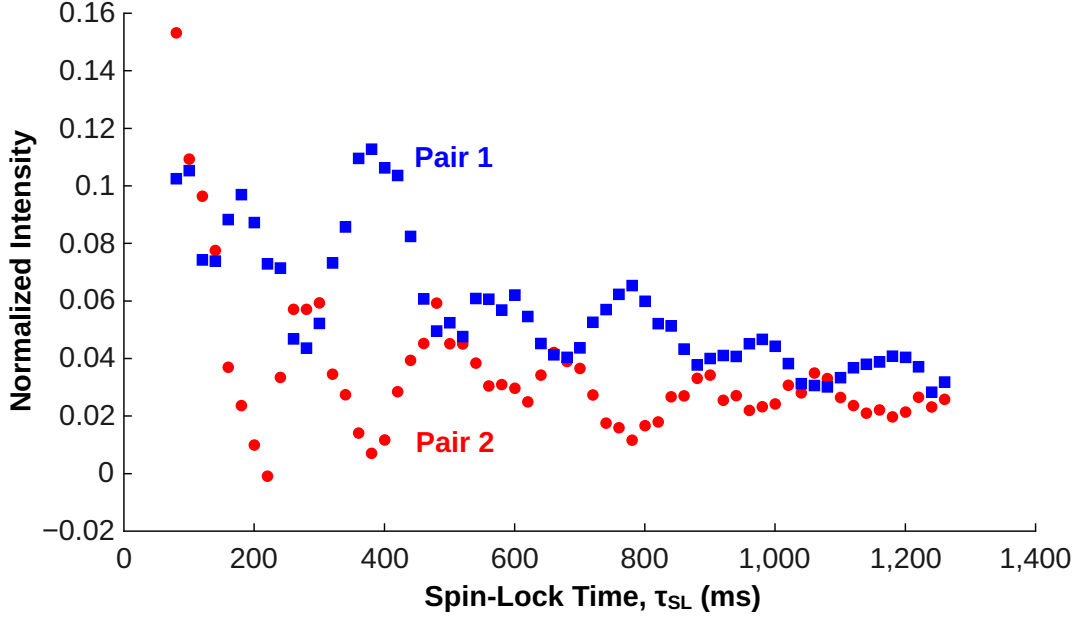
Figure 4.11: Measurement of singlet transfer using the double Rabi experiment. The spin-lock during the singlet transfer stage is applied for time τ_{SL} twice, once with phase y and once with phase $-y$. A full period of oscillation occurs when $2\tau_{\text{SL}} = 1/|J_{\text{cis}} - J_{\text{trans}}|$, indicating that the transfer occurs simultaneously for both triplet components $|\phi_+\rangle$ and $|\phi_-\rangle$ rather than in separate stages.

shown in Fig. 4.8. Singlet state was prepared in spin pair 1, 500 Hz spin-locking was applied to spin pair 1 as in previous measurements, and the singlet state was read out from either spin pair 1 or 2. The results (Fig. 4.11) show oscillations with a period $T = 1/(2|J_{\text{cis}} - J_{\text{trans}}|)$, as expected if entanglement is lost. As a consequence, only one of the two spin-lock phases needs to be applied to transfer the full amount of accessible singlet state from one spin pair to the other. Moreover, since the triplet state identity can be ignored, the Ramsey experiment can be viewed as taking place solely within a singlet-singlet subspace. The triplet states only act to make the singlet-singlet interactions accessible by bringing the states into resonance.

Phenylalanine-glycine-glycine

For measurements of singlet state transfer in phe-gly-gly, we employed the pulse sequences of Fig. 4.7, but we used the three-pulse sequence to prepare and read out singlet state from the proton pair at $\delta = 3.89$ ppm (center of molecule), while still using a SLIC sequence for the proton pair at $\delta = 3.71$ ppm (end of molecule). As in the glutamate Rabi experiment, singlet state was first prepared in one of the two proton pairs, followed by a period of spin-locking for τ_{SL} with an applied nutation rate ν_n. The singlet state was then converted back to transverse magnetization in either the original proton pair or the adjacent pair before acquisition of the FID signal.

Figure 4.12a presents measurements of singlet transfer in phe-gly-gly between the center spin pair at $\delta = 3.89$ ppm and the end spin pair at $\delta = 3.71$ ppm when $\nu_n = 280$ Hz ($\Delta\nu_n = 2.3$ Hz). Results are shown for two cases: (1) the singlet state is created in the end pair and read out from the center pair (black points), and (2) the singlet state is created in the center pair and read out from the end pair (red points). In both cases, the transmitter is set to $\delta = 3.89$ ppm for spin-locking to ensure a good lifetime for the spin-locked singlet. Notice that unlike the results for glutamate, no oscillation is observed, only a buildup of singlet state followed by a long decline. From a fit, we estimate a value $|J_{\mathrm{cis}} - J_{\mathrm{trans}}| \approx 10$ mHz and a decay time of $T_{\mathrm{Rabi}} \approx 12$ seconds, which is slightly lower than the central spin pair's singlet lifetime $T_S = 14.5$ s.

The transfer appears less effective when transferring the singlet state from the center pair to the end pair, possibly because the singlet state can also be transferred in the other direction to the third spin pair of the chain. We attempted to increase the
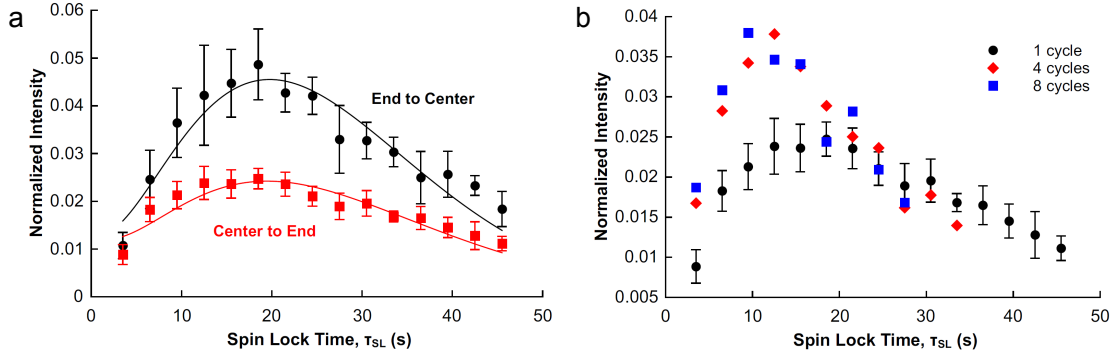
Figure 4.12: Measurement of singlet state transfer in the phenylalanine-glycine-glycine molecule. (a) The singlet state is created in one spin pair and read out from the adjacent spin pair. Best-fit curves of the form $A[\sin^2(\pi f \tau_{\rm SL}) + c] \exp(-\tau_{\rm SL}/T_{Rabi})$ indicate a transfer rate $f = |J_{cis} - J_{trans}| \approx 10$ mHz. (b) The singlet state is created in the center spin pair and transferred to the end spin pair multiple times before readout in order to increase the total amount of singlet transferred.

total amount of the singlet state transferred using a "pumping" scheme to transfer the singlet state multiple times. We created singlet state polarization on the center spin pair using the three-pulse sequence and spin-locked at $\nu_n = 280$ Hz to transfer the singlet state to the end pair. We then removed spin-locking for time $5T_1 = 3.1$ s, created singlet state polarization in the center spin pair again using the three-pulse sequence, and repeated the spin-locking to induce a second singlet state transfer. This process was repeated multiple times before finally reading out the singlet state from the end pair using a SLIC sequence. After four of these pumping cycles, we were able to achieve a significant increase in the singlet state population of the end pair versus a single transfer sequence (Fig. 4.12b). Further increasing the number of cycles to eight had little effect, as the 25 second lifetime of the end spin pair's singlet state likely limits the total amount of singlet state buildup achievable.

4.2.4 Discussion

We have demonstrated that interactions between two singlet states within a molecule can produce coherent transfer of singlet order between one spin pair and another. The resonance condition needed to effectuate this transfer is controllable, allowing unitary operations to be performed in a subspace spanned by two singlet states. Because singlet state relaxation is slow compared to spin-lattice relaxation, this represents a step toward a decoherence-free subspace (DFS) in which quantum information can be stored beyond conventional relaxation times. A DFS consisting of four spins has been proposed before [82, 83], using the two spin-zero states $|S_0 S_0\rangle$ and $(|T_+ T_-\rangle - |T_0 T_0\rangle + |T_- T_+\rangle)/\sqrt{3}$. Our system differs in that we utilize the individual singlet states of each spin pair. Decoherence within the DFS then occurs through depopulation of the singlet states as well as dephasing due to fluctuations in the singlet state energy levels. Since the singlet state energy levels are defined by the geminal J-coupling between spins, they are sensitive to scalar relaxation of the first kind, which is generally extremely slow compared with other relaxation mechanisms [24]. However, our measurements of glutamate indicate a depopulation time greater than T_1 but a dephasing time similar to T_1, indicating that a detailed study of the dephasing mechanism will be needed.

We have also demonstrated the measurement of weak J-coupling differences on the order of 10 mHz. Such measurements could be useful for the determination of molecular structures, especially proteins and macromolecules, as the difference in *cis* and *trans* J-couplings is a function of the molecular geometry [80, 81]. Many current multidimensional NMR methodologies for structure determination, such as COSY

and TOCSY [84], depend on coherence transfer among states that relax on the order $1/T_2$ or $1/T_{1\rho}$. As proton spin lifetimes rarely exceed a few seconds, this sets a lower limit of the order 100 mHz for coupling resolution, which limits the ability to detect long-range coupling differences. Singlet state transfer may provide a way to detect weaker coupling differences that provide information about structure at distances five or more bond lengths apart, as well as allow for measurements across chains such as phe-gly-gly that contain only distantly-spaced protons.

Chapter 5

Low-Field J-Coupling Spectroscopy

Up to this point, we have discussed NMR measurements performed in a high-field 4.7 T (200 MHz proton resonance frequency) superconducting magnet. At high magnetic fields, liquid-state NMR spectra exhibit features originating from chemical shifts and scalar coupling. We now turn to measurements in a low-field magnet operating at 6.5 mT (276 kHz proton resonance frequency). At such a low magnetic field, homonuclear chemical shifts are typically much weaker than scalar coupling ($\Delta\nu \ll J$). As a consequence, a homonuclear spin system exists in a strongly-coupled regime and its energy levels are best described by dressed eigenstates. Chemical shifts are not detectable, and only a single spectral line appears.

Despite this apparent limitation, low-field spectroscopy is of interest for applications where high magnetic fields are prohibitive, such as in mobile spectrometers and in the presence of ferromagnetic or paramagnetic substances. To gain useful spectral information from proton NMR at low magnetic fields, a substance can be synthesized containing a heteronucleus such as ^{15}N or ^{13}C. The heteronucleus breaks the chemical

equivalence of the spin system, thereby making previously forbidden NMR transitions accessible. The result is a complex spectrum in which the primary separation between spectral lines results from scalar coupling [85–89].

The need for a heteronucleus is a severe limitation when trying to characterize natural samples, as only a few percent of molecules will contain a ^{13}C nucleus. We develop an alternative method for J-coupling spectroscopy that does not require the sample to contain a heteronucleus. Our technique is based on the same principles as the SLIC sequence demonstrated in section 4.1, only instead of investigating a level crossing between the singlet state and a triplet state composed of two spins, we map out level crossings among a larger number of dressed states, each with contributions from many spins. We perform demonstrations of SLIC spectroscopy on ethanol samples and show that the spectral information obtained can be used to determine molecular properties.

5.1   Theory

Methods have been developed for predicting spectra from both zero-field [90, 91] and low-field [92, 93] pulsed NMR experiments. The calculation is normally approached in three steps: (1) The eigenstates are determined for groups of identical spins by dressing the product states with the scalar couplings among those spins. Since the spins are identical, the eigenstates can easily be found using the Clebsch-Gordan coefficients. (2) Proton-heteronucleus interactions are added. If the magnetic field is weak enough that heteronuclear scalar coupling is greater than the proton-heteronucleus frequency difference, then new dressed eigenstates are calculated via

diagonalization. Otherwise perturbation theory is used. (3) Perturbation theory is used to calculate splittings caused by weaker proton-proton couplings between chemically inequivalent spin groups. This technique leads to eigenstates that are convenient for predicting the transition frequencies and intensities for the heteronuclear spin system.

However, when such an analysis is performed for a homonuclear spin system, one finds that many of the NMR transitions are forbidden. For example, Emondts *et al.* demonstrated a nuclear spin singlet state at zero magnetic field between a ^{13}C nucleus and a proton. In that case, the system can be manipulated via a magnetic pulse through the interaction

$$\langle T_0|\gamma_I B_0 \hat{I}_z + \gamma_S B_0 \hat{S}_z|S_0\rangle = (\gamma_S - \gamma_I)B_0/2, \tag{5.1}$$

where S refers to the ^{13}C spin and I refers to the ^{1}H spin. The interaction strength is proportional to the difference in gyromagnetic ratios. In the case of two identical protons, the gyromagnetic ratio is identical and this interaction term is equal to zero, so no such manipulation is possible. Only transitions within the triplet subspace can be addressed. The same conundrum appears when considering interactions in systems with more numerous spins; only transitions within each spin subspace are addressable.

The addition of even a weak static magnetic field causes chemical shifts to break the protons' chemical equivalence, which makes transitions between different spin subspaces theoretically accessible. Unfortunately, as long as $\Delta\nu \ll J$, the transition probabilities are suppressed by a factor $\sim \Delta\nu^2/4J^2$ and are too small to be easily detected from a FID measurement. However, we note that this situation is closely

analogous to the nearly-equivalent proton pairs studied at high field. In that case, we showed that spin-locking could induce energy crossings at which the weak interactions take effect, and we measured the crossings by detecting a dip in x-axis magnetization. Here, we show that the same behavior occurs for more complex spin systems, thereby allowing the otherwise suppressed J-couplings to be measured. We discuss the case of ethanol in appendix B and summarize the procedure for finding its level crossings here.

For a hydrated ethanol molecule, one only needs to consider the aliphatic protons, as the alcohol proton exchanges at a rate much faster than the J-coupling. We first combine groups of spins that are magnetically equivalent even in the presence of a B_0 field. These are the methylene group (2 geminal protons) and the methyl group (3 geminal protons). The methylene group eigenstates consist of one singlet and three triplet states, whereas the methyl group eigenstates consist of four spin-3/2 states and four spin-1/2 states. The energies of these states are defined by the geminal J-couplings between the protons, which are present but undetectable in conventional NMR measurements for magnetically equivalent spins.

We then form dressed states from the proton groups coupled by the next-strongest scalar couplings. In ethanol, this is the vicinal J-coupling between methylene and methyl group protons. These states are identified by angular momentum quantum numbers F and m_F (i.e., states $|F, m_F\rangle$) and now include protons that have different chemical shifts. We define the eigenstates as if the chemical shifts were identical and then consider the chemical shift difference as an interaction term $\propto \Delta\nu$ between the dressed states, as in the analysis of the SLIC technique for singlet and triplet states

discussed in section 4.1.2.

Finally, we consider the effects of spin-locking applied at the single resonance line measured at low field. All protons are spin-locked with nutation frequency ν_n, which dresses the states within each F subspace and splits those dressed states proportionally to $m_F \nu_n$. At specific nutation frequencies, energy levels cross (spin-lock induced crossing); however, not all crossings have associated interactions. As discussed in appendix B, the interactions produced by chemical shift differences only occur between spin-locked states with $\Delta F' = \pm 1$ and $\Delta m_{F'} = \pm 1$. In these cases, the interaction terms drive a polarization transfer between states, which is detected as a drop in x-axis magnetization. For hydrated ethanol, the dips are predicted to occur at $\frac{3}{2}J$ and $\frac{5}{2}J$, whereas for dehydrated ethanol a more complex spectrum is predicted due to perturbations by the alcohol proton.

5.2 Experiment

To create a J-coupling spectrum, we perform either of the SLIC pulse sequences shown in Fig. 5.1. In Fig. 5.1a, we apply a $\pi/2$ pulse to create x-axis magnetization and then spin-lock at nutation frequency ν_n for time τ_{SL}. This is followed by the acquisition of a FID signal. In Fig. 5.1b, we perform the same experiment but split the spin-lock into two halves, applied with opposite phase and divided by a π pulse that helps reverse the effects of B_0 detuning.

We performed measurements in a custom-built low-field magnetic resonance imager operating at 6.5 mT (276 kHz proton resonance frequency) [94], shown in Fig. 5.1c. The system is centered around a four-coil bi-planar electromagnet powered by a
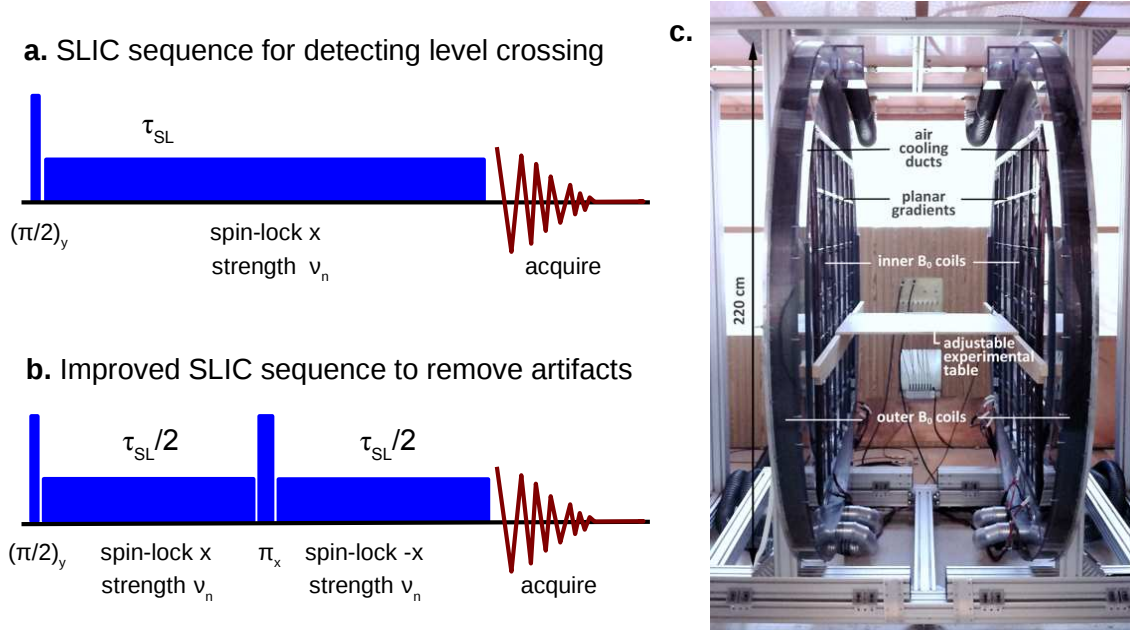
Figure 5.1: SLIC spectroscopy experiment. (a) Standard SLIC pulse sequence for detecting a level crossing. (b) Modified SLIC pulse sequence with echo to remove effects from shifts in B_0. (c) Image of the low-field magnetic resonance system.

Danfysik System 8500 power supply. Gradient coils, powered by Techron 7782 amplifiers, enable imaging as well as shimming of the static field. With shimming enabled, we consistently achieve linewidths on the order of 1 Hz. Pulse sequences are synthesized by a Tecmag Redstone console and amplified by a Tomco BT00500-AlphaS 500W RF power amplifier before being sent to the probe coil via a transmit/receive (T/R) switch. The system's passive T/R switch (a quarter-wave small signal diode transcoupler) prevented us from performing the experiment with a single coil, as the voltages applied during low-power spin-locking were below the diode threshold voltage needed to turn the switch on. Therefore, we performed the experiment using crossed coils. A 25 cm diameter solenoidal coil (29 cm long with 62 turns) was used as a transmitter with its axis oriented along the x-direction, and a smaller 7 mm

solenoidal receive coil (4 cm long with 40 turns) containing the sample was placed inside, oriented along the y-axis. The FID signal is sent via a Miteq AU-1583, 36 dB gain preamplifier to the Tecmag console.

5.3   Results and Discussion

Conventional NMR spectra are shown in Fig. 5.2 for anhydrous ethanol acquired at both 4.7 T and 6.5 mT. From the high-field spectrum, we find $J_{AB} = 7.1$ Hz coupling between the methyl group and methylene group protons, and $J_{AC} = 4.8$ Hz coupling between the methyl group protons and the alcohol proton. The low-field spectrum shows a single featureless line. The 2.4 ppm chemical shift between methyl and methylene group protons corresponds to only 0.66 Hz at 6.5 mT, much weaker than the scalar couplings, leading other spectral transitions to be suppressed by a factor of ~ 420.

SLIC spectra at 6.5 mT, acquired using the pulse sequence in Fig. 5.1b, are shown in Fig. 5.2c for anhydrous ethanol and a 9:1 ethanol:water mixture. The addition of a small percentage of water greatly increases the alcohol proton's chemical exchange rate and eliminates the effects of the coupling J_{AC}. Measurement results were also simulated with *SpinDynamica* and are shown for comparison. The depths of the features range between 5% and 25% of the signal intensity. Both the positions and depths of the dips are in general agreement with the simulations, but significant noise is present even after applying a moving window average. Moreover, some positions deviate $\sim 1 - 2$ Hz from calculated values, possibly due to miscalibration of the nutation frequency vs. spin-locking power or drifts in B_0.
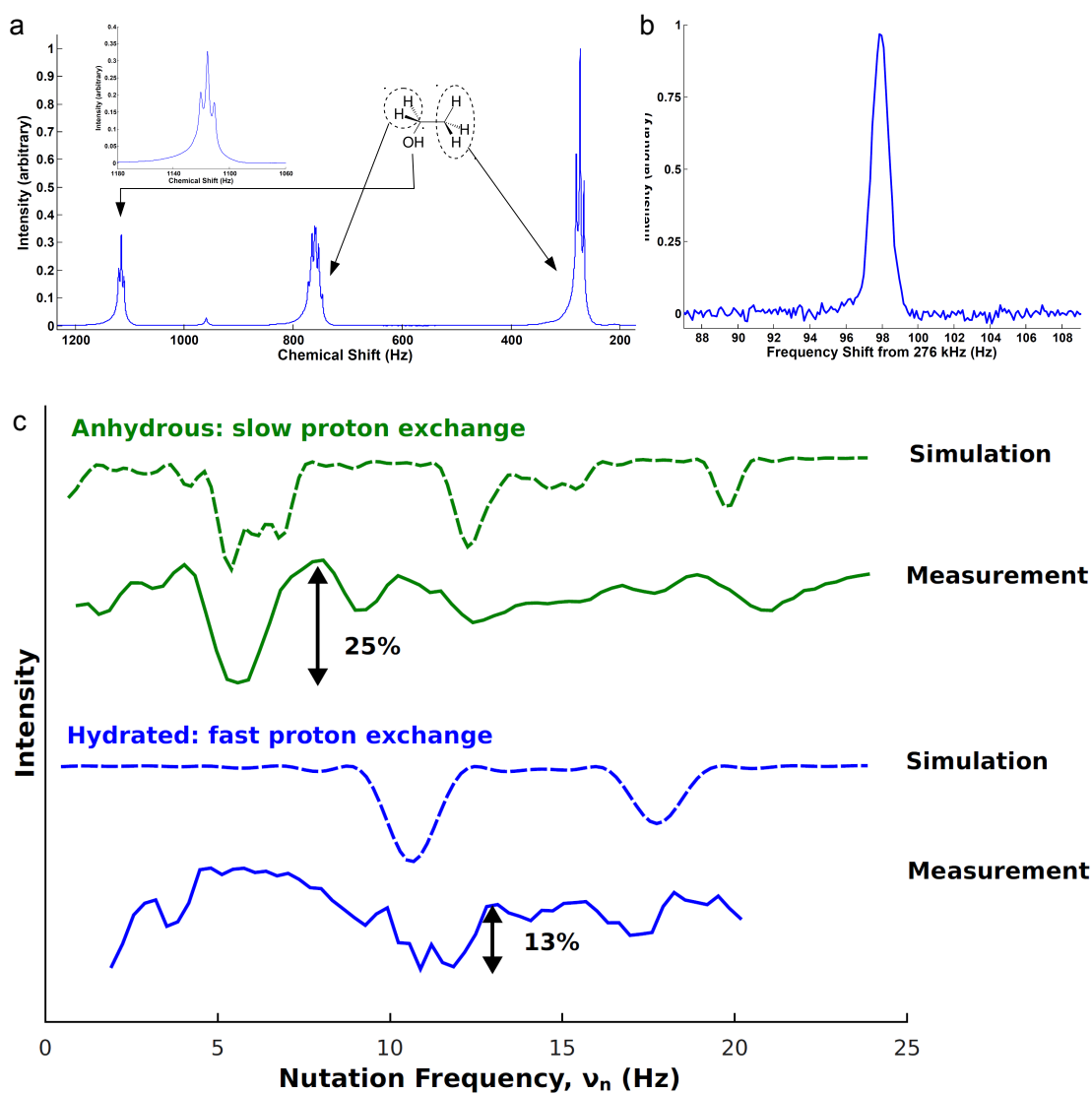
Figure 5.2: Conventional and SLIC spectra of ethanol. (a) In a 200 MHz spectrometer, the conventional spectrum exhibits a typical splitting pattern due to J-coupling. The alcohol proton experiences little chemical exchange and also shows a splitting pattern (inset). The spectral assignments are indicated. (b) In a 6.5 mT spectrometer, $\Delta \nu \ll J$, and no spectral features are observed. (c) Modified SLIC spectra at 6.5 mT of anhydrous and hydrated ethanol exhibit dips corresponding to J-coupling strengths within the molecule. For anhydrous ethanol, 8 averages with $\tau_{SL} = 2$s were acquired, and data were smoothed with a 3-point moving window average. For hydrated ethanol, 16 averages with $\tau_{SL} = 1$s were acquired, and data were smoothed with a 3-point moving window average.

We found that a significant source of noise was fluctuations in the B_0 field caused by the movement of cars and trucks outside the lab. At times these shifted the spectral line by 4 Hz, enough to significantly change the effective spin-locking power given that the nutation rates are on the order of 10 Hz. When the sequence in Fig. 5.1a was employed, signal intensity was highly sensitive to shifts in B_0, with even small shifts creating 50% dips in x-axis magnetization. The addition of a π pulse in sequence 5.1b decreased but did not eliminate the effects.

Applying feedback to the electromagnet to stabilize the B_0 field or using a shielded low-field NMR system should lead to significant improvements in the SNR. SLIC spectroscopy could also be performed following pre-polarization in a high-field magnet or following Overhauser enhancement [95, 96]. This would not only improve the SNR, but it would also provide a way to measure the spin-lattice relaxation times of the interacting dressed states by recording SLIC spectra following a range of delays after the polarization step.

In conclusion, we have demonstrated a novel method of J-coupling spectroscopy at low magnetic field that does not require the addition of a heteronucleus. This may provide a path to chemical identification using mobile low-field spectrometers and magnetic resonance imagers. More generally, it is applicable to any strongly-coupled spin system. Examples include protons at moderate and high magnetic fields, where it may be used to extract extra information in conjunction with conventional NMR techniques, and spin ensembles in condensed matter systems such as those found in diamond, where it may be used to identify couplings among surface electrons or nuclei in the lattice.

Chapter 6

Introduction to Nitrogen-Vacancy Centers in Diamond

The nitrogen-vacancy (NV) center is a crystallographic defect in diamond with unique optical and spin properties that makes it useful for a wide variety of applications, ranging from measurements of magnetic and electric fields to quantum information processing [97–107]. As a color center, the NV exhibits fluorescence when excited with visible light. As an electronic defect, the NV$^-$ charge state contains six non-bonding electrons arranged in an $S = 1$ spin configuration [108, 109]. The electronic and optical properties are linked via spin-orbit coupling, leading to both spin-state-dependent fluorescence intensity and optical pumping into the ground spin state [110]. These features make it possible to perform electronic spin resonance (ESR) on the spins of a single defect by controlling the spin state with microwave pulses and both preparing and detecting the spin state optically.

A nitrogen-vacancy center is created when a substitutional nitrogen atom becomes

adjacent in the lattice to a vacancy, either during diamond synthesis or as the vacancy diffuses through the lattice during high-temperature annealing (See Fig. 6.1a for a diagram of the structure). The NV center is more stable than the two separate defects [111], so NV formation is thermodynamically favorable. The NV center can exist in either the NV^0 or NV^- charge state, with the latter possessing the optical and spin properties described above. In this work, "NV center" will refer to NV^-. These defects can be found at low concentrations in natural diamond, but they can also be formed controllably at high concentrations in synthetic diamonds. The best results are achieved using chemical vapor deposition (CVD). In this technique, the diamond is grown slowly from methane in the presence of hydrogen gas. Nitrogen gas can be added, leading to nitrogen impurities at well-controlled concentrations. A small fraction ($< 1\%$) combine with vacancies to form NV centers. If nitrogen gas is added throughout the growth process, this leads to NV formation throughout the diamond [112], whereas if nitrogen is added for a short period of growth, a "delta doped" NV layer can be created [113]. An alternative method for forming an NV layer is to start with an undoped CVD diamond and implant nitrogen using an ion beam. This allows the defect depth and density to be well controlled. Annealing to mobilize vacancies then spurs the formation of NV centers within the layer of implanted nitrogen. At low implantation energies, NV centers can be produced very close to the surface (< 10 nm) [114, 115].

The NV center's six non-bonding electrons fill four molecular orbitals (MO) defined by their point group symmetry as a_1', a_1, e_x, and e_y. The lower-energy a_1' orbital is filled by a pair of electrons, leaving the remaining four electrons to populate the

three higher-energy MOs in a number of combinations [108, 116]. The ground state of these electronic configurations is $a_1^2 e^2$. Orbital parity symmetrization leads different combinations within this subspace to possess either triplet or singlet spin states. The electrons can populate either the spin ground state $^3A_2$ triplet level or one of two singlet levels, $^1A_1$ and ^1E. The next excited electronic state is $a_1 e^3$, which possesses a spin ground state triplet ^3E and a higher-energy singlet $^1E'$. The system can be excited from the ground electronic state to the first excited state through the absorption of an optical photon whose wavelength is between the zero-phonon line at 637 nm and an upper vibronic band limit of ~ 475 nm. The excited state most commonly decays back to the ground state through fluorescence at wavelengths between 637 nm and ~ 800 nm with a lifetime of ~ 13 ns. However, the excited state can also decay non-radiatively into the $^1A_1$ singlet state, which occurs preferentially from the $m_s = \pm 1$ state and is followed by radiative decay at 1043 nm to the ^1E singlet state and then non-radiative decay to the $^3A_2$ ground state, all on a timescale of ~ 300 ns [117]. The non-radiative decay from the excited state to $^1A_1$ is believed to occur via spin-orbit coupling as a result of the $^1A_1$ and ^3E energy levels being close in energy, although the exact mechanism is not yet understood [108]. Since the decay through the singlet state is spin-state dependent, continuous pumping from ground to excited electronic state results in a buildup of state $m_s = 0$ in the ground state. This feature provides a way to create spin polarization, typically at levels between 80% and 95% [104, 107, 117–120]. Moreover, the fluorescence intensity is stronger for $m_s = 0$, which allows for optical detection of the spin state. The energy levels and transitions are summarized in Fig. 6.1b.
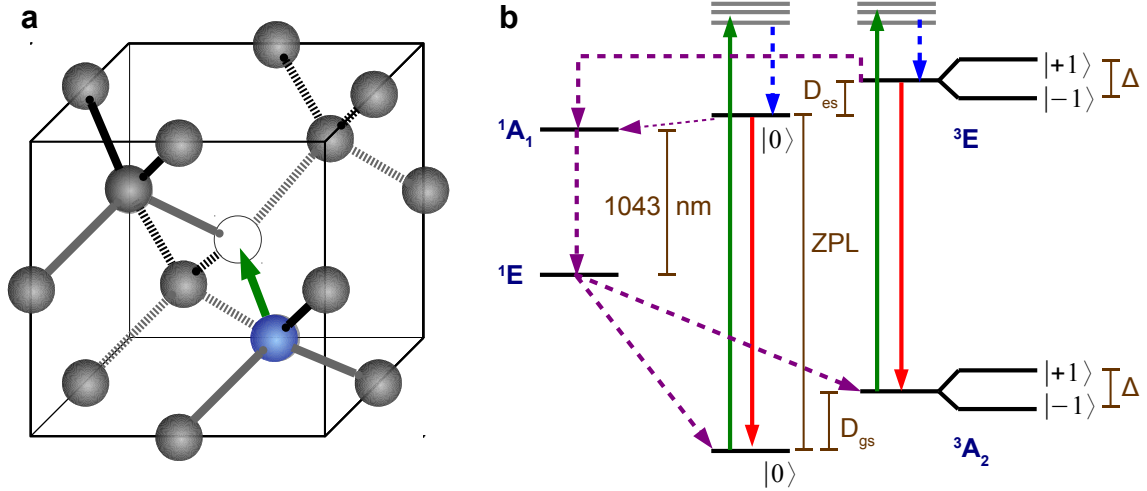
Figure 6.1: NV center structure, energy levels, and dynamics. (a) The NV center structure consists of a substitutional nitrogen atom (blue) and a vacancy (white circle). The NV center axis is defined by the vector between the nitrogen atom and the vacancy (green arrow). There are four possible axes, depending on the position of the nitrogen atom around the vacancy. (b) NV center energy levels and transitions. The ground triplet state $^3A_2$ is split into three energy levels by a zero-field splitting $D_{gs} = 2.87$ GHz, and by Zeeman splitting $\Delta = B_z \times 2.8$ MHz/G. The excited triplet state ^3E is split into three energy levels by a zero-field splitting $D_{es} = 1.41$ GHz, and by Zeeman splitting $\Delta = B_z \times 2.8$ MHz/G. The ground and excited electronic states are separated by an energy equivalent to the zero-phonon line ZPL = 632 nm. The lower ground state singlet ^1E is separated from the upper ground state singlet $^1A_1$ by an energy equivalent to the wavelength 1043 nm. Light with a wavelength shorter than the ZPL (green line) excites the ground state to high vibronic levels of the excited state, which then decay non-radiatively to the lowest vibronic level of the excited state (blue dashed line). The system can then either fluoresce with emission of red light (red line) or decay non-radiatively to the singlet states via an inter-system crossing (purple dashed line) and eventually back to the ground triplet state. The inter-system crossing is faster when the spin is in the $|\pm 1\rangle$ spin state than in the $|0\rangle$ spin state. This leads to optical pumping and spin-state-dependent fluorescent intensity.

117

The NV center spin states can also be manipulated through electron spin resonance (ESR) using microwaves. The $m_s = 0$ state is split from the $m_s = \pm 1$ state by a zero-field splitting $D_{gs} = 2.87$ GHz. In the presence of a magnetic field, $m_s = +1$ is separated from $m_s = -1$ by the Zeeman interaction $\Delta = 2\gamma_e B_z$, where $\gamma_e \approx 2.8 MHz/G$ is the electron gyromagnetic ratio and B_z is the magnetic field projection along the NV center's axis. This axis is defined by the direction of the vector connecting the nitrogen atom and the vacancy. Magnetic fields along the x and y axes (i.e., B_x and B_y) lead to state mixing, which lowers the fluorescence contrast and perturbs the energy levels [121, 122]. Hyperfine interactions between the electrons and the nitrogen nuclear spins lead to further structure for the $m_s = \pm 1$ states. The energy levels can be elucidated via measurements of the optical fluorescence during the simultaneous application of laser light and microwaves (Fig. 6.2a). The fluorescence decreases when the microwaves are on resonance with a transition. Ultimately, the ESR spectrum of a single NV center in a static magnetic field consists of six resonances for a ^{14}N defect ($I = 1$) and four resonances for a ^{15}N defect ($I = 1/2$).

By applying microwaves to a single resonance, the spin states can be coherently manipulated to create superposition states. The simplest experiment, a Rabi nutation, measures the NV fluorescence after optical pumping followed by a microwave pulse (Fig. 6.2b). As the microwave pulse length or power are varied, a sinusoid is mapped out as the spin state is driven around the longitudinal axis of the Bloch sphere. A pulse length can be chosen to rotate the magnetization vector from $|0\rangle$ to $|1\rangle$, thereby defining a π pulse, or from $|0\rangle$ to $(|0\rangle + |1\rangle)/\sqrt{2}$, defining a $\pi/2$ pulse. A Ramsey experiment can be performed by optically pumping, applying a $\pi/2$ pulse,
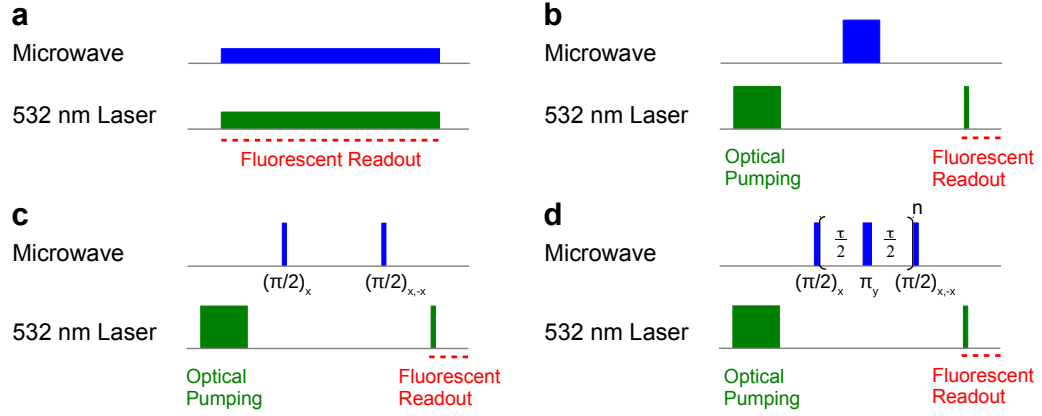
Figure 6.2: Four common pulse sequences for NV ESR experiments. (a) CW ESR for detecting resonance frequencies. (b) Rabi nutation for pulse length calibration. (c) Ramsey experiment for measuring T_2^* and resonance frequencies. (d) Hahn echo (n = 1) and dynamical decoupling (n > 1) for extending coherence time and measuring T_2.

and then allowing the state to evolve. A second $\pi/2$ pulse projects the remaining coherence back into state $|0\rangle$ or $|1\rangle$ (Fig. 6.2c), and a fluorescence measurement is used to determine how much the coherence decayed. This decay, characterized by the dephasing time T_2^*, results from magnetic fluctuations in the spin bath (and magnetic inhomogeneities when measuring multiple NV centers in an ensemble).

Dephasing from slow fluctuations can be reversed using a Hahn echo sequence. This places a π pulse in the middle of the Ramsey sequence, thereby flipping the spin state and reversing the time evolution of the coherence (Fig. 6.2d). Decay of the coherence still occurs if the integrated environmental noise after the π pulse is different from that before the pulse. In this way, the Hahn echo is a form of auto-correlation measurement of the magnetic environment. The signal intensity is subsequently a function of the correlation time of the magnetic noise. The Hahn echo signal decreases as the sequence length increases, and the characteristic time scale is the decoherence time T_2. (Note that this is a different definition of T_2 than what is

commonly used in NMR literature, as the measurements are performed differently.)

One can also view the Hahn echo sequence as defining a filter for the NV coherence's sensitivity to its environment [123–126]. In an echo experiment, the coherence is not sensitive to high-frequency fluctuations, as the integral over the fluctuations averages to zero during each half of the sequence. It is also not sensitive to very slow fluctuations, since in that case the environment appears approximately identical during each half of the sequence. However, it is particularly sensitive to fluctuations on the time scale $1/\tau$, where τ is the Hahn echo sequence length. One can increase the sensitivity by repeating the Hahn echo again any number of times before the final $\pi/2$ pulse. This is called a dynamical decoupling (DD) sequence, as it decouples the coherence from environmental noise at all frequencies *except* for particular resonances. While the goal of dynamical decoupling sequences is normally to extend the coherence lifetime, the fact that the sequences show particular sensitivity to specific frequencies gives these sequences a dual purpose. By sweeping DD sequences through their resonances and monitoring the spin state coherence loss for each frequency step, one can extract a spectrum of the magnetic environment [126].

The following chapter describes how a dynamical decoupling technique applied to the NV center spins can be used to detect the magnetic fields of nuclei on the diamond surface in proximity to the NV center. As the nuclei precess in a magnetic field, they create an oscillating magnetic signal at their Larmor frequency that can be detected through the effect on the NV center's spin coherence. The signal they create is locally large but drops off quickly with distance ($\sim 1/d^3$), resulting in the ability of an NV center to detect only nearby nuclei, on the scale of nanometers.

This makes it possible to perform nanoscale nuclear magnetic resonance spectroscopy and nanoscale magnetic resonance imaging for the first time. Moreover, it provides a convenient way to measure the depth of an NV center below the diamond surface.

Chapter 7

Nanoscale NMR Spectroscopy and Imaging

Nuclear magnetic resonance (NMR) spectroscopy and magnetic resonance imaging (MRI) provide non-invasive information about multiple nuclear species in bulk matter, with wide-ranging applications from basic physics and chemistry to biomedical imaging [127]. However, the spatial resolution of conventional NMR and MRI is limited to several microns even at large magnetic fields ($>$ 1 tesla) [128], which is inadequate for many frontier scientific challenges such as single molecule spectroscopy and *in vivo* imaging of individual biological cells. Here we demonstrate nanoscale NMR spectroscopy and imaging of multiple nuclear species (^{1}H, ^{19}F, ^{31}P) under ambient conditions and at moderate magnetic fields ($\sim$ 20 millitesla) using two complementary sensor modalities that exploit optical measurements of nitrogen-vacancy (NV) color centers in diamond. We interrogate single shallow NV centers in a diamond chip to perform simultaneous multi-species NMR spectroscopy on few-

nanometer-sized samples, placed on the diamond surface, which have a statistical spin polarization equivalent to ~ 100 polarized nuclei. We also employ a diamond chip containing a shallow, high-density NV layer, to demonstrate wide-field optical NMR spectroscopy and imaging with sub-micron resolution of samples containing multiple nuclear species. This work lays the foundation for far-ranging NMR and MRI applications at the nanoscale, such as determining the structure and dynamics of single proteins and other biomolecules, identification of transition states in surface chemical reactions, and functional biological imaging with subcellular resolution and tissue field-of-view.

The spatial resolution of conventional NMR and MRI is limited to macroscopic length scales due to the modest signal-to-noise ratio (SNR) provided by inductively-detected thermal spin polarization, even in large (> 1 tesla) magnetic fields [129–131], and the finite strength of externally-applied magnetic field gradients used for Fourier k-space imaging [128]. Other precision magnetic sensors have only macroscopic resolution, e.g., semiconductor Hall effect sensors [132] and atomic magnetometers [133], and/or require operation at cryogenic temperatures, e.g., superconducting quantum interference devices (SQUIDs) [134] and magnetic resonance force microscopy [135, 136]. Alternatively, NV centers in diamond have recently been shown to provide sensitive, nanoscale magnetic sensing and imaging for a wide range of operational conditions [97, 98, 137]. In particular, NV centers in room-temperature diamond can be brought within a few nanometers of magnetic field sources of interest while maintaining long NV electronic spin coherence times ($\sim 100~\mu$s), a large Zeeman shift of the NV spin states ($\sim$ Bohr magneton), and optical preparation and readout of

the NV spin (Fig. 7.1a). Highlights of NV-diamond magnetic sensing to date, all performed under ambient conditions, include sensitive spectroscopy [104, 126, 138] and imaging [139–141] of electron and nuclear spin impurities within the diamond sample; single electron spin imaging external to the diamond sensor [142]; sensing of nanoscale ensembles of proton spins in samples placed on the diamond surface [143–145]; targeted detection of single paramagnetic molecules attached to the diamond surface [146]; and wide-field magnetic imaging of living magnetotactic bacteria, with sub-micron resolution [102].

In the present work, we employ two complementary sensor modalities to demonstrate nanoscale NMR spectroscopy and imaging of samples containing multiple nuclear species placed on the diamond surface. In the first modality (Fig. 7.1b), a scanning confocal microscope interrogates a single NV center about 8 nm below the surface of a high-purity diamond chip. In the second modality (Fig. 7.1c), the fluorescence from a shallow (5 - 15 nm deep), high-density (3.5×10^{11} cm^{-2}) NV ensemble layer near the surface of a diamond chip is imaged onto a CCD camera. This wide-field microscope provides pixel-by-pixel multi-species NMR spectroscopy and imaging with sub-micron resolution and wide field-of-view, in a robust device that does not rely on identifying and addressing an optimally chosen NV center, while the confocal microscope can extract thickness information of layered thin films containing different nuclear species, with sub-nanometer resolution.
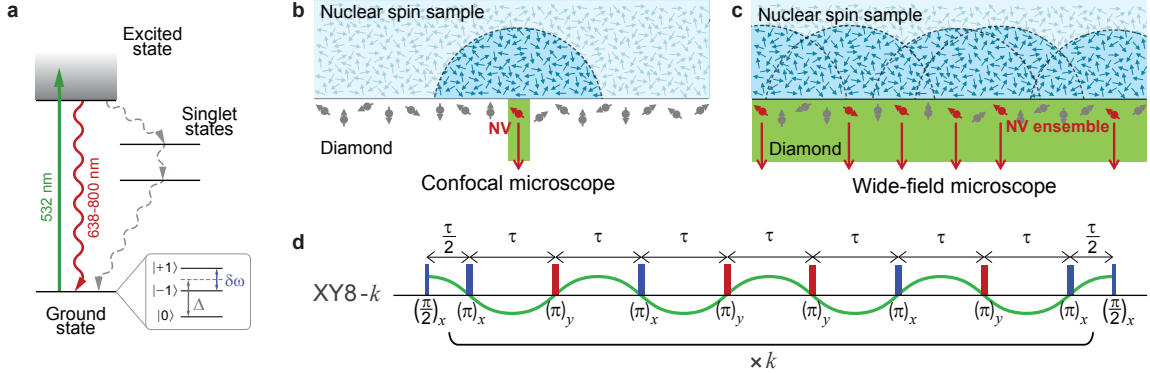
Figure 7.1: NV NMR Experiment. (a) NV center energy level diagram; see Methods for details. (b) A confocal microscope interrogates a single shallow NV center, which detects NMR signals from a few-nanometer region of sample on the diamond surface. (c) A wide-field microscope images fluorescence from a shallow, high-density layer of NV centers allowing detection of NMR signals from overlapping nanoscale regions of sample on the diamond surface. Only NV centers of the same orientation (shown in red) contribute to the ensemble NV NMR signal. (d) Larmor precessing nuclear spins in the sample produce an effective AC magnetic field (such as the one shown by the green line) that is detected by NV sensors in a frequency-selective manner using an XY8-k pulse sequence.

7.1 Experiment

For both sensor modalities, an NV NMR measurement proceeds in the following way. First, an 8 μs long 532 nm laser pulse optically pumps the NV electronic spins into the $|0\rangle$ state. Resonant microwave pulses are then applied to the NV electronic spins: first, a $\pi/2$ pulse prepares a coherent superposition of ground spin states $(|0\rangle + |1\rangle)/\sqrt{2}$; next, an XY8-$k$ sequence allows the NV spins to probe the local magnetic environment [147]; and finally, a $\pi/2$ pulse projects the evolved NV spin coherence onto a $|0\rangle$, $|1\rangle$ state population difference, which is detected via the NV spin-state dependent fluorescence intensity after a 500 ns 532 nm laser pulse. The XY8-k pulse sequence consists of a block of eight sequential π-rotation pulses repeated k times (Fig. 7.1d) and serves two purposes. First, the sequence dynamically

decouples NV spins from the background magnetic environment (e.g., spin impurities in diamond and other sources of magnetic noise), so that the NV spin coherence time T_2 is extended beyond the inhomogeneous dephasing time T_2^* and the single Hahn-echo coherence time [148–152]. Second, the XY8-k sequence gives the NV spins narrow-band sensitivity to NMR signals centered at frequency $\nu = 1/2\tau$, where τ is the delay time between π pulses, and with detection bandwidth $\Delta\nu = 0.111/k\tau$ [125, 126, 153]. The presence of an NMR signal resonant with the XY8-k sequence is detected as a spectrally-specific change in the NV optical fluorescence signal. See appendix E for information about the hardware used in the experiment.

For the NV NMR experiments described here, the magnetic signal of interest is produced by nuclear spins on the diamond surface interacting with shallow NV centers through magnetic dipole-dipole coupling. The specific components of the dipole-dipole Hamiltonian that are responsible for the measured signal stem from the $S_z I_x$ and $S_z I_y$ terms, where S_z is the z component of the NV spin (defined by the NV symmetry axis) and $I_{x,y}$ are the x and y components of the nuclear spin. These terms couple the NV spin to the transverse component of the nuclear spin, which precesses in a static magnetic field at the nuclear Larmor frequency. A nearby permanent magnet aligned with the NV center quantization axis sets the static magnetic field, B_0. A single measurement consists of repeating the optical pumping, XY8-k sequence, and optical detection a few hundred times in order to collect sufficient photons at the detector. The measurement is then repeated for a series of XY8-k pulse delay times, τ, to determine the spectrum of the magnetic environment. When τ matches a half-period of the nuclear spin precession, the magnetic coupling effectively drives the NV

spin away from the initial spin state, which is detected as a change in NV fluorescence intensity. These dips in the signal occur at the Larmor frequencies of nuclei on the surface (or other sources of noise, such as nuclear impurities within the diamond).

To perform NV NMR measurements, two fluorescence measurements F_1 and F_2 were acquired for each pulse sequence delay with the final $\pi/2$ pulse 180° out of phase. This procedure removes common-mode noise from laser intensity fluctuations. Normalized contrast, C, was then calculated as

$$C = \frac{F_2 - F_1}{F_2 + F_1}. \tag{7.1}$$

The broad decrease in contrast resulting from intrinsic NV decoherence was removed with a linear baseline correction. The corrected contrast was fit with the function

$$C(\omega) = \exp\left(-\sum_i \chi_i(\omega)\right), \tag{7.2}$$

where $\chi_i(\omega)$ describes the NV decoherence due to each nuclear species, i. It is a function of the frequency-dependent variance in the magnetic field signal (spectral density), $\langle|B_z^i(\Omega, \omega_L)|^2\rangle$, created by the nuclear spins, as well as a function $g(\Omega, \tau, N)$ describing the NV sensor response to the pulse sequence:

$$\chi_i(\omega) = \frac{\gamma_e^2}{4\pi} \int_{-\infty}^{+\infty} \langle|B_z^i(\Omega, \omega_L)|^2\rangle\, |g(\Omega, \tau, N)|^2\, d\Omega. \tag{7.3}$$

The function $g(\Omega, \tau, N)$ is the Fourier transform of $g(t)$, where $g(t)$ is a function describing the sign of NV spin phase accumulation during the pulse sequence. For the primary resonance of the XY8-k sequence,

$$|g(\Omega, \tau, N)|^2 \approx \frac{4}{\pi^2}(N\tau)^2\mathrm{sinc}^2\left(\frac{N\tau}{2}\left(\Omega - \frac{\pi}{\tau}\right)\right). \tag{7.4}$$

The magnetic signal created by a semi-infinite layer of spin-1/2 nuclei with density ρ near an NV center oriented along the [1 0 0] crystallographic axis is

$$\langle |B_z(\Omega, \omega_L)|^2 \rangle = \rho \frac{5\pi}{48} \left(\frac{\mu_0 \hbar \gamma_n}{4\pi} \right)^2 \left(\frac{1}{(d_{NV} + z_1)^3} - \frac{1}{(d_{NV} + z_2)^3} \right) \frac{T_2^{*-1}}{(\Omega - \omega_L)^2 + (T_2^{*-1})^2},$$

(7.5)

where ω_L is the nuclear Larmor frequency, T_2^* is the nuclear spin dephasing time, d_{NV} is the depth of the NV center below the diamond surface, z_1 is the distance from the diamond surface to the lower bound of the layer, and z_2 is the distance from the diamond surface to the upper bound of the layer. Combining these expressions and using the relationship $\omega = \pi/\tau$ for the filter resonance condition gives

$$\chi_i(\omega) = \rho_i \frac{5}{48\pi} \left(\frac{\mu_0 \gamma_{n,i} \gamma_e \hbar}{4\pi} \right)^2 \left(\frac{1}{(d_{NV} + z_1)^3} - \frac{1}{(d_{NV} + z_2)^3} \right) I_i(\omega),$$

(7.6)

where $I_i(\omega)$ is the convolution between the Lorentzian lineshape of the nuclear spin signal from species i and the $\text{sinc}^2(\omega)$ lineshape of the filter function for the XY8-k sequence. It can be expressed as

$$I_i(\omega) = \frac{2T_{2,i}^{*2}}{\left[1 + T_{2,i}^{*2} (\omega_{L,i} - \omega)^2 \right]^2} \left\{ e^{-\frac{N\pi}{\omega T_{2,i}^*}} \left[\left[1 - T_{2,i}^{*2} (\omega_{L,i} - \omega)^2 \right] \cos \left[\frac{N\pi}{\omega} (\omega_{L,i} - \omega) \right] \right. \right.$$

$$\left. - 2T_{2,i}^* (\omega_{L,i} - \omega) \sin \left[\frac{N\pi}{\omega} (\omega_{L,i} - \omega) \right] \right]$$

$$\left. + \frac{N\pi}{\omega T_{2,i}^*} \left[1 + T_{2,i}^{*2} (\omega_{L,i} - \omega)^2 \right] + T_{2,i}^{*2} (\omega_{L,i} - \omega)^2 - 1 \right\},$$

(7.7)

where $N = 8k$ is the total number of π pulses. See appendix C for a derivation of the model equations.

Importantly, the strength of the NV NMR signal and the number of nuclear spins detected per NV are sensitively dependent on the NV depth and the density of nuclear spins in the sample. To calibrate NV depth, we used NV NMR measurements from

protons in immersion oil (a well-understood sample with uniform ^{1}H density) placed on the diamond surface, together with a model of magnetic field fluctuations at each NV center induced by the ensemble of statistically polarized nuclear spins in the sample. We used the resulting NV depth and the nuclear magnetic field model to determine the number of sensed nuclear spins in each sample studied. To estimate the depth of single NV centers, NV NMR measurements were performed with a drop of immersion oil (Olympus Type-F Low Auto-Fluorescence) on the diamond surface. The parameters d_{NV} and T_2^* were determined by fitting the NV NMR signal contrast with equation 7.2 using a density $\rho = 60$ protons nm^3 [145].

7.2 Results and Discussion

Figure 7.2 shows example results for multi-species nanoscale NMR spectroscopy of a fluorinated sample measured with a single NV center, whose depth was determined by the aforementioned calibration process to be ~ 8 nm below the diamond surface. The fluorinated sample was prepared by mixing 2 mmol of solid sodium hydroxide with 2 mmol of liquid perfluorooctanesulfonyl fluoride (POSF) to produce a mixture containing sodium perfluorooctanesulfonate (PFOS). The mixture was applied to the diamond surface and allowed to dry, leaving a solid sample of PFOS on the surface.

Employing an XY8-10 pulse sequence, we measured NV NMR spectra of the fluorinated residue and observed resonances corresponding to ^{19}F and ^{1}H nuclei over a range of applied static magnetic fields, B_0, oriented along one NV axis. Several representative NMR spectra are shown in Fig. 7.2a, where we fit the measured NV fluorescence to the model function in equation 7.2 in order to extract the frequencies
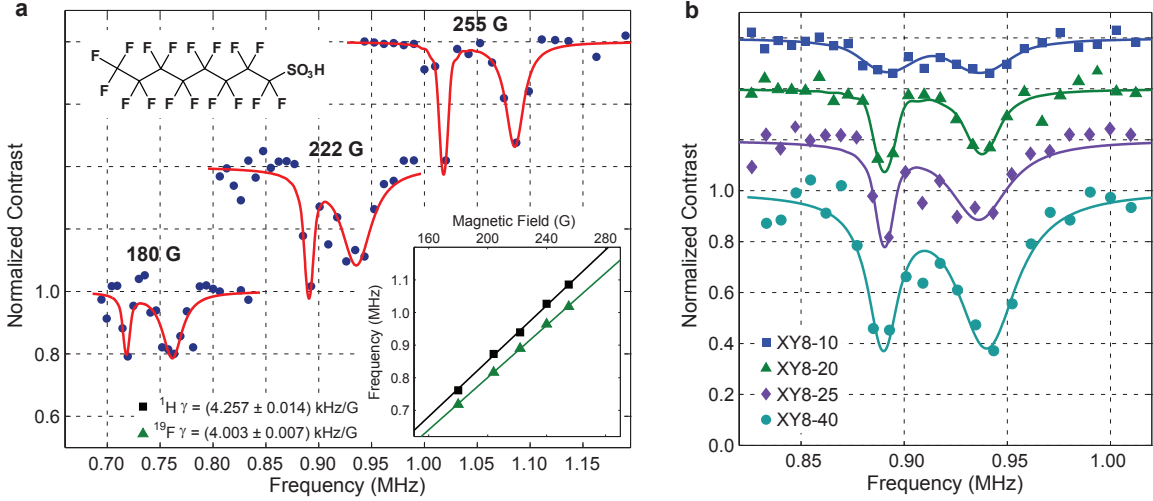
Figure 7.2: Multi-species nanoscale NMR with a single shallow NV center. (a) ^{1}H and ^{19}F NMR spectra of a fluorinated sample (PFOS/POSF) at several magnetic fields, measured with an XY8-10 sequence and fit with a model for the NV NMR lineshape. The PFOS molecular structure is indicated schematically. Inset: Measured ^{1}H and ^{19}F NMR resonance frequencies as a function of applied static magnetic field B_0. Linear fits yield gyromagnetic ratios in good agreement with literature. (b) Series of NV NMR spectra of the fluorinated sample acquired with an increasing number of repetitions k of the XY8-k pulse sequence. Measurement sensitivity and spectral selectivity improve with increased repetitions k. (Note: in both a and b, spectra are offset vertically for clarity of display.)

and linewidths of the NMR resonance dips. For the ^{19}F NMR resonance, we estimate that 50% of the observed NV NMR signal results from $\sim 20{,}000$ unpolarized fluorine nuclei in a $(10 \text{ nm})^3$ volume, which has a statistical spin polarization equivalent to ~ 140 polarized fluorine nuclei. In Fig. 7.2a we also plot the measured resonance frequency ν_0 of each nuclear species as a function of B_0, with an observed linear dependence $\nu_0 = \frac{\gamma_n}{2\pi} B_0$, consistent with the gyromagnetic ratios of ^{19}F and [1]H [154].

To characterize the inhomogeneous dephasing time T_2^* for each nuclear species, we varied the number of repetitions k in the XY8-k pulse sequence and observed the effect on the measured NV NMR resonance features. As shown in Fig. 7.2b, we found

that increasing k, and thereby creating a narrower spectral filter for the NV NMR measurement, results in a narrowing and deepening of the resonance dips, setting lower limits of $T_2^* \geq 32$ μs for ^{19}F and $T_2^* \geq 11$ μs for ^{1}H for this nanoscale sample on the diamond surface. Dephasing results from both spin-spin interactions and diffusion above the NV center (described in appendix D.)

To further investigate the omnipresent proton signal, observed from both the fluorinated PFOS/POSF sample and a SiO_2-coated region of the diamond (described below), we applied Fomblin Y HVAC 140/13 oil to the surface of a diamond directly after acid cleaning. NV NMR measurements of the Fomblin oil, which contains 40 ^{19}F nuclei/nm^3 and no ^{1}H, yield strong NMR signals of both ^{19}F and ^{1}H nuclei for each of the single NV centers probed (see Fig. 7.3a). The different relative strengths of the ^{19}F and ^{1}H signals, dependent on the depth of the probed NV center, is most consistent with a thin proton-containing layer (most likely water) between the diamond chip and a thick layer of Fomblin oil (Fig. 7.3b). Applying the NV NMR lineshape model to the proposed sample geometry yields a water layer thickness of 0.8 ± 0.2 nm. This analysis represents a first proof-of-principle demonstration of the capability of the NV NMR technique to extract thickness information for multi-layered thin films containing multiple nuclear spin species of known density, with sub-nanometer resolution.

As shown in figure 7.4, we also acquired consistent multi-species nanoscale NMR spectra using an ensemble of high-density, shallow-implanted NV centers in a wide-field microscope setup, with the NV fluorescence signal detected by a CCD camera and integrated across the few-micron-wide laser spot. For this diamond chip, the mean lateral distance between NV centers of the same orientation is ~ 30 nm (determined
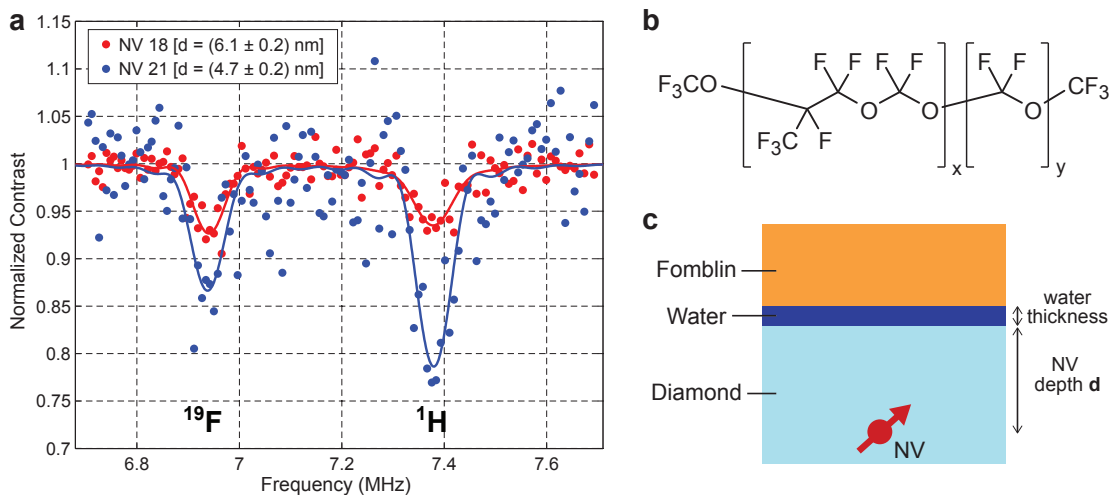
Figure 7.3: Determination of surface proton layer thickness. (a) NMR signal from Fomblin Y oil on the diamond surface measured with two NV centers. NV depths are presented, as calculated from the lineshape model. (b) Chemical structure of Fomblin Y oil. (c) Description of the hypothesized sample structure resulting from Fomblin Y oil floating above a thin layer of water on the diamond surface.

from the NV fabrication process and wide-field fluorescence measurements); and the mean NV depth ~ 10 nm (determined by the calibration process outlined above). In particular, the results in figure 7.4 demonstrate that high sensitivity nuclear spin sensing can be provided by NV ensembles, without choosing an optimal single NV sensor. In the first example (Fig. 7.4a), we again measured a fluorinated sample (PFOS/POSF) dried on the diamond surface. Both ^{1}H and ^{19}F NMR signals are resolved, albeit with broader linewidths than for the single NV center data of figure 7.2. In the second example (Fig. 7.4b), we performed NV NMR measurements of ^{31}P nuclei for a sample of powdered adenosine triphosphate disodium (ATP) salt on the diamond surface. The observed ^{31}P NMR signal is weaker than for the ^{1}H and ^{19}F NV NMR measurements, due to the relatively smaller ^{31}P gyromagnetic ratio and lower phosphorus spin density in the ATP salt sample. A plot of the measured ^{1}H,

Figure 7.4: Multi-species nanoscale NMR with a shallow NV ensemble. (a) NMR spectra of a fluorinated sample (PFOS/POSF) at several magneti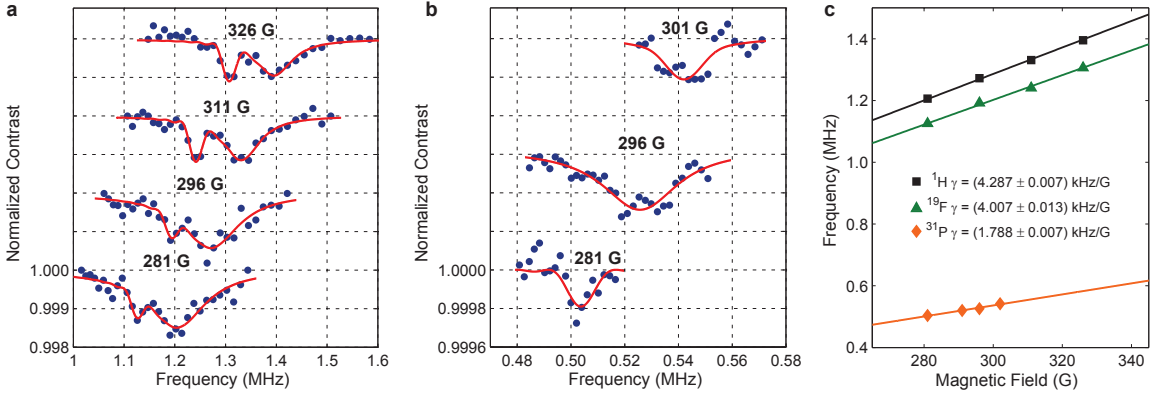c fields. As with single-NV measurements, both ^{1}H and ^{19}F NMR signals are observed and fit with a model lineshape. (b) ^{31}P NMR spectra from a powdered adenosine triphosphate (ATP) sample at several magnetic fields, smoothed and fit with the model lineshape. (Note: in both a and b, spectra are offset vertically for clarity of display.) (c) Measured ^{1}H, ^{19}F, and ^{31}P NMR resonance frequencies as a function of applied static magnetic field B_0. Linear fits yield gyromagnetic ratios for ^{1}H and ^{19}F in good agreement with literature, with the value for ^{31}P exceeding the literature value by about 4%.

^{19}F, and ^{31}P resonance frequencies versus magnetic field (Fig. 7.4c) are in reasonable agreement with the known gyromagnetic ratios of these nuclear species [154]. Note, however, that the effective gyromagnetic ratio for ^{31}P derived from these NV NMR measurements is about 4% higher than the free ^{31}P value, which may result from dipole-dipole couplings within the ATP molecule.

We next used the wide-field NV microscope to demonstrate NMR imaging of spatially-varying concentrations of ^{19}F nuclear spins, again using the fluorinated sample (PFOS/POSF). We fabricated a shaped structure (mask) of SiO_2 on the diamond surface via atomic-layer deposition. This structure covered part of the diamond surface, with a sub-micron edge going from the full thickness of the SiO_2 layer (90 nm) to bare diamond. Fig. 7.5a shows a white light image of a corner defined by this struc-

ture. We introduced the fluorinated sample onto the diamond surface and applied the sensing protocol described above, which provided an NMR spectrum for each pixel of the CCD camera: i.e., optical MRI with about 500 nm lateral resolution, 50 μm field-of-view, and sensitivity to nuclear spins within $\sim$ 20 nm of the diamond surface. An example ^{19}F NMR image is shown in figure 7.5b; with single-pixel NMR spectra on the bare diamond surface and under the SiO$_2$ structure shown in figure 7.5c. The SiO$_2$ structure prevented underlying NV centers from detecting the NMR signal from ^{19}F nuclear spins in the sample, due to the strong $(1/d^3)$ distance dependence of NV sensitivity to magnetic dipole fields. In contrast, the NV centers remained sensitive to ^{19}F nuclear spins in the sample on the bare diamond surface. Remnant protons are known to be present on diamond surfaces except under extreme conditions [143–145]; hence an ^{1}H NMR signal was observed across the full diamond surface. These results illustrate the ability of our technique to provide nuclear-species-specific spectroscopic and imaging information for nanoscale samples across a wide field-of-view.

7.3   Conclusion

In conclusion, we demonstrated a new capability for nanoscale, optically-detected NMR spectroscopy and imaging of multiple nuclear species (^{1}H, ^{19}F, ^{31}P) using shallow NV centers in diamond. We performed simultaneous multi-species NMR spectroscopy under ambient conditions, employing both single NV centers, suitable for probing few-nanometer sized samples containing $\sim$ 100 polarized nuclear spins as well as extracting thickness information for multiple layers of thin films with sub-nanometer resolution; and high-density NV ensembles in a thin layer near the sur-
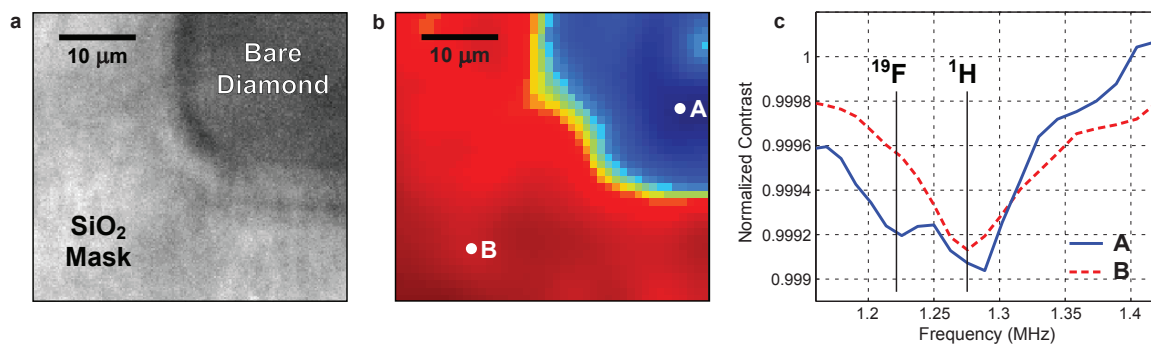
Figure 7.5: Optical MRI of multi-species sample with sub-micron structure. (a) White-light transmission image of shaped SiO_2 structure (90 nm thick mask) on the surface of a diamond containing a shallow, high-density NV layer. (b) Optical MRI of ^{19}F nuclear spin density in the fluorinated sample (PFOS/POSF) within $\sim$20 nm of surface. Blue represents a deep ^{19}F NMR contrast dip and hence high fluorine concentration on the bare diamond surface as measured by the NV ensemble. Red represents no ^{19}F NMR signal detected by the NV ensemble underneath the SiO_2 layer. For display, the image was processed with a 3-pixel width Gaussian blur. (c) NV NMR spectra from two points of the image in (b). On the bare diamond surface (A), NMR signals are observed for both ^1H and ^{19}F. Under the SiO_2 structure (B), only remnant ^1H spins are detected, as the SiO_2 layer displaces the fluorinated sample $\sim$90 nm away from the diamond surface and NV sensors.

face, suitable for wide-field spectroscopy and imaging with sub-micron resolution. Importantly, the NV ensemble results show that high-sensitivity nanoscale NMR does not require choosing an optimal single NV sensor. These complementary NV sensor modalities provide utility well beyond current NMR and MRI technology, opening the door to wide-ranging applications at the nanoscale, from studies of surface catalyst reactions to the identification of single protein structure and dynamics to functional MRI within living cells. Future challenges include improving the sensitivity and resolution of NV NMR and MRI, e.g., by realizing very shallow NV centers with good optical and spin properties and employing Fourier k-space imaging techniques with pulsed magnetic field gradients, respectively.

Chapter 8

Conclusions and Outlook

This thesis has demonstrated a number of novel techniques, but significant work remains to bring each to its full potential. Advances will most likely be driven by both improved pulse sequences and better materials.

8.1 Singlet States

Many groups are focused on using singlet states to store spin polarization for extended periods in hyperpolarized media, and we have helped advance that ability with the SLIC sequence. Further research on the relaxation properties of the singlet state in both nearly-equivalent and equivalent spin pairs may eventually lead to designer-molecules with extremely long singlet lifetimes. However, there are also a number of other applications that should not be overlooked. In particular, the SUC-CESS sequence offers a way to target the NMR signal of a large variety of endogenous molecules. Its major drawback at this point is the decrease in singlet creation and

readout efficiency as molecular complexity increases. One solution is to apply pulse sequences better tailored to the target molecule's Hamiltonian. These might be derived via optimal control theory [155] or even genetic algorithms [156–158] and may include adiabatic, chirped, or SLIC pulses to complement the simple pulses we employed. Additionally, the use of gradients as a quantum filter rather than phase cycling should improve the ability to remove background signals by reducing errors caused by imperfect signal subtraction.

There is a surging interest in low-field NMR spectroscopy, as it avoids the great expense and lack of portability of high-field superconducting magnets. Each year at the ENC conference, it seems that a new low-field NMR company appears! J-coupling spectroscopy using SLIC could significantly boost the information that these devices extract from a spectrum. However, pulse sequence and hardware improvements are needed to overcome the sensitivity to B_0 shifts and inhomogeneities as well as B_1 stability. Perhaps more importantly, computational algorithms must be produced to more easily predict and interpret the spectra produced.

The creation of a decoherence-free subspaces using combinations of singlet states has been proposed in the context of quantum information processing, and the ability of NMR to test such a system should not be overlooked. While NMR quantum computing has fallen out of favor due to its lack of scalability, NMR provides an excellent way to test quantum algorithms that can be applied to better quantum processors in the future. We have demonstrated one possible approach using SLIC sequences to control multiple pairs of strongly-coupled spins. The next steps are to better understand and optimize the pulse sequences to improve the accuracy of

the unitary operations and to fully characterize the sources of decoherence in such a subspace. Moreover, a way to perform logical operations to transfer quantum information from other spins into the subspace must be derived. Other combinations of singlet states can also form a DFS, and the SLIC sequence may find applications in those cases as well.

Finally, there is the possibility that singlet state studies can be used to measure magnetic parameters that are currently not detectable with NMR, such as J-couplings between magnetically equivalent nuclei. For example, a spin-lock induced crossing between singlet and triplet states of identical spins will not lead to coherent polarization transfer, but it may reveal dynamics caused by higher-order interactions. The analysis of ethanol energy levels at low-field shows that there are many energy crossings in which polarization transfer is forbidden by first-order processes, but further analysis is needed to reveal how spin-locking at these crossings may affect spin relaxation to reveal other spin transitions.

8.2   NV NMR

The rapid advancements in magnetometry using nitrogen-vacancy centers in diamond are breaking down sensitivity and size barriers that have plagued magnetic resonance for decades. However, NV NMR spectroscopy is still in its infancy and significant improvements will be necessary for it to compete with conventional NMR. Because it is currently a low-field technique, NV NMR cannot resolve the chemical shifts that give NMR much of its utility for chemistry. This may be overcome by NV NMR's potential ability to directly image the location of nuclear spins, which is

being advanced using strong nanoscale magnetic gradients in the Walsworth group and using novel pulse sequences by our colleagues in the Cappellaro group. Such methods might make it possible to map out the positions of nuclei in biomolecules. Employing diamonds at high-field where chemical shifts are dominant is also possible and is a largely unexplored area of research.

A major goal of NV NMR is to detect a single nuclear spin with a single NV center, and it appears that with the proper diamond preparation and pulse sequence this will be achieved in the near future. The major materials challenge is to produce very shallow NV centers with good coherence properties. A number of groups are attacking the problem experimentally, and it should be possible to use NV NMR to better characterize the diamond surface to promote this goal. New pulse sequences making use of spin-locking and nearby surface electronic spins should provide better sensitivity as well.

Finally, a number of other NV NMR applications can be imagined. As discussed in appendix D, NV NMR measurements are very sensitive to diffusion and may better reveal diffusion dynamics at the nanoscale, near surfaces, and in thin films. Subcellular imaging of living cells may be possible using NV ensembles, similar to DC magnetic measurements already demonstrated [102]. It should also be possible to extend NV NMR to measurements of quadrupolar nuclei, revealing quadrupole interactions and consequently electric field gradients in samples at the nanoscale. These and other novel uses for NV NMR are ready to be explored by the next generation of graduate students following in my footsteps.

Appendix A

Singlet State Relaxation

Detailed models of singlet state relaxation have been derived by Pileio *et al.* in ref. [35, 36, 159]. This appendix discusses other aspects of singlet state relaxation, including the relaxation properties of the long-lived coherence, the effects of off resonance spin-locking, and the dependence of singlet state relaxation on temperature and paramagnetic impurities.

A.1 Long-Lived Coherence Relaxation

The maximum lifetime of the long-lived coherence (LLC) under zero RF spin-locking power can be found using the conventional two-spin dipole-dipole relaxation model of Solomon [25, 41], which predicts that in most cases $T_{LLC} = 3T_1$. Demonstration of this relation is accomplished by comparing the long-lived coherence experiment with a standard inversion recovery experiment. In the latter case the system is initialized to the state $I_{1z}(0) = I_{2z}(0) = -M_0$, where $I_{nz}(t)$ is the magnetization of

140

nucleus n at time t, and M_0 is the magnetization of the spins at thermal equilibrium. The Bloch equations then describe the magnetization as a function of time with two relaxation rates, ρ and σ:

$$I_Z = M_0 \left(1 - 2\exp\left[t/T_1\right]\right) = M_0 \left(1 - 2\exp\left[-(\rho + \sigma)t\right]\right). \tag{A.1}$$

These two relaxation rates are the result of zero, single, and double quantum transitions with rates W_0, W_1 and, W_2 respectively:

$$\sigma = W_2 - W_0$$

$$\rho = W_0 + 2W_1 + W_2. \tag{A.2}$$

For small molecules, which rotate quickly (GHz rates), the short correlation times result in transition rates that can be related to one another through a constant k:

$$k = 10W_0 = 20/3W_1 = 5/3W_2, \tag{A.3}$$

where the numerical prefactors for W_0, W_1 and, W_2 are determined from averaging the relative interaction strength of each transition over all angular configurations. Combining equations A.1, A.2, and A.3 allows one to write T_1 in terms of k:

$$T_1 = 1/(\rho + \sigma) = \frac{2}{3}\frac{1}{k}. \tag{A.4}$$

The long-lived coherence, ρ_{LLC}, represents a population difference

$$\rho_{LLC} = |\uparrow\downarrow\rangle\langle\uparrow\downarrow| - |\downarrow\uparrow\rangle\langle\downarrow\uparrow| = I_{1z} - I_{2z}. \tag{A.5}$$

It results from a selective inversion of the spins rather than the inversion of both spins. The initial conditions for magnetization are $I_{1Z}(0) = -I_{2Z}(0) = M_0$. In this

case relaxation is found to be bi-exponential for the individual magnetizations and exponential for the magnetization difference. The Bloch equations for the magnetization of spins one and two are

$$I_{1z} = M_0 \left(1 - \exp\left[-(\rho + \sigma)t \right] + \exp\left[(\sigma - \rho)t \right] \right) \tag{A.6}$$

and

$$I_{2z} = M_0 \left(1 - \exp\left[-(\rho + \sigma)t \right] - \exp\left[(\sigma - \rho)t \right] \right). \tag{A.7}$$

The difference between these equations describes the magnetization of the long-lived coherence:

$$I_{1z} - I_{2z} = 2M_0 \exp\left[-t/T_{LLC} \right] = 2M_0 \exp\left[(\sigma - \rho)t \right]. \tag{A.8}$$

This results in a lifetime $T_{LLC} = 1/(\rho - \sigma)$, which can be written in terms of T_1 as

$$T_{LLC} = \frac{1}{2(W_0 + W_1)} = \frac{2}{k} = 3T_1. \tag{A.9}$$

The enhancements are smaller for the long-lived coherence when the molecules have long correlation times, since the assumptions leading to equation A.3 are no longer valid. For example, larger molecules rotate more slowly, which can lead to $W_2 \approx 0$. In that case

$$T_1 = 1/(2W_1) = \frac{10}{3}\frac{1}{k}$$
$$T_{LLC} = \frac{1}{2(W_0 + W_1)} = \frac{2}{k} = \frac{3}{5}T_1. \tag{A.10}$$

Bornet *et al.* studied a similar long-lived coherence in which an additional $\pi/2$ pulse rotated $I_{1z} - I_{2z}$ into $I_{1x} - I_{2x}$, which they subsequently spin-locked [40]. They found that $T_{LLC} = 3T_2$ for short coherence times and $T_{LLC} = 9T_2$ for longer coherence times. The advantage of using the $I_{1z} - I_{2z}$ is that a lifetime enhancement can be

achieved without the use of spin-locking. This enhancement is contingent on T_1 being dominated by intra-pair interactions. The more outside spins contribute to spin-lattice relaxation, the smaller the enhancement will be.

A.2   Effect of Off-Resonance RF Spin-Locking

We found that increased lifetime enhancement (T_S/T_1) was achieved in glycerol formal when the RF power was applied slightly off-resonance. Glycerol formal is special because it exists in two interconverting structures and has overlapping spectral lines. We refer to the peaks from one structure as "a" and "b" and from the other structure as "b" and "c", since the "b" peaks are completely overlapping. Peak "c" was found to have a longer lifetime when the RF transmitter frequency was centered between "a" and "b." Table A.1 summarizes the measurements made with the RF transmitter frequency centered at the two different positions. In Fig. 3.5 and Table 3.3 of the main text we present measurements for peak "c" with the RF transmit frequency centered between "b" and "c."

Table A.1: Measured values of spin-lattice, singlet, and long-lived coherence relaxation times for glycerol formal.

Transmit	Peak	$T_1(s)$	$T_S(s)$	T_S/T_1	$T_{LLC}(s)$	T_{LLC}/T_1
a & b	a	0.95 ± 0.01	1.07 ± 0.01	1.13 ± 0.02	1.3 ± 0.2	1.4 ± 0.2
	b	0.68 ± 0.01	2.81 ± 0.03	4.13 ± 0.08	1.4 ± 0.2	2.1 ± 0.3
	c	0.68 ± 0.01	2.09 ± 0.02	3.07 ± 0.05	1.12 ± 0.06	1.65 ± 0.09
b & c	a	0.95 ± 0.01	1.30 ± 0.05	1.37 ± 0.05	1.14 ± 0.04	1.20 ± 0.04
	b	0.68 ± 0.01	2.07 ± 0.05	3.04 ± 0.09	1.06 ± 0.08	1.6 ± 0.1
	c	0.68 ± 0.01	1.91 ± 0.03	2.81 ± 0.06	1.37 ± 0.02	2.01 ± 0.04

We also measured the maximum singlet lifetime in citric acid when the transmitter frequency of the RF spin-lock was moved away from the average resonance frequency
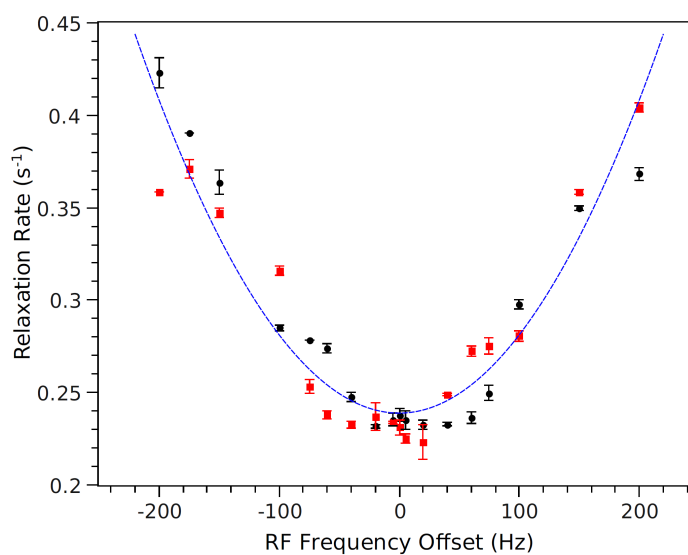
Figure A.1: For citric acid prepared with a mixture of singlet population and long-lived coherence, we measured an approximately quadratic relationship between the singlet relaxation rate and the frequency offset of the RF spin-locking field from the average frequency of the proton spin pair. Note the significant deviations between the relaxation rates of the lower-frequency proton (red squares) and the higher-frequency proton (black circles).

of the proton pair. A theoretical analysis predicts that the relaxation rate should increase quadratically with RF-field offset for relatively small frequency shifts [35, 160]. We set the RF spin-locking nutation frequency to 565 Hz and employed a mixture of singlet and long-lived coherence. As seen in Fig. A.1, the measured large-scale increase in relaxation rate is quadratic, but deviations are clearly evident between the lifetimes of each proton of the pair. At RF frequency offsets between 30 and 90 Hz, the relaxation rate decreases for the proton whose resonance frequency is closer to the RF transmitter frequency while the relaxation rate of the other proton increases. This trend differs from what we observed in glycerol formal, where we measured a longer singlet lifetime when the RF spin-locking field frequency was moved away from the resonance frequency by 20 Hz.

A.3   Temperature Effects

Figure A.2 shows measurements for citric acid of the spin-lattice relaxation time T_1 and the maximum singlet lifetime T_S at high RF spin-locking power for temperatures between 22 and 54 °C. Both T_1 and T_S increase linearly with temperature, and the enhancement ratio (T_S/T_1) changes little over the temperature range. This trend matches previous results [19]. Both T_1 and temperature are inversely proportional to the molecular correlation time because in solution small molecules are in the extreme-narrowing regime. Therefore, a linear relationship between T_1 and temperature is expected. Since the singlet lifetime is also linear with temperature, we conclude that it must be inversely proportional to correlation time as well, and thus the magnetic quadrupolar interaction is the dominant relaxation mechanism.
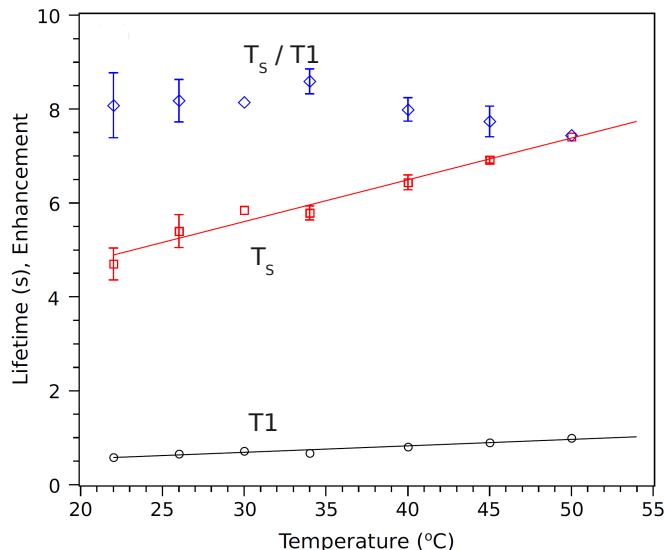
Figure A.2: Measured temperature dependences of T_1 (black circles) and the maximum singlet lifetime T_S (red squares) are linear for citric acid. (T_1 error bars are smaller than symbol size.) Lifetime enhancement ratio T_S/T_1 (blue diamonds) has little temperature dependence.

A.4 Sensitivity of the Long-Lived Coherence and Singlet State to Paramagnetic Impurities

We studied the sensitivity of the long-lived coherence and singlet state lifetimes to paramagnetic impurities, specifically oxygen, by comparing lifetimes in solutions with different oxygen concentrations. The effect of paramagnetic relaxation on the singlet state was studied by Tayler and Levitt for the alanine-glycine molecule [161]. They measured the strength of relaxation versus paramagnetic spin concentration. However, the relaxation rates $1/T_1$, $1/T_{LLC}$, and $1/T_S$ should be affected differently depending on the molecular geometry, especially the internuclear distance between the spins comprising the singlet. Singlet states created in more closely spaced nuclei

are expected to experience weaker paramagnetic relaxation because the two spins are more likely to experience identical interactions with the paramagnetic spins. We verified this hypothesis by measuring relaxation times in molecules with a variety of structures.

The molecules considered are shown in Fig. A.3. Nitrous oxide was investigated elsewhere [162], and the results are used for comparison. For the others, 100 mM solutions were prepared in D_2O or CCl_4, and the relaxation times T_1, T_{LLC}, and T_S were measured as described in chapter 3. Measurements were then repeated after bubbling N_2 gas through each solution for 5 min to displace dissolved oxygen. The relaxation rates due to oxygen are then given by

$$k_1[O_2] = T_1^{-1}(O_2) - T_1^{-1}(N_2)$$

$$k_{LLC}[O_2] = T_{LLC}^{-1}(O_2) - T_{LLC}^{-1}(N_2)$$

$$k_S[O_2] = T_S^{-1}(O_2) - T_S^{-1}(N_2). \tag{A.11}$$

Note that although the rates depend on the oxygen concentration, $[O_2]$, we are interested in rate ratios such as k_S/k_1, which can be measured without knowing the value of $[O_2]$.

Results are summarized in Table A.2. For a number of molecules, hardware limitations prevented us from applying enough RF power to fully convert the prepared state to the singlet eigenstate. The column "% singlet" lists the singlet character of the prepared state during spin-locking, i.e., $\langle \psi | S_0 \rangle$. The internuclear distance between the spins comprising the singlet state is also listed. Fig. A.4 plots the sensitivity as a function of internuclear distance. It shows that the sensitivity of both the singlet and long-lived coherence to oxygen increases as the nuclear spacing increases.
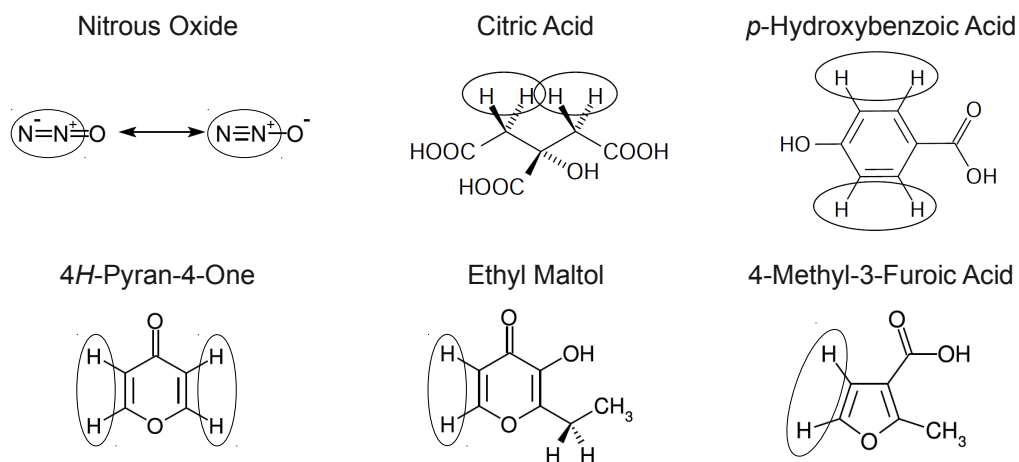
Figure A.3: Structures of molecules tested for oxygen sensitivity. The nuclei on which the singlet state was prepared are indicated.

Table A.2: Oxygen sensitivity of singlets vs. internuclear distance.

Molecule	Solvent	% Singlet	R (Å)	k_{LLC}/k_1	k_{LLC}/k_S	k_S/k_1
nitrous oxide	Blood	100%	1.13	-	-	0.015
						0.026
citric acid	D_2O	100%	1.76	0.5	1.2	0.4
$4H$-pyran-4-one	D_2O	96%	2.44	1.0	0.8	1.3
ethyl maltol	D_2O	96%	2.44	0.9	0.8	1.2
p-hydroxybenzoic acid	D_2O	98%	2.47	0.6	0.7	0.9
2-methyl-3-furoic acid	D_2O	99%	2.77	0.9	1.0	0.9
2-methyl-3-furoic acid	CCl_4	99%	2.77	0.8	1.0	0.8
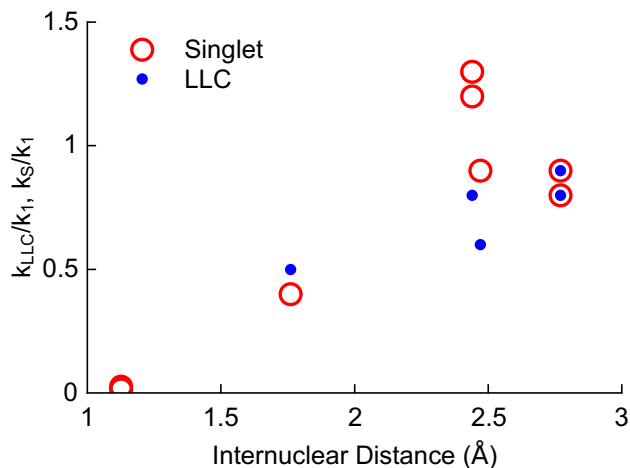
Figure A.4: The ratios k_{LLC}/k_1 and k_S/k_1 increase as a function of internuclear distance.

With knowledge of the spin state oxygen sensitivity, it is possible to derive an expression relating the enhanced lifetime of the long-lived coherence (T_{LLC}/T_1) to that of the singlet state (T_S/T_1). Consider the isolated proton pair on which the singlet or long-lived coherence is prepared. We have shown previously that

$$\frac{1}{T_S} = 0 \tag{A.12}$$

$$\frac{1}{T_1} = k_{DD} \tag{A.13}$$

$$\frac{1}{T_{LLC}} = \frac{1}{3}k_{DD}, \tag{A.14}$$

where k_{DD} is the relaxation rate due to dipole-dipole coupling.

Now consider the addition of more spins to the system. These could be nearby protons on the molecule or oxygen in the solution. Each state's relaxation rate will increase in response to the concentration of these spins. Let $[A]$ represent their

concentration and k_n represent the relaxation of state n per unit $[A]$. Then

$$\frac{1}{T_S} = k_S[A] \tag{A.15}$$

$$\frac{1}{T_1} = k_1[A] + k_{DD} \tag{A.16}$$

and

$$\frac{1}{T_{LLC}} = k_{LLC}[A] + \frac{1}{3}k_{DD} \tag{A.17}$$

Subsequently, the lifetime enhancements are

$$\frac{T_S}{T_1} = \frac{k_{DD} + k_1[A]}{k_S[A]} \tag{A.18}$$

and

$$\frac{T_{LLC}}{T_1} = \frac{k_{DD} + k_1[A]}{k_{LLC}[A] + \frac{1}{3}k_{DD}} \tag{A.19}$$

We seek a function $T_{LLC}/T_1 = f(T_S/T_1)$. Using the relationships

$$\frac{T_{LLC}}{T_1} = \frac{k_S[A]}{k_{LLC}[A] + \frac{1}{3}k_{DD}} \frac{T_S}{T_1} \tag{A.20}$$

and

$$k_{DD} = k_S[A]\frac{T_S}{T_1} - k_1[A] \tag{A.21}$$

we arrive at

$$\frac{T_{LLC}}{T_1} = \frac{k_S[A]}{k_{LLC}[A] + \frac{1}{3}(k_S[A]\frac{T_S}{T_1} - k_1[A])} \frac{T_S}{T_1} \tag{A.22}$$

Canceling out $[A]$ and performing some rearrangement gives

$$\frac{T_{LLC}}{T_1} = \frac{3\frac{T_S}{T_1}}{\frac{T_S}{T_1} + \left(\frac{3k_{LLC}-k_1}{k_S}\right)} \tag{A.23}$$

We can now define a new parameter, α, such that

$$\frac{T_{LLC}}{T_1} = \frac{3\frac{T_S}{T_1}}{\frac{T_S}{T_1} + \alpha} \tag{A.24}$$

Table A.3: α calculated from oxygen sensitivity experiments.

Molecule	α
citric acid	1.1
$4H$-pyran-4-one	1.6
ethyl maltol	1.6
p-hydroxybenzoic acid	1.0
2-methyl-3-furoic acid	1.8

and

$$\alpha = \frac{3k_{LLC} - k_1}{k_S}. \tag{A.25}$$

Table A.3 shows the calculated values of α using the oxygen sensitivity measurements of Table A.2. They range between 1 and 1.8. Figure A.5 plots the lifetime enhancement of the long-lived coherence versus that of the singlet state for a number of molecules measured here and in chapter 3. Most values lie between the dashed curves defined by $\alpha = 0.8$ and $\alpha = 2$, while the best-fit value is $\alpha = 1.4$ (solid line).

For relaxation from a random magnetic field, one would expect $k_{LLC} = k_1$ and $k_S/k_1 \leq 2$, which would result in $\alpha \geq 1$ [29]. In that situation, higher α should correspond to lower values of k_S/k_1. However, we see considerable deviation from such a trend, with $k_{LLC} < k_1$ for most cases. This indicates that the long-lived state is exhibiting some correlated behavior, possibly because natural couplings are producing an admixture with the singlet state. More detailed measurements are needed to further elucidate this behavior.
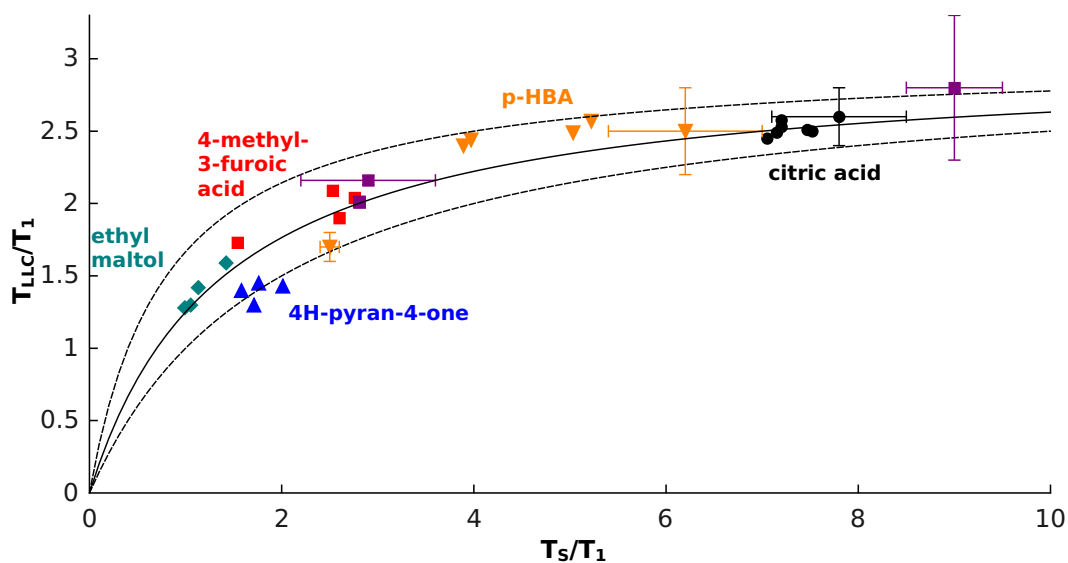
Figure A.5: A plot of measured lifetime enhancements for the long-lived coherence (T_{LLC}/T_1) versus measured enhancements for the singlet state (T_S/T_1) show that values roughly follow the relationship given by equation A.24. Dotted lines plot the relationship for $\alpha = 0.8$ (upper bound) and $\alpha = 2$ (lower bound), while the solid line represents the best-fit value $\alpha = 1.4$. The molecules from the oxygen sensitivity experiment associated with each set of points is indicated. Purple points indicate values from aspartic acid, *trans*-1,4-cyclohexanediol, and glycerol formal given in Table 3.3.

Appendix B

Low-Field Energy Level

Calculations

The position of dips measured in a SLIC spectrum can be calculated in a similar way to zero-field spectra [90, 91], but with modifications to consider a homonuclear system and the effects of RF spin-locking. Here, we demonstrate the procedure for hydrated ethanol, which is also applicable to more complex systems by repeating the necessary steps for all spin groups and couplings.

Hydrated ethanol contains two spin groups: a methylene group (labeled A) consisting of two protons J-coupled with strength J_{AA}, and a methyl group (labeled B) consisting of three protons each J-coupled to the other with strength J_{BB}. The values for scalar couplings within these spin groups are unknown because there is currently no way to measure the couplings between magnetically equivalent spins. Protons from group A are coupled to protons of group B by the coupling J_{AB}, with a value $J_{AB} = 7.1$ Hz measured in a 4.7 T spectrometer.

The methylene group protons are magnetically equivalent and the spins form three triplet states and one singlet state. The dressed state definitions and energies are:

$$
\begin{aligned}
|1,-1\rangle_A &= |\uparrow\uparrow\rangle & E &= \frac{1}{4}J_{AA} \\
|1,0\rangle_A &= \frac{|\uparrow\downarrow\rangle + |\downarrow\uparrow\rangle}{\sqrt{2}} & E &= \frac{1}{4}J_{AA} \\
|1,+1\rangle_A &= |\downarrow\downarrow\rangle & E &= \frac{1}{4}J_{AA} \\
|0,0\rangle_A &= \frac{|\uparrow\downarrow\rangle - |\downarrow\uparrow\rangle}{\sqrt{2}} & E &= -\frac{3}{4}J_{AA}.
\end{aligned}
\tag{B.1}
$$

The methyl group spins are also magnetically equivalent and can combine in three different ways. There is a spin-$\frac{3}{2}$ subspace with states

$$
\begin{aligned}
\left|\frac{3}{2},-\frac{3}{2}\right\rangle_B &= |\uparrow\uparrow\uparrow\rangle & E &= \frac{3}{4}J_{BB} \\
\left|\frac{3}{2},-\frac{1}{2}\right\rangle_B &= \frac{|\uparrow\uparrow\downarrow\rangle + |\uparrow\downarrow\uparrow\rangle + |\downarrow\uparrow\uparrow\rangle}{\sqrt{3}} & E &= \frac{3}{4}J_{BB} \\
\left|\frac{3}{2},+\frac{1}{2}\right\rangle_B &= \frac{|\downarrow\downarrow\uparrow\rangle + |\downarrow\uparrow\downarrow\rangle + |\uparrow\downarrow\downarrow\rangle}{\sqrt{3}} & E &= \frac{3}{4}J_{BB} \\
\left|\frac{3}{2},+\frac{3}{2}\right\rangle_B &= |\downarrow\downarrow\downarrow\rangle & E &= \frac{3}{4}J_{BB}.
\end{aligned}
\tag{B.2}
$$

There are two spin-$\frac{1}{2}$ subspaces, one corresponding to an $m_z = 0$ triplet state paired with a proton and the other corresponding to a singlet state paired with a proton:

$$
\begin{aligned}
\left|\frac{1}{2},-\frac{1}{2}\right\rangle_B &= -\frac{2|\uparrow\uparrow\downarrow\rangle - |\uparrow\downarrow\uparrow\rangle - |\downarrow\uparrow\uparrow\rangle}{\sqrt{6}} & E &= -\frac{3}{4}J_{BB} \\
\left|\frac{1}{2},+\frac{1}{2}\right\rangle_B &= \frac{2|\downarrow\downarrow\uparrow\rangle - |\downarrow\uparrow\downarrow\rangle - |\uparrow\downarrow\downarrow\rangle}{\sqrt{6}} & E &= -\frac{3}{4}J_{BB} \\
\left|\frac{1}{2},-\frac{1}{2}\right\rangle_{BS} &= \frac{|\uparrow\downarrow\uparrow\rangle - |\downarrow\uparrow\uparrow\rangle}{\sqrt{2}} & E &= -\frac{3}{4}J_{BB} \\
\left|\frac{1}{2},+\frac{1}{2}\right\rangle_{BS} &= \frac{|\uparrow\downarrow\downarrow\rangle - |\downarrow\uparrow\downarrow\rangle}{\sqrt{2}}\rangle & E &= -\frac{3}{4}J_{BB}.
\end{aligned}
\tag{B.3}
$$

Next, the methylene and methyl group states are combined into product states and then dressed to form 32 new eigenstates whose energies are also determined by

J_{AB}. The internal energies of the states (i.e., J_{AA}, J_{BB}) determine which product states combine, as the J-coupling will only be effective between product states of the same energy. The first group is:

$$\left|\frac{5}{2},-\frac{5}{2}\right\rangle = \left|\frac{3}{2},-\frac{3}{2}\right\rangle_B |1,-1\rangle_A$$

$$\left|\frac{5}{2},-\frac{3}{2}\right\rangle = \sqrt{\frac{2}{5}}\left|\frac{3}{2},-\frac{3}{2}\right\rangle_B |1,0\rangle_A + \sqrt{\frac{3}{5}}\left|\frac{3}{2},-\frac{1}{2}\right\rangle_B |1,-1\rangle_A$$

$$\left|\frac{5}{2},-\frac{1}{2}\right\rangle = \sqrt{\frac{1}{10}}\left|\frac{3}{2},-\frac{3}{2}\right\rangle_B |1,+1\rangle_A + \sqrt{\frac{3}{5}}\left|\frac{3}{2},-\frac{1}{2}\right\rangle_B |1,0\rangle_A + \sqrt{\frac{3}{10}}\left|\frac{3}{2},+\frac{1}{2}\right\rangle_B |1,-1\rangle_A$$

$$\left|\frac{5}{2},+\frac{1}{2}\right\rangle = \sqrt{\frac{1}{10}}\left|\frac{3}{2},+\frac{3}{2}\right\rangle_B |1,-1\rangle_A + \sqrt{\frac{3}{5}}\left|\frac{3}{2},+\frac{1}{2}\right\rangle_B |1,0\rangle_A + \sqrt{\frac{3}{10}}\left|\frac{3}{2},-\frac{1}{2}\right\rangle_B |1,+1\rangle_A$$

$$\left|\frac{5}{2},+\frac{3}{2}\right\rangle = \sqrt{\frac{2}{5}}\left|\frac{3}{2},+\frac{3}{2}\right\rangle_B |1,0\rangle_A + \sqrt{\frac{3}{5}}\left|\frac{3}{2},+\frac{1}{2}\right\rangle_B |1,+1\rangle_A$$

$$\left|\frac{5}{2},+\frac{5}{2}\right\rangle = \left|\frac{3}{2},+\frac{3}{2}\right\rangle_B |1,+1\rangle_A ,$$

$$(B.4)$$

all with energy $E = \frac{3}{2}J_{AB} + \frac{1}{4}J_{AA} + \frac{3}{4}J_{BB}$,

$$\left|\frac{3}{2},-\frac{3}{2}\right\rangle = -\sqrt{\frac{3}{5}}\left|\frac{3}{2},-\frac{3}{2}\right\rangle_B |1,0\rangle_A + \sqrt{\frac{2}{5}}\left|\frac{3}{2},-\frac{1}{2}\right\rangle_B |1,-1\rangle_A$$

$$\left|\frac{3}{2},-\frac{1}{2}\right\rangle = -\sqrt{\frac{2}{5}}\left|\frac{3}{2},-\frac{3}{2}\right\rangle_B |1,+1\rangle_A - \sqrt{\frac{1}{15}}\left|\frac{3}{2},-\frac{1}{2}\right\rangle_B |1,0\rangle_A + \sqrt{\frac{8}{15}}\left|\frac{3}{2},+\frac{1}{2}\right\rangle_B |1,-1\rangle_A$$

$$\left|\frac{3}{2},+\frac{1}{2}\right\rangle = \sqrt{\frac{2}{5}}\left|\frac{3}{2},+\frac{3}{2}\right\rangle_B |1,-1\rangle_A + \sqrt{\frac{1}{15}}\left|\frac{3}{2},+\frac{1}{2}\right\rangle_B |1,0\rangle_A - \sqrt{\frac{8}{15}}\left|\frac{3}{2},-\frac{1}{2}\right\rangle_B |1,+1\rangle_A$$

$$\left|\frac{3}{2},+\frac{3}{2}\right\rangle = \sqrt{\frac{3}{5}}\left|\frac{3}{2},+\frac{3}{2}\right\rangle_B |1,0\rangle_A - \sqrt{\frac{2}{5}}\left|\frac{3}{2},+\frac{1}{2}\right\rangle_B |1,+1\rangle_A ,$$

$$(B.5)$$

all with energy $E = -J_{AB} + \frac{1}{4}J_{AA} + \frac{3}{4}J_{BB}$, and

$$\left|\frac{1}{2},-\frac{1}{2}\right\rangle = \sqrt{\frac{1}{2}}\left|\frac{3}{2},-\frac{3}{2}\right\rangle_B |1,+1\rangle_A - \sqrt{\frac{1}{3}}\left|\frac{3}{2},-\frac{1}{2}\right\rangle_B |1,0\rangle_A + \sqrt{\frac{1}{6}}\left|\frac{3}{2},+\frac{1}{2}\right\rangle_B |1,-1\rangle_A$$

$$\left|\frac{1}{2},+\frac{1}{2}\right\rangle = \sqrt{\frac{1}{2}}\left|\frac{3}{2},+\frac{3}{2}\right\rangle_B |1,-1\rangle_A - \sqrt{\frac{1}{3}}\left|\frac{3}{2},+\frac{1}{2}\right\rangle_B |1,0\rangle_A + \sqrt{\frac{1}{6}}\left|\frac{3}{2},-\frac{1}{2}\right\rangle_B |1,+1\rangle_A ,$$

$$(B.6)$$

155

all with energy $E = -\frac{5}{2}J_{AB} + \frac{1}{4}J_{AA} + \frac{3}{4}J_{BB}$.

The second group is:

$$
\begin{aligned}
\left|\frac{3}{2}, -\frac{3}{2}\right\rangle_T &= \left|\frac{1}{2}, -\frac{1}{2}\right\rangle_B |1, -1\rangle_A \\
\left|\frac{3}{2}, -\frac{1}{2}\right\rangle_T &= \sqrt{\frac{1}{3}}\left|\frac{1}{2}, +\frac{1}{2}\right\rangle_B |1, -1\rangle_A + \sqrt{\frac{2}{3}}\left|\frac{1}{2}, -\frac{1}{2}\right\rangle_B |1, 0\rangle_A \\
\left|\frac{3}{2}, +\frac{1}{2}\right\rangle_T &= \sqrt{\frac{1}{3}}\left|\frac{1}{2}, -\frac{1}{2}\right\rangle_B |1, +1\rangle_A + \sqrt{\frac{2}{3}}\left|\frac{1}{2}, +\frac{1}{2}\right\rangle_B |1, 0\rangle_A \\
\left|\frac{3}{2}, +\frac{3}{2}\right\rangle_T &= \left|\frac{1}{2}, +\frac{1}{2}\right\rangle_B |1, +1\rangle_A \\
\left|\frac{3}{2}, -\frac{3}{2}\right\rangle_S &= \left|\frac{1}{2}, -\frac{1}{2}\right\rangle_{BS} |1, -1\rangle_A \\
\left|\frac{3}{2}, -\frac{1}{2}\right\rangle_S &= \sqrt{\frac{1}{3}}\left|\frac{1}{2}, +\frac{1}{2}\right\rangle_{BS} |1, -1\rangle_A + \sqrt{\frac{2}{3}}\left|\frac{1}{2}, -\frac{1}{2}\right\rangle_{BS} |1, 0\rangle_A \\
\left|\frac{3}{2}, +\frac{1}{2}\right\rangle_S &= \sqrt{\frac{1}{3}}\left|\frac{1}{2}, -\frac{1}{2}\right\rangle_{BS} |1, +1\rangle_A + \sqrt{\frac{2}{3}}\left|\frac{1}{2}, +\frac{1}{2}\right\rangle_{BS} |1, 0\rangle_A \\
\left|\frac{3}{2}, +\frac{3}{2}\right\rangle_S &= \left|\frac{1}{2}, +\frac{1}{2}\right\rangle_{BS} |1, +1\rangle_A,
\end{aligned}
\tag{B.7}
$$

all with energy $E = \frac{1}{2}J_{AB} + \frac{1}{4}J_{AA} - \frac{3}{4}J_{BB}$, and

$$
\begin{aligned}
\left|\frac{1}{2}, -\frac{1}{2}\right\rangle_T &= -\sqrt{\frac{2}{3}}\left|\frac{1}{2}, +\frac{1}{2}\right\rangle_B |1, -1\rangle_A + \sqrt{\frac{1}{3}}\left|\frac{1}{2}, -\frac{1}{2}\right\rangle_B |1, 0\rangle_A \\
\left|\frac{1}{2}, +\frac{1}{2}\right\rangle_T &= \sqrt{\frac{2}{3}}\left|\frac{1}{2}, -\frac{1}{2}\right\rangle_B |1, +1\rangle_A - \sqrt{\frac{1}{3}}\left|\frac{1}{2}, +\frac{1}{2}\right\rangle_B |1, 0\rangle_A \\
\left|\frac{1}{2}, -\frac{1}{2}\right\rangle_S &= -\sqrt{\frac{2}{3}}\left|\frac{1}{2}, +\frac{1}{2}\right\rangle_{BS} |1, -1\rangle_A + \sqrt{\frac{1}{3}}\left|\frac{1}{2}, -\frac{1}{2}\right\rangle_{BS} |1, 0\rangle_A \\
\left|\frac{1}{2}, +\frac{1}{2}\right\rangle_S &= \sqrt{\frac{2}{3}}\left|\frac{1}{2}, -\frac{1}{2}\right\rangle_{BS} |1, +1\rangle_A - \sqrt{\frac{1}{3}}\left|\frac{1}{2}, +\frac{1}{2}\right\rangle_{BS} |1, 0\rangle_A
\end{aligned}
\tag{B.8}
$$

all with energy $E = -J_{AB} + \frac{1}{4}J_{AA} - \frac{3}{4}J_{BB}$.

There is a final group of 8 states consisting of product states with the singlet $|0, 0\rangle$,

but J_{AB} does not act on the singlet and no dressing is necessary:

$$
\begin{aligned}
\left|\frac{3}{2},-\frac{3}{2}\right\rangle_B |0,0\rangle_A &\quad E = \frac{3}{4}J_{BB} - \frac{3}{4}J_{AA} \\[4pt]
\left|\frac{3}{2},-\frac{1}{2}\right\rangle_B |0,0\rangle_A &\quad E = \frac{3}{4}J_{BB} - \frac{3}{4}J_{AA} \\[4pt]
\left|\frac{3}{2},+\frac{1}{2}\right\rangle_B |0,0\rangle_A &\quad E = \frac{3}{4}J_{BB} - \frac{3}{4}J_{AA} \\[4pt]
\left|\frac{3}{2},+\frac{3}{2}\right\rangle_B |0,0\rangle_A &\quad E = \frac{3}{4}J_{BB} - \frac{3}{4}J_{AA} \\[4pt]
\left|\frac{1}{2},-\frac{1}{2}\right\rangle_B |0,0\rangle_A &\quad E = -\frac{3}{4}J_{BB} - \frac{3}{4}J_{AA} \\[4pt]
\left|\frac{1}{2},+\frac{1}{2}\right\rangle_B |0,0\rangle_A &\quad E = -\frac{3}{4}J_{BB} - \frac{3}{4}J_{AA} \\[4pt]
\left|\frac{1}{2},-\frac{1}{2}\right\rangle_{BS} |0,0\rangle_A &\quad E = -\frac{3}{4}J_{BB} - \frac{3}{4}J_{AA} \\[4pt]
\left|\frac{1}{2},+\frac{1}{2}\right\rangle_{BS} |0,0\rangle_A &\quad E = -\frac{3}{4}J_{BB} - \frac{3}{4}J_{AA}
\end{aligned}
\tag{B.9}
$$

A more complicated molecule would require further rounds of dressing to build up the full complement of eigenstates describing the system. This quickly becomes tedious and is more easily accomplished computationally by simply diagonalizing the full spin Hamiltonian of the molecule.

The previous states were derived with no spin-locking applied. Spin-locking requires the states to be dressed with the RF Hamiltonian. Fortunately, the RF Hamiltonian only drives transitions Δm_F within each F subspace, so one only needs to consider how each subspace rearranges. Diagonalization reveals the following general

formulas to define new spin-locked states $|F', m_{F'}\rangle$. Spin-$\frac{5}{2}$:

$$
\begin{aligned}
\left|\frac{5}{2}, -\frac{5}{2}\right\rangle_{rot} &= -\frac{1}{4\sqrt{2}}\left|\frac{5}{2}, -\frac{5}{2}\right\rangle + \frac{\sqrt{5}}{4\sqrt{2}}\left|\frac{5}{2}, -\frac{3}{2}\right\rangle - \frac{\sqrt{10}}{4\sqrt{2}}\left|\frac{5}{2}, -\frac{1}{2}\right\rangle \\
&\quad + \frac{\sqrt{10}}{4\sqrt{2}}\left|\frac{5}{2}, +\frac{1}{2}\right\rangle - \frac{\sqrt{5}}{4\sqrt{2}}\left|\frac{5}{2}, +\frac{3}{2}\right\rangle + \frac{1}{4\sqrt{2}}\left|\frac{5}{2}, +\frac{5}{2}\right\rangle \\
\left|\frac{5}{2}, -\frac{3}{2}\right\rangle_{rot} &= \frac{5}{4\sqrt{2}}\left|\frac{5}{2}, -\frac{5}{2}\right\rangle - \frac{3}{4\sqrt{2}}\left|\frac{5}{2}, -\frac{3}{2}\right\rangle + \frac{\sqrt{10}}{4\sqrt{2}}\left|\frac{5}{2}, -\frac{1}{2}\right\rangle \\
&\quad + \frac{\sqrt{10}}{4\sqrt{2}}\left|\frac{5}{2}, +\frac{1}{2}\right\rangle - \frac{3}{4\sqrt{2}}\left|\frac{5}{2}, +\frac{3}{2}\right\rangle + \frac{5}{4\sqrt{2}}\left|\frac{5}{2}, +\frac{5}{2}\right\rangle \\
\left|\frac{5}{2}, -\frac{1}{2}\right\rangle_{rot} &= -\frac{\sqrt{10}}{4\sqrt{2}}\left|\frac{5}{2}, -\frac{5}{2}\right\rangle + \frac{\sqrt{2}}{4\sqrt{2}}\left|\frac{5}{2}, -\frac{3}{2}\right\rangle + \frac{2}{4\sqrt{2}}\left|\frac{5}{2}, -\frac{1}{2}\right\rangle \\
&\quad - \frac{2}{4\sqrt{2}}\left|\frac{5}{2}, +\frac{1}{2}\right\rangle - \frac{\sqrt{2}}{4\sqrt{2}}\left|\frac{5}{2}, +\frac{3}{2}\right\rangle + \frac{\sqrt{10}}{4\sqrt{2}}\left|\frac{5}{2}, +\frac{5}{2}\right\rangle \\
\left|\frac{5}{2}, +\frac{1}{2}\right\rangle_{rot} &= \frac{\sqrt{10}}{4\sqrt{2}}\left|\frac{5}{2}, -\frac{5}{2}\right\rangle + \frac{\sqrt{2}}{4\sqrt{2}}\left|\frac{5}{2}, -\frac{3}{2}\right\rangle - \frac{2}{4\sqrt{2}}\left|\frac{5}{2}, -\frac{1}{2}\right\rangle \\
&\quad - \frac{2}{4\sqrt{2}}\left|\frac{5}{2}, +\frac{1}{2}\right\rangle + \frac{\sqrt{2}}{4\sqrt{2}}\left|\frac{5}{2}, +\frac{3}{2}\right\rangle + \frac{\sqrt{10}}{4\sqrt{2}}\left|\frac{5}{2}, +\frac{5}{2}\right\rangle \\
\left|\frac{5}{2}, +\frac{3}{2}\right\rangle_{rot} &= -\frac{1}{4\sqrt{2}}\left|\frac{5}{2}, -\frac{5}{2}\right\rangle - \frac{\sqrt{5}}{4\sqrt{2}}\left|\frac{5}{2}, -\frac{3}{2}\right\rangle - \frac{\sqrt{10}}{4\sqrt{2}}\left|\frac{5}{2}, -\frac{1}{2}\right\rangle \\
&\quad + \frac{\sqrt{10}}{4\sqrt{2}}\left|\frac{5}{2}, +\frac{1}{2}\right\rangle + \frac{\sqrt{5}}{4\sqrt{2}}\left|\frac{5}{2}, +\frac{3}{2}\right\rangle + \frac{1}{4\sqrt{2}}\left|\frac{5}{2}, +\frac{5}{2}\right\rangle \\
\left|\frac{5}{2}, +\frac{5}{2}\right\rangle_{rot} &= \frac{1}{4\sqrt{2}}\left|\frac{5}{2}, -\frac{5}{2}\right\rangle + \frac{\sqrt{5}}{4\sqrt{2}}\left|\frac{5}{2}, -\frac{3}{2}\right\rangle + \frac{\sqrt{10}}{4\sqrt{2}}\left|\frac{5}{2}, -\frac{1}{2}\right\rangle \\
&\quad + \frac{\sqrt{10}}{4\sqrt{2}}\left|\frac{5}{2}, +\frac{1}{2}\right\rangle + \frac{\sqrt{5}}{4\sqrt{2}}\left|\frac{5}{2}, +\frac{3}{2}\right\rangle + \frac{1}{4\sqrt{2}}\left|\frac{5}{2}, +\frac{5}{2}\right\rangle,
\end{aligned}
\tag{B.10}
$$

Spin-$\frac{3}{2}$:

$$
\begin{aligned}
\left|\frac{3}{2}, -\frac{3}{2}\right\rangle_{rot} &= -\frac{1}{2\sqrt{2}}\left|\frac{3}{2}, -\frac{3}{2}\right\rangle + \frac{\sqrt{3}}{2\sqrt{2}}\left|\frac{3}{2}, -\frac{1}{2}\right\rangle - \frac{\sqrt{3}}{2\sqrt{2}}\left|\frac{3}{2}, +\frac{1}{2}\right\rangle + \frac{1}{2\sqrt{2}}\left|\frac{3}{2}, +\frac{3}{2}\right\rangle \\
\left|\frac{3}{2}, -\frac{1}{2}\right\rangle_{rot} &= \frac{\sqrt{3}}{2\sqrt{2}}\left|\frac{3}{2}, -\frac{3}{2}\right\rangle - \frac{1}{2\sqrt{2}}\left|\frac{3}{2}, -\frac{1}{2}\right\rangle - \frac{1}{2\sqrt{2}}\left|\frac{3}{2}, +\frac{1}{2}\right\rangle + \frac{\sqrt{3}}{2\sqrt{2}}\left|\frac{3}{2}, +\frac{3}{2}\right\rangle \\
\left|\frac{3}{2}, +\frac{1}{2}\right\rangle_{rot} &= -\frac{\sqrt{3}}{2\sqrt{2}}\left|\frac{3}{2}, -\frac{3}{2}\right\rangle - \frac{1}{2\sqrt{2}}\left|\frac{3}{2}, -\frac{1}{2}\right\rangle + \frac{1}{2\sqrt{2}}\left|\frac{3}{2}, +\frac{1}{2}\right\rangle + \frac{\sqrt{3}}{2\sqrt{2}}\left|\frac{3}{2}, +\frac{3}{2}\right\rangle \\
\left|\frac{3}{2}, +\frac{3}{2}\right\rangle_{rot} &= +\frac{1}{2\sqrt{2}}\left|\frac{3}{2}, -\frac{3}{2}\right\rangle + \frac{\sqrt{3}}{2\sqrt{2}}\left|\frac{3}{2}, -\frac{1}{2}\right\rangle + \frac{\sqrt{3}}{2\sqrt{2}}\left|\frac{3}{2}, +\frac{1}{2}\right\rangle + \frac{1}{2\sqrt{2}}\left|\frac{3}{2}, +\frac{3}{2}\right\rangle,
\end{aligned}
\tag{B.11}
$$

Spin-$\frac{1}{2}$:

$$\left| \frac{1}{2}, -\frac{1}{2} \right\rangle_{rot} = -\frac{1}{\sqrt{2}} \left| \frac{1}{2}, -\frac{1}{2} \right\rangle + \frac{1}{\sqrt{2}} \left| \frac{1}{2}, +\frac{1}{2} \right\rangle$$

$$\left| \frac{1}{2}, +\frac{1}{2} \right\rangle_{rot} = \frac{1}{\sqrt{2}} \left| \frac{1}{2}, -\frac{1}{2} \right\rangle + \frac{1}{\sqrt{2}} \left| \frac{1}{2}, +\frac{1}{2} \right\rangle,$$

(B.12)

The final step is to find which level crossings induce a polarization transfer. The interaction Hamiltonian takes the form $\nu_A \hat{I}_{z,A} + \nu_B \hat{I}_{z,B}$. Since this only involves $\hat{I}_z$ operators, for the interaction to be nonzero, the two dressed states it connects must share identical bare-spin product states. This limits the interactions to dressed states formed from the same group of product states (i.e., within the group B.4, B.5, B.6 or within the group B.7, B.8). Moreover, inspection shows that the two dressed states must be separated by $\Delta F = \pm 1$. The connected states must also share the same symmetry, otherwise the interaction terms will sum to zero. If we were working in the laboratory frame, we would find the condition $\Delta m_F = 0$, as in the case of the zero-field experiments. However, spin-locking produces symmetric and antisymmetric combinations of those states, which leads to the condition $\Delta m'_F = \pm 1$, where m'_F is the spin quantum number for the dressed state in the rotating frame.
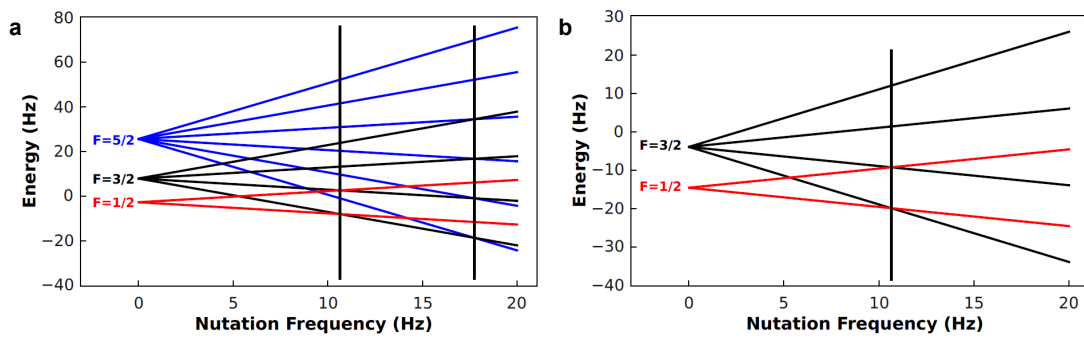
Figure B.1: Energy levels of ethanol spin states under spin-locking. (a) The group consisting of dressed states given by equations B.4, B.5, and B.6. (b) The group consisting of dressed states given by equations B.7 and B.8. The positions of the crossings at which polarization transfer occurs are indicated by vertical lines.

Appendix C

NV NMR Lineshape

In this appendix, a derivation is presented for the signal expected from an NV NMR measurement made with a dynamical decoupling sequence.

Throughout this document, we adopt the non-unitary Fourier transform in angular frequency units, such that the Fourier transform pair for $f(t)$ is defined as [163]

$$f(t) = \mathscr{F}^{-1}(f(\omega)) = \frac{1}{2\pi}\int_{-\infty}^{+\infty} f(\omega)e^{i\omega t}\mathrm{d}t \qquad f(\omega) = \mathscr{F}(f(t)) = \int_{-\infty}^{+\infty} f(t)e^{-i\omega t}\mathrm{d}t.$$
(C.1)

With the previous expression, Parseval's theorem reads as

$$\int_{-\infty}^{+\infty} f(t)g^*(t)\mathrm{d}t = \frac{1}{2\pi}\int_{-\infty}^{+\infty} f(\omega)g^*(\omega)\mathrm{d}\omega \rightarrow \int_{-\infty}^{+\infty} |f(t)|^2\mathrm{d}t = \frac{1}{2\pi}\int_{-\infty}^{+\infty} |f(\omega)|^2\mathrm{d}\omega,$$
(C.2)

and the expressions for the Dirac delta and convolution functions are

$$\delta(\omega - \omega') = \frac{1}{2\pi}\int_{-\infty}^{+\infty} e^{it(\omega - \omega')}\mathrm{d}t \qquad \mathscr{F}(f * g) = f(\omega)g(\omega).$$
(C.3)

C.1 Signal from a Dynamical Decoupling Sequence

As described in the main text, two spin-state-dependent fluoresence measurements $F_1(\tau)$ and $F_2(\tau)$ are acquired from independent dynamical decoupling experiments with π-pulses spaced by time τ. For $F_1(\tau)$, the final $\pi/2$-pulse projects the coherence into the $|\pm 1\rangle$ state, whereas for $F_2(\tau)$ the pulse phase is reversed to project the coherence into $|0\rangle$. This procedure removes common-mode noise from laser fluctuations. The fluorescence signals are described as a signal contrast, $C(\tau)$, of the form

$$C(\tau) = \frac{F_2(\tau) - F_1(\tau)}{F_2(\tau) + F_1(\tau)}. \tag{C.4}$$

The contrast is effectively measuring the projection of the coherence state after the sequence into its state at the beginning of the sequence. During the sequence, the coherence has accumulated some phase $\Delta\phi(\tau)$, thereby rotating out of its original state. The contrast is related to the accumulated phase by

$$C(\tau) = \langle \cos(\Delta\phi(\tau)) \rangle. \tag{C.5}$$

The brackets around $\cos(\Delta\phi(\tau))$ reflect that a typical fluorescence measurement is an average over many repeated dynamical decoupling experiments. If the accumulated phase $\Delta\phi(\tau)$ follows a normal distribution centered at the zero with variance $\langle \Delta\phi^2(\tau) \rangle$, then the average over the cosine can be converted to an exponential function of the variance using the relationship [ref]

$$\langle f(X) \rangle = \int_{-\infty}^{\infty} f(x)p(x)\mathrm{d}x, \tag{C.6}$$

where $p(x)$ is the probability distribution function for random variable X. Applying the integral of Eq. (C.6) to Eq. (C.5) produces

$$C(\tau) = \exp(-\langle \Delta\phi^2(\tau)\rangle/2). \tag{C.7}$$

Phase is accumulated during the dynamical decoupling sequence as the NV electron spins Larmor precess in the presence of a magnetic field signal $B_z(t)$, where z is the NV quantization axis. (The Larmor precession from the static background field B_0 is removed by working in the rotating reference frame). The sign of phase accumulation (i.e., positive or negative phase accumulation) is reversed by each π-pulse of the sequence, and can be represented over time as a function $g(t)$, as shown in Fig. 1a. The total phase accumulated at the end of the sequence is then

$$\Delta\phi(\tau) = \gamma_e \int_0^{N\tau} g(t)B_z(t)\mathrm{d}t, \tag{C.8}$$

where γ_e is the gyromagnetic ratio for the electron (in units of rad/s) and N is the number of π-pulses in the sequence. The accumulated phase variance can be expressed in terms of a correlation function between measurements across times t and t':

$$\langle \Delta\phi^2(\tau)\rangle = \gamma_e^2 \langle \int g(t)B_z(t)\mathrm{d}t \int g(t')B_z(t')\mathrm{d}t'\rangle, \tag{C.9}$$

For a function with temporal translational invariance, such as $B_z(t)B_z(t')$ (which depends only on the time difference $t - t'$), one can write: [164]

$$B_z(t)B_z(t') = \frac{1}{2\pi}\int B_z(\omega)B_z(-\omega)e^{i\omega(t-t')}\mathrm{d}\omega = \frac{1}{2\pi}\int |B_z(\omega)|^2\, e^{i\omega(t-t')}\mathrm{d}\omega. \tag{C.10}$$

The last passage follows from the fact that $B_z(t)$ contains Hermitian operators, so that the complex conjugate $B_z(\omega)^* = B_z(-\omega)$. In this way, spectral density $S_B(\omega)$ is

computed as

$$S_B(\omega) = \langle |B_z(\omega)|^2 \rangle = \int_0^{N\tau} \langle B_z(t)B_z(t') \rangle e^{-i\omega(t-t')} dt. \tag{C.11}$$

Similarly, one finds

$$|g(\omega)|^2 = \int_0^{N\tau} \langle g(t)g(t') \rangle e^{-i\omega(t-t')} dt. \tag{C.12}$$

Equation (C.9) then simplifies to

$$\langle \Delta\phi^2(\tau) \rangle = \frac{\gamma_e^2}{2\pi} \int_{-\infty}^{+\infty} S_B(\omega) \, |g(\omega, \tau, N)|^2 \, d\omega, \tag{C.13}$$

where $g(\omega, \tau, N)$ is the Fourier transform of $g(t)$ for the dynamical decoupling pulse sequence. $B_z(\omega)$ is the Fourier transform of the time-dependent magnetic signal along the NV axis z.

C.2 Application to Signals from Nuclear Spins

C.2.1 Correlation Functions

We consider magnetic signal $B_z(t)$ originating from nuclear spins in the vicinity of the NV center. As the nuclear spins Larmor precess about the applied static field, they produce periodic magnetic field fluctuations along z. For an ensemble of point dipoles, $B_z(t)$ at the NV center can be written as:

$$B_z(t) = \sum_j D_j \left[3u_x^j u_z^j S_x^j(t) + 3u_y^j u_z^j S_y^j(t) + (3u_z^j u_z^j - 1)S_z^j(t) \right], \tag{C.14}$$

where the NV is coupled to many nuclear spins j at positions given by a distance r_j and a unit vector u^j (which can be written in terms of of its coordinates u_x^j, u_y^j, u_z^j). The coupling factor is $D_j = (\mu_0 \hbar \gamma_n)/(4\pi r_j^3)$, where γ_n is the gyromagnetic ratio of

the nuclei and r_j is a distance between the NV center and nuclear spin j. Terms $S_{x,y,z}^j$

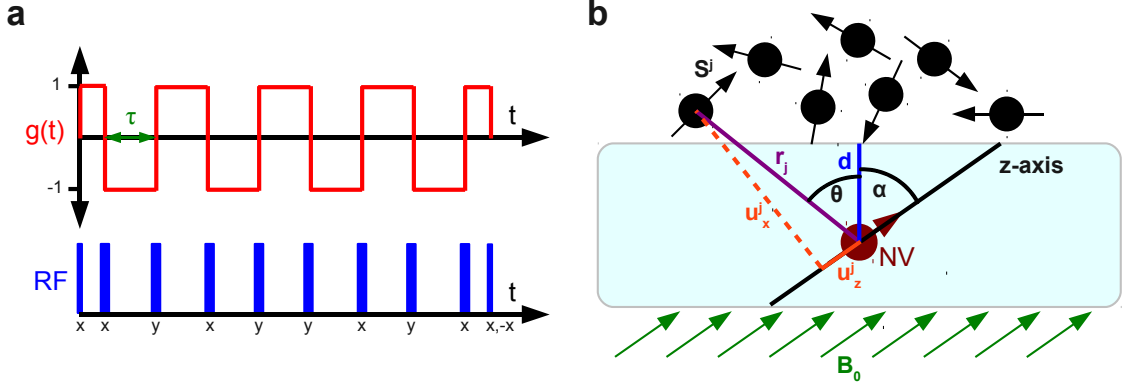represent the projection of nuclear spin j along the x, y, and z axes. Then the time

Figure C.1: (a) The dynamical decoupling sequence defines a function $g(t)$ describing the direction of spin precession in response to a magnetic signal $B_z(t)$. (b) An NV center with depth d sits below an ensemble of nuclei. Each nucleus has spin vector S^j and position u_x^j, u_y^j, u_z^j. The NV axis, and the axis for magnetic quantization, is at angle α with respect to the vector normal to the diamond surface. For purposes of integration across the sample, the spherical coordinates r, θ, ϕ are used.

correlator is expressed using Eq. (C.14) to obtain

$$\langle B_z(t)B_z(t')\rangle = \sum_j D_j(r_j) \left[3u_x^j u_z^j S_x^j(t) + 3u_y^j u_z^j S_y^j(t) + (3u_z^j u_z^j - 1)S_z^j(t)\right]$$

$$\sum_i D_i(r_i) \left[3u_x^i u_z^i S_x^i(t') + 3u_y^i u_z^i S_y^i(t') + (3u_z^j u_z^j - 1)S_z^i(t')\right]. \quad \text{(C.15)}$$

For an ensemble of nuclear spins that do not interact with each other, correlators can

be defined for each spin's projection along each of its axes:

$$\langle S_\alpha^j(t)S_\beta^i(t')\rangle = \delta_{\alpha,\beta}\delta^{i,j}f^{\alpha,\beta}(S,T,t-t'). \quad \text{(C.16)}$$

Note that the correlator is a function of the nuclear spin's total spin quantum number

S as well as the temperature T. In the simple case in which the external magnetic

field for the nuclei is applied along the NV axis one can write $f^{x,x} = f^{y,y}$, i.e., behavior

in the transverse plane is independent of phase. Moreover, all nuclear spins of the same species have the same correlator, and so the index j is dropped for $f^{\alpha,\beta}$. Then

$$\langle B_z(t)B_z(t')\rangle = \sum_j D_j^2(r_j)\left[9f^{x,x}\left((u_x^j u_z^j)^2 + (u_y^j u_z^j)^2\right) + f^{z,z}\left(3u_z^j u_z^j - 1\right)^2\right]. \quad (C.17)$$

Assuming that the energy of the state $|m_z\rangle$ is $\hbar\omega_{m_z}m_z$, the transverse $f^{x,x}$, $f^{y,y}$ and longitudinal $f^{z,z}$ spin-spin correlation functions have their natural expression in frequency-space with the definition in Eq. (C.1). The relevant spin projections S_α for each nucleus are found using their respective operators:

$$S_\alpha = \langle m_z|\hat{S}_\alpha|n_z\rangle \quad (C.18)$$

Then in the spectral representation

$$f^{\alpha,\alpha}(S,T,\omega) = \mathscr{F}(f^{\alpha,\alpha}(t)) = \int \langle S_\alpha(t)S_\alpha(0)\rangle e^{-i\omega t}\mathrm{d}t$$

$$= \frac{2\pi}{Z}\sum_{n,m}e^{-\frac{E_n}{k_B T}}|\langle m_z|\hat{S}_\alpha|n_z\rangle|^2\delta\left(\frac{E_m - E_n}{\hbar} - \omega\right), \quad (C.19)$$

where Z is the partition function. In the high temperature limit where $E_n \ll k_B T$, the eigenstates are equally populated, and

$$f^{\alpha,\alpha}(S,\omega) = \frac{2\pi}{\mathrm{tr}(\mathrm{I})}\sum_{n,m}\left|\langle m_z|\hat{S}_\alpha|n_z\rangle\right|^2\delta\left(\frac{E_m - E_n}{\hbar} - \omega\right). \quad (C.20)$$

We now make use of the definitions for the z and x spin projections:

$$S_z = \langle n_z|\hat{S}_z|m_z\rangle = m_z\langle n_z|m_z\rangle$$

$$S_x = \langle n_z|\frac{\hat{S}^+ + \hat{S}^-}{2}|m_z\rangle, \quad (C.21)$$

where

$$\hat{S}^\pm|S,m_z\rangle = \sqrt{S(S+1) - m_z(m_z \pm 1)}|S, m_z \pm 1\rangle. \quad (C.22)$$

Then the longitudinal correlator is

$$f^{z,z}(S,\omega) = \frac{2\pi}{\text{tr(I)}} \hat{\sum}_z |\langle m_z|S_z|m_z\rangle|^2 \delta(\omega). \tag{C.23}$$

The correlator (C.23) can be computed by noting that a Curie-Weiss prefactor appears due to the relation $\sum_z m_z^2/\text{tr(I)} = S(S+1)/3$. Because the diagonal correlator is centered at zero energy, it will not contribute to the final integral (C.13) as long as $g(\omega = 0, \tau, N) = 0$ (i.e., the dynamical decoupling pulse sequence is not sensitive to DC fields). The transverse correlator is

$$f^{x,x}(S,\omega) = \frac{2\pi}{\text{tr(I)}} \sum_{n,m} \left|\langle m_z|\hat{S}_x|n_z\rangle\right|^2 \delta\left(\frac{E_m - E_n}{\hbar} - \omega\right), \tag{C.24}$$

which is non-zero only when m_z, n_z are adjacent energy levels. For the case of spin-1/2 nuclei $(S = 1/2)$, where the nuclear spins precess at Larmor frequency $\omega_L = \gamma_n B_0$, we evaluate (C.24) as:

$$f^{x,x}(S = 1/2, \omega) = \frac{2\pi}{8} \left(\delta(\omega - \omega_L) + \delta(\omega + \omega_L)\right) \tag{C.25}$$

The two contributions in (C.25) represent the Stokes and anti-Stokes lines, equal in the limit $T \to \infty$ due to the fluctuation-dissipation theorem.

The expression for magnetic field correlation is now

$$\langle B_z(t)B_z(t')\rangle = 9f^{x,x} \sum_j D_j^2(r_j) \left[(u_x^j u_z^j)^2 + (u_y^j u_z^j)^2\right], \tag{C.26}$$

for which we have calculated $f^{x,x}$. By writing $1 - (u_z^j)^2 = (u_x^j)^2 + (u_y^j)^2$, the geometry-dependent terms can be collected into one factor

$$\Gamma = \sum_j D_j^2(r_j)(u_z^j)^2 \left(1 - (u_z^j)^2\right), \tag{C.27}$$

which we evaluate in the following section.

C.2.2 Calculation of the Geometrical Factor

The geometrical factor (or "form factor", in a spectroscopic notation) can be computed according to the user's needs. While Eq. (C.26) can be calculated directly from a random sample of nuclear locations, it is more convenient to assume a sample of nuclear density ρ continuously distributed on the surface. This is a particularly good assumption for liquid samples in which nuclear locations vary on a time scale short compared with the dynamical decoupling sequence length. Then the summation of Eq. (C.27) can be converted to the integral

$$\Gamma = \rho \int dV \left[\left(\frac{\mu_0 \hbar \gamma_n}{4\pi} \right)^2 \frac{(u_z^j)^2 (1 - (u_z^j)^2)}{r^6} \right]$$
$$= \rho \left(\frac{\mu_0 \hbar \gamma_n}{4\pi} \right)^2 \tilde{\Gamma}. \tag{C.28}$$

Spherical coordinates are used with the conventions of Fig. 1b. The polar angle origin $\theta = 0$ is defined to be orthogonal to the surface of the diamond, while ϕ is the azimuthal angle with arbitrary origin. The NV axis $\mathbf{z}$ points along a direction $\mathbf{z} = [\sin(\alpha)\cos(\beta), \sin(\alpha)\sin(\beta), \cos(\alpha)]$. The projection u_z needed for Eq. (C.28) will in general depend on all four angles just introduced. In particular, $u_z = \mathbf{z} \cdot \mathbf{u}_r$, where $\mathbf{u}_r = [\sin(\theta)\cos(\phi), \sin(\theta)\sin(\phi), \cos(\theta)]$.

The integral for $\tilde{\Gamma}$ is then

$$\tilde{\Gamma} = \int_0^{2\pi} \int_0^{\pi/2} \int_{d_{NV}/\cos(\theta)}^{\infty} \frac{(u_z)^2 (1 - (u_z)^2)}{r^4} \sin(\theta) dr d\theta d\phi, \tag{C.29}$$

where d_{NV} is the NV depth below the diamond surface. The sample height is assumed to be semi-infinite, thereby allowing integration of the radial component from the diamond surface to infinity. Other sample geometries can be accomodated with the

proper integral limits and choice of coordinate system (i.e., spherical, cylindrical, etc.). Evaluating the integral produces a simple expression for $\Gamma(d_{NV})$:

$$\Gamma(d_{NV}) = \rho \left(\frac{\mu_0 \hbar \gamma_n}{4\pi} \right)^2 \left(\frac{\pi \left[8 - 3\sin^4(\alpha) \right]}{288 d_{NV}^3} \right). \qquad \text{(C.30)}$$

The expression is maximal when $\alpha = 0$, where $\tilde{\Gamma}(d_{NV}) = \pi/(36 d_{NV}^3)$ However, in most samples the NV axis is aligned along [100] direction, so that $\alpha = 54.7°$. At this angle, $\tilde{\Gamma}(d_{NV}) = 5\pi/(216 d_{NV}^3)$. With the correlation functions and geometric factors now evaluated, the spectral density can be written as

$$S_B(\omega) = \langle |B_z(S = 1/2, \omega)|^2 \rangle = \Gamma(d_{NV}) \frac{9\pi}{4} \left(\delta(\omega - \omega_L) + \delta(\omega + \omega_L) \right). \qquad \text{(C.31)}$$

The spectral density can be related to the magnetic field variance by

$$S_B(\omega) = \pi B_{RMS}^2 \left(\delta(\omega - \omega_L) + \delta(\omega + \omega_L) \right), \qquad \text{(C.32)}$$

where

$$B_{RMS}^2 = \frac{9}{4} \Gamma(d_{NV}) = \rho \left(\frac{\mu_0 \hbar \gamma_n}{4\pi} \right)^2 \left(\frac{\pi \left[8 - 3\sin^4(\alpha) \right]}{128 d_{NV}^3} \right). \qquad \text{(C.33)}$$

For NV centers oriented at $\alpha = 54.7°$ this simplifies to

$$B_{RMS}^2 = \rho \left(\frac{\mu_0 \hbar \gamma_n}{4\pi} \right)^2 \left(\frac{5\pi}{96 d_{NV}^3} \right). \qquad \text{(C.34)}$$

C.2.3   The Filter Function $|g(\omega, \tau)|^2$

To complete Eq. (C.13), the filter function $|g(\omega, \tau)|^2$ must be evaluated for the dynamical decoupling sequence. For a CPMG or XY8 sequence with N π pulses, such as that in Fig. 1a, the Fourier transform is

$$g(\omega, \tau, N) = \frac{2}{\pi} \sum_{k=-\infty}^{+\infty} \frac{N\tau(-1)^k}{2k+1} \mathrm{sinc} \left[\frac{N\tau}{2} \left(\omega - \frac{(2k+1)\pi}{\tau} \right) \right] e^{-i\frac{N\tau}{2} \left(\omega - \frac{(2k+1)\pi}{\tau} \right)}. \qquad \text{(C.35)}$$

For most purposed, only the first-order terms need to be retained. The expansion must include $k = 0, -1$ to be symmetric around $\pm\omega$. However, the integral over positive and negative frequencies will be equivalent to twice the integral over positive frequencies as long as $k_{\mathrm{B}}T \gg \hbar\omega_L$. Note that some other models use a different definition of the filter function, $F(\omega)$, in which

$$F(\omega t) = \frac{\omega^2}{2}|g(\omega, \tau)|^2 \tag{C.36}$$

If the nuclear spin dephasing time is assumed to be infinite, such that the nuclear spin signal can be described by delta functions, we can now obtain a final formula for the contrast in the $S = 1/2$ case:

$$C(\tau) = \exp\left(-\frac{2}{\pi^2}\gamma_e^2 B_{RMS}^2 (N\tau)^2 \left[\mathrm{sinc}^2\left[\frac{N}{2}(\omega_L\tau - \pi)\right] + \mathrm{sinc}^2\left[\frac{N}{2}(\omega_L\tau + \pi)\right]\right.\right.$$
$$\left.\left.+ \mathrm{sinc}\left[\frac{N}{2}(\omega_L\tau - \pi)\right]\mathrm{sinc}\left[\frac{N}{2}(\omega_L\tau + \pi)\right]\right]\right). \tag{C.37}$$

The off-resonant terms contribute very weakly to the lineshape and can be ignored, resulting in an approximate formula:

$$C(\tau) \approx \exp\left[-\frac{2}{\pi^2}\gamma_e^2 B_{RMS}^2 (N\tau)^2 \mathrm{sinc}^2\left(\frac{N\tau}{2}\left(\omega_L - \frac{\pi}{\tau}\right)\right)\right]. \tag{C.38}$$

C.3 Nuclear dephasing time

In the previous section, we assumed that the nuclear spin signal could be represented by a delta function, meaning that it has a coherence time much longer than the length of the dynamical decoupling sequence. However, the effective nuclear spin

linewidth is broadened due to both dephasing from spin-spin interactions and diffusion through the NV interaction volume. In order to take these effects into account, we substitute the delta functions of Eq. (C.25) with normalized Lorentzian functions such that:

$$f^{x,x}(S = 1/2, \omega) = \frac{2\pi}{8} \left(\frac{1}{\pi} \frac{T_2^{*-1}}{(\omega - \omega_L)^2 + (T_2^{*-1})^2} + \frac{1}{\pi} \frac{T_2^{*-1}}{(\omega + \omega_L)^2 + (T_2^{*-1})^2} \right), \quad \text{(C.39)}$$

where T_2^* is the effective dephasing time of the nuclei. As before, we need to compute:

$$C(\tau) = \exp\left(-\frac{\langle \Delta\phi^2(\tau) \rangle}{2} \right) = \exp\left(-\frac{1}{\pi}\gamma_e^2 B_{RMS}^2 \int_\omega f^{x,x}(S, \omega) \, |g(\omega, \tau, N)|^2 \, \mathrm{d}\omega \right),$$

$$\text{(C.40)}$$

Once again, symmetry allows us to simplify the experession using only the positive-frequency component if we multiply the expression by two, leading to

$$C(\tau) = \exp\left(-\frac{2}{\pi^2}\gamma_e^2 B_{RMS}^2 \int_\omega \frac{1}{\pi} \frac{T_2^{*-1}}{(\omega - \omega_L)^2 + (T_2^{*-1})^2} (N\tau)^2 \mathrm{sinc}^2\left[\frac{N\tau}{2} \left(\omega - \frac{\pi}{\tau} \right) \right] \mathrm{d}\omega \right).$$

$$\text{(C.41)}$$

It is evident that the integral is a convolution between a Lorentzian $l(\omega)$ and a function $\psi(\omega) \sim \mathrm{sinc}^2(u)$. Using the convolution theorem, the integral can be solved by multiplying the respective Fourier transforms and then taking the inverse Fourier transform of the result. The Lorentzian component is

$$l(\omega) = \frac{1}{\pi} \frac{T_2^{*-1}}{(\omega - \omega_L)^2 + (T_2^{*-1})^2}. \quad \text{(C.42)}$$

Its Fourier transform is

$$L(t) = \left(e^{-tT_2^{*-1} - it\omega_L} H(t) + e^{tT_2^{*-1} - it\omega_L} H(-t) \right), \quad \text{(C.43)}$$

where $H(t)$ is the Heaviside step function. The $\mathrm{sinc}^2(u)$ component is

$$\psi(\omega) = (N\tau)^2 \mathrm{sinc}^2\left[\frac{N\tau}{2} (\omega) \right]. \quad \text{(C.44)}$$

171

Notice that the frequency offset π/τ has been removed to simplify the Fourier transform. The Fourier transform is

$$\Psi(t) = \pi \left((t - N\tau) \operatorname{sgn}(t - N\tau) - 2t \operatorname{sgn}(t) + (t + N\tau) \operatorname{sgn}(t + N\tau) \right). \quad \text{(C.45)}$$

Taking the inverse Fourier transform $I(\omega) = \mathcal{F}^{-1}(L(t)\Psi(t))$, and using the identity $\omega = \pi/\tau$ for the filter function resonance condition, gives the expression

$$
I(\tau) = \frac{2T_2^{*2}}{\left[1 + T_2^{*2}\left(\omega_L - \frac{\pi}{\tau}\right)^2\right]^2} \left\{ e^{-\frac{N\tau}{T_2^*}} \left[\left[1 - T_2^{*2}\left(\omega_L - \frac{\pi}{\tau}\right)^2\right] \cos\left[N\tau\left(\omega_L - \frac{\pi}{\tau}\right)\right] \right. \right.
$$
$$
- 2T_2^*\left(\omega_L - \frac{\pi}{\tau}\right) \sin\left[N\tau\left(\omega_L - \frac{\pi}{\tau}\right)\right] \Big]
$$
$$
\left. + \frac{N\tau}{T_2^*}\left[1 + T_2^{*2}\left(\omega_L - \frac{\pi}{\tau}\right)^2\right] + T_2^{*2}\left(\omega_L - \frac{\pi}{\tau}\right)^2 - 1 \right\}. \quad \text{(C.46)}
$$

The final expression for contrast including nuclear spin dephasing is

$$C(\tau) \approx \exp\left(-\frac{2}{\pi^2}\gamma_e^2 B_{RMS}^2 I(\tau)\right) \qquad \text{(C.47)}$$

Once again, for comparison with other models using $F(\omega)$ as the filter function, the relationship is

$$F(\omega t) = \frac{2\omega^2}{\pi^2} I(\tau). \qquad \text{(C.48)}$$

Ultimately, an experimental determination of a T_2 dominated or of a T_2 non-dominated regime can be carried out by checking scaling of the dip amplitude and width as a function of N and τ. Figure 4 shows what the dip looks like for three values of nuclear T_2.

C.4 Pseudospin Derivation

An alternative derivation can be obtained using the pseudospin formalism. The contrast is a product of the pseudo-spin signal $\mathcal{S}^j$ from each nuclear spin j:

$$C(\tau) = \prod_j \mathcal{S}^j. \tag{C.49}$$

For a CPMG sequence (or XY8) with N pulses, the pseudo-spin signal for nuclear spin j is

$$\mathcal{S}^j = 1 - 2\vec{\omega}_0^j \times \vec{\omega}_1^j \sin^2\left(\frac{\Omega_0^j \tau}{4}\right) \sin^2\left(\frac{\Omega_1^j \tau}{4}\right) \frac{\sin^2(N\alpha^j/2)}{\cos^2(\alpha^j/2)}, \tag{C.50}$$

where

$$\cos(\alpha^j) = \cos\left(\frac{\Omega_0^j \tau}{2}\right)\cos\left(\frac{\Omega_1^j \tau}{2}\right) - \vec{\omega}_0^j \cdot \vec{\omega}_1^j \sin\left(\frac{\Omega_0^j \tau}{2}\right)\sin\left(\frac{\Omega_1^j \tau}{2}\right) \tag{C.51}$$

is the effective rotation angle during one cycle. Here the vectors $\vec{\omega}_i^j = \Omega_i^j \vec{\omega}_i^j$ represent the nuclear spin Hamiltonians in the two subspaces of the NV electronic spin, i.e., i takes the value of the NV center spin state -1, 0, or 1. In the case of spin-1/2, we have $\vec{\omega}_0^j = \omega_L^j \hat{z}$, where ω_L is the nuclear spin Larmor frequency. On the other hand, $\vec{\omega}_1^j = \omega_L^j \hat{z} + \vec{A}_z^j$, where $\vec{A}_z^j$ is the dipolar coupling component along the NV z axis. Then the dip in the signal, $\mathcal{D}^j = 1 - \mathcal{S}^j$, can be related to contrast by

$$C(\tau) = \prod_j \mathcal{S}^j = \prod_j [1 - \mathcal{D}^j]$$
$$= \prod_j \left[1 - 2(\vec{\omega}_0^j \times \vec{\omega}_1^j)\sin^2\left(\frac{\Omega_0^j \tau}{4}\right)\sin^2\left(\frac{\Omega_1^j \tau}{4}\right)\frac{\sin^2(N\alpha^j/2)}{\cos^2(\alpha^j/2)}\right]. \tag{C.52}$$

The expression can be further simplified in the limit $\omega_L \gg |A_z^j|$, where $\vec{A}_z^j = A_z^j[\cos\varphi\sin\vartheta, \sin\varphi\sin\vartheta, \cos\vartheta]$. Then, to second order in A_z^j, the signal is given

by

$$\mathcal{S}^j \approx 1 - \frac{2(A_z^j)^2 \sin^2(\vartheta)}{\omega_L^2} \frac{\sin^4(\omega_L \tau/4) \sin^2(N\omega_L \tau/2)}{\cos^2(\omega_L \tau/2)}. \tag{C.53}$$

For simplicity in the following steps, we define $\kappa_j = A_z^j \sin(\vartheta^j) = (A_{zx}^j)^2 + (A_{zy}^j)^2$. We can also show that

$$|g(\omega_L, \tau)|^2 = \frac{16}{\omega_L^2} \frac{\sin^4(\omega_L \tau/4) \sin^2(N\omega_L \tau/2)}{\cos^2(\omega_L \tau/2)}. \tag{C.54}$$

Then the signal from an ensemble of nuclear spins precessing at Larmor frequency ω_L is

$$C(\tau) = \prod_j \left(1 - \tfrac{1}{8}|g(\omega_L, \tau)|^2 \kappa_j^2\right) \tag{C.55}$$

This product can be reconciled with the exponential form of the previous section in the following manner. First a variance of the effective field is defined as

$$\langle \kappa^2 \rangle = \frac{1}{n} \sum_{j=1}^{n} \kappa_j^2. \tag{C.56}$$

The variance is just an average of the individual κ_j^2 values. If the number of spins n is large, one can assume that each spin acts like an average spin, and κ_j^2 can be replaced with $\langle \kappa^2 \rangle$. Then the product simplifies to

$$C(\tau) = \prod_j \left(1 - \tfrac{1}{8}|g(\omega_L, \tau)|^2 \kappa_j^2\right) \Rightarrow \left(1 - \tfrac{1}{8}|g(\omega_L, \tau)|^2 \langle \kappa^2 \rangle\right)^n. \tag{C.57}$$

Substitution with Eq. (C.56) yields

$$C(\tau) = \left(1 - \frac{1}{8}|g(\omega_L, \tau)|^2 \frac{1}{n} \sum_j \kappa_j^2\right)^n. \tag{C.58}$$

Note that for large n this is the definition of the exponential! Then

$$C(\tau) = \lim_{n \to \infty} \left(1 - \frac{1}{8}|g(\omega_L, \tau)|^2 \frac{1}{n} \sum_j \kappa_j^2\right)^n = \exp\left(-\frac{1}{8}|g(\omega_L, \tau)|^2 \sum_j \kappa_j^2\right). \tag{C.59}$$

The term $\sum_j \kappa_j^2$ can converted into an integral of the form $\int \rho(\vec{r})\kappa^2(\vec{r})\mathrm{d}^3 r$ and integrated over the sample. Since A_z represents the frequency shift from dipolar coupling, one can show from the definition of κ that

$$\sum_j \kappa_j^2 = 9\gamma_e^2 \sum_j D_j^2(r_j)(u_z^j)^2 \left(1 - (u_z^j)^2\right) = 4\gamma_e^2 B_{RMS}^2. \tag{C.60}$$

This along with the approximated expression of the filter function finally allows Eq. (C.59) to be written as

$$
\begin{aligned}
C(\tau) &\approx \exp\left(-\frac{1}{2}\gamma_e^2 |g(\omega_L, \tau)|^2 B_{RMS}^2\right) \\
&= \exp\left(-\frac{2}{\pi^2}\gamma_e^2 (N\tau)^2 \mathrm{sinc}^2\left(\frac{N\tau}{2}\left(\omega_L - \frac{\pi}{\tau}\right)\right) B_{RMS}^2\right).
\end{aligned} \tag{C.61}
$$

The expression for contrast exactly matches that derived in Eq. (C.38).

Appendix D

Effects of Diffusion in NV NMR

The NV NMR protocol detects a nuclear spin signal via the dipole-dipole interaction, which makes it extremely sensitive to changes in nuclear spin position. As a consequence of the strong distance dependence of dipolar coupling, nuclei diffusing in a liquid move in and out of the sensing volume very quickly, which limits the interaction time between the NV and nucleus. As a result, the linewidth of the nuclear spin signal is broadened. This is in contrast to conventional NMR detection via an inductive coil surrounding the sample, in which the nuclei can be fully contained within the sensing volume and changes in nuclear position have little effect on the signal. In the model describing the NV NMR signal (appendix C), we approximated the line broadening effect by assuming the nuclear spin fluctuations were described by a Lorentzian function with a broadening defined by the T_2^* parameter. In this appendix, we use Monte Carlo simulations to more thoroughly model the effect of molecular diffusion on the NV NMR signal. We show that for a semi-infinite sample (stretching from the surface to a distance well beyond the sensing volume), the

176

linewidth can be satisfactorily described by a simple equation defining the correlation time for diffusing particles. We also find that the spectral density of the nuclear spin fluctuations is not described by either a Lorentzian or Gaussian distribution. Finally, we show that the linewidth can be significantly narrowed by confining the sample to a thin layer.

D.1 Estimated Linewidth Calculated from Correlation Time

Translational diffusion limits the amount of time a nucleus interacts with the NV center. Typically, one assumes that the interaction lasts for a characteristic correlation time, τ_d, and that the probability finding the particles interacting drops off exponentially in time. By taking the Fourier transform, one finds that this behavior produces a Lorentzian lineshape $L(\tau, \omega)$ typically written as

$$L(\tau, \omega) = \frac{1}{\pi} \frac{\tau_d}{1 + \omega^2 \tau_d^2}. \tag{D.1}$$

This can also be written in a standard Lorentzian form

$$L(\tau, \omega) = \frac{1}{\pi} \frac{1/\tau_d}{\omega^2 + 1/\tau_d^2}. \tag{D.2}$$

The full width at half maximum (FWHM) is then $2/\tau_d$.

The translational diffusion correlation time for two spins in three dimensions can be related to molecular geometries and diffusion coefficients by [96, 165]

$$\tau_d = \frac{d^2}{D_{av}}, \tag{D.3}$$

177

where d is the distance of closest approach between two spins and D_{av} is the average of the diffusion coefficients for the two spins. Since the NV center is immobile, we can assume that its diffusion coefficient is zero. The distance of closest approach is the NV depth, d_{NV}. Then the correlation time becomes

$$\tau_d = \frac{2d_{NV}^2}{D_{nuc}}, \tag{D.4}$$

where D_{nuc} is the diffusion coefficient of the nuclei.

We will consider two substances of interest, water and immersion oil. The diffusion coefficient of water at room temperature is 2.3×10^{-9} m^2/s [166]. The diffusion coefficient of the immersion oil used in our experiments is unknown, but it can be approximated from the known viscosity of 450 cSt [167]. Low-fluorescent immersion oil is typically composed of liquid polybutadiene mixed with smaller amounts of paraffins and carboxylic acid esters [168]. In one example of an immersion oil with kinematic viscosity $\nu = 450$ cSt [168], the polybutadiene component has an average molecular weight of 1600 g/mol. The hydrodynamic radius of the molecule is on the order of $r \sim 1$ nm [169], and the density is $\rho \sim 0.9$ g/mL. The dynamic viscosity is then

$$\eta = \rho\nu = 0.405 \text{ cP}. \tag{D.5}$$

Using the Stokes-Einstein relationship

$$D = \frac{k_B T}{6\pi\eta r} \tag{D.6}$$

gives a diffusion coefficient $D_{oil} \approx 5 \times 10^{-13}$ m^2/s.

Figure D.1a plots the estimated linewidth for water and immersion oil as a function of NV center depth calculated using equation D.4, while Fig. D.1b plots the estimated
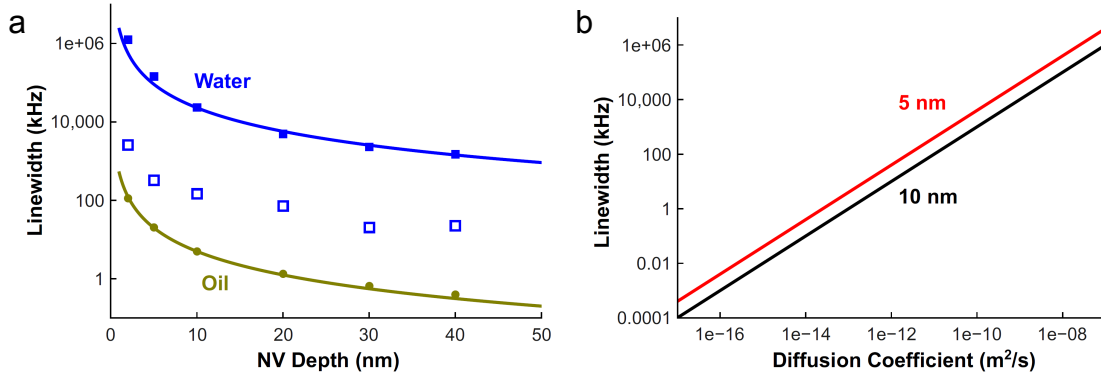
Figure D.1: Estimate of nuclear spin spectral density linewidth for NV NMR experiment. (a) Linewidth as a function of NV depth for water and immersion oil. Solid lines are calculations based on the correlation time defined by equation D.4. Solid symbols are values calculated from the Monte Carlo simulation described in section D.2. Open symbols are values for the water linewidth when the water layer is confined to 1 nm height above the diamond surface, calculated with a Monte Carlo simulation. (b) Linewidth as a function of diffusion coefficient for NV centers 5 and 10 nm deep, calculated with equation D.4.

linewidth versus diffusion coefficient for 10 nm and 5 nm deep NV centers. The estimated nuclear spin linewidths for a 10 nm deep NV center are 23 MHz for water and 5 kHz for immersion oil.

D.2   Monte Carlo Simulations

To better-characterize the lineshape of the nuclear spin signal, we modeled diffusion of oil and water molecules with a Monte Carlo simulation. We chose a diffusion simulation based on a lattice model in which the molecule moves along each axis (x, y, z) either backward or forward one lattice site with a 50% probability at each step [170]. This is more convenient than a continuous-space model for dealing with the boundary condition defined by the diamond surface. For a step in which the

nucleus would move to a lattice site inside the diamond, the nucleus instead remains in place. The lattice step size, dl, is related to the diffusion coefficient D and the time step dt by $dl = \sqrt{2Ddt}$. At each time step, a coupling factor with the NV is calculated. We ignore the dipole-dipole coupling prefactors as they do not matter for the final result. The coupling factor is

$$c = \frac{u_z^2(1 - u_z^2)}{r^6}, \tag{D.7}$$

where r is the distance between the NV center and the nucleus, and u_z contains the angular terms in spherical coordinates for the vector connecting the NV center and the molecule:

$$u_z = \cos(\alpha)\cos(\theta) + \sin(\alpha)\sin(\theta)\cos(\phi). \tag{D.8}$$

Here α is the angle of the NV axis, 54.7°, θ is the polar angle, and ϕ is the azimuthal angle.

The simulation records a trajectory of x, y, z, and c values. We are most interested in c, as this represents the envelope of the sinusoidal Larmor precession signal that the NV measures. Fourier transformation of c subsequently gives the lineshape of the nuclear spin spectral density.

We first verified that the algorithm properly simulates diffusion. Figure D.2a plots the probability of finding the molecule at locations x, y, and z after 40 microseconds for an immersion oil molecule whose origin (which we define as coordinates (0,0,0)) is on the diamond surface directly above the NV center. The results were collected from 5000 simulation runs. Figure D.2b shows a Gaussian curve fit to the probability density for the x-axis. From the standard deviation of the fit, we find a diffusion co-efficient $D = 5.00009 \times 10^{-13}$ m^2/s, in excellent agreement with the assigned diffusion
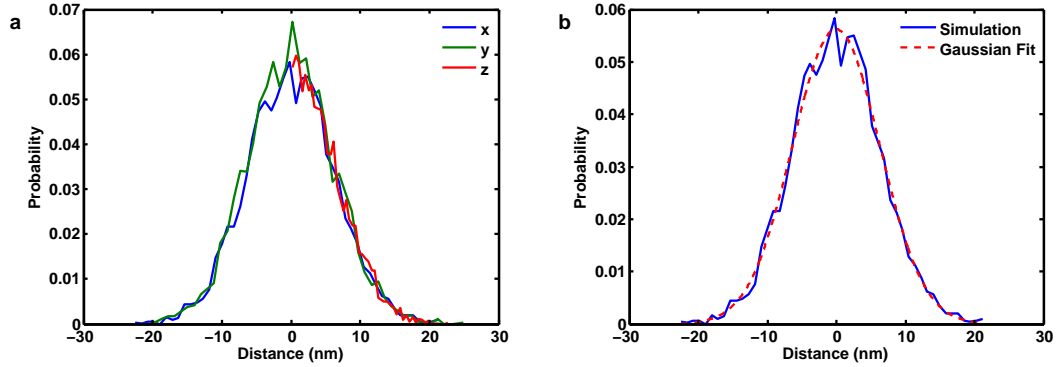
Figure D.2: Confirmation of diffusion model. (a) Probability of finding the oil nucleus at a given distance after 40 microseconds of diffusion. (b) A Gaussian fit of the probability function along the x-axis agrees with the diffusion coefficient of oil.

coefficient for immersion oil.

We next calculated the coupling factor as a function of time using simulation lengths appropriate for the diffusion coefficient of each substance and the NV depth, making sure that the average coupling coefficient was near zero by the end of the simulation. For immersion oil, timecourses ranged between 4 and 16 ms, while for water, timecourses ranged between 160 and 800 μs. An average timecourse was calculated from 1000 simulation runs and Fourier transformed to produce a plot of coupling factor versus frequency. The full-width at half maximum value was then extracted numerically.

Results for immersion oil above a 10 nm deep NV center are shown in Fig. D.3. For the time domain, results are shown for both a single run and the average of 1000 runs. Coupling decreases to nearly zero within the first 100 μs as the nucleus diffuses away from the NV center, although within a single run the nucleus often moves back into the sensing volume. In the frequency domain, the lineshape is clearly not
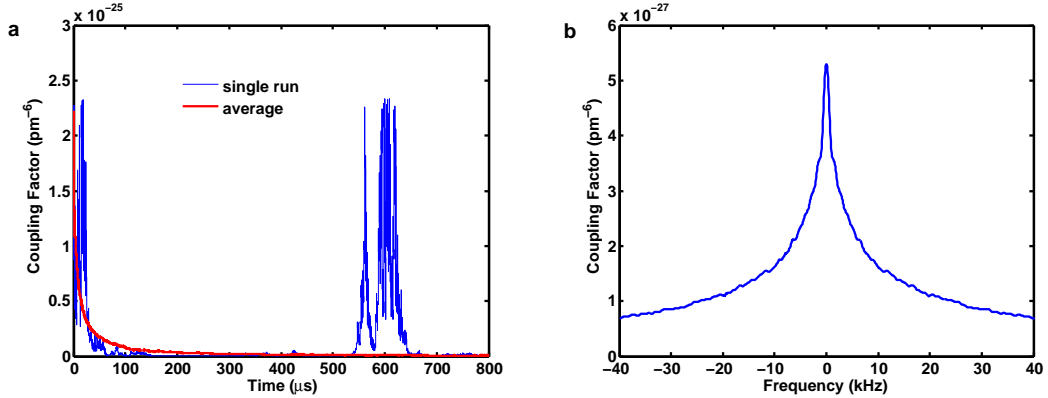
Figure D.3: Simulation of an oil molecule above a 10 nm deep NV center. (a) Coupling factor as a function of time for a single run (blue) and an average of 1000 runs (red). (b) Fourier transform of the average timecourse for the coupling factor. The FWHM linewidth is 5.01 kHz.

Lorentzian nor Gaussian, but rather exhibits a sharply-peaked shape. This is likely a consequence of the $1/r^6$ distance dependence of the coupling factor. Nevertheless, the FWHM linewidth of 5.01 kHz matches very well with the calculation based on correlation time (Eq. D.4).

Figure D.4 plots the results for the coupling factor between water and a 10 nm deep NV center. The results are qualitatively very similar to those of immersion oil, but the larger diffusion coefficient leads to a faster dropoff in coupling strength and a broader linewidth. Again the FWHM linewidth value of 23.5 MHz matches well with calculations based on the correlation time (Eq. D.4).

We plot the results from simulations at a range of NV depths in figure D.2 (closed symbols) and find strong agreement between the simulation and the calculation based on correlation time. We also plot the results from simulations in which the water layer is confined to 1 nm height above the diamond surface (i.e. in the z direction) (open squares). We suspect a ~ 1 nm water layer of water is normally present on the surface
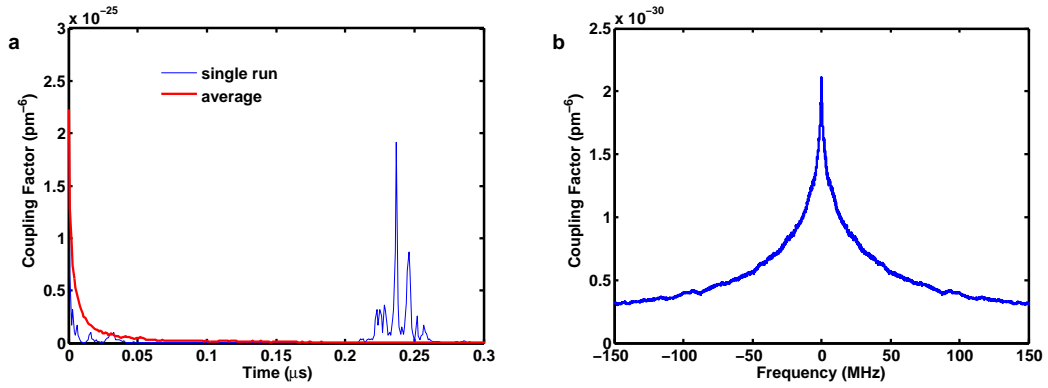
Figure D.4: Simulation of a water molecule above a 10 nm deep NV center. (a) Coupling factor as a function of time for a single run (blue) and an average of 1000 runs (red). (b) Fourier transform of the average timecourse for the coupling factor. The FWHM linewidth is 23.5 MHz.

due to hydration from moisture in the air. Confining the water in this way narrows the linewidth between 2 and 3 orders of magnitude, giving a value of ~ 100 kHz for a 10 nm deep NV center. This is significant because bulk water's linewidth of 23.5 MHz would be much too broad to detect, but the decrease in linewidth for a thin layer can narrow the signal sufficiently to be measured. The predicted 100 kHz linewidth is still broader than that detected in our experiments, indicating that other effects may also be confining the water or lowering its diffusion coefficient near the surface. Such a phenomenon has been predicted by molecular dynamics simulations [171], which calculated a diffusion coefficient near a hydrophilic diamond surface that is only 31% the value for bulk water.

In conclusion, our calculations demonstrate that NV NMR is strongly sensitive to diffusion effects for liquid samples. NV NMR measurements consequently can provide novel information about a sample's diffusion coefficients and confinement volume, which may elucidate new interfacial phenomena.

Appendix E

Hardware for NV Center Experiments

This appendix describes the NV NMR setup used for experiment in chapter 7.

E.1   Diamond samples

The diamond for single NV measurements of PFOS/POSF was a $2 \times 2 \times 0.4$ mm 99.999% ^{12}C high-purity chemical vapor deposition (CVD) chip from Element 6 with an unpolished surface, implanted with 2.5-keV ^{14}N$^+$ ions and annealed at 900 °C for 8 hours. The NV centre chosen for NV NMR measurements was in a region with a 2D NV density of 8×10^7 cm^{-2}, and its Hahn echo T_2 was 26 μs. The diamond for single NV measurements of Fomblin was a $4 \times 4 \times 0.5$ mm 99.999% ^{12}C high-purity chemical vapor deposition (CVD) chip from Element 6 with an unpolished surface, implanted with 2-keV ^{15}N$^+$ ions at a dose of 1×10^9 cm^{-2}. It was annealed at 800 °C

for z hours and cleaned in a three-acid mixture (1:1:1 nitric:sulfuric:perchloric acids). The diamond for NV ensemble measurements was a $4 \times 4 \times 0.3$ mm 99.6% ^{12}C CVD chip from Element 6 implanted with 6 keV ^{14}N$^+$ ions at a dose of 2×10^{13} cm^{-2}. The diamond was annealed at 800 °C for 2 hours, producing NV centres with a 2D density of 3.5×10^{11} cm^{-2} in a ~ 10 nm thick layer at an average depth of ~ 10 nm, estimated by Monte Carlo simulations. The ensemble Hahn echo T_2 was 3 μs.

E.2   Confocal microscope

Measurements of single NV centres were performed using a custom-built scanning confocal microscope. Optical excitation was provided by a 800 mW 532 nm diode pumped solid-state (DPSS) laser (Changchun New Industries Optoelectronics Tech MLLIII532-800-1), focused onto the diamond using a 100×, 1.3 NA oil immersion objective (Nikon CFI Plan Fluor 100× oil). The excitation laser was pulsed by focusing it through an acousto-optical modulator (Isomet 1205C-2). NV fluorescence was collected through the same objective and separated from the excitation beam using a dichroic filter (Semrock LM01-552-25). The light was additionally filtered (Semrock LP02-633RS-25) and focused onto a single-photon counting module (Perkin-Elmer SPCM-ARQH-12). Microwaves were delivered to the diamond using a 900 μm-diameter loop fabricated on a glass cover slip, with the diamond glued to the cover slip and in contact with the loop. The loop was driven by an amplified (Mini-circuits ZHL-16W-43-S+) microwave synthesizer (Windfreak SynthNV). The phase of microwave pulses was controlled using an in-phase/quadrature (IQ) mixer (Marki IQ1545LMP). Microwave and optical pulses were controlled using a computer-based digital delay

generator (SpinCore PulseBlaster ESR400). Measurement protocols (pulse sequences, data acquisition, etc.) were controlled by custom software. The static magnetic field was applied with a permanent magnet whose distance and position relative to the NV centre was controlled with a three-axis stage.

E.3   Wide-field microscope

Measurements of NV ensembles were performed using a custom-built wide-field microscope. Optical excitation was provided by a 532 nm LaserQuantum mpc6000 laser focused through a glass coverslip and the diamond chip onto the opposite diamond surface, containing the shallow, high-density NV layer, by a $100\times$ 0.9 NA air objective (Olympus MPlan N). The diamond was attached to the coverslip with Norland Blocking Adhesive 107 (Norland, Cranbury, NJ), which was cured under a UV lamp for 30 minutes. The laser was controlled with an acousto-optical modulator (Isomet M1133-aQ80L-1.5). The NV fluorescence signal was collected through the same objective and separated from the excitation beam with a dichroic mirror (Semrock LM01-552-25) and optical filters (Semrock LP02-633RS-25 and FF01-750SP-25) before being imaged onto a CCD camera (Starlight Express SXVR-H9). An optical chopper was used to block fluorescence during optical state preparation of the NV centres. Microwaves were synthesized with a signal generator (Agilent E8257D), amplified (Mini-circuits ZHL-16W-43-S+), and applied to the sample with a small wire loop placed against the diamond. The microwave pulse phase was controlled by an IQ mixer (Marki IQ1545LMP). Microwave and optical pulses were controlled by a pulse generator (SpinCore PulseBlasterESR-PRO 500 MHz) governed by custom software.

The static magnetic field was applied with a permanent magnet whose distance and position relative to the NV ensemble was controlled with a three-axis stage.

The laser spot on the diamond had a FWHM size of ~ 60 μm. For the white light image, each CCD pixel represented 200 nm x 200 nm on the diamond surface. For the NV fluorescence measurement, each CCD pixel represented 1 x 1 μm on the diamond surface, although the point spread function of the detection optics was ~ 500 nm. Smaller CCD pixels could be used, with reduced SNR. Each NV NMR measurement average was performed for 500 ms (2000 chopper cycles) at each dynamical decoupling delay, and a full dataset consisted of ~ 800 averages. For simple spectroscopic measurements, a 26 μm x 20 μm field of view was sampled and the measurements from each pixel were averaged together before further processing. For imaging, a larger field of view was sampled and each pixel was analyzed separately.

E.4   SiO$_2$ structure

The diamond used for NV ensemble NMR imaging was prepared by cleaning in piranha solution (2 parts H$_2$SO$_4$ to 1 part H$_2$O$_2$ v/v) for more than 1 hour. Using atomic layer deposition (ALD, Savannah Atomic Layer Deposition S200), a 3 nm layer of Al$_2$O$_3$ was grown on the diamond surface followed by a 90 nm layer of SiO$_2$. The deposition temperature of the substrate was 250 °C, and deposition rate was 0.5 nm/min. The SiO$_2$-coated diamond was cleaned with acetone and isopropanol and then baked for 2 minutes on a hot plate at 115 °C to remove water. The diamond was then spin coated with hexamethyldisilazane followed by photoresist S1805 and once again heated at 115 °C for 90 seconds. It was exposed with a photomask using a

Suss MicroTec MJB4 and developed with CD26 for 45 s, rinsed with deionized water, and blown dry with nitrogen. SiO_2 was etched with buffered oxide etchant (BOE) for 1 minute at an etch rate of 330 nm/min. Photoresist was then removed by soaking in acetone for 5 minutes. Finally, the diamond was cleaned in piranha solution for 1 hour.

Bibliography

[1] Gorter, C. J. & Boorse, H. A. Bad luck in attempts to make scientific discoveries. *Physics Today* **20**, 76–81 (1967).

[2] Purcell, E. M., Torrey, H. C. & Pound, R. V. Resonance absorption by nuclear magnetic moments in a solid. *Phys. Rev.* **69**, 37–38 (1946).

[3] Bloch, F., Hansen, W. W. & Packard, M. Nuclear induction. *Phys. Rev.* **69**, 127 (1946).

[4] Golman, K., in't Zandt, R., Lerche, M., Pehrson, R. & Ardenkjaer-Larsen, J. H. Metabolic imaging by hyperpolarized ^{13}C magnetic resonance imaging for *in vivo* tumor diagnosis. *Cancer Research* **66**, 10855–10860 (2006).

[5] Golman, K. & Petersson, J. S. Metabolic imaging and other applications of hyperpolarized ^{13}C. *Academic Radiology* **13**, 932–942 (2006).

[6] Yu, H. Extending the size limit of protein nuclear magnetic resonance. *Proc Natl Acad Sci USA* **96**, 332–334 (1999).

[7] Callaghan, P. T. *Principles of Nuclear Magnetic Resonance Microscopy* (Oxford University Press, Oxford, Eng., 1991).

[8] Farkas, A. *Orthohydrogen, Parahydrogen, and Heavy Hydrogen* (Cambridge University Press, Cambridge, Eng., 1935).

[9] International Institute of Refrigeration, Université de Grenoble (ed.) *Liquid hydrogen: properties, production and applications* (Pergamon Press, Oxford, UK, 1966).

[10] Carravetta, M., Johannessen, O. & Levitt, M. H. Beyond the T1 limit: Singlet nuclear spin states in low magnetic field. *Physical Review Letters* **92** (2004).

[11] Pileio, G., Carravetta, M., Hughes, E. & Levitt, M. H. The long-lived singlet state of 15N-nitrous oxide in solution. *Journal of the American Chemical Society* **130**, 12582–12583 (2008).

[12] Emondts, M. *et al.* Long-lived heteronuclear spin-singlet states in liquids at a zero magnetic field. *Physical Review Letters* **112**, 077601 (2014).

[13] Carravetta, M. & Levitt, M. H. Long-lived nuclear spin states in high-field solution NMR. *Journal of the American Chemical Society* **126**, 6228–6229 (2004).

[14] Pileio, G., Concistré, M., Carravetta, M. & Levitt, M. H. Long-lived nuclear spin states in the solution NMR of four-spin systems. *Journal of Magnetic Resonance* **182**, 353–357 (2006).

[15] Pileio, G. & Levitt, M. H. J-stabilization of singlet states in the solution NMR of multiple-spin systems. *Journal of Magnetic Resonance* **187**, 141–145 (2007).

[16] Vasos, P. R. *et al.* Long-lived states to sustain hyperpolarized magnetization. *Proceedings of the National Academy of Sciences USA* **106**, 18469–18473 (2009).

[17] Ahuja, P., Sarkar, R., Vasos, P. R. & Bodenhausen, G. Long-lived states in multiple-spin systems. *ChemPhysChem* **10** (2009).

[18] Sarkar, R., Ahuja, P., Vasos, P. R. & Bodenhausen, G. Measurement of slow diffusion coefficients of molecules with arbitrary scalar couplings via long-lived spin states. *ChemPhysChem* **9**, 2414–2419 (2008).

[19] Cavadini, S., Dittmer, J., Antonijevic, S. & Bodenhausen, G. Slow diffusion by singlet state NMR spectroscopy. *Journal of the American Chemical Society* **127**, 15744–15748 (2005).

[20] Sarkar, R., Vasos, P. R. & Bodenhausen, G. Singlet-state exchange NMR spectroscopy for the study of very slow dynamic processes. *Journal of the American Chemical Society* **129**, 328–334 (2006).

[21] Tayler, M. C. D. & Levitt, M. H. Singlet nuclear magnetic resonance of nearly-equivalent spins. *Physical Chemistry Chemical Physics* **13**, 5556–5560 (2011).

[22] Feng, Y., Davis, R. M. & Warren, W. S. Accessing long-lived nuclear singlet states between chemically equivalent spins without breaking symmetry. *Nature Physics* **8**, 831–837 (2012).

[23] Warren, W. S., Jenista, E., Branca, R. T. & Chen, X. Increasing hyperpolarized spin lifetimes through true singlet eigenstates. *Science* **323**, 1711–1714 (2009).

[24] Abragam, A. *The Principles of Nuclear Magnetism* (Oxford University Press, Oxford, Eng., 1994).

[25] Slichter, C. P. *Principles of Magnetic Resonance* (Springer-Verlag, Berlin, 1990).

[26] Ernst, R. R., Bodenhausen, G. & Wokaun, A. *Principles of Nuclear Magnetic Resonance in One and Two Dimensions* (Oxford University Press, Oxford, UK, 1987).

[27] Levitt, M. H. *Spin Dynamics: Basics of Nuclear Magnetic Resonance* (John Wiley and Sons Ltd., Chichester, Eng., 2008).

[28] Tomonaga, S. *The Story of Spin* (University of Chicago Press, Chicago, IL, 1997).

[29] Tayler, M. C. D., Marie, S., Ganesan, A. & Levitt, M. H. Determination of molecular torsion angles using nuclear singlet relaxation. *Journal of the American Chemical Society* **132**, 8225–8227 (2010).

[30] Bottomley, P. A., Redington, R. W., Edelstein, W. A. & Schenck, J. F. Estimating radiofrequency power deposition in body NMR imaging. *Magnetic Resonance in Medicine* **2**, 336–349 (1985).

[31] *International standard, medical equipment–part 2: particular requirements for the safety of magnetic resonance equipment for medical diagnosis, 2nd revision* (Geneva: International Electrotechnical Commission, 2002).

[32] Collins, C. M. & Wang, Z. Calculation of radiofrequency electromagnetic fields and their effects in mri of human subjects. *Magnetic Resonance in Medicine* **65**, 1470–1482 (2011).

[33] Levitt, M. H. Singlet and other states with extended lifetimes. *Encyclopedia of Magnetic Resonance* (2010).

[34] Some of the work in this article employed the SpinDynamica code for Mathematica, programmed by Malcolm H. Levitt, available at www.SpinDynamica.soton.ac.uk.

[35] Pileio, G. & Levitt, M. H. Theory of long-lived nuclear spin states in solution nuclear magnetic resonance. ii. singlet spin locking. *Journal of Chemical Physics* **130**, 214501 (2009).

[36] Pileio, G. & Levitt, M. H. Relaxation theory of nuclear singlet states in two spin-1/2 systems. *Progress in Nuclear Magnetic Resonance Spectroscopy* **56**, 217–231 (2010).

[37] Vinogradov, E. & Grant, A. K. Hyperpolarized long-lived states in solution NMR: Three-spin case study in low field. *Journal of Magnetic Resonance* **194**, 46–57 (2008).

[38] Vinogradov, E. & Grant, A. K. Long-lived states in solution NMR: Selection rules for intramolecular dipolar relaxation in low magnetic field. *Journal of Magnetic Resonance* **188**, 176–182 (2007).

[39] Sarkar, R., Ahuja, P., Vasos, P. R. & Bodenhausen, G. Long-lived coherences for homogeneous line narrowing in spectroscopy. *Physical Review Letters* **104**, 053001 (2010).

[40] Bornet, A., Sarkar, R. & Bodenhausen, G. Life-times of long-lived coherences under different motional regimes. *Journal of Magnetic Resonance* **206**, 154–156 (2010).

[41] Solomon, I. Relaxation processes in a system of two spins. *Physical Review* **99**, 559–565 (1955).

[42] Wheaton, A. J. *et al.* In vivo quantitation of $T_{1\rho}$ using a multislice spin-lock pulse sequence. *Magnetic Resonance in Medicine* **52**, 1453–1458 (2004).

[43] Sammet, S., Bock, M., Schlemmer, H.-P. & Bachert, P. Fast $T_{1\rho}$-NMR imaging and relaxometry of brain tumors in patients at 1.5 t. *Proceedings of the International Society for Magnetic Resonance in Medicine* **8**, 1097 (2000).

[44] Pileio, G. & Levitt, M. H. Isotropic filtering using polyhedral phase cycles: Application to singlet state NMR. *Journal of Magnetic Resonance* **191**, 148–155 (2008).

[45] Claytor, K., Theis, T., Feng, Y. & Warren, W. Measuring long-lived 13c2 state lifetimes at natural abundance. *Journal of Magnetic Resonance* **239**, 81 – 86 (2014).

[46] Wevers, R. A., Engelke, U. & Heershap, A. High-resolution ^{1}H-NMR spectroscopy of blood plasma for metabolic studies. *Clinical Chemistry* **40**, 1245–1250 (1994).

[47] Zuppi, C. *et al.* ^{1}H NMR spectra of normal urines: Reference ranges of the major metabolites. *Clinica Chimica Acta* **265**, 85–97 (1997).

[48] Coen, M., Holmes, E., Lindon, J. C. & Nicholson, J. K. NMR-based metabolic profiling and metabonomic approaches to problems in molecular toxicology. *Chemical Research in Toxicology* **21**, 9–27 (2008).

[49] Soares, D. P. & Law, M. Magnetic resonance spectroscopy of the brain: review of metabolites and clinical applications. *Clinical Radiology* **64**, 12–21 (2009).

[50] Ross, B. & Bluml, S. Magnetic resonance spectroscopy of the human brain. *The Anatomical Record (New Anat.)* **265**, 54–84 (2001).

[51] Dumoulin, C. L. & Vatis, D. Water suppression in 1H magnetic resonance images by the generation of multiple-quantum coherence. *Magnetic Resonance in Medicine* **3**, 282–288 (1986).

[52] Star-Lack, J. M. & Spielman, D. M. Zero-quantum filter offering single-shot lipid suppression and simultaneous detection of lactate, choline, and creatine resonances. *Magnetic Resonance in Medicine* **46**, 1233–1237 (2001).

[53] Lei, H. & Peeling, J. A localized double-quantum filter for in vivo detection of taurine. *Magnetic Resonance in Medicine* **42**, 454–460 (1999).

[54] Thompson, R. B. & Allen, P. S. A new multiple quantum filter design procedure for use on strongly coupled spin systems found in vivo: Its application to glutamate. *Magnetic Resonance in Medicine* **39**, 762–771 (1998).

[55] Wilman, A. H. & Allen, P. S. *In vivo* NMR detection strategies for γ-aminobutyric acid, utilizing proton spectroscopy and coherence-pathway filtering with gradients. *Journal of Magnetic Resonance, Series B* **101**, 165–171 (1993).

[56] de Graaf, R. A., Rothman, D. L. & Behar, K. L. High resolution NMR spectroscopy of rat brain *in vivo* through indirect zero-quantum-coherence detection. *Journal of Magnetic Resonance* **187**, 320–326 (2007).

[57] Doddrell, D. M. & Brereton, I. M. A selective excitation/B_0 gradient technique for high-resolution ^{1}H NMR studies of metabolites via zero-quantum coherence and polarization transfer. *NMR in Biomedicine* **2**, 39–43 (1989).

[58] Dijk, J. E. v., Mehlkopf, A. F. & Boveé, W. M. M. J. Comparison of double and zero quantum NMR editing techniques for *in vivo* use. *NMR in Biomedicine* **5**, 75–86 (1992).

[59] Rance, M., Dalvit, C. & Wright, P. E. Simplification of ^{1}H NMR spectra of proteins by one-dimensional multiple quantum filtration. *Biochemical and Biophysical Research Communications* **131**, 1094–1102 (1985).

[60] Cavanagh, J., Fairbrother, W. J., Palmer, III, A. G., Rance, M. & Skelton, N. J. *Protein NMR Spectroscopy: Principles and Practice* (Academic Press, Amsterdam, 2006).

[61] Müller, N., Ernst, R. R. & Wüthrich, K. Multiple-quantum-filtered two-dimensional correlated NMR spectroscopy of proteins. *Journal of the American Chemical Society* **108**, 6482–6492 (1986).

[62] Snyder, S. R., Kirsch, S., Kraus, K. & Bachert, P. Two-dimensional zero-quantum coherence ^{1}H NMR spectroscopy of glutamate and glutamine. *Proceedings of the International Society for Magnetic Resonance in Medicine* **16**, 1564 (2008).

[63] Thompson, R. B. & Allen, P. S. Response of metabolites with coupled spins to the STEAM sequence. *Magnetic Resonance in Medicine* **45**, 955–965 (2001).

[64] Cudalbu, C. *et al.* Metabolite concentration estimates in the rat brain by magnetic resonance spectroscopy using QUEST and two approaches to invoke prior knowledge. *IEEE Proc. ProRISC, Veldhoven, Netherlands* 609–614 (2005).

[65] Sarchielli, P. *et al.* Absolute quantification of brain metabolites by proton magnetic resonance spectroscopy in normal-appearing white matter of multiple sclerosis patients. *Brain* **122**, 513–521 (1999).

[66] Birken, D. L. & Oldendorf, W. H. N-acetyl-l-aspartic acid: A literature review of a compound prominent in ^{1}H-NMR spectroscopic studies of brain. *Neuroscience and Biobehavioral Reviews* **13**, 23–31 (1989).

[67] Wallwork, J. C. & Sandstead, H. H. Effect of zinc deficiency on appetite and free amino acid concentrations in rat brain. *Journal of Nutrition* **113**, 47–54 (1983).

[68] Choi, C. *et al.* Proton spectral editing for discrimination of lactate and threonine 1.31 ppm resonances in human brain in vivo. *Magnetic Resonance in Medicine* **56**, 660–665 (2006).

[69] Schubert, F., Gallinat, J., Seifert, F. & Rinneberg, H. Glutamate concentrations in human brain using single voxel proton magnetic resonance spectroscopy at 3 Tesla. *NeuroImage* **21**, 1762–1771 (2004).

[70] Mason, G. F. *et al.* Detection of brain glutamate and glutamine in spectroscopic images at 4.1 T. *Magnetic Resonance in Medicine* **32**, 142–145 (1994).

[71] Choi, C. *et al.* Measurement of brain glutamate and glutamine by spectrally-selective refocusing at 3 Tesla. *Magnetic Resonance in Medicine* **55**, 997–1005 (2006).

[72] Hu, J. *et al.* Simultaneous detection of resolved glutamate, glutamine, and γ-aminobutyric acid at 4 T. *Journal of Magnetic Resonance* **185**, 204–213 (2007).

[73] Lee, H. K., Yaman, A. & Nalcioglu, O. Homonuclear J-refocused spectral editing technique for quantification of glutamine and glutamate by ^{1}H NMR spectroscopy. *Magnetic Resonance in Medicine* **34**, 253–259 (1995).

[74] Yang, S., Hu, J., Kou, Z. & Yang, Y. Spectral simplification for resolved glutamate and glutamine measurement using a standar STEAM sequence with optimized timing parameters at 3, 4, 4.7, 7, and 9.4 T. *Magnetic Resonance in Medicine* **59**, 236–244 (2008).

[75] DeVience, S. J., Walsworth, R. L. & Rosen, M. S. Dependence of nuclear spin singlet lifetimes on RF spin-locking power. *Journal of Magnetic Resonance* **218**, 5–10 (2012).

[76] Pileio, G. & Levitt, M. H. Theory of long-lived nuclear spin states in solution nuclear magnetic resonance. II. singlet spin locking. *The Journal of Chemical Physics* **130** (2009).

[77] Hartmann, S. R. & Hahn, E. L. Nuclear double resonance in the rotating frame. *Physical Review* **128**, 2042–2053 (1962).

[78] Theis, T., Feng, Y., Wu, T. & Warren, W. S. Composite and shaped pulses for efficient and robust pumping of disconnected eigenstates in magnetic resonance. *The Journal of Chemical Physics* **140**, 014201 (2014).

[79] Massiot, D. *et al.* Detection and use of small j couplings in solid state NMR experiments. *Comptes Rendus Chimie* **13**, 117–129 (2010).

[80] Karplus, M. Contact electron-spin coupling of nuclear magnetic moments. *Journal of Chemical Physics* **30**, 11–15 (1958).

[81] Karplus, M. Vicinal proton coupling in nuclear magnetic resonance. *Journal of the American Chemical Society* **85**, 2870–2871 (1963).

[82] Lidar, D. A. Review of decoherence free subspaces, noiseless subsystems, and dynamical decoupling. *arXiv:1208.5791v3* (2012).

[83] Antonio, B. & Bose, S. Two-qubit gates for decoherence-free qubits using a ring exchange interaction. *Phys. Rev. A* **88**, 042306 (2013).

[84] Aue, W. P., Bartholdi, E. & Ernst, R. R. Twodimensional spectroscopy. application to nuclear magnetic resonance. *The Journal of Chemical Physics* **64**, 2229–2246 (1976).

[85] Blanchard, J. W. *et al.* High-resolution zero-field nmr j-spectroscopy of aromatic compounds. *Journal of the American Chemical Society* **135**, 3607–3612 (2013).

[86] Mohori, A. & Stepinik, J. NMR in the earths magnetic field. *Progress in Nuclear Magnetic Resonance Spectroscopy* **54**, 166 – 182 (2009).

[87] Blmich, B., Casanova, F. & Appelt, S. Nmr at low magnetic fields. *Chemical Physics Letters* **477**, 231–240 (2009).

[88] Ledbetter, M. P. *et al.* Optical detection of NMR J-spectra at zero magnetic field. *Journal of Magnetic Resonance* **199**, 25–29 (2009).

[89] McDermott, R. *et al.* Liquid-state NMR and scalar couplings in microtesla magnetic fields. *Science* **295**, 2247–2249 (2002).

[90] Theis, T. *et al.* Chemical analysis using¡ i¿ j¡/i¿-coupling multiplets in zero-field nmr. *Chemical Physics Letters* **580**, 160–165 (2013).

[91] Butler, M. C. *et al.* Multiplets at zero magnetic field: The geometry of zero-field nmr. *The Journal of chemical physics* **138**, 184202 (2013).

[92] Appelt, S., Häsing, F. W., Kühn, H. & Blümich, B. Phenomena in J-coupled nuclear magnetic resonance spectroscopy in low magnetic fields. *Physical Review A* **76**, 023420 (2007).

[93] Halse, M. E., Callaghan, P. T., Feland, B. C. & Wasylishen, R. E. Quantitative analysis of earths field {NMR} spectra of strongly-coupled heteronuclear systems. *Journal of Magnetic Resonance* **200**, 88–94 (2009).

[94] Tsai, L. L., Mair, R. W., Rosen, M. S., Patz, S. & Walsworth, R. L. An open-access, very-low-field mri system for posture-dependent ^{3}he human lung imaging. *Journal of Magnetic Resonance* **193**, 274–285 (2008).

[95] Halse, M. E. & Callaghan, P. T. A dynamic nuclear polarization strategy for multi-dimensional earths field {NMR} spectroscopy. *Journal of Magnetic Resonance* **195**, 162 – 168 (2008).

[96] Potenza, J. Measurement and applications of dynamic nuclear polarization. *Advances in Molecular Relaxation Processes* **4**, 229–354 (1972).

[97] Maze, J. R. *et al.* Nanoscale magnetic sensing with an individual electronic spin in diamond. *Nature* **455**, 644–647 (2008).

[98] Taylor, J. M. *et al.* High-sensitivity diamond magnetometer with nanoscale resolution. *Nature Physics* **4**, 810–816 (2008).

[99] Maertz, B. J., Wijnheijmer, A. P., Fuchs, G. D., Nowakowski, M. E. & Awschalom, D. D. Vector magnetic field microscopy using nitrogen vacancy centers in diamond. *Applied Physics Letters* **96**, 092504 (2010).

[100] Steinert, S. *et al.* High sensitivity magnetic imaging using an array of spins in diamond. *Review of Scientific Instruments* **81**, 043705 (2010).

[101] Pham, L. M. *et al.* Magnetic field imaging with nitrogen-vacancy ensembles. *New Journal of Physics* **13**, 045021 (2011).

[102] Le Sage, D. *et al.* Optical magnetic imaging of living cells. *Nature* **496**, 486–489 (2013).

[103] Dolde, F. *et al.* Electric-field sensing using single diamond spins. *Nature Physics* **7**, 459–463 (2011).

[104] Childress, L. *et al.* Coherent dynamics of coupled electron and nuclear spin qubits in diamond. *Science* **314**, 281–285 (2006).

[105] Maurer, P. C. *et al.* Room-temperature quantum bit memory exceeding one second. *Science* **336**, 1283–1286 (2012).

[106] Jiang, L. *et al.* Repetitive readout of a single electronic spin via quantum logic with nuclear spin ancillae. *Science* **326**, 267–272 (2009).

[107] Togan, E. *et al.* Quantum entanglement between an optical photon and a solid-state spin qubit. *Nature* **466**, 730–734 (2010).

[108] Doherty, M. W., Manson, N. B., Delaney, P. & Hollenberg, L. C. The negatively charged nitrogen-vacancy centre in diamond: the electronic solution. *New Journal of Physics* **13**, 025019 (2011).

[109] Schirhagl, R., Chang, K., Loretz, M. & Degen, C. L. Nitrogen-vacancy centers in diamond: Nanoscale sensors for physics and biology. *Annual Review of Physical Chemistry* **65**, 83–105 (2014).

[110] Jelezko, F. & Wrachtrup, J. Single defect centres in diamond: A review. *physica status solidi (a)* **203**, 3207–3225 (2006).

[111] Deák, P., Aradi, B., Kaviani, M., Frauenheim, T. & Gali, A. Calculation ofthe transitions and migration of nitrogen and vacancy related defects, with implications on the formation of NV centers in bulk diamond. *arXiv:1311.6598* (2013).

[112] Edmonds, A. *et al.* Production of oriented nitrogen-vacancy color centers in synthetic diamond. *Physical Review B* **86**, 035201 (2012).

[113] Ohno, K. *et al.* Engineering shallow spins in diamond with nitrogen delta-doping. *Applied Physics Letters* **101**, 082413 (2012).

[114] Ofori-Okai, B. *et al.* Spin properties of very shallow nitrogen vacancy defects in diamond. *Physical Review B* **86**, 081406 (2012).

[115] Orwa, J. O. *et al.* Engineering of nitrogen-vacancy color centers in high purity diamond by ion implantation and annealing. *Journal of Applied Physics* **109**, 083530 (2011).

[116] Maze, J. *et al.* Properties of nitrogen-vacancy centers in diamond: the group theoretic approach. *New Journal of Physics* **13**, 025025 (2011).

[117] Robledo, L., Bernien, H., van der Sar, T. & Hanson, R. Spin dynamics in the optical cycle of single nitrogen-vacancy centres in diamond. *New Journal of Physics* **13**, 025013 (2011).

[118] Neumann, P. *et al.* Quantum register based on coupled electron spins in a room-temperature solid. *Nature Physics* **6**, 249–253 (2010).

[119] Fuchs, G. D. *et al.* Excited-state spin coherence of a single nitrogen vacancy centre in diamond. *Nature Physics* **6**, 668–672 (2010).

[120] Waldherr, G. *et al.* Dark states of single nitrogen-vacancy centers in diamond unraveled by single shot nmr. *Physical Review Letters* **106**, 157601 (2011).

[121] Maze, J. R. *Quantum manipulation of nitrogen-vacancy centers in diamond: from basic properties to applications.* Ph.D. thesis, Harvard University (2010).

[122] Tetienne, J. *et al.* Magnetic-field-dependent photodynamics of single nv defects in diamond: an application to qualitative all-optical magnetic imaging. *New Journal of Physics* **14**, 103033 (2012).

[123] Almog, I. *et al.* Direct measurement of the system–environment coupling as a tool for understanding decoherence and dynamical decoupling. *Journal of Physics B: Atomic, Molecular and Optical Physics* **44**, 154006 (2011).

[124] Álvarez, G. A. & Suter, D. Measuring the spectrum of colored noise by dynamical decoupling. *Physical Review Letters* **107**, 230501 (2011).

[125] Bylander, J. *et al.* Noise spectroscopy through dynamical decoupling with a superconducting flux qubit. *Nature Physics* **7**, 565–570 (2011).

[126] Bar-Gill, N. *et al.* Suppression of spin-bath dynamics for improved coherence of multi-spin-qubit systems. *Nature communications* **3**, 858 (2012).

[127] Mansfield, P. Snapshot magnetic resonance imaging (nobel lecture). *Angewandte Chemie International Edition* **43**, 5456–5464 (2004).

[128] Glover, P. & Mansfield, P. Limits to magnetic resonance microscopy. *Reports on Progress in Physics* **65**, 1489 (2002).

[129] Edelstein, W. A., Glover, G. H., Hardy, C. J. & Redington, R. W. The intrinsic signal-to-noise ratio in NMR imaging. *Magnetic Resonance in Medicine* **3**, 604–618 (1986).

[130] Kraus, R. H., Jr., Espy, M. A., Magnelind, P. E. & Volegov, P. L. *Ultra-Low Field Nuclear Magnetic Resonance: A New MRI Regime* (Oxford University Press, Oxford, Eng., 2014).

[131] Kovacs, H., Moskau, D. & Spraul, M. Cryogenically cooled probes – a leap in NMR technology. *Progress in Nuclear Magnetic Resonance Spectroscopy* **46**, 131–155 (2005).

[132] Bending, S. J. Local magnetic probes of superconductors. *Advances in Physics* **48**, 449–535 (1999).

[133] Budker, D. & Romalis, M. Optical magnetometry. *Nature Physics* **3**, 227–234 (2007).

[134] Nowack, K. C. *et al.* Imaging currents in hgte quantum wells in the quantum spin hall regime. *Nature materials* **12**, 787–791 (2013).

[135] Rugar, D., Budakian, R., Mamin, H. J. & Chui, B. W. Single spin detection by magnetic resonance force microscopy. *Nature* **430**, 329–332 (2004).

[136] Degen, C., Poggio, M., Mamin, H., Rettner, C. & Rugar, D. Nanoscale magnetic resonance imaging. *Proceedings of the National Academy of Sciences* **106**, 1313–1317 (2009).

[137] Balasubramanian, G. *et al.* Nanoscale imaging magnetometry with diamond spins under ambient conditions. *Nature* **455**, 648–651 (2008).

[138] Belthangady, C. *et al.* Dressed-state resonant coupling between bright and dark spins in diamond. *Physical Review Letters* **110**, 157601 (2013).

[139] Kolkowitz, S., Unterreithmeier, Q. P., Bennett, S. D. & Lukin, M. D. Sensing distant nuclear spins with a single electron spin. *Physical review letters* **109**, 137601 (2012).

[140] Taminiau, T. *et al.* Detection and control of individual nuclear spins using a weakly coupled electron spin. *Physical review letters* **109**, 137602 (2012).

[141] Grinolds, M. S. *et al.* Sub-nanometer resolution in three-dimensional magneti resonance imaging of individual dark spins. *Nature Nanotechnology* **9**, 279–284 (2014).

[142] Grinolds, M. *et al.* Nanoscale magnetic imaging of a single electron spin under ambient conditions. *Nature Physics* **9**, 215–219 (2013).

[143] Mamin, H. J. *et al.* Nanoscale nuclear magnetic resonance with a nitrogen vacancy center. *Science* **339**, 557–560 (2013).

[144] Staudacher, T. *et al.* Nuclear magnetic resonance spectroscopy on a (5-nanometer)^3 sample volume. *Science* **339**, 561–563 (2013).

[145] Loretz, M., Pezzagna, S., Meijer, J. & Degen, C. L. Nanoscale nuclear magnetic resonance with a 1.9-nm-deep nitrogen-vacancy sensor. *Applied Physics Letters* **104**, 033102 (2014).

[146] Sushkov, A. O. *et al.* All-optical sensing of a single-molecule electron spin. *Physical Review Letters* (2014). (In Press).

[147] Gullion, T., Baker, D. B. & Conradi, M. S. New, compensated carr-purcell sequences. *Journal of Magnetic Resonance* **89**, 479–484 (1990).

[148] de Lange, G., Ristè, D., , Dobrovitski, V. V. & Hanson, R. Single-spin magnetometry with multi-pulse dynamical decoupling sequences. *Physical Review Letters* **106**, 080802 (2011).

[149] Naydenov, B. *et al.* Dynamical decoupling of a single-electron spin at room temperature. *Physical Review B: Rapid Communications* **83**, 081201 (2011).

[150] Ryan, C. A., Hodges, J. S. & Cory, D. G. Robust decoupling techniques to extend quantum coherence in diamond. *Physical Review Letters* **105**, 200402 (2010).

[151] Bar-Gill, N., Pham, L. M., Jarmola, A., Budker, D. & Walsworth, R. Solid-state electronic spin coherence time approaching one second. *Nature Communications* **4** (2013).

[152] Cywiński, L., Lutchyn, R. M., Nave, C. P. & Das Sarma, S. How to enhance dephasing time in superconducting qubits. *Physical Review B* **77**, 174509 (2008).

[153] Hall, L. T., Cole, J. H., Hill, C. D. & Hollenberg, L. C. L. Sensing of fluctuating nanoscale magnetic fields using nitrogen-vacancy centers in diamond. *Physical Review Letters* **103**, 220802 (2009).

[154] Fuller, G. H. *Nuclear Spins and Moments* (American Chemical Society, New York, NY, USA, 1976).

[155] Werschnik, J. & Gross, E. K. U. Quantum optimal control theory. *Journal of Physics B: Atomic, Molecular and Optical Physics* **40**, R175 (2007).

[156] Rethinam, M. J., Javali, A. K., Behrman, E., Steck, J. & Skinner, S. A genetic algorithm for finding pulse sequences for nmr quantum computing. *arXiv preprint quant-ph/0404170* (2004).

[157] Manu, V. & Kumar, A. Singlet-state creation and universal quantum computation in nmr using a genetic algorithm. *Physical Review A* **86**, 022324 (2012).

[158] Ajoy, A. & Kumar, A. Hierarchical genetic algorithm approach to determine pulse sequences in nmr. *arXiv preprint arXiv:0911.5465* (2009).

[159] Pileio, G. Singlet state relaxation via intermolecular dipolar coupling. *The Journal of Chemical Physics* **134**, 214505 (2011).

[160] Gopalakrishnan, K. & Bodenhausen, G. Lifetimes of the singlet-states under coherent off-resonance irradiation in NMR spectroscopy. *Journal of Magnetic Resonance* **182**, 254–259 (2006).

[161] Tayler, M. C. D. & Levitt, M. H. Paramagnetic relaxation of nuclear singlet states. *Phys. Chem. Chem. Phys.* **13**, 9128–9130 (2011).

[162] Ghosh, R. K. *et al.* Measurements of the persistent singlet state of N_2O in blood and other solvents–potential as a magnetic tracer. *Magnetic Resonance in Medicine* **66**, 1177–1180 (2011).

[163] Bracewell, R. N. *The Fourier Transform and Its Applications, 3rd Ed.* (New York: McGraw-Hill, 2000).

[164] Schwabl, F. *Advanced Quantum Mechanics* (Berlin: Springer, 2005).

[165] Hubbard, P. S. Nuclear magnetic relaxation by intermolecular dipole-dipole interactions. *Physical Review* **131**, 275 (1963).

[166] O'Reilly, D. E. Self-diffusion coefficients and rotational correlation times in polar liquids. VI. Water. *Journal of Chemical Physics* **60**, 1607–1618 (1974).

[167] Immersion oil type-f (Accessed May 15, 2014). URL `http://www.scientificimagingcompany.com/products/immersion-oil-type-f`.

[168] Tanaka, T. Immersion oil composition having low fluorescence emissions for microscope (1988). URL `https://www.google.com/patents/US4789490`. US Patent 4,789,490.

[169] Fetters, L., Hadjichristidis, N., Lindner, J. & Mays, J. Molecular weight dependence of hydrodynamic and thermodynamic properties for well-defined linear polymers in solution. *Journal of physical and chemical reference data* **23**, 619–640 (1994).

[170] Ruiz Barlett, V., Hoyuelos, M. & Martin, H. Comparison between fixed and gaussian steplength in monte carlo simulations for diffusion processes. *Journal of Computational Physics* **230**, 3719–3726 (2011).

[171] Sendner, C., Horinek, D., Bocquet, L. & Netz, R. R. Interfacial water at hydrophobic and hydrophilic surfaces: Slip, viscosity, and diffusion. *Langmuir* **25**, 10768–10781 (2009).